



HAL
open science

Biomechanics between the cerebrospinal fluid and the spinal central nervous system: towards a modelling of fluid-structure interactions.

Patrice Sudres

► **To cite this version:**

Patrice Sudres. Biomechanics between the cerebrospinal fluid and the spinal central nervous system: towards a modelling of fluid-structure interactions.. Biotechnology. Université Aix-Marseille, 2021. English. NNT: . tel-03137767

HAL Id: tel-03137767

<https://amu.hal.science/tel-03137767>

Submitted on 10 Feb 2021

HAL is a multi-disciplinary open access archive for the deposit and dissemination of scientific research documents, whether they are published or not. The documents may come from teaching and research institutions in France or abroad, or from public or private research centers.

L'archive ouverte pluridisciplinaire **HAL**, est destinée au dépôt et à la diffusion de documents scientifiques de niveau recherche, publiés ou non, émanant des établissements d'enseignement et de recherche français ou étrangers, des laboratoires publics ou privés.

THÈSE DE DOCTORAT

Soutenue à Aix-Marseille Université
le 5 Mars 2021 par

Patrice SUDRES

Biomechanics between the cerebrospinal fluid and the spinal central nervous system: towards a modelling of fluid-structure interactions

Discipline

Sciences du Mouvement Humain

École doctorale

463 – Sciences du Mouvement Humain

Laboratoire/Partenaires de recherche

Laboratoire de Biomécanique Appliquée

UMR T24

Laboratoire International Associé iLab-Spine

• Composition du jury

- **Sébastien LAPORTE** Rapporteur
- ENSAM- Institut de biomécanique Humaine Georges
- Charpak
- **Stéphane AVRIL** Rapporteur
- MINES Saint -Etienne - Centre for Biomedical and
- Healthcare Engineering
- **David FLETCHER** Examineur
- The university of Sydney – School of Chemical and
- Biomolecular Engineering
- **Arnaud DAGAIN** Examineur
- Service de Neurochirurgie HIA Sainte Anne
- **Pierre-Hugues ROCHE** Examineur
- Département Neurochirurgie, APHM, Hôpital Nord
- **Pierre-Jean ARNOUX** Directeur de thèse
- AMU/UGE - Laboratoire de Biomécanique Appliquée
- **Morgane EVIN** Co-directrice de thèse
- AMU/UGE - Laboratoire de Biomécanique Appliquée

"Je suis pessimiste par l'intelligence, mais optimiste par la volonté. "

Antonio Gramsci (*Lettres de prison*, 1947),
Citation inspirée de Romain Rolland

Affidavit

I, undersigned, Patrice SUDRES, hereby declare that the work presented in this manuscript is my own work, carried out under the scientific direction of Pierre-Jean ARNOUX and Morgane EVIN, in accordance with the principles of honesty, integrity and responsibility inherent to the research mission. The research work and the writing of this manuscript have been carried out in compliance with both the French national charter for Research Integrity and the Aix-Marseille University charter on the fight against plagiarism.

This work has not been submitted previously either in this country or in another country in the same or in a similar version to any other examination body.

Place: MARSEILLE, date: 11 Janvier 2021



Cette œuvre est mise à disposition selon les termes de la Licence Creative Commons Attribution - Pas d'Utilisation Commerciale - Pas de Modification 4.0 International.

Résumé

La myélopathie cervicale dégénérative (DCM) est une cause fréquente de lésion de la moelle épinière chez les populations âgées. Pour mieux comprendre les interactions biomécaniques entre le système nerveux central du rachis et l'écoulement du fluide céphalo-rachidien dans une population saine ainsi que mieux comprendre la physiopathologie de la DCM. Pour ce faire, la modélisation biomécanique est nécessaire. Cette thèse vise à fournir une description morphométrique du canal cervical et une description mécanique des méninges du rachis qui pourront conduire au futur développement de modèles numériques avec des interactions fluide-structure.

Dans la première partie, une méthodologie a été développée pour décrire la morphométrie du canal cervical avec de nouvelles métriques à l'aide d'IRM de populations saines et avec DCM. Cette méthodologie pourrait également être utilisée pour l'amélioration du diagnostic dans un contexte de recherche clinique et pour la définition de la géométrie spécifique au sujet dans un contexte de modélisation biomécanique.

Dans la deuxième partie, deux protocoles de test mécanique ont été réalisés pour décrire les propriétés mécaniques en tension les méninges de rachis porcins choisis comme un modèle similaire à l'humain. Des tests uni-axiaux ont tout d'abord permis de fournir de nouvelles données relatives à une description élastique et hyper-élastique isotrope des méninges montrant une tendance à la dépendance au niveau rachidien des propriétés mécaniques, tandis que des tests biaxiaux ont été effectués pour détailler le comportement du tissu en comparant des lois constitutives hyper-élastiques isotropes et anisotropes. Ces données expérimentales jouent un rôle crucial dans la modélisation biomécanique numérique des interactions entre le liquide céphalo-rachidien et le système nerveux central rachidien.

Dans la troisième partie, la formulation mathématique d'un problème d'interaction fluide-structure entre un fluide newtonien et un solide élastique linéaire a été développée. Ainsi, un modèle FSI préliminaire et simplifié a été développé avec un solveur explicite (RADIOSS) comme preuve de concept. Enfin, d'autres approches FSI ont été discutées en tant que solutions de modélisation alternatives. Cette thèse pourrait ainsi aider la communauté scientifique à développer des modèles biomécaniques du canal rachidien en prenant en compte le rôle du flux céphalo-rachidien et des tissus nerveux dans des cas sains ou pathologiques.

Mots clés : canal rachidien, morphométrie, propriétés mécaniques, interactions fluide-structures, biomécanique.

Abstract

Degenerative cervical myelopathy (DCM) is a common cause of spinal cord injury for elderly population. To better understand the biomechanical interactions between the spinal central nervous system and the cerebrospinal flow in healthy population as well as the pathophysiology of DCM, biomechanical modeling is necessary. This PhD aims to provide morphometrical description of the cervical canal and mechanical description of spinal meninges which will drive to the preliminary development of numerical models with fluid-structure interactions in healthy of pathological conditions such as for DCM.

In the first part, a methodology was developed for 3D MRI-based detailed morphometrical descriptions of healthy and DCM populations. This methodology could be equally used for diagnosis improvement in a clinical research context and for subject-specific geometry definition in a biomechanical context.

In the secondly part, two mechanical testing protocol were performed to describe tensile mechanical properties of spinal porcine meninge as human model. Uni-axial tests firstly provided new elastic and isotropic hyperelastic description of meninges showing a tend to spinal level dependency while bi-axial tests were performed to more detailed the tissue in comparing isotropic and anisotropic hyperelastic constitutive laws. These experimental data plays a crucial role in the numerical biomechanical modelling of the interactions between the cerebrospinal fluid and the spinal central nervous system.

In the third part, the mathematical formulation of a fluid-structure interaction problem between a Newtonian fluid and a linear elastic solid was developed. Thus, a preliminary simplistic FSI model was developed with an explicit solver (RADIOSS) as a proof-of -concept. Finally, others FSI approaches were discussed as alternative modelling solutions.

Thus, this PhD might help scientific community to develop biomechanical models of the spinal canal in taking into account the role of cerebrospinal flow and the nervous tissues in healthy or an in pathological cases.

Keywords: spinal canal, morphometry, mechanical properties, fluid-structure interactions, biomechanics

Remerciements

Ce travail de thèse a pu être réalisable grâce à la participation et à la collaboration de nombreux acteurs, institutions et personnes. Cette thèse s'est déroulée grâce un environnement riche en interactions scientifiques ainsi qu'à un soutien infini des gens avec qui j'ai pu travailler et de mes proches. J'aimerais exprimer des remerciements appuyés envers les personnes citées ci-dessous.

Merci à ma directrice Morgane EVIN et à mon directeur Pierre-Jean ARNOUX de m'avoir fait confiance, de m'avoir accueilli au sein du LBA, de m'avoir soutenu dans mes phases d'angoisses récurrentes, dans mes doutes, dans mes prises de décisions et d'avoir été constamment disponible. Merci pour votre présence à tous les horaires du jour et de la nuit, et merci pour votre positivité à toute épreuve !

Merci à l'Université Aix-Marseille d'avoir financièrement soutenu cette thèse par une bourse de recherche obtenue sur Concours de l'Ecole Doctorale Sciences du Mouvement Humain 463.

Merci à l'Université Gustave Eiffel qui fournit une partie des ressources du LBA.

Merci à Virginie CALLOT d'avoir accepté de collaborer dans le cadre du laboratoire international associé iLab Spine sur ce travail de thèse. Grâce à tes connaissances en imagerie par résonance magnétique et en morphométrie humaine, à ta disponibilité et à ton soutien, nous avons pu transformer une partie de ce travail en publication ! Merci pour ta constante bonne humeur.

Merci à Yvan PETIT et Eric WAGNAC d'avoir accepté de collaborer dans le cadre du laboratoire international associé iLab-Spine et de réaliser une partie de ce travail de thèse dans leur laboratoire au sein du Laboratoire d'Imagerie en Orthopédie, de l'Ecole de Technologie Supérieure de Montréal et de l'Hôpital du Sacré-Cœur de Montréal. Vous m'avez conseillé et m'avez donné accès à des ressources essentielles pour mener à bien l'étude de caractérisation uni-axiale de méninges porcines. Vous avez également su rester disponible dans les moments les plus délicats de la thèse. Merci pour votre accueil et votre gentillesse !

Merci à Yannick Tillier et Christophe Pradille pour avoir accepté de nous prêter leur machine bixax pour réaliser nos pré-tests ainsi que pour leur aide au Centre de Mise En Forme des Matériaux MINES ParisTech (Sophia Antipolis).

Merci aux membres du jury pour leur participation. J'aimerais remercier Sébastien Laporte et Stéphane Avril d'avoir accepté d'évaluer ma thèse en tant que rapporteur et David Fletcher, Pierre-Hugues Roche et Arnaud Dagain d'avoir accepté d'être examinateurs de ce travail de thèse .

J'aimerais également remercier le laboratoire CEMEREM-CRMBM ainsi que toutes les personnes avec qui j'ai pu interagir dans ce laboratoire durant ces trois années : Héli, Amira, Aurélien, Simon, Arash.

Merci à tout le personnel ainsi qu'à tous les étudiants que j'ai pu rencontrer lors de mes deux voyages à Montréal dans l'ensemble des institutions québécoises qui collaborent au sein laboratoire international associé iLab-Spine (Ecole de Technologie Supérieure de Montréal, Hôpital du Sacré-Cœur de Montréal, Polytechnique Montréal, CHU Sainte Justine). Merci à Nicolas (pour nos expé nocturnes, ta gentillesse et ta disponibilité !), Marie-Hélène (pour toutes nos discussions, nos moments partagés et ton accueil à Montréal), Florian (pour ton accueil et tes conseils sur la Bose !), Annie, Jean-Michel, Lucien (pour ta disponibilités et tes réponses toujours aussi précises !), Elizabeth (côté ETS) et Roxanne (pour toutes nos discussions, nos moments partagés et ton accueil à Montréal) (côté Poly Montréal) ainsi qu'à ceux que j'aurais oublié dans cette liste.

Merci à Frédéric Brocard pour son aide et pour l'accès à l'imagerie bi-photon de l'Institut de Neurosciences de la Timone (Marseille).

Merci à la « 1656 » et à Pipot !, une colocation où le mot sommeil n'existe pas et qui a su m'accueillir dans le plus chaleureux des appartements. On se revoit très bientôt...

Merci à Anthony MELOT pour les discussions passionnantes qu'on a pu avoir ainsi que pour ta patience lors de nos premiers essais expérimentaux.

Merci à tout le personnel et aux étudiants du LBA pour votre aide directe ou indirecte: Lucie, Audrey, Yves, Lionel, Catherine, Jean-Louis, Max, Michel, Maxime, Guillermo (et Glawdys), Manon, Oscar, Floriane, Nawfal, Caroline, Audrey, Andrea, Wei, Arthur, Marine, Quentin (l'étudiant), Quentin (le thanato), Axel, Claire, Pierre-Guillaume, Guillaume, en espérant n'oublier personne et en saluant ceux que j'aurais omis dans cette liste. Nos passionnantes discussions et votre gentillesse ont été omniprésentes pendant ces trois ans !

Merci à Brieg, tes « saluuuut miiiiinooooooooo » matinaux vont me manquer. Grâce à toi, on a pu traverser ensemble nos galères avec de bonnes grosses rigolades pendant cette thèse minot ! Merci également à Mégane de nous avoir supporté et d'avoir pu partager plein de bons moments entre néo-aixoïses ! En parlant de néo-aixoïses, merci à Tristan et Iris pour tous ces moments partagés, au travail et en dehors, merci pour ton infinie gentillesse !

Merci à Donatien et Fred avec qui j'ai (très souvent) pu découvrir Marseille by night !

J'aimerais remercier tous les copains de Paris que j'ai rencontré pendant (« L'auberge du strabisme » !) et en dehors de mes études et qui m'ont soutenu chacun à leur manière : Pierre, Thibault, Brahim, Magatte, Tristan, Christophe et Clément (merci pour votre accueil si chaleureux pour mes retours sur Paris), Christophe, Nolwenn, Mickael. Un grand merci à Chloé et Adrian pour toutes les découvertes culturelles et fêtardes qu'on a partagé ensemble et pour votre très confortable clic-clac !

Un merci très particulier aux « Patoubateuws » : à Fano, JV, Léa, Jérémy, Pauline, Vanina, Pechaud et Benji, et à ceux arrivés en route Raphaël et Kalyani, vous avez su me transmettre votre motivation et vos encouragements depuis nos premières années d'étude !

Merci aux copains du « FRAMMPL » : Fanny, Robin, Antoine (et Anaïs), Marion, Marie et Pierre-Louis. Le temps passe et vous êtes toujours présents depuis si longtemps !

Merci Mr Thibaut, Mr Fontès, Mr Swider, Mr Watier, Maxim Van Den Abbeele, Emmanuelle Ferrero et Mme Skalli de m'avoir transmis leur goût de la connaissance, leur curiosité et leur confiance à différents moments de mon parcours académique. Vos conseils me sont encore essentiels !

J'aimerais bien évidemment remercier ma famille, en particulier mes parents pour leur soutien inébranlable, leur patience envers mon caractère (pas toujours) facile. Merci à Romain et Morgane pour leur patience, leur soutien, tous les moments partagés ensemble et pour l'énergie qu'ils ont su me transmettre. Merci à Lise pour ces encouragements inestimables.

Merci à mes grands-parents pour tout.

Ces quelques phrases ne sont pas assez pour vous décrire ma profonde affection.

A ceux que je ne reverrais plus,
A qui j'ai pensé, je pense et je penserai encore très fort...

Table of Contents

Affidavit	5
Résumé.....	6
Abstract	7
Remerciements	8
List of figures	11
List of tables	13
General Introduction	14
Chapter 1 - Anatomy	18
1.The spine and the spinal canal	20
2.Biomechanical characteristics, physiology, motion and pulsation of the CSF system	30
3.Clinical and biomechanical contexts	33
Chapter 2 – Literature Review	49
1.Studying cervical spinal canal morphometry	50
2.Studying mechanical properties of the mechanical properties of the CNS and the CSF	51
3.Studying the CSF flow and the central nervous system modelling.....	58
Chapter 3 - Morphometry of the human cervical canal	74
1.Cervical canal morphology : effects of neck flexion in normal conditions – New elements for Biomechanical simulations and surgical management.....	75
2. Degenerative cervical myelopathy morphology : effects of decompressive surgery by laminectomy -New elements for patient follow-up.....	90
3. References	115
Chapter 4.....	120
Mechanical properties of spinal porcine meninges	120
1. Tensile Mechanical Properties of the Cervical, Thoracic and Lumbar Porcine Spinal Meninges.....	121
2. Experimental Bi-axial Tensile Tests of Meningeal Tissues and Constitutive Models Comparison	148
3. References	169
Chapter 5 - Towards fluid-structure modelling.....	175
1. Mathematical background.....	176
2. Monolithics FSI modelling investigation in RADIOSS.....	186
General conclusions and perspectives.....	194
1. Main results and limitations	194
2. Perspectives.....	195
3. References - Chapter 5 and General conclusions and perspectives	198
Scientific communications.....	199
Research grants	199

List of figures

FIGURE 1 ANATOMICAL PLANES	19
FIGURE 2 GLOBAL OVERVIEW OF THE SPINE.	20
FIGURE 3 VERTEBRAL CANAL AND CENTRAL NERVOUS SYSTEM.	21
FIGURE 4 FUNCTIONAL AND DESCRIPTIVE ANATOMY OF THE SPINAL CORD	22
FIGURE 5 SPINAL NERVES.	23
FIGURE 6 HUMAN LUMBAR DURA MATER SAMPLE	25
FIGURE 7 HUMAN LAMINA ARACHNOID.....	26
FIGURE 8 PIA MATER.....	27
FIGURE 9 THE DENTICULATE LIGAMENTS.	28
FIGURE 10 SKELETAL PORCINE ANATOMY	29
FIGURE 11 CSF CIRCULATION IN THE SUBARACHNOID SPACE	32
FIGURE 12 CSF VELOCITY PROFILE OF YOUNG FEMALE AND MALE OVER A TYPICAL VENTRICULAR CARDIAC CYCLE.....	32
FIGURE 13 DEGENERATIVE CHANGES THAT CONTRIBUTE TO COMPRESSION OF THE SPINAL CORD LEADING TO CERVICAL MYELOPATHY ..	33
FIGURE 14 GLOBAL MAPS OF NON-TRAUMATIC SPINAL CORD INJURIES EPIDEMIOLOGICAL OUTCOMES	34
FIGURE 15 TYPES OF DCM	36
FIGURE 16 DISTRIBUTION OF CERVICAL ROM AMONG FUNCTIONAL SPINE UNITS	38
FIGURE 17 DEGENERATIVE IMPINGEMENT CAUSING COMPRESSION, STRETCHING AND BENDING OF THE SPINAL CORD.....	40
FIGURE 18 CERVICAL AND TYPICAL VERTEBRAE.	41
FIGURE 19 CERVICAL LIGAMENTS.....	41
FIGURE 20 TYPICAL STRUCTURE OF A NEURON	42
FIGURE 21 SAGITTAL VIEW WITH SUPERIMPOSED 3D RECONSTRUCTION OF THE SC AND MAIN POST-PROCESSING STEPS.....	77
FIGURE 22 MEAN CROSS-SECTIONAL AREA OF THE CERVICAL SUBARACHNOID SPACE AND MEAN OCCUPATION RATIO.....	81
FIGURE 23 MEAN AP AND LR ECCENTRICITY INDICES ; MEAN COMPRESSION RATIO	82
FIGURE 24 BOXPLOTS OF CHARACTERISTICS LENGTHS IN THE CERVICAL SEGMENT	83
SUPPLEMENTAL DIGITAL CONTENT 4 - FIGURE 25 SPINAL CORD CROSS-SECTIONAL AREA	88
FIGURE 26 CLASSIFICATION OF MAIN COMPRESSION TYPES OBSERVED IN DCM.....	94
FIGURE 27 GLOBAL SCHEMA OF THE 3D RECONSTRUCTION METHODOLOGY	96
FIGURE 28 PATIENT 1. QUANTIFICATION OF MORPHOMETRICS METRICS	100
FIGURE 29 PATIENT 1. QUANTIFICATION OF A LOCAL CANAL AREA BY SLICE	101
FIGURE 30 PATIENT 1. 3D CARTOGRAPHY OF THE SC RADIUS OVER CANAL RADIUS RATIO COMPUTED FOR EACH POINT OF SLICE	102
FIGURE 31 PATIENT 2. QUANTIFICATION OF MORPHOMETRICS METRICS	105
FIGURE 32 PATIENT 2. QUANTIFICATION OF A LOCAL CANAL AREA BY SLICE	105
FIGURE 33 PATIENT 2. 3D CARTOGRAPHY OF THE SC RADIUS OVER CANAL RADIUS RATIO COMPUTED FOR EACH POINT OF SLICE	104
FIGURE 34 PATIENT 3. QUANTIFICATION OF MORPHOMETRICS METRICS.....	108
FIGURE 35 PATIENT 3. QUANTIFICATION OF A LOCAL CANAL AREA BY SLICE	106
FIGURE 36 PATIENT 3. 3D CARTOGRAPHY OF THE SC RADIUS OVER CANAL RADIUS RATIO COMPUTED FOR EACH POINT OF SLICE	107
FIGURE 37 PATIENT 1. EVALUATION OF THE 4 SIMILARITY INDICES (DICE, JACCARD, HAUSDORFF AND MSD)	112
FIGURE 38 PATIENT 2. EVALUATION OF THE 4 SIMILARITY INDICES (DICE, JACCARD, HAUSDORFF AND MSD)	113
FIGURE 39 PATIENT 3. EVALUATION OF THE 4 SIMILARITY INDICES (DICE, JACCARD, HAUSDORFF AND MSD)	114
FIGURE 40 MECHANICAL TESTING SET UP.....	125
FIGURE 41 TYPICAL IMPOSED DISPLACEMENT OVER TIME FOR EACH MECHANICAL TENSILE TEST	125
FIGURE 42 IDENTIFICATION OF THE LINEAR ELASTIC REGION OF INTEREST	126
FIGURE 43 MECHANICAL CORRIDOR OF THE TISSUE SAMPLES	128
FIGURE 44 SCHEMA OF PROPAGATION OF DISTRIBUTIONS.....	139
FIGURE 45 CAUSE-EFFECT DIAGRAM FOR THE SURFACE OF THE SAMPLE UNCERTAINTY ESTIMATION.....	140
FIGURE 46 COMPARISON OF EXPERIMENTAL CURVES WITH OGDEN FITTED CURVES.....	143
FIGURE 47 TYPICAL PIA MATER SAMPLE DIC PATTERNS TESTED IN THE LONGITUDINAL LOADING DIRECTION.....	144
FIGURE 48 TYPICAL DAC SAMPLE DIC PATTERNS TESTED IN THE CIRCUMFERENTIAL LOADING DIRECTION.....	145
FIGURE 49 TYPICAL DAC SAMPLE DIC PATTERNS TESTED IN THE LONGITUDINAL LOADING DIRECTION.....	146
FIGURE 50 TYPICAL EXAMPLE OF NOT FULLY ATTACHED SAMPLE BY A LACK OF TISSUE CLAMPED IN THE JAWS	147

FIGURE 51 PRELIMINARY ANALYSIS OF FAILURE LOCATION ON THE SAMPLES BY TYPE OF TISSUE	147
FIGURE 52 TYPICAL FAILURE PATTERNS OF SAMPLES.....	147
FIGURE 53 SAMPLE PREPARATION	153
FIGURE 54 TEST SYSTEM AND SPINE SEGMENT.	153
FIGURE 55 DAC AND PM BIAxIAL TENSILE TEST RESULTS ACCORDING WITH SPINAL LEVELS, LONGITUDINAL AND CIRCUMFERENTIAL .	158
FIGURE 56 COLLAGEN FIBRES IN DIFFERENT LEVEL OF DURA MATER	159
FIGURE 57 COLLAGEN FIBRES IN DIFFERENT LEVEL OF PIA MATER	160
FIGURE 58 LAGRANGIAN AND EULERIAN DESCRIPTIONS OF MOTION	181
FIGURE 59 THE THREE DOMAINS NEEDED IN THE ALE FORMULATION	182
FIGURE 60 THE DIFFERENT FSI MODEL PARTS, CSF FLOW PROFILE AND MAXIMUM VON MISES STRESS.....	190
FIGURE 61 MAXIMUM VON MISES STRESSES OF THE SPINAL CORD OVER TIME.....	191

List of tables

TABLE 1 OVERVIEW OF NON-EXHAUSTIVE STUDIES OF MORPHOMETRICS ANALYSIS OF THE HUMAN SPINAL CANAL	53
TABLE 2 OVERVIEW OF THE EXPERIMENTAL MECHANICAL TESTING OF THE CEREBROSPINAL FLUID.....	54
TABLE 3 OVERVIEW OF MECHANICAL TEST AND PROPERTIES OF THE SPINAL MENINGES	57
TABLE 4 NON-EXHAUSTIVE OVERVIEW OF THE FREQUENTLY CITED CFD MODELS OF THE CEREBROSPINAL SYSTEM	61
TABLE 5 NON-EXHAUSTIVE OVERVIEW OF THE FREQUENTLY CITED FSI MODELS OF THE CEREBROSPINAL SYSTEM	65
TABLE 6 OVERVIEW OF THE MECHANICAL TESTS AND PROPERTIES CHARACTERISTICS OF THE SPINAL CORD	66
TABLE 7 OVERVIEW OF THE MECHANICAL TESTS AND PROPERTIES CHARACTERISTICS OF THE NERVES AND NERVE ROOTS	67
TABLE 8 CSA RELATIVE ERROR BETWEEN MANUAL AND AUTOMATIC CSA MEASUREMENTS FOR 5 SUBJECTS RANDOMLY SELECTED	78
TABLE 9 INTRA-OPERATOR RELATIVE ERRORS.....	79
TABLE 10 DISTANCE ERRORS PER VERTEBRA LANDMARKS (INTER AND INTRA OPERATOR VARIABILITY).....	83
TABLE 11 SUMMARY TABLE OF THE MAIN RESULTS FOR EACH INDEX	84
SUPPLEMENTAL DIGITAL CONTENT 3 - TABLE 12 STATISTICAL SUMMARY [MEAN ± STD (MIN/MAX)] OF EACH MEASURED PARAMETE	87
TABLE 13 REVIEW TABLE OF MORPHOLOGICAL STUDIES OF DCM PATIENTS. CSM : CERVICAL SPONDYLOSIS MYELOPATHY.....	92
TABLE 14 DEMOGRAPHIC CHARACTERISTICS OF SUSPICIOUS DCM POPULATION.....	93
TABLE 15 CLINICAL SCORES AND COMPRESSION TYPE CLASSIFICATION OF EACH PATIENT	94
TABLE 16 SIMILARITY INDICES EVALUATING THE QUALITY OF THE QAS SEGMENTATION OF THE HEALTHY POPULATION AND THE DCM POPULATION	97
TABLE 17 SUMMARIZED DESCRIPTION OF NUMBER OF SAMPLES	130
TABLE 18 SUMMARY OF SAMPLE DIMENSIONS	130
TABLE 19 COMPARISON TABLE OF SAMPLES’ ELASTIC MODULUS BETWEEN FRESH AND FLASH-FREEZING CONSERVATION METHODS .	131
TABLE 20 SUMMARY OF POST-PROCESSED QUANTITIES BY SPINAL SEGMENT	130
TABLE 21 COMPARATIVE LITERATURE TABLE OF MECHANICAL CHARACTERIZATION OF SPINAL MENINGES.....	132
TABLE 22 ONE DEGREE OGDEN MODEL MATERIAL CONSTANTS AND SHEAR MODULUS	133
TABLE 23 SUMMARY OF PRE-PROCESSED MEASUREMENTS BY SPINAL SEGMENT	142
TABLE 24 DESCRIPTION OF CONSTITUTIVE MODELS	161
TABLE 25 DAC BIAXIAL TENSILE TEST RESULTS AND CONSTITUTIVE MODEL PARAMETERS.....	162
TABLE 26 PM BIAXIAL TENSILE TEST RESULTS AND CONSTITUTIVE MODEL PARAMETERS	163
TABLE 27 BIAXIAL TENSILE TEST RESULTS ACCORDING WITH SAMPLE SPINAL LEVELS.....	164
TABLE 28 FIBRES CHARACTERISTICS MEASURED ON BI-PHOTON MICROSCOPY FOR DAC AND PM SAMPLES	165
TABLE 29 STRUCTURE AND FLUID MATERIAL PROPERTIES	189

General Introduction

The cervical spinal canal protected by the spine is a mechanically and morphometrically heterogeneous structure surrounding a cavity in which the CSF flows. This fluid physico-chemically interacts with the spinal central nervous system to maintain a homeostasis while the neural cells also called axons allow motor and sensory information to spread between the brain and the body. Traumatic or a degenerative structural alteration of the canal can lead to spinal cord injury (SCI) involving up to 500,000 people in the world [OMS website]. Then, cervical stenosis occurs in 5% of the adult population in occident [Kalsi-Ryan et al. 2013] with a high risk to lead to degenerative cervical myelopathy (DCM), a non-traumatic SCI disease, characterized by a compression of the spinal cord. Thus DCM is the most common reported spinal cord pathology for the population aged over 55 years [Roisin T. Dolan et al. 2016]. Moreover, the DCM can lead to a moderate or devastating impact, to a fast and/or lately effect on the lifetime of the patient.

Medical solutions to DCM exist such as non-surgical or surgical approach. The spinal decompressive surgery seems to be the most efficient solution against conservative approach [Davies et al. 2018] even if the decision-making process depend on factors including duration of symptoms, degree of compression, neuro-motor assessment, physical examination of the patient, and medical imaging findings [Kato et al. 2018, Nouri et al. 2017]. Nevertheless, diagnostic associated to DCM is not easy and late diagnosis will lead to worsening of the patient condition [Behrbalk et al. 2013]. The multifactorial and patient-specific symptoms makes the associated patient assessment challenging and can lead to potential delay in diagnosis and surgical management which might affect the neurologic outcome and the further patient recovery [Kato et al. 2016]. Quantitative patient follow-up for a reliable and efficient diagnosis and a prognosis in case of further surgery revision is needed.

The collaboration between the Laboratoire de Biomécanique Appliquée and the international associate laboratory iLab-Spine aims at improving the treatment and protection of the spine and spinal cord in the context of traumas and degenerative pathologies using multidisciplinary approaches based on biomechanics, multimodal magnetic resonance imaging and modelling. Relating to the cervical spine and spinal canal research, remarkable progresses were made in the recent years in this collaborative effort. Spinal cord and canal numerical biomechanical modelling were done [Beausejour et al. 2020, Lévy et al. 2020, Bianco et al. 2019, Fournely et al. 2020] based on magnetic resonance imaging (MRI) research and on innovative protocol for mechanical characterization. On one hand , morphometrics criteria based on *in vivo* high-resolution anatomical 3T magnetic resonance imaging were established to morphologically characterize spinal cord and location of the cord in the canal in healthy volunteers as well as in cervical degenerative myelopathy [Fradet et al. 2014]. On the other hand, mechanical characterization of spinal cord with pia mater was performed on murine models [Fournely et al. 2018] as well as on porcine models [Fradet et al.2016b] and preliminary fluid-structure interactions (FSI) modelling were investigated during transversal impact [Fradet et al. 2016a].

This PhD work aims at to build the fundamental bricks which will drive to the development of subject-specific numerical models with FSI of healthy cervical spinal and with cervical degenerative myelopathy. Long term objective is to better understand the mechanical interactions between the cerebrospinal flow and the cervical spinal central nervous system, and to provide complementary biomechanical analysis

for a more accurate diagnosis and prognosis of patients with cervical degenerative myelopathy. Towards a deeper investigation of the pathophysiological mechanisms associated with both traumatic and degenerative pathologies, this work has been performed in collaboration with V. Callot from the Center for Magnetic Resonance in Biology and Medicine (CRMBM) for the MRI-based investigation and Y. Petit and E. Wagnac from the Ecole de Technologie Supérieure (ETS) and from the Laboratoire de recherche en Imagerie et Orthopédie (LIO) de Montréal for the mechanical testing part.

To reach this goal, the general objective was organized in three steps. Firstly, the MRI-based morphological characterization by morphometrics criteria initially developed in [Fradet et al. 2014] was generalized to a 3D canal-based methodology enabling specific definition of the subarachnoid space. Once 3D reconstructions were obtained from segmentations of clinical T2 MRI scans, a quasi-continuous description of morphometrics criteria was done along the healthy cervical canal. Then, in order to avoid the time-consuming of a manual segmentation as well as for the possibility to improve the reproducibility of the segmentation, a T2 MRI-based quasi-automatic segmentation of the cervical canal was developed and new morphological criteria were proposed for a detailed DCM morphological analysis.

Secondly, mechanical properties of anatomical structures are needed for the simulation of fluid-structure interactions in subject-specific cervical spinal canal. From literature analysis, meningeal tissues were studied by the scientific community without necessarily leading to a consensus about the structure and mechanical properties. A previous study investigated compressive mechanical properties of spinal cord as a whole including pia mater [Fradet et al. 2016b]. In this context, tensile uni-axial and bi-axial mechanical characterizations of meningeal tissues were conducted. In addition, a comparison of fitted constitutive model were done on bi-axial measurements to estimate the most appropriate constitutive law for meningeal tissues.

Thirdly, numerical approach was studied in three steps to develop models able to mechanically reproduce the cerebrospinal flow in healthy cervical spinal canal as well as in canal with DCM while taking into account the structural behavior of tissues. The first step was to mathematically describe an FSI formulation. The second step was to propose a simple FSI modelling of the cerebrospinal fluid flow as proof-of-concept and to discuss its reliability. Finally, the third step was to develop subject-specific computational fluid dynamics (CFD) models of the cerebrospinal fluid flow in the cervical spinal canal using previous 3D reconstructions described above. CFD modelling will be discussed in the perspective of using a partitioned FSI approach.

Chapter 1 reminds the descriptive and the functional anatomy of the structures composing the human cervical spinal canal in terms of the central nervous system (spinal cord and nerves), the meninges, the denticulate ligaments and the cerebrospinal fluid. In addition, the analogy between human and porcine models is also described. Then, the clinical and biomechanical aspects involved in the cervical spine and canal are addressed in regards to the PhD topic.

Chapter 2 concerns an overview of the state-of-the-art of literature associated to the three next chapters. It is divided in three parts. First, a description concerning the morphology methodologies and results performed on healthy and pathological populations provided by the scientific literature. Secondly, a description of mechanical characterization studies of structures composing the vertebral canal was presented. Thirdly, a description of non-exhaustive CFD and FSI models of the cerebrospinal fluid and spinal canal was presented. Supplementary literature was added in the introduction sections of chapters 3, 4 and 5.

Chapter 3 is divided in two sub-chapters. The first part concerns a new method based on 3D MRI-based reconstruction which was developed to morphologically characterize in the cervical canal of a healthy

population. The second part concerns the improvement associated to segmentation and the application of this new methodology for a morphological analysis of a population with DCM. The 3D reconstructions of the two populations were used in the numerical modeling in the chapter 5.

Chapter 4 is divided in two parts and is focusing on the mechanical characterization of porcine spinal meningeal tissues (dura and arachnoid maters as well as pia mater) which is used in the modeling of cervical human canal. The tissue elastic properties against the spinal levels, the loading direction as well as the conservative method of the tissue samples were quantified by an uni-axial tensile testing approach. In the second part, the isotropic and anisotropic hyperelastic constitutive models were fitted and compared to experimental measurements performed by a bi-axial tensile testing approach applied on the porcine spinal segments.

Chapter 5 addresses the aspects of fluid-structure interactions. Firstly, a mathematical description was proposed. Secondly, a proof-of-concept of monolithics FSI modelling was developed and discussed. Thirdly, the advances concerning the subject-specific CFD models of the cerebrospinal flow along the cervical human canal are presented and discussed for a further development of subject-specific FSI models based on partitioned coupled approach between a computational fluid dynamics and a computational structural dynamics solvers.

Finally, the general conclusion summarizes the main findings of this PhD project whereas the perspectives are discussed.

Nota bene: it was chosen to include the appendices in the chapter from the chapter 1 to chapter 5 for ease of reading.

Chapter 1

Anatomy

1. The spine and the spinal canal.....	19
1.1.The spine	19
1.2.The spinal canal.....	20
1.3.The spinal central nervous system	21
1.4.The nerve and nerve roots	23
1.5.The meninges	24
1.6.The denticulate ligaments	27
1.7.The porcine model	28
2.Biomechanical characteristics, physiology, motion and pulsation of the CSF system	29
2.1.Characteristics and physiology of CSF	29
2.2.Circulation of the cerebrospinal fluid	29
2.3.Pulsation of the cerebrospinal fluid	30
3.Clinical and biomechanical contexts.....	32
3.1.Epidemiology of cervical myelopathy	32
3.2.Pathophysiology of degenerative cervical myelopathy	32
3.3.Clinical management.....	35
3.4.Biomechanics of the cervical spine and canal	35
4.Appendices	40
5.References.....	42

Abbreviations

ASIA : American Spine Injury Association score
BMI : body mass index
CNS : central nervous system
CSD : computational structural dynamics
CSF : cerebrospinal fluid
CT : computed tomography
DCM : degenerative cervical myelopathy
DL : denticulate ligaments
DOF : degrees of freedom
FSU : functional spine unit
IVD : intervertebral disc
IVF : intervertebral foramen
JOA : Japanese Orthopedic Association
mJOA : modified Japanese Orthopedic Association
MRI : magnetic resonance image

OPPL : ossification of the posterior longitudinal ligament
 OSSL : ossification of spinal ligament
 PNS : peripheral nervous system
 ROM : range of motion
 SAS : subarachnoid space
 SC : spinal cord
 SCI : spinal cord injury
 VM : Von Misès

In the first chapter, literature review will address the descriptive, the functional anatomy and the biomechanical roles of the spine, of the central nervous system and of the cerebrospinal fluid in healthy and in DCM cases. In the second chapter, different ways to investigate the morphometrics changes in in the cervical spinal canal will be presented. The third chapter will focus on studies of the mechanical properties of the structure in the spinal canal. Finally, a review of the different existing biomechanical numerical models of the cervical spinal canal will be introduced. The global context of this PhD will be presented by describing the current research and published studies.

In the rest of the document, the following considerations will be adopted : anatomical planes of reference for the human and the pig are presented in Figure 1. The sagittal plane is the plane separating right from left; the horizontal or axial plane is a plane parallel to the ground, separating the body into the upper and lower parts. The coronal or frontal plane is the plane perpendicular to the two others. Anterior (or ventral) direction defines the direction toward the front of the body while the posterior defines the direction toward the back of the body. Cranial (or superior) describes a position above another part of the body while caudal (or inferior) describes the opposite. The cranio-caudal direction is also called the longitudinal direction. Lateral defines the right or left side of the body. Flexion refers to a movement in the sagittal plane towards the anterior direction while the extension refers to a movement in the sagittal plane towards the posterior direction.

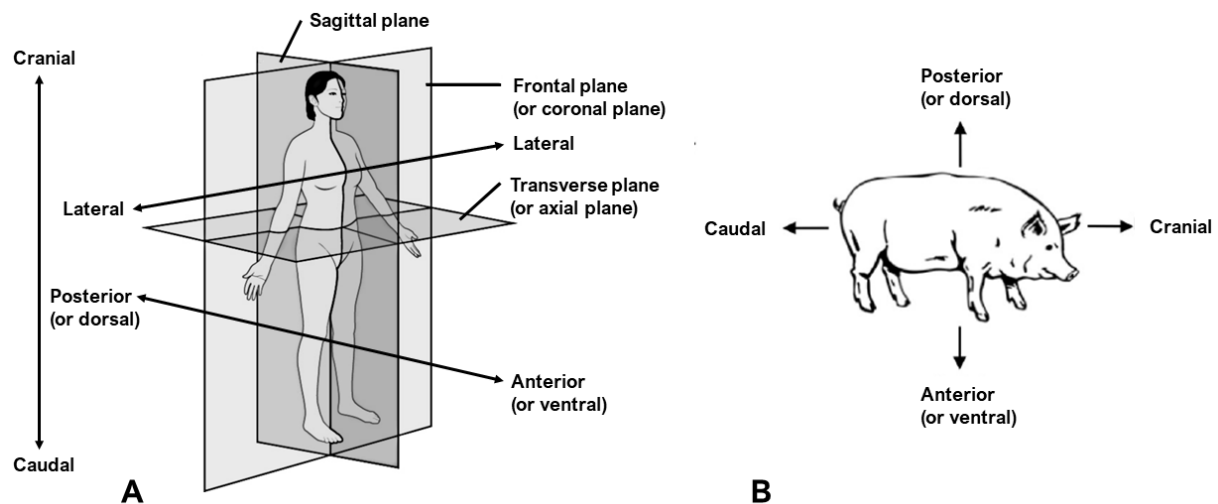


Figure 1. Anatomical planes : human (left) + pig (right) – Modified from <https://cnx.org/> (Human anatomy and dissection reader – Anatomical planes) and from [Jones 2011]

1. The spine and the spinal canal

1.1. The spine

The vertebral column (Fig. 2) is composed of alternating vertebrae and intervertebral discs (IVD) alternatingly supported by robust spinal ligaments and muscles. All of these elements, bony, cartilaginous, ligamentous, and muscular, are essential to the structural integrity of the spine. The osteo-ligamentous structure of the spine serves four vital functions : protecting the spinal cord and spinal nerves, transmitting the weight of the body above the pelvis, providing a central flexible axis around which the motion is organized and controlled. Finally, the spine has an essential function to stabilize the posture and the motion of the body in considering the muscles and the central nervous system. Indeed, the passive spine mobility is provided by the addition of motions of segments of two vertebrae linked by an intervertebral discs (IVD). The incompressibility properties of IVD, provided by a major water composition, enables the absorption of the energy transmitted along the spine. The spine can be divided into three parts: the sacrum and the coccyx which are fixed together, the vertebrae (cervical to lumbar) and the ribcage which are mobile. The vertebrae are organized as follows : the seven cervical vertebrae (C1 to C7, Appendix – Fig. 19), the twelve thoracic vertebrae (T1 to T12), the five lumbar vertebrae (L1 to L5). The spine has a physiological shape defined in the sagittal plane : the cervical lordosis, the thoracic kyphosis, and the lumbar lordosis. The whole spine is inserted in the pelvis which allows the transmission and the absorption of the stresses resulting from the gravity and from ground reactions to the body through sacro-iliac junction.

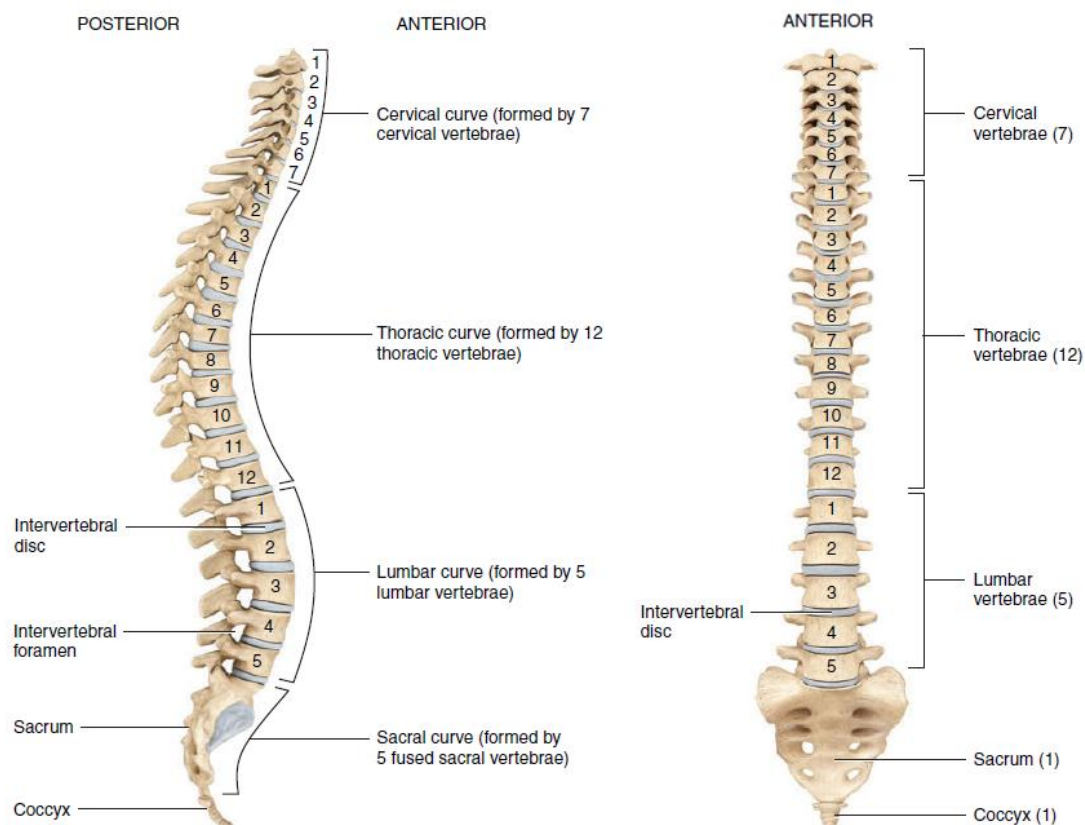


Figure 2. Global overview of the spine. Right lateral view (left) and anterior view (right) [from Tortora, 14th edition]

1.2.The spinal canal

The vertebrae, the IVD, and the ligaments delineate spinal canals in which the central nervous system (the cord, the nerves and nerve roots) and the arteries are inserted (Fig. 3) These channels include :

the central canal (also called vertebral foramen) that surrounds and protects the cord and the cauda equina. It is continuous, through the foramen magnum (cranial base), with the cranial cavity of the head and ends in the sacrum.

The root canals that surround and protect the roots, called the intervertebral foramina. They are formed on each side of the central canal, by the zygapophysial joint posteriorly and the intervertebral disc anteriorly, and by the vertebral notch on the pedicle above and below the foramen. It is a space surrounded by bone, ligaments and cartilage. Pathology in the intervertebral foramina can affect the structures within these structures.

The description arteries and venous is briefly addressed in the manuscript. However, further details could be found in [Bosmia et al. 2015]. The spinal canal opens into the cranial cavity through the occipital foramen, or foramen magnum, and ends caudally, in a flute-like beak at the distal end of the sacral canal.

The spinal canal has a strategic role both from an anatomical point of view but also from a biomechanical point of view. The latter was developed in section 3.4.2 in this chapter.

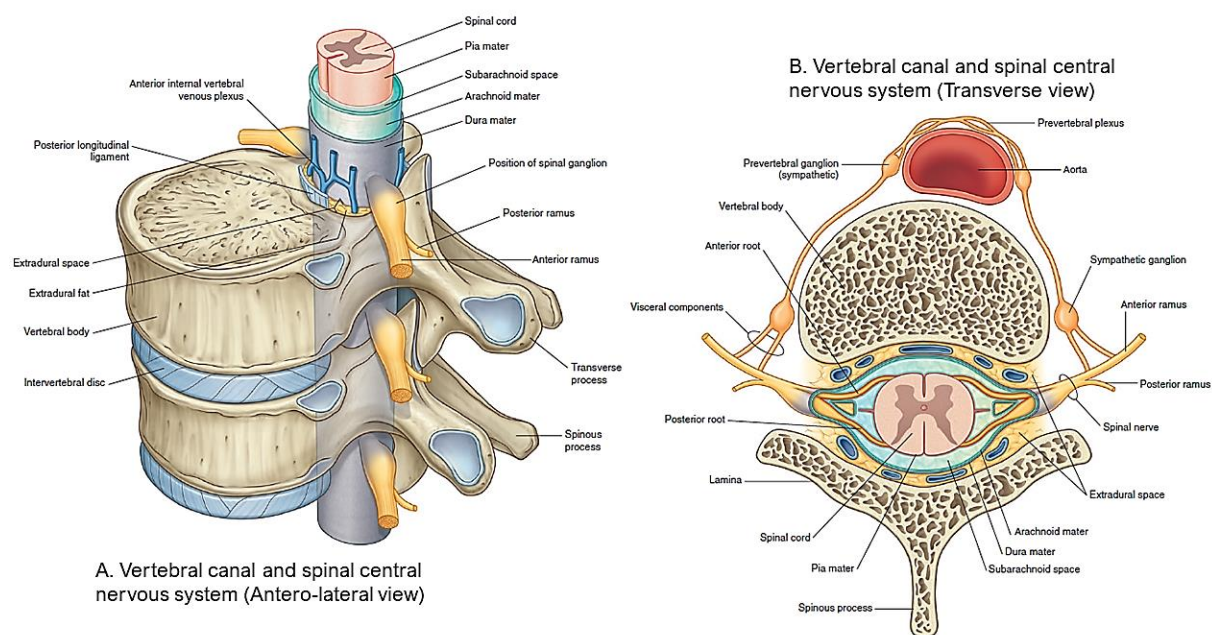


Figure 3. Vertebral canal and central nervous system [from *Gray's Anatomy for Students, 4th Edition (2020)*].

1.3.The spinal central nervous system

The spinal cord, which is located in the vertebral canal, is cranially continuous until the medulla oblongata of the brain stem and terminates caudally with a tapered inferior end of lumbosacral roots called the cauda equina (Fig. 5). In addition to the protection of the bony-ligamentous structure, the cord is well protected by the CSF and a group of membranes, collectively called the meninges. The spinal cord does not lie immediately adjacent to the bone and ligaments but it is separated from them by fluid, meninges, fat, subarachnoid trabeculae, denticulate ligaments and a venous plexus.

The spinal cord and brain develop from the same embryologic structure (the neural tube) and together they form the central nervous system (CNS). One end, the neural tube is encased in the skull, whereas the remainder of the neural tube is encased in the vertebral column, occupying about the upper two thirds of the vertebral spinal canal [Darby 2014]. The cord segments, delimited by the nerve roots, are not necessarily located at the same level as their corresponding vertebrae. The relationship between cord segments and vertebral levels is still unclear [Cadotte et al. 2014].

A transverse section of the spinal cord reveals regions of white matter that surround an inner core of gray matter (Fig. 4). The white matter of the spinal cord consists primarily of bundles of myelinated axons of neurons. Two grooves penetrate the white matter of the spinal cord and divide it into right and left sides. The gray matter of the spinal cord is shaped like a butterfly or the letter H; it consists of dendrites and cell bodies of neurons, unmyelinated axons, and neuroglia (Appendix – Fig. 20). The gray commissure forms the crossbar of the H. In the center of the gray commissure, there is a small space called the central canal [Tortora, 14th edition] ; it extends in the entire length of the spinal cord and encompasses an internal system of CSF cavities that include the cerebral ventricles, aqueduct of Sylvius, and fourth ventricle [Saker et al. 2016].

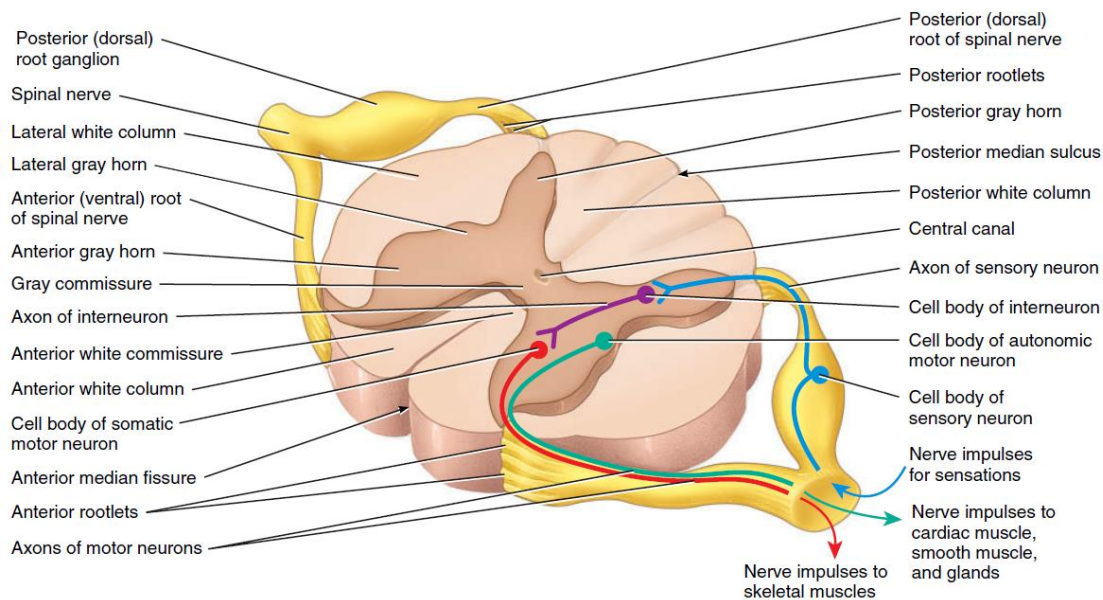


Figure 4. Functional and descriptive anatomy of the spinal cord (transverse antero-lateral view) [from Tortora, 14th edition].

The spinal cord has two principal functions: nerve impulse propagation and integration of information. The white matter tracts in the spinal cord are highways for nerve impulse propagation through axons of nervous fibres. Sensory inputs travels along these tracts toward the brain, and motor outputs travels from the brain along these tracts toward skeletal muscles and other effector tissues such as vital organs. The gray matter of the spinal cord receives and integrates incoming and outgoing information through the dendrite of the nervous fiber. Information are electrically propagated along a nervous fiber and transmitted to another nervous fiber by chemical exchanges of neurotransmitters at the synapse levels [Tortora, 14th edition].

For the CNS to respond to the environment it requires inputs from structures peripheral to the CNS and, in turn, a way to send output to structures called effectors. The sensory inputs begins in peripheral receptors found throughout the entire body in skin, muscles, tendons, joints, and viscera. These receptors send electrical currents (action potentials) toward the spinal cord of the CNS via the nerves

that compose the peripheral nervous system (PNS). The sensory receptors respond to general sensory information such as pain, temperature, touch (pressure, vibrations), or proprioception (the perception of body position and movement). The PNS is also used when the CNS sends outputs to the body's effectors, which are the smooth muscles, cardiac muscles, skeletal muscles, glands of the body and the vital organs. Thus, the PNS consists of the body's peripheral nerves and is the way by which the CNS communicates with its surrounding environment [Darby 2014].

The white matter is organized within the SC into the following three parts: posterior, lateral, and anterior. Those fibers form tracts that eventually represent the components of sensory, motor, propriospinal, and autonomic pathways.

The blood supply to the SC is provided craniocaudally by one anterior and two posterior spinal arteries and horizontally by several radicular arteries originating at various levels, whereas the radicular arteries vascularize the ventral and dorsal roots. Originating from the fusion of the vertebral arteries, the anterior spinal artery, irrigated notably by the Adamkiewicz artery, is located within the pia mater in the median sulcus [Ganau et al. 2019]. Surrounding the arteries and veins, fluid channels called perivascular spaces provide a conduit between the cerebrospinal fluid (CSF) in the subarachnoid space and parenchymal interstitial fluid, facilitating solute transport and waste clearance [Thomas JH. 2019].

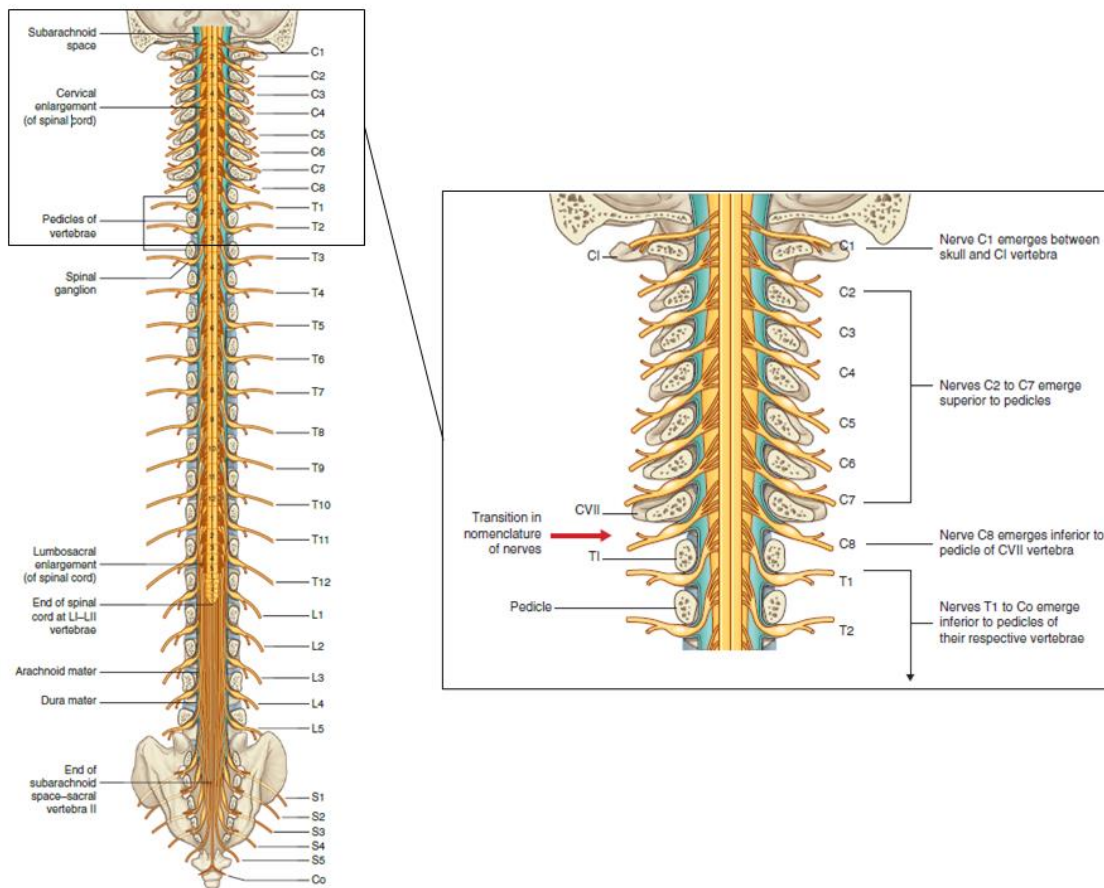


Figure 5. Spinal nerves. (Left) vertebral canal, spinal cord and spinal nerves, (right) nomenclature of the spinal nerves [from Gray's Anatomy for Students, 4th Edition (2020)]

The mechanical role of the spinal cord was firstly addressed with its pathological involvement in the section 3.4.2. of this chapter 1. Its kinematics description was secondly developed in the chapter 2 from the literature review, and studied in the chapter 3. Finally, the mechanical properties of the spinal cord

and the other structures described below composing the spinal central nervous system were described in the chapter 2 section 2.

1.4.The nerves and nerve roots

Spinal nerve roots provide functional and structural neural continuity between peripheral nervous system (PNS) and spinal cord. Also, these tissues differ in cellular composition, organization and function, and in amount of connective material. Due to the organization of the nerve roots as well as the nerves along the cord, they may be susceptible to be inflamed and damaged because of tensile or compressive forces from surrounding structural modifications such as disk herniation, foraminal stenosis and avulsion injuries. That could lead to demyelination and then cause pain, paresthesia (alteration of sensorial functions) and loss of motor control [Beel et al. 1986, Singh et al. 2006].

31 pairs of nerves roots called the spinal nerves attach to the spinal cord and communicate with structures primarily located in the neck, trunk, and extremities. These cord segments are numbered similarly to the numbering of the spinal nerves: 8 cervical, 12 thoracic, 5 lumbar, 5 sacral, and 1 coccygeal cord segment (the first seven cervical nerves exit the intervertebral foramen (IVF) above their corresponding vertebra, and the remaining nerves exit below their corresponding vertebra. This allows one more cervical spinal nerve than cervical vertebrae (Fig. 5).

A spinal nerve is composed by the unification of two roots within the IVF (Fig 4). On one hand, the dorsal roots contain fibers of various diameters and conduction velocities that convey all types of sensory information. On the other hand, the ventral roots contain axons of motor neurons which conduct nerve signals from the CNS to muscles or glands. As the roots approaches the spinal cord within the vertebral canal, it divides into approximately six to eight dorsal rootlets, or filaments. These rootlets attach in a vertical row to the cord's dorsolateral sulcus (i.e. a groove in Latin) [Tortora, 14th edition].

1.5.The meninges

This section was inspired by [Reina et al. 2020, Gassner et al. 2017, Sakka et al. 2016].

The meninges are concentric connective tissue layers wrapping the central nervous system from the caudal side with the *filum terminale* to the cranial side with the brain. They have morphologies and physiologies which are involved in immunologic, trophic, metabolic, thermal and biomechanical protection of the spinal cord. They begin into the radially inner direction after the osteofibrous wall of the vertebral canal and the epidural space, filled by a loose connective tissue (extracellular matrix) and epidural fat. Their locations protect the spinal cord from the potential injuries related to the movements of the vertebral column. The epidural fat, the internal vertebral venous plexus and the cerebrospinal fluid (CSF) between meninges behave as the mechanical cushion probably acting as a damping element between the spinal cord and the bone enclosure. Then, the mechanical properties of the spinal meninges were more deeply studied by mechanical testing approaches in the chapter 4.

The meninges are categorized in four main tissues organized from the outermost layer to the innermost layer : the dura mater, the arachnoid mater forming the dural sac, the pia mater and the denticulate ligaments which are the bridges between the pia and the arachnoid maters.

1.5.1.The dura mater

It is a sheath described as a white, thick, and resistant membrane formed by a dense connective tissue poorly vascularized. Cranially, the spinal dura mater begins and is fixed at the foramen magnum.

Caudally, the dural sheath wrapped the spinal cord, the spinal nerve roots and contracts into the filum terminale.

The dura mater forms 90 % of the outer layer of the dural sac. This fibrous structure, although permeable, forms a mechanical barrier. The dura mater thickness varies along the spinal cord. Dura mater is comprised of concentric dural laminae containing a ratio collagen fibers (collagen do not seem to have been clearly identify) on elastin fibers which varies radially [Chauvet et al. 2010]. No consensus about the fibers' organization was highlighted by the literature in an histological point of view. On one side, papers showed a distribution of fibers at randomly distributed in all spatial directions (Fig. 6) [Reina et al. 2020, 1997] and on other side, papers showed a predominantly longitudinally orientation [Patin et al. 1993, Chauvet et al. 2010] (all human specimen). The biomechanical literature tends to confirm the longitudinal fiber orientation as mechanical characterization experiments showed a greater longitudinal tensile stiffness compared to transverse stiffness.

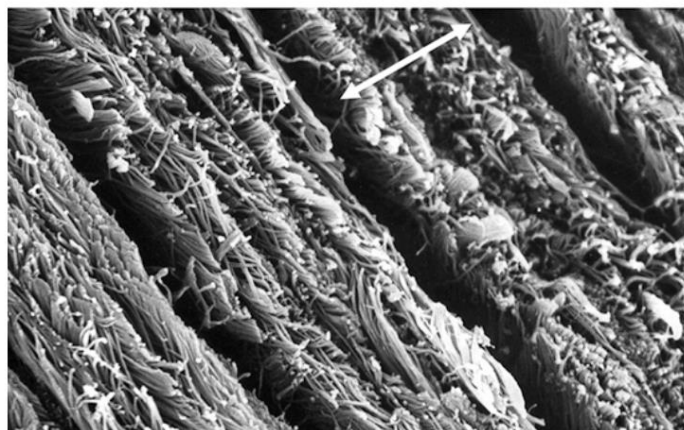


Figure 6. Human lumbar dura mater sample - SEM - Magnification x 4000 [from Reina et al. 2020].

1.5.2. The arachnoid mater

The arachnoid mater can be described as an outer layer attached to the dura mater by thin fibers of collagen so that there is no subdural space (Fig. 7). The remaining internal 10% of the dural sac is formed by the arachnoid layer and consists in a thin transparent membrane forms of several cell layers and mainly composed of collagen and elastin fibers. The arachnoid is semi-permeable and regulates the passage of substances through the dural sac [Reina et al. 2008].

The arachnoid mater is attached to the pia via a framework of fine connective trabeculae and is connected to an inner layer by the *septum posticum* of Schwalbe to bridge the subarachnoid space (in the dorsal direction of the median sulcus of the SC). The trabecular arachnoid surrounds the structures inside the subarachnoid space, including spinal cord, nerve roots, and blood vessels that are scattered within the space. These easily cuttable attachments are called arachnoid *trabeculae* [Sakka et al. 2016, Mortazavi et al. 2017], sheet-like *trabeculae* [Adeeb et al. 2013] or leptomeningeal layer [Gassner et al. 2017].

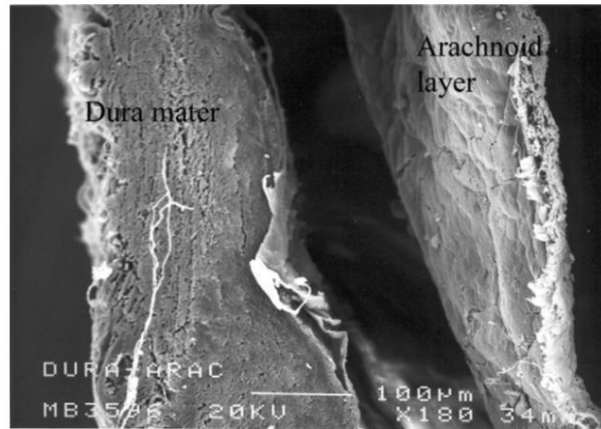


Figure 7. Human lamina arachnoid. Scanning electron microscopy. Magnification x180 ; Bar: 100 μ m [from [Reina et al. 2008](#)].

1.5.3. The pia mater

The spinal pia mater is described as a thin tissue closely adhering to the spinal cord glia limitans or subpial layer, which covers the outer surface of the spinal cord and is situated immediately subjacent to the pia mater. The glia limitans is a dynamic structure of exchange between the CSF and the cord ([Fig 8](#)). Cranially, the spinal pia mater continues the cranial pia mater at the foramen magnum. Below the conus terminalis, it forms a thin tubular ligament, the filum terminale. The spinal pia mater is composed of mainly longitudinally orientated collagen fibers, in which is embedded carry larger branches of the spinal vasculature. The morphology of the pia mater differs between spinal and cranial location; the spinal pia mater is thicker, more compact, and less vascular.

The subpial compartment has large amounts of collagen fibers, a few elastin fibers and, fibroblasts, and a small number of macrophages as well as blood vessels. The subpial compartment is enclosed between the pial cellular layer and a basal membrane that is in contact with neuroglial cells on the spinal cord side and separates the CSF from the spinal cord. The orientation of fibers was not clearly proved and no study showed a preferential uni-axial direction from a mechanical point of view for human subjects. Moreover, most of the above considerations were observed at the lumbar spinal level.

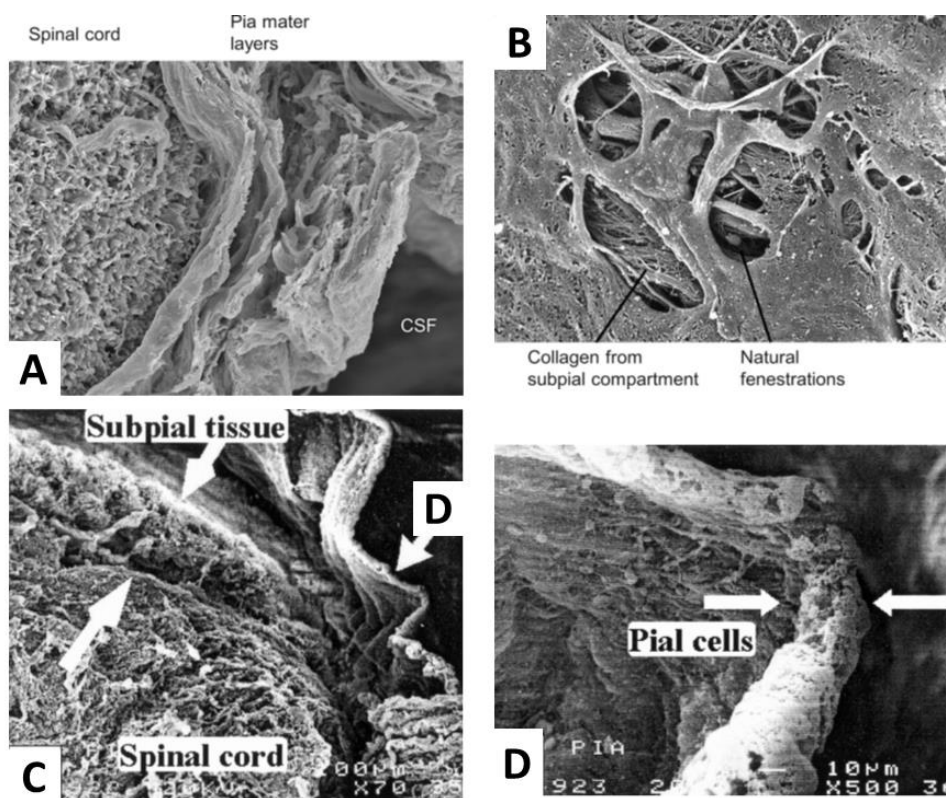


Figure 8. **A** - Pia mater. Human spinal pia mater at spinal cord level. Scanning electron Microscopy, magnification: x300. **B** - Natural fenestration within human spinal pia mater at spinal cord level. Scanning electron microscopy, magnification: x2000. [From [Reina et al. 2020](#)]. **C** - Fraction of the pial cellular layer, presumably detached during dissection. Subpial tissue with collagen fibers is placed between the pial layer and spinal cord. The space seen between the pial layer and the subpial tissue is an artifact. The "D" arrow marks the area that has been magnified in **D**. Scanning electron microscopy, magnification: x70. **D** - Pial cellular layer. The arrows delimit the pia mater thickness. Scanning electron microscopy, magnification x 500. [From [Reina et al. 2002](#)].

The subarachnoid space, also named perimedullar space at the level of the spinal cord, occupies the space between the arachnoid and pia maters. It fills around a third of the vertebral canal. The subarachnoid space contains cerebrospinal fluid and extracellular collagen and fibroblasts.

1.6.The denticulate ligaments

The denticulate ligaments (DL) or subarachnoid ligaments have a similar composition to arachnoid *trabeculae*, although they are composed of more collagen fibers and are therefore more resistant to mechanical forces. The denticulate ligaments have been shown histologically to consist of thick collagenous bundles that merge medially with subpial collagen and laterally are attached to the spinal dura mater ([Fig. 9](#)). The narrow fibrous strip portion of the DL consisted of longitudinal collagen fibers whereas the triangular extensions featured transverse and oblique collagen fibers. Collagen fibers were thicker and more abundant in the cervical DL than in the thoracic DL.

The DL have a biomechanical role of stabilization of the spinal cord in the dural sac due to their mechanical properties in tension [[Polak et al. 2019, 2014](#), [Ceylan et al. 2012](#), [Tubbs et al. 2001](#)]. Indeed, DL were more resistant when stress was applied to the cord in the caudal as opposed to cranial direction. The DL in the cervical region were strongest, and their strength decreased with respect to the lower spinal levels. They are less able to resist anteriorly directed forces as the cord descends and overall, inferior to T8, the cord was shown to come into contact with the anterior spinal canal before the denticulate ligaments tie [[Ceylan et al. 2012](#), [Tubbs et al. 2001](#)].

The number of DL range from 18 to 21 dentate ligaments at each side of the spinal cord [Ceylan et al.2012, Reina et al. 2020]. They are mainly located in the cervical and thoracic regions (ending around T12) of the spine.

The apex (i.e. the tip of a pyramidal/triangular structure) attached craniomedially to the dura mater to the intervertebral foramen of the vertebrae at the spinal level below. Each DL is laterally attached to the pia mater between the ventral and dorsal roots of the spinal nerves. Each ligament had lateral triangular extensions oriented perpendicular to the long axis of the vertebral column.

The amount of space between them differed according to spinal level and the distance from the dural attachment site to the intervertebral foramen increased according to such level from upper to lower levels of the spine. The dural attachments of the ligament were not always bilaterally symmetrical.

The anatomy and histology of DL correspond with the motion capacity of each different region of the vertebral column. Indeed, due to a high mobility of the cervical segment, the DL in that region have to allow the necessary motion of the cervical portion of the spinal cord within the canal. The direct apical attachments at the thoracic levels may reflect the lower mobility of vertebrae in that region of the spine. No presence of DL was reported was reported in the lumbar region [Ceylan et al. 2012].

Finally, the DL are clinically significant reference markers as they divide the spinal canal into anterior and posterior compartments[Ceylan et al. 2012].

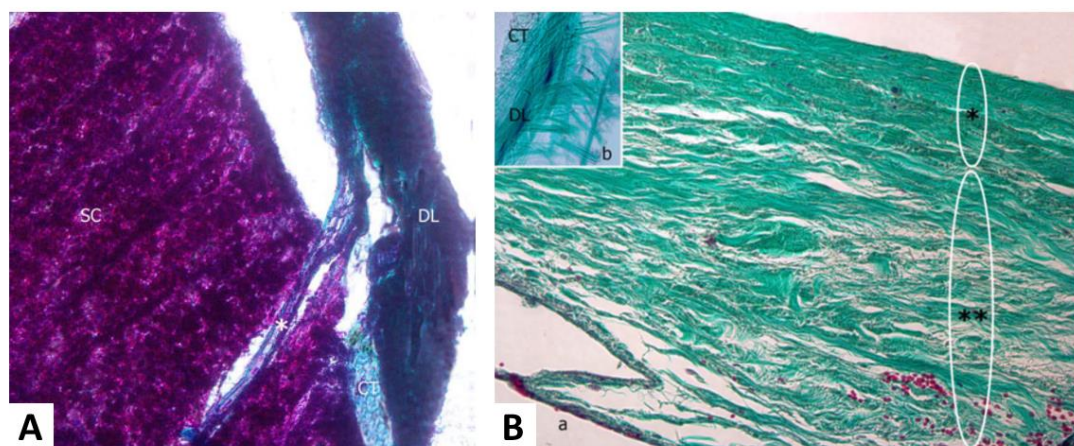


Figure 9. The denticulate ligaments. **A** - The spinal attachments of the DL. The DLs are attached to the spinal cord by loose connective tissue throughout the length of the spine. At cervical levels (*), there were also collagen fibers penetrating the substance of the spinal cord at various intervals, creating a firmer attachment. Magnification $\times 10$ (DL: denticulate ligament, SC: spinal cord, CT: connective tissue). **B** - a and b Histological structure of the DL. The DLs were composed of collagen fiber bundles. The narrow fibrous strip portion (*) of the DL consisted of longitudinal collagen fibers, whereas the triangular extensions (**) featured transverse and oblique collagen fibers. a) Magnification $\times 10$, b) magnification $\times 20$. (DL: denticulate ligament, CT: connective tissue) [From Ceylan et al. 2012].

1.7. The porcine model

The porcine model (Fig. 10) becomes a preferential model for spine research [Kim et al. 2019, Brummund et al. 2017, Fradet et al. 2016b, Swinidel et al. 2013] due to a high similarity with the human species. Indeed, the genetic, anatomical [Fig. 1.7], physiological, pathophysiological [Schomberg et al. 2017], histological [Kinaci et al. 2020], biomechanical (in particular in term of ROM of the upper cervical, upper

and middle thoracic sections) [Wilke et al. 2011] of this quadruped makes the best transversal models for human research, next to non-human primates [Schomberg et al. 2017].

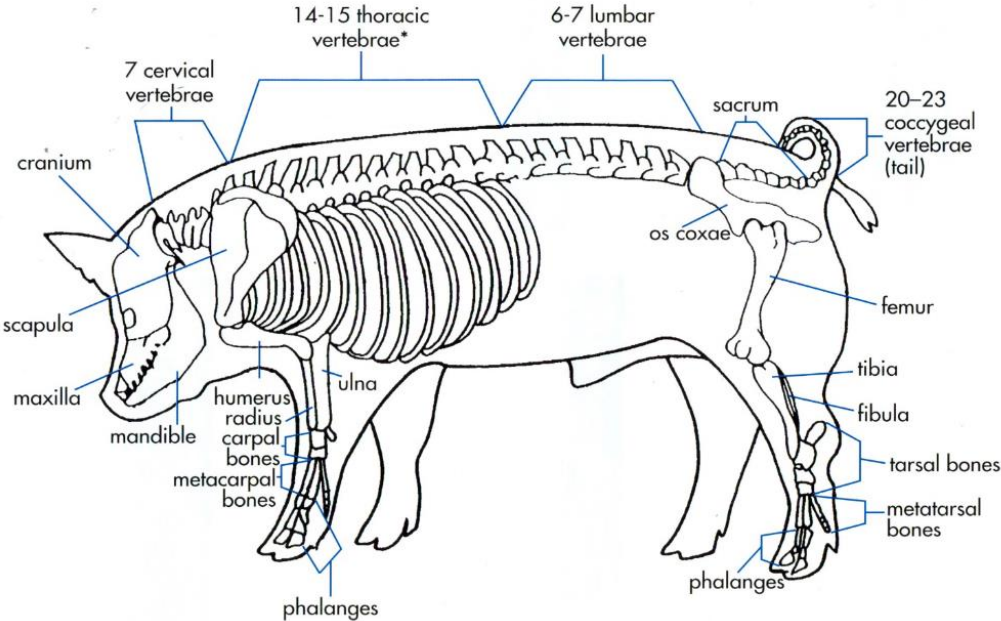


Figure 10. Skeletal porcine anatomy. *Some pigs may have up to 17 thoracic vertebrae [From Swine Resource Handbook for Market and Breeding Projects, page 3-15].

2. Biomechanical characteristics, physiology, motion and pulsation of the CSF system

The dynamics and physiology of the cerebrospinal fluid need to be deeply understood to investigate many traumatic or degenerative axonal diseases such as spinal cord injuries [Kwon et al. 2016], Alzheimer's disease [Hansson et al. 2019], cerebral malaria [Datta et al. 2019] or migraine [Van Dogen et al. 2017], and also to develop potential high impact solution as intrathecal drug delivery [Fowler et al. 2020].

2.1.Characteristics and physiology of CSF

Cerebrospinal fluid has an estimated total volume ranging from 250 to 400 mL in adult humans, with a ratio of $\frac{3}{4}$ in the intracranial part. It renews itself 3 to 4 times a day. The CSF motion is mainly located within the intracranial space (cortical subarachnoid space, cisterns and ventricles) and the spine (spinal subarachnoid space).

This fluid serves several physiological functions such as :

- structural protection [Fradet et al. 2016a, Persson et al. 2011], acting as a damping element.
- mechanical regulation (intracranial pressure/compliance) to adapt to sudden fluctuations caused by obstruction of venous outflow and/or expanding mass lesion [Garnotel et al. 2017, Marmarou et al. 1975].
- metabolic homeostasis of the CNS, by providing nutrients to neural and glial cells, to eliminate metabolic wastes (neurotoxic wastes products, neurotransmitters, hormones, etc ...) due to the activities of these cells [Sakka et al. 2011]
- immunological support of the CNS [Villar et al. 2014].

2.2.Circulation of the cerebrospinal fluid

There is no consensus in the literature regarding the circulation of CSF. Two hypothesis emerges from the literature : a classical one developed for more than one hundred years and a more recent hypothesis dating from ten years.

According the first hypothesis, CSF is produced by the epithelial cells of the choroid plexus of the brain ventricles and flows from the lateral ventricles through the foramina of Monro to the third ventricle. From there, the CSF flows through the aqueduct of Sylvius into the fourth ventricle. CSF exits the ventricular system through the median aperture (also called foramen of Magendie) and the two lateral apertures of Luschka, and enters the cisterns surrounding the cerebellum in the inferior cranial SAS. The CSF bulk flow continues to move superiorly and inferiorly to the cranial and spinal SAS, respectively (Fig. 11). The bulk flow is driven by a dynamic combination between CSF secretion, absorption and resistance to flow [Sakka et al. 2011]. Thus, CSF pressure is maintained by equalization of the rates of CSF secretion and reabsorption. Changes in CSF pressure can occur rapidly when the rates of CSF secretion and reabsorption are not balanced, leading to cranial SAS volume gain such as hydrocephalus [Simon and Iliff 2016].

According the second one, CSF is consistently produced and absorbed throughout the whole CSF system through the capillary walls into the surrounding CNS tissues. Its volume is regulated by the hydrostatic and osmotic forces between CSF and neural tissues. As such, a significant portion of CSF formation seems to occur outside the brain ventricles, from blood to interstitial fluid channels surrounding the

vascular vessels or arterial capillaries with high capillary pressure. These interstitial fluid channels are directly linked to the subarachnoid space. Based on this model, CNS venous capillaries that are under low hydrostatic pressure are the main spots for CSF reabsorption due to their large surface area. Meanwhile, arachnoid granulations and perineural sheaths of the cranial and spinal nerves serve as accessory pathways for CSF absorption, which becomes significant when substances are infused into CSF under high experimental pressure. Glymphatic system is another potential pathway for the exchange of CSF and interstitial fluid within the CNS tissue, which would facilitate clearance of potential neurotoxic wastes products [Martin and Pahlavian 2019]. This second hypothesis seems to be more and more support by the scientific community [Berliner et al. 2019, Liff and Simon 2019, Rey and Sartinoranont 2018].

2.3. Pulsation of the cerebrospinal fluid

The CSF flow is craniocaudally oriented during cardiac systole (heart contraction) and in the reverse direction during diastole (relaxation of the heart) (Fig. 12). And then the initiating point of CSF velocity pulsation (point where the pulse spreads outward in both cranial and caudal directions) was estimated at the foramen magnum (base of brain) level. In addition, the CSF pulse wave velocity in the human cervical spine has been measured to be 4.6 m/s in the craniocaudal direction during systole [Kalata et al. 2009] but velocity can range from 2 to 20 cm/s (in pathological cases) and stroke volume of about 0.5-2ml per CSF flow cycle.

These variations could be explained by several factors. Indeed, cerebrospinal fluid pulsations have a significant sensitivity to the cardiac cycle, venous pressure and respiratory cycle. However, the main mechanisms leading to CSF flow are still not fully understood. The phase-contrast MRI techniques tends to explain the nature of CSF pulsatile flow by a change in brain volume resulting from alterations in intracranial blood perfusion during cardiac and respiratory cycles. The total cerebral blood volume is reported to change by the same amount as the CSF exchange between the cranial and spinal SAS (0.5–2.0 mL per cardiac cycle) and then the intracranial blood flow must compensate by the CSF flow to and from the cranial subarachnoid space. CSF system compliance in healthy humans (i.e., cranial and spinal combined) has been estimated to range from roughly 0.5 to 2.0 mL/mmHg (i.e. 3.8 to 15.0 mL/kPa). Concerning the brain volume changes due to respiratory cycle, the increase cranial CSF flow analyzed during deep inhalation could be explained by the reduction of the cerebral blood volume, which is caused by the decreasing thoracic pressure during deep inhalation [Kalata et al. 2009]. In opposite, during deep exhalation, an increase in thoracic pressure reduces the cranial venous blood returning from the brain and resulting in caudally directed CSF flow to compensate for increased intracranial venous blood volume. Others intense respiratory events such as coughing, sneezing, the Valsalva maneuver could disturbate the pressure environments which would affect the CSF flow pulse magnitude, frequency and flow direction [Martin and Pahlavian 2019].

In the two theories of CSF circulation, it was shown that the CSF pulsation is driven by the respiratory pulsation. Indeed, echo planar imaging measurements showed respiratory influence rose the maximum CSF flow velocity by 19% at C1 and by 28% at T12 [Friese et al. 2004] whereas a coupling MRI ECG-cardiac-gated acquisition showed that the cardiac and the arterial pulsations is the greatest influence [Kiviniemi et al. 2016].

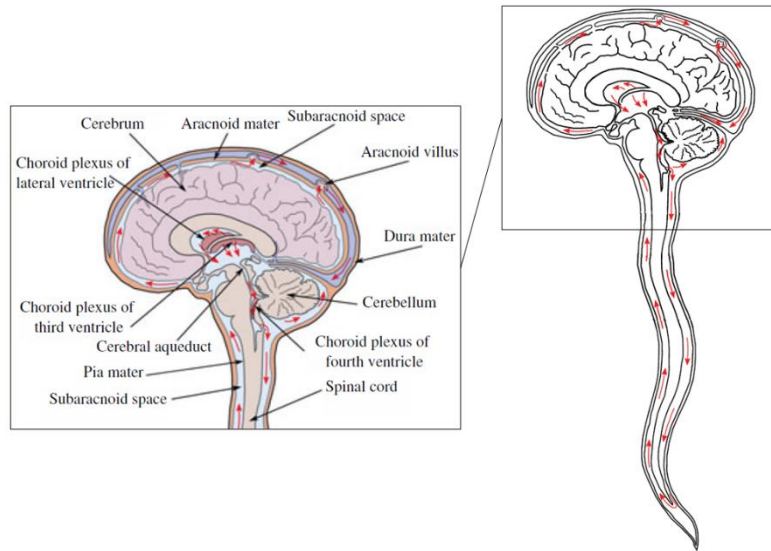


Figure 11. CSF circulation in the subarachnoid space. Schematic view of the anatomical features of the cranial cavity and the spinal canal with the motion of CSF indicated by red arrows [From Sánchez et al. 2018].

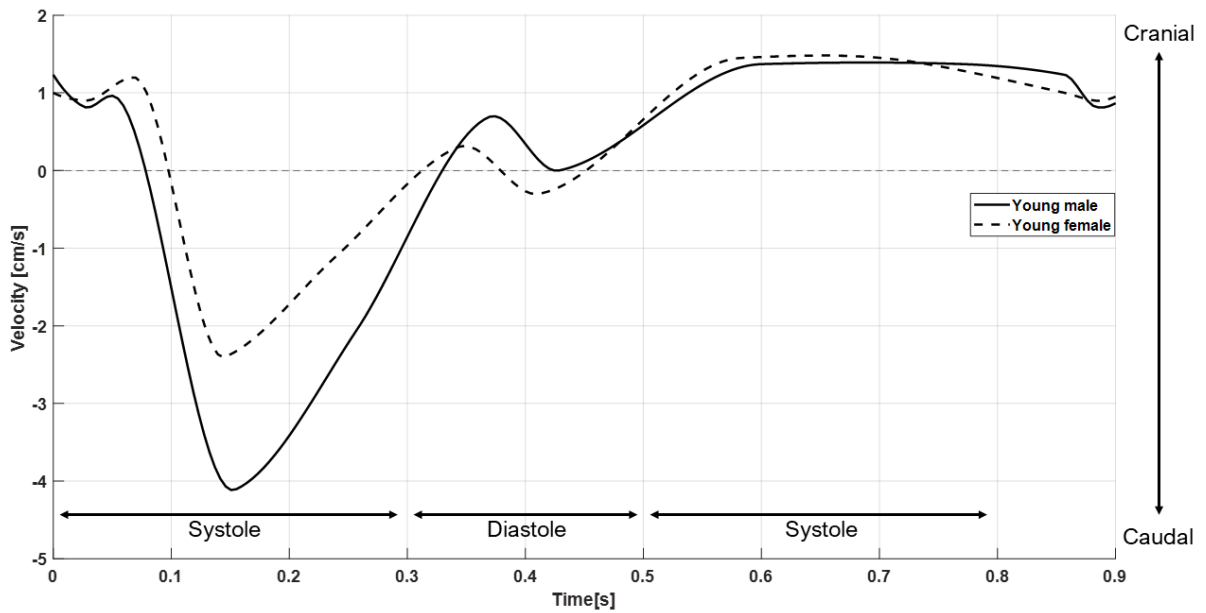


Figure 12. CSF velocity profile of young female and male over a typical ventricular cardiac cycle [From Daners et al. 2012].

3. Clinical and biomechanical contexts

3.1. Epidemiology of cervical myelopathy

Occurrence of non-traumatic spinal cord injuries was estimated to be 59% in Japan, 54% in United States, 31% in Europe, 22% in Australia and between 4% and 30% in Africa between 1959 and 2011 [Fig. 14, New et al. 2014]. Among the non-traumatic spinal cord injuries, degenerative cervical myelopathy (DCM) is a chronic degenerative disease occurring in the cervical vertebral canal. The rapid or slow degenerative process of stenosis development may lead to a compression of the spinal cord with a risk of damage of the neuronal pathway. It remains challenging for the clinician to establish a diagnosis with a high degree of confidence. For this reason, the incidence of DCM is difficult to quantify and has great chance to be under estimated.

This disease is a common cause of SCI for elderly population aged over 55 years. Northover et al. [2012] showed a correlation between the degree of antero-posterior stenosis and the age as well as the number of cervical levels affected. Moreover, earlier affection was found in women in comparison to men (57.0 y against 66.5 y) with lower number of affected levels (2 against 3) and an inferior degree of stenosis in the antero-posterior direction. Abnormalities in the cervical canal were detected in 14%, and disk herniation in 28% of people under 40 years. These percentage doubled for people over 40 years. Spatially, the C5/C6 IVD is the most commonly impacted level, followed by the C6/C7 and the C4/C5 levels. Then, no global epidemiological data was found on the occurrence of single-level DCM compared to multi-level DCM [Northover et al. 2012].

3.2. Pathophysiology of degenerative cervical myelopathy

Only the progressive or chronic DCM are described in this section. Traumatic DCM (post-fall) or Shneider syndrome are excluded.

This section was inspired by Roisin T Dolan et al. [2016].

Pathogenesis of the cervical spine develops with respect to time as a consequence of external structural load, repetitive micro-trauma, and age-related physiological changes of hard tissues such as bone or soft tissues such as muscles, ligaments and IVD (Fig. 13, 15). The degenerative process acts such as a vicious circle depending on two key factors : static or dynamic mechanical factors.

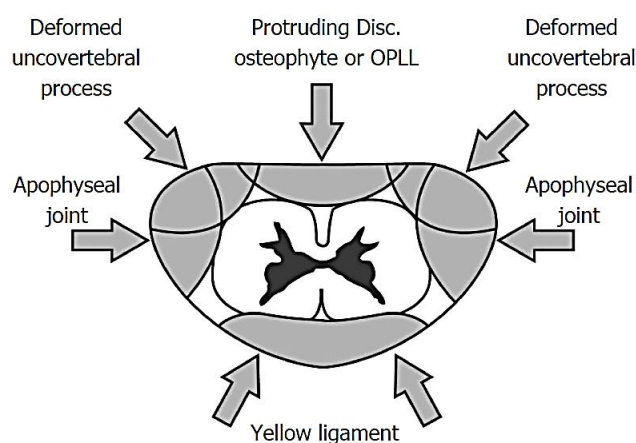


Figure 13. Degenerative changes that contribute to compression of the spinal cord leading to cervical myelopathy. OPPL : ossification of the posterior ligament [From Roisin T Dolan 2016].

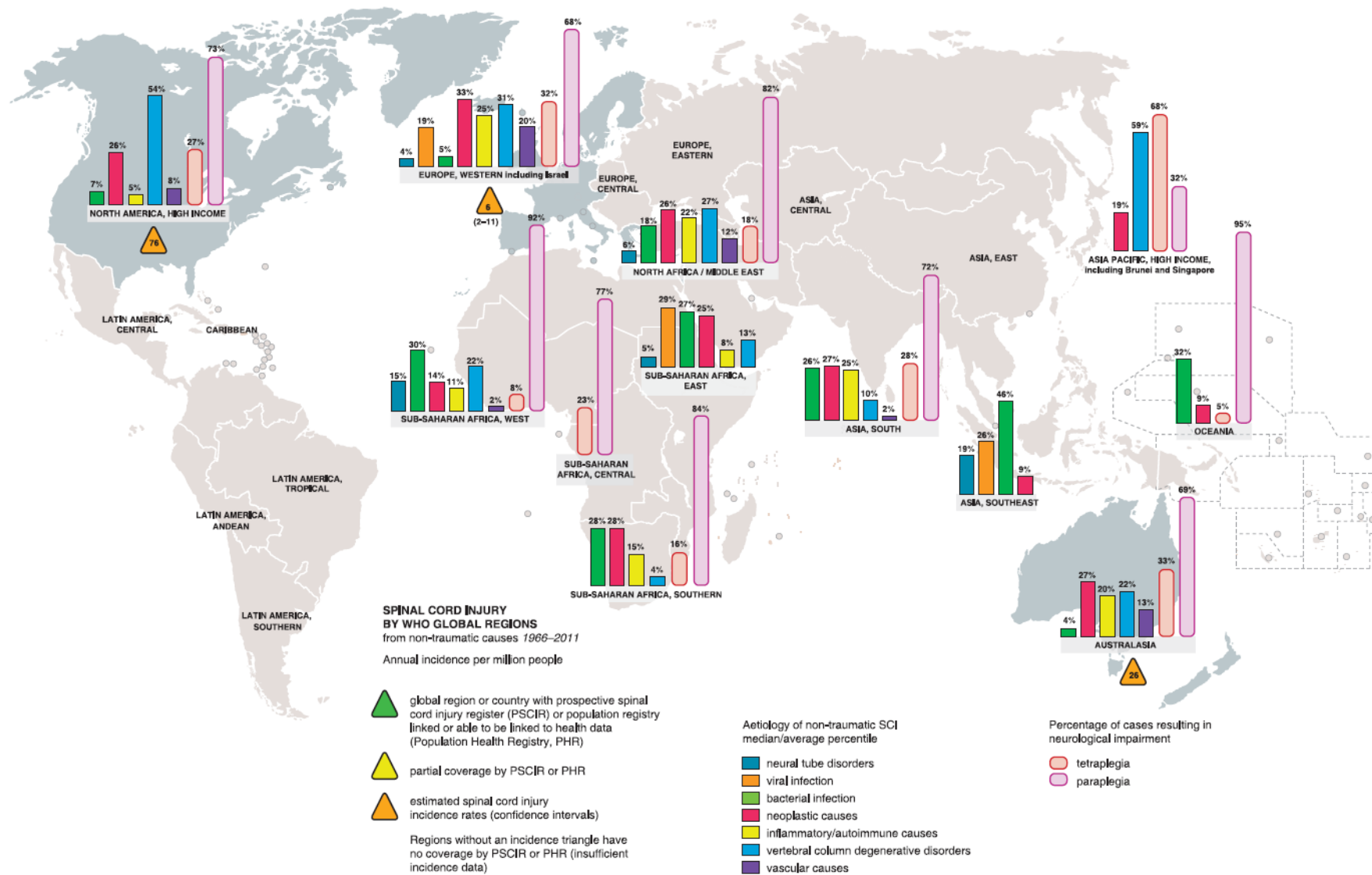


Figure 14. Global maps of non-traumatic spinal cord injuries epidemiological outcomes (1959–2011) by WHO global regions [From New et al. 2014].

3.2.1. Static pathophysiological mechanisms

The origins of static pathophysiological mechanisms are multiple in terms of involved structures : intervertebral discs, vertebrae, ligaments. Among the pathophysiological mechanisms, the main degenerative processes are listed as followed:

Spondylosis or disc degeneration: the intervertebral discs homogeneously bear and distribute the forces and the moments acting on vertebral endplates and facet joints. A loss of proteoglycans and water over time decreases the elasticity of the disc, change its shape and the balance of effort distribution. Then, this local degeneration leads to a cascade of progressive changes: disc herniation, an ossification of the ligament such as the ligamentum flavum or the posterior longitudinal ligament, an ossification of the posterior side of the vertebral body corners (osteophytes) or disc bulging due to disc herniation. A combination of such multi-degenerative factors can lead to cervical canal stenosis and spinal cord compression. Furthermore, the compression can compromise the structure and the function of the vertebral arteries or the spinal nerves. The compression of nerves called cervical radiculopathy can lead to demyelination of sensor or motor tracts.

Ossification of spinal ligament (OSSL): OSSL is a common pathology developed by repetitive external loading on the ligament and genetic factor. Calcifications allow ligamentum flavum to fuse with adjacent lamina, whereas in ossification of the posterior longitudinal ligament (OPLL), the ligament adheres to the posterior aspects of the vertebral bodies and intervertebral disks.

Osteophytes : an osteophyte is a fibrocartilage-capped bony outgrowth causing osteoarthritis. Risk factors for development of osteophytes include age, body mass index (BMI), physical activity, genetic and environmental factors. They can cause pain, limit range of motion, affect quality of life and lead to multiple spinal diseases such as myelopathy.

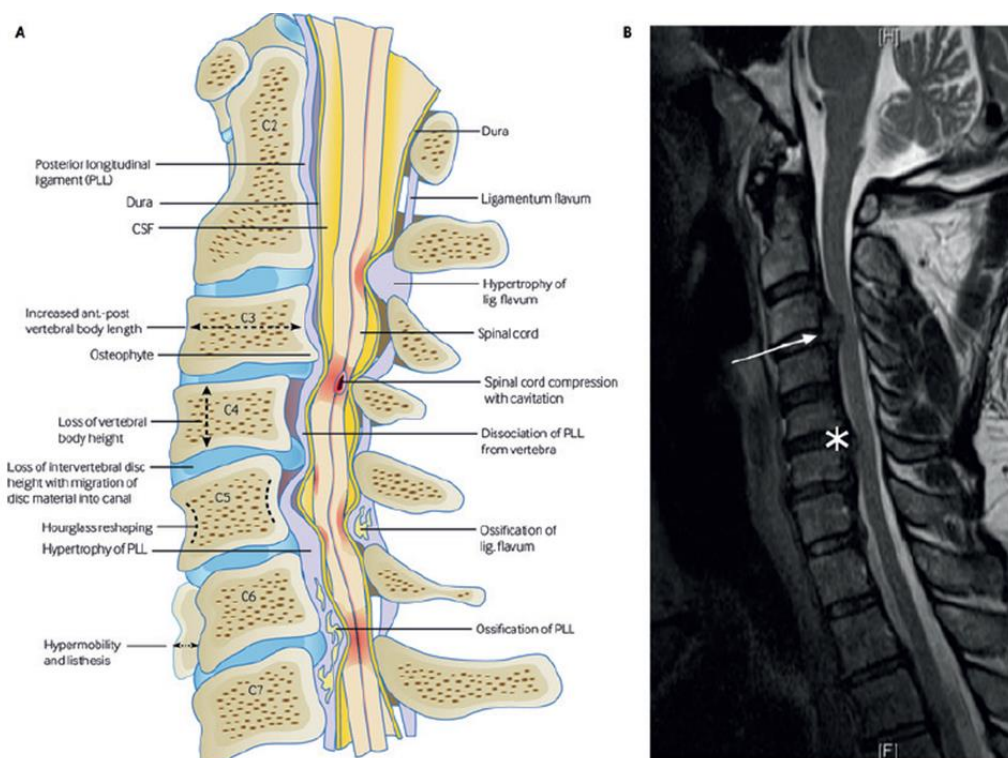


Figure 15. Types of DCM. **A** - Anatomy of an initially healthy spine (C2 level), with examples of the potential pathological changes that can occur and cause DCM.1 **B** - Sagittal section from a T2-weighted MRI scan showing multilevel degenerative changes in the cervical spine. The spinal cord is compressed at C3/4 by a disc prolapse (white arrow) and at C5/6 by spondylosis, thickening of the posterior longitudinal ligament, and a disc-osteophyte complex (white star) [From [Davies et al. 2018](#)].

3.2.2. Dynamic pathophysiological mechanisms

Spinal cord can move in the spinal canal. During phases of hyperflexion or hyperextension, repetitive loading could drive to degenerative process of the canal. During extension of the neck in a patient with a cervical canal stenosis, a buckling of the ligamentum flavum is created, acting on the lamina and leading to a compressive pinch effect on the spinal cord. In flexion, the spinal cord is positioned more anteriorly and can easily be compressed against a degenerated IVD level or an osteophytes. However, the viscoelastic properties of the SC, i.e. the mechanical properties dependent on the time, allows to store and to dissipate energy created for example by a dynamic compression. It allows to mitigate the dynamic effect on the SC tissue.

These mechanisms may contribute to ischemic injury [[Ellingson et al. 2019](#)], blood-brain barrier alteration [[Blume et al. 2020](#)] and demyelination process [[Liu et al. 2018](#)] without any warranty of initial recovery of the sensory-motor functions of the patient.

3.2.3. Cerebrospinal flow

In clinical routine, the cerebrospinal flow is not considered in the diagnosis or prognosis of the patient but the signal representing the cerebrospinal fluid on the MR images (also called) provides clues on the state of the canal. In clinical research, studies highlighted a decrease of the maximal CSF velocity associated to stenosis severity [[Bae et al. 2017](#), [Im et al. 2014](#), [Watabe et al. 1999](#)]. In parallel, biomechanical models highlighted a pressure drop at the stenosis level [[Bertram et al. 2016](#), [Cheng et al. 2014](#)]. This decrease of velocity could be explained by an axial enforced circulation of the CSF by the interstitial channels (also called perivascular spaces) surrounding the vessels through the spinal cord. This assumption is based on the recent CSF circulation theory in these channels described previously in the section 2.2 [[Berliner et al. 2019](#), [Liff and Simon 2019](#), [Rey and Sarntinoranont 2018](#)].

3.3. Clinical management

3.3.1. Diagnosis

Detecting early progressive DCM can be challenging as its exact physio-pathology remains unclear. The consequences and symptoms associated with the cervical cord compression varies depending on the spatiality in the axial and longitudinal direction, the advancement of the compression and the biological characteristics of each individual.

The most common initial symptoms of chronic DCM are subtle and include difficulties with hand dexterity, gait instability, headaches, muscle cramps and neck pain. As multiple symptoms can be induced by sensory or motor damages at different spinal cord levels and are commons to other pathologies, the physical exam remains complex to be directly associated with the DCM.

Initially, the DCM symptoms were evaluated by the Nurick scale based on gait instabilities. Clinical and scientific research communities preferred to use another score based on sensory and motor criteria called the Japanese Orthopedic Association Myelopathy Evaluation Questionnaire (JOA). A revised version of JOA score (mJOA) including the shoulder and elbow function is also used with a high

correlation coefficient between the two scores (0.87). One of drawbacks is that the evaluation is based on patient's dexterity using chopsticks which is not so common and differently evaluated in western population [Kato et al. 2015], creating clinician-derived subjective interpretation. Another drawback is the JOA and mJOA scores are patient-derived subjective score [McGregor et al. 2019]. Moreover the score presented in this paragraph are not so used in clinical routine and the American Spine Injury Association score (ASIA) or a simplified ASIA score (faster) is currently preferred. This last observation comes from discussions with a small sample of local neurosurgeons. ASIA score is considered as an objective measurement tool based on sensory and motor evaluation. However, in a recent study, no correlation was found between ASIA score and mJOA for postoperative patient [McGregor et al. 2019]. This observation highlights ambiguity in the establishment of a prognosis.

The diagnosis is confirmed by an imaging evaluation which can be plain (2d) x-ray radiography, computed tomography (CT) scans and anatomical magnetic resonance imaging (MRI). Anatomical MRI (T2 sequence) remains the most reliable approach to confirm the diagnosis and to evaluate postoperative evolution. Each imaging approach has advantages and drawbacks: CT is the cheapest imaging tool, noninvasive but remains irradiant for the patient. Only hard tissue such as bones are observable depending on the bone density. MRI is noninvasive and non-irradiant and allows a detailed visualization of hard and soft tissue but this imaging tool has a high economical cost [McCormick et al. 2019].

In clinical routine, few quantitative and qualitative factors are used to define a DCM on imaging scans: antero-posterior diameter of the canal in mid-sagittal plane, Torg-Pavlov ratio (i.e. anteroposterior diameter of the cervical canal over the anteroposterior diameter of the vertebral body ratio <0.8) and visualization of hypersignal in the spinal cord at the level of the compression which could reveal an ischemia [McCormick et al. 2019]. Due to the high inter-individual anatomical variability, quantitative indices such as antero-posterior canal diameter are unreliable. Torg-Pavlov ratio is not always used for DCM diagnosis [McCormick et al. 2019].

All those previously described difficulties inherent to DCM diagnosis lead to a problematic delay in diagnosis [Hilton et al. 2018]. A mean time delay in diagnosis of DCM was estimated at 2.2 ± 2.3 years [Behrbalk et al. 2013] while an older study highlighted an average time delay of 6.3 years with a decrease of the clinical score up to the 4th Nurick grade (assistance for walking) [Sadasivan et al. 1993].

Once DCM is diagnosed, the primary decision to be made is to manage the solution surgically or not. When nonsurgical treatments are considered, the rates of significant activities of daily life impairments are 6% at 1 year, 21% at 2 years, 28% at 3 years and 56% at 10 years [McCormick et al. 2019].

3.3.2. Surgery management

Guidelines from AOSpine an international community of spine surgeons recommend surgery in patients with moderate or severe DCM or with fast disease progression based on JOA score [Fehlings et al. 2017].

In a clinical routine, it is still challenging to predict the benefit of the surgery in the long term. The recovery of the patient is maximal between 6 and 12 months. After this post-operative period, residual symptoms such as functional deficit (falls, reduced mobility, incontinence, depression, sleep deficit and pain) can still persist [Davies et al. 2018]. However, a recent study developed a statistical model enable to predict a prognosis up to 12 months [Archer et al. 2020].

Multiple surgery approaches are considered for DCM decompression which are an anterior, posterior, or combined approach depending on the patient's state. Patient with a hyper-kyphosis, or OPPL are generally treated with anterior approach. Anterior surgery consists in anterior discectomy (partial or

total resection of an intervertebral disc) and fusion (surgical device to connect two or more vertebrae to eliminate motion between them), anterior corpectomy (resection of one or several vertebral bodies to decrease the compression on the spinal cord) and fusion or disc arthroplasty (restoring the biomechanical functions of a joint by resurfacing the bone or by using prosthetics such as artificial discs). Then, when the patient has a multi-level DCM, posterior compression or congenital stenosis, a posterior approach is considered. It consists in laminectomy with or without fusion and laminoplasty [McCormick et al. 2019]. The decompression by laminectomy can create impingement effect at upper cervical levels, in particular during flexion/extension of the neck [Stoner et al. 2020, 2019].

3.4. Biomechanics of the cervical spine and canal

The description of this section is limited to the neutral and flexion posture of the spine in order to align with the studies which are presented throughout the rest of the manuscript.

3.4.1. The cervical spine

Six degrees (3 in translation and 3 in rotation) of freedom (DOF) are considered for each functional spine unit (FSU).

In vitro experiment showed that the physiological charges at the intervertebral joint level in upright position vary from 100 to 400 N depending on the loading direction whereas the torque is 2 Nm for axial rotation. Others postures such as sedentary working posture in front of a computer for example or handling posture might increase the load range described above, and overloading the intervertebral joint, in particular because of the shear stresses [Laporte et al. 2017].

The range of motion (ROM) or motion magnitude is limited by the facet joints and the IVD in terms of antero-posterior shear, while the flexion is limited by the facet joints, the anterior part of the vertebral canal and by the posterior ligaments [Laporte et al. 2017].

Fig. 16 describes the distribution of the ROM by FSU. The flexion-extension of the C4-C5, the C5-C6 and the C6-C7 segments, which are the most involved FSU in DCM, is responsible for 43.3 % of the total ROM. The lateral bending of the same segments represents 37.7 % of the total ROM while their axial rotation represents 19.2 % of the total ROM.

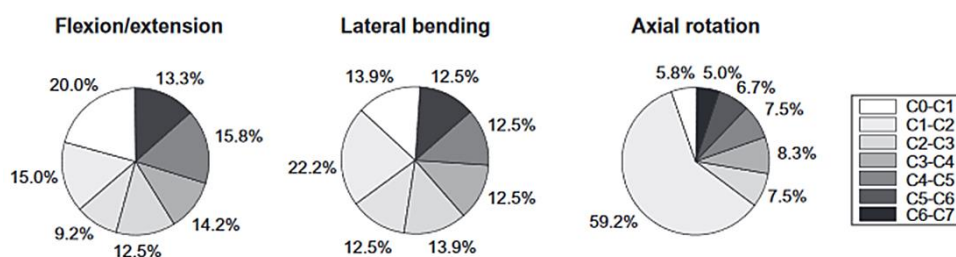


Figure 16. Distribution of cervical ROM among functional spine units [From Laporte et al. 2017].

3.4.2. The cervical canal

The cervical canal forms by the vertebrae foramen end-to-end connected longitudinally in which the spinal cord is enclosed and protected. The spinal cord and the anterior part of the canal lengthen during physiological flexion and lateral bending while the cross-sectional area decreases. The incompressibility (no volume change) of the spinal cord tissue demonstrated in literature [Jannesar et al. 2016] force the tissue to change its geometry when it submits strains such as elastomers. That explains the use of

constitutive laws often used in elastomers modeling and described in Chapter 4. Moreover, the spinal cord is also protected by the surrounding soft tissues: the meninges, the subarachnoid space filled by the CSF and the epidural fat outside the dura mater. It was assumed that these tissues protect the central nervous system [White and Panjabi 1990] in combination with the role of shock absorber by the CSF described in the Chapter 2 section 2. Several studies converged toward this interpretation of the protective role of the meninges, in particular in dynamic conditions [Ramo et al. 2018a, b, c]. Indeed, the viscoelasticity of these tissue allows a capacity to store and to dissipate energy. To the best of our knowledge, the mechanical properties of epidural fat was not measured but we thought that due to the rheological behavior close to viscoelasticity of other types of adipose tissue (i.e. fat) in the body [Alkhouli et al. 2013], its protective role could be assumed.

The mechanical spinal cord behavior is often considered with gray and white matter. The behavior in axial compression of the spinal cord tends to be strain-rate dependent with a non-linear behavior described by the “J” shape of the stress/strain curves [Karimi et al. 2017, Fradet et al. 2016b]. The toe-region is large : up to 40% of strain at 0.5, 5 and 50 s⁻¹ [Fradet et al. 2016b] and up to almost 30% of strain at a test velocity of 5mm/min [Karimi et al. 2017]. In terms of longitudinal tension, the tensile properties of spinal cord also tends to be strain-rate dependent and non-linear [Ramo et al. 2018b, Ramo et al. 2018c]. A loss of myelin (sheath around the axons), which can occurs when the nervous tissues are damaged, decreases the tensile stiffness of the spinal cord [Shreiber et al. 2009]. Thus, scientific community converges toward a non-linear viscoelasticity description of the spinal cord. In addition, a mechanical anisotropy behavior was also highlighted [Koser et al. 2015].

The large toe region is probably due to the kinematics of the cord directly driven by the high mobility of the cervical spine. The lateral stability of the spinal cord provided by the denticulate ligaments, the nerves roots and the CSF allow to partially maintain a central position, maximizing its mechanical protection from shock or structural degeneracies. The spinal cord without the pia mater has a viscous aspect which cannot keep its initial shape [White and Panjabi 1990].

3.4.3. Biomechanics of the degenerative cervical myelopathy

Local narrowing of the canal can be induced by multiple cases including the most common cases: 1) an hypertrophy of the *ligamentum flavum* due to a loss of elasticity caused by multifactor such as the activity level, age, mechanical stresses [Sairyo et al. 2005] ; 2) abnormal disc bulge due to disc herniation caused by a dehydration of the disc leading to a loss of viscoelastic properties. It alters the load-bearing function and the load transfer along the cervical spine with increased age; 3) Osteophytes stabilize adjacent vertebrae whose hypermobility is caused by the degeneration of the disk. Indeed, the loss of disk function leads to a greater stress on the vertebral endplates [Baptiste and Fehlings 2006] ; 4) Ossification of the posterior longitudinal ligament (common in Eastern Asia [Wu et al 2018]) which is known to be an idiopathic and multifactorial disease, in which genetic factors and non-genetic factors including diet, obesity, physical strain on the posterior longitudinal ligament, age, and diabetes mellitus [Nam et al. 2019]. The DCM patient can also develop a combination of these degenerative cases.

Neck flexion motion of a patient with one or several of these degenerative processes have much chance to create a local pinch effect where the canal is narrowed as described in Fig. 17.

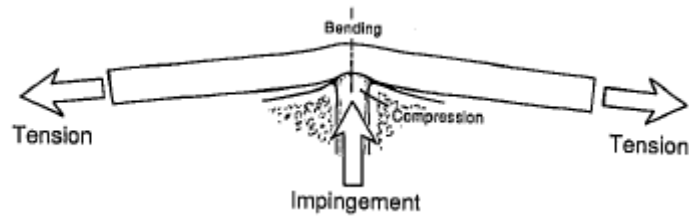


Figure 17. Degenerative impingement causing compression, stretching and bending of the spinal cord [Panjabi and White 1998].

From a biomechanical point of view, the pinch effect could be divided into three simple loads in a first approach and as a combination of them as a further biomechanical interpretation according to Panjabi and White [1998].

The three loads consist in: 1) in a compression due to the pinch created by the degenerative structure (IVD, vertebra, ligament); 2) producing shear stress in the cross section orthogonal to the direction of compression; 3) in a tension due to the flexion of the neck and a bending load due to the change of direction of the spinal cord imposed by the degenerative structure. The compression load applied in the antero-posterior direction decreases in magnitude moving away from the contact point while the shear load is then equaled to zero at the contact point and increase up to a maximum shear stress point corresponding to the centroid of the cross-section of the spinal cord. The tensile load is applied at the extremities of the spinal cord considering an uniform distribution of the tensile load along it. The bending of the cord due to the pinch is decomposed in two loads : a compression load in the concave part of the cord and a tensile load in the convex one where the maximum of magnitude is reached on the outer side of the concave and the convex sides [Panjabi and White 1998]. The three loads presented above are elementary and theoretical cases. In reality, the spinal cord submits a combination of these loads or a combination of several directions of compression loads in the axial plane as shown in Lévy et al. [2020]. These simplistic circular beam analogy based on solid mechanics could help in the understanding on how a more complex structure such as spinal cord behaves in decomposing the principal stresses by a quite simple approach.

To finish, in many biomechanical models of the spinal cord, the computational structure dynamics (CSD) analysis is often reduced to show a Von Misès (VM) stress field, a stress measurement taking into account the normal and shear Cauchy stress interpreted like an average value. Few papers described the stress field of all the normal and shear components independently. Moreover, the Von Misès stress measurement was initially developed to analyze the behavior for isotropic ductile structures while most of soft tissues have anisotropic behavior. The non-linearity of tissues is more and more implemented in numerical models. For this type of modelling, the VM measurement could be questioned while other type of stress criteria would be more adapted for anisotropic fibrous soft tissues such as the Tsai–Hill model [Korenczuk et al. 2017].

4. Appendices

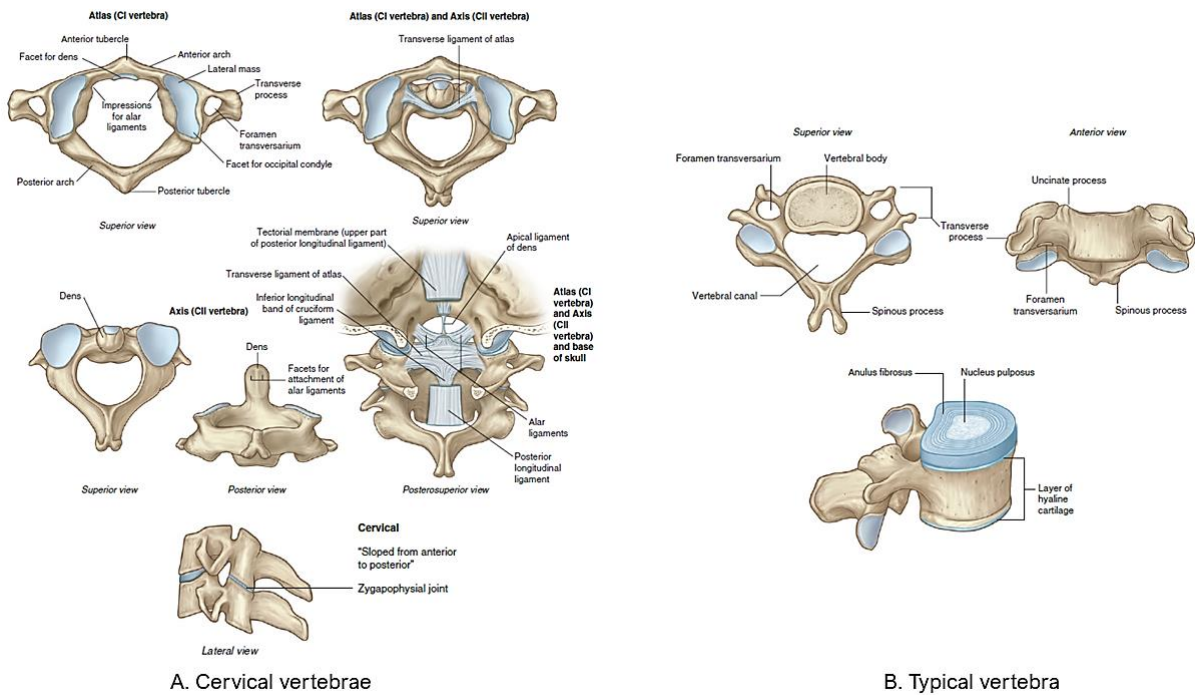


Figure 18. Cervical and typical vertebrae. Gray's Anatomy for Students, 4th Edition (2020)

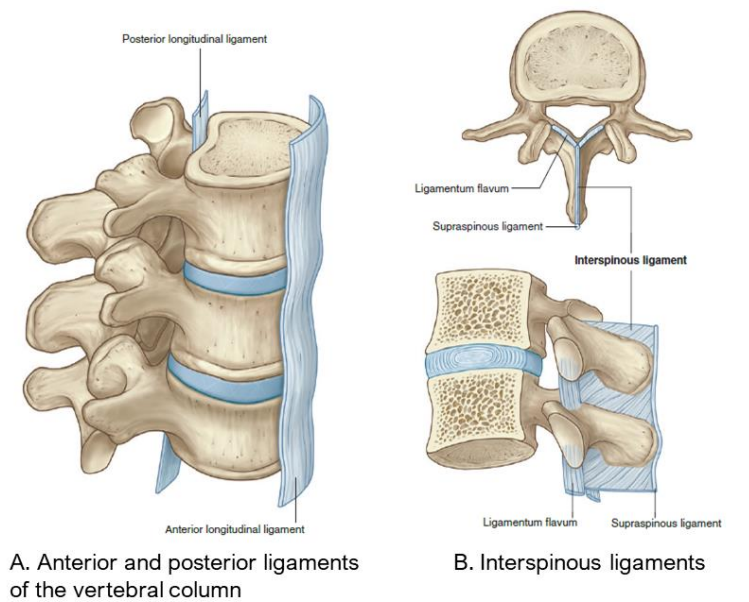


Figure 19. Cervical ligaments. Gray's Anatomy for Students, 4th Edition (2020)

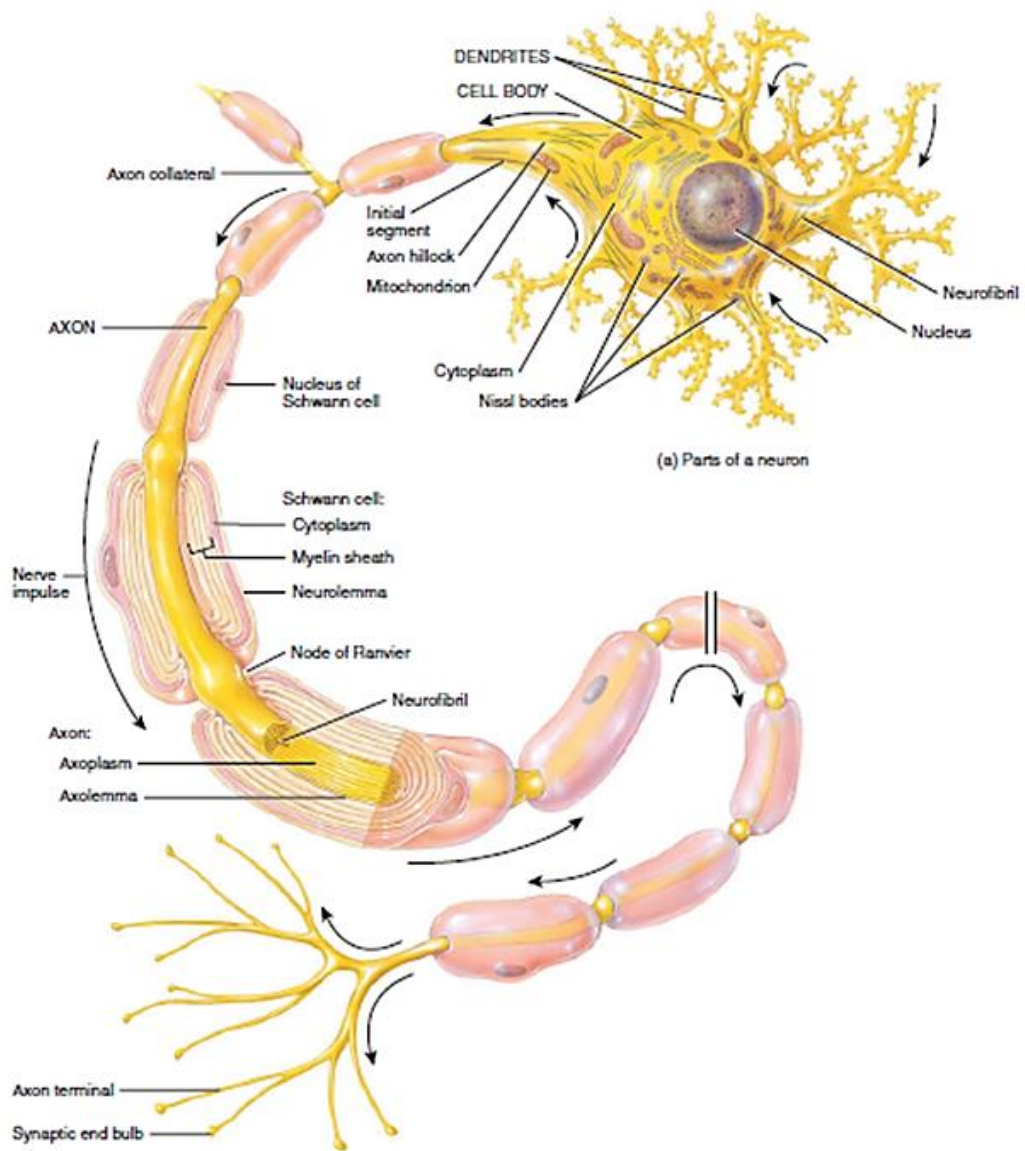


Figure 20. Typical structure of a neuron [from *Principals of anatomy and physiology – Tortora, 14th edition*]

5. References

- [Adeeb et al. 2013] Adeeb, N., Mortazavi, M.M., Deep, A., Griessenauer, C.J., Watanabe, K., Shoja, M.M., Loukas, M., Tubbs, R.S., 2013. The pia mater: a comprehensive review of literature. *Childs Nerv Syst* 29, 1803–1810. <https://doi.org/10.1007/s00381-013-2044-5>
- [Alkhoul et al. 2013] Alkhoul, N., Mansfield, J., Green, E., Bell, J., Knight, B., Liversedge, N., Tham, J.C., Welbourn, R., Shore, A.C., Kos, K., Winlove, C.P., 2013. The mechanical properties of human adipose tissues and their relationships to the structure and composition of the extracellular matrix. *American Journal of Physiology-Endocrinology and Metabolism* 305, E1427–E1435. <https://doi.org/10.1152/ajpendo.00111.2013>
- [Archer et al. 2020] Archer, K.R., Bydon, M., Khan, I., Nian, H., Pennings, J.S., Harrell, F.E.J., Sivaganesan, A., Chotai, S., McGirt, M.J., Foley, K.T., Glassman, S.D., Mummaneni, P.V., Bisson, E.F., Knightly, J.J., Shaffrey, C.I., Asher, A.L., Devin, C.J., Sites, Q.V., 2020. Development and Validation of Cervical Prediction Models for Patient-Reported Outcomes at 1 Year After Cervical Spine Surgery for Radiculopathy and Myelopathy. *Spine* 45, 1541–1552. <https://doi.org/10.1097/BRS.0000000000003610>
- [Bae et al. 2017] Bae, Y.J., Lee, J.W., Lee, E., Yeom, J.S., Kim, K.-J., Kang, H.S., 2017. Cervical compressive myelopathy: flow analysis of cerebrospinal fluid using phase-contrast magnetic resonance imaging. *Eur Spine J* 26, 40–48. <https://doi.org/10.1007/s00586-016-4874-9>
- [Baptiste and Fehlings 2006] Baptiste, D.C., Fehlings, M.G., 2006. Pathophysiology of cervical myelopathy. *The Spine Journal, Special Issue on Cervical Myelopathy* 6, S190–S197. <https://doi.org/10.1016/j.spinee.2006.04.024>
- [Beauséjour et al. 2020] Beauséjour, M.-H., Petit, Y., Hagen, J., Arnoux, P.-J., Thiong, J.-M.M., Wagnac, E., 2020. Contribution of injured posterior ligamentous complex and intervertebral disc on post-traumatic instability at the cervical spine. *Computer Methods in Biomechanics and Biomedical Engineering* 23, 832–843. <https://doi.org/10.1080/10255842.2020.1767776>
- [Beel et al. 1986] Beel, J.A., Stodieck, L.S., Luttges, M.W., 1986. Structural properties of spinal nerve roots: Biomechanics. *Experimental Neurology* 91, 30–40. [https://doi.org/10.1016/0014-4886\(86\)90023-3](https://doi.org/10.1016/0014-4886(86)90023-3)
- [Behrbalk et al. 2013] Behrbalk, E., Salame, K., Regev, G.J., Keynan, O., Boszczyk, B., Lidar, Z., 2013. Delayed diagnosis of cervical spondylotic myelopathy by primary care physicians. *Neurosurgical Focus* 35, E1. <https://doi.org/10.3171/2013.3.FOCUS1374>
- [Berliner et al. 2019] Berliner, J., Hemley, S., Najafi, E., Bilston, L., Stoodley, M., Lam, M., 2020. Abnormalities in spinal cord ultrastructure in a rat model of post-traumatic syringomyelia. *Fluids and Barriers of the CNS* 17, 11. <https://doi.org/10.1186/s12987-020-0171-4>
- [Bertram et al. 2016] Bertram, C.D., Heil, M., 2016. A Poroelastic Fluid/Structure-Interaction Model of Cerebrospinal Fluid Dynamics in the Cord With Syringomyelia and Adjacent Subarachnoid-Space Stenosis. *J Biomech Eng* 139, 011001-011001–10. <https://doi.org/10.1115/1.4034657>
- [Bianco et al. 2019] Bianco, R.-J., Arnoux, P.-J., Mac-Thiong, J.-M., Aubin, C.-E., 2019. Thoracic pedicle screw fixation under axial and perpendicular loadings: A comprehensive numerical analysis. *Clinical Biomechanics* 68, 190–196. <https://doi.org/10.1016/j.clinbiomech.2019.06.010>
- [Blume et al. 2020] Blume, C., Geiger, M.F., Brandenburg, L.O., Müller, M., Mainz, V., Kalder, J., Albanna, W., Clusmann, H., Mueller, C.A., 2020. Patients with degenerative cervical myelopathy have signs of blood spinal cord barrier disruption, and its magnitude correlates with myelopathy severity: a prospective comparative cohort study. *Eur Spine J* 29, 986–993. <https://doi.org/10.1007/s00586-020-06298-7>
- [Bosmia et al. 2015] Bosmia, A.N., Hogan, E., Loukas, M., Tubbs, R.S., Cohen-Gadol, A.A., 2015. Blood supply to the human spinal cord: Part I. Anatomy and hemodynamics. *Clinical Anatomy* 28, 52–64. <https://doi.org/10.1002/ca.22281>
- [Brummund et al. 2017] Brummund, M., Brailovski, V., Petit, Y., Facchinello, Y., Mac-Thiong, J.-M., 2017. Impact of anchor type on porcine lumbar biomechanics: Finite element modelling and in-vitro validation. *Clinical Biomechanics* 43, 86–94. <https://doi.org/10.1016/j.clinbiomech.2017.02.007>
- [Cadotte et al. 2014] Cadotte DW, Cadotte A, Cohen-Adad J, et al. Characterizing the location of spinal and vertebral levels in the human cervical spinal cord. *AJNR Am J Neuroradiol*. 2015;36(4):803-810.
- [Ceylan et al. 2012] Ceylan D, Tatarli N, Abdullaev T, et al. The denticulate ligament: anatomical properties, functional and clinical significance. *Acta Neurochir*. 2012;154(7):1229-1234.
- [Chauvet et al. 2010] Chauvet, D., Carpentier, A., Allain, J.-M., Polivka, M., Crépin, J., George, B., 2010. Histological and biomechanical study of dura mater applied to the technique of dura splitting decompression in Chiari type I malformation. *Neurosurg Rev* 33, 287–295. <https://doi.org/10.1007/s10143-010-0261-x>
- [Cheng et al. 2014] Cheng, S., Fletcher, D., Hemley, S., Stoodley, M., Bilston, L., 2014. Effects of fluid structure interaction in a three dimensional model of the spinal subarachnoid space. *Journal of Biomechanics* 47, 2826–2830. <https://doi.org/10.1016/j.jbiomech.2014.04.027>
- [Daners et al. 2012] Schmid Daners, M., Knobloch, V., Soellinger, M., Boesiger, P., Seifert, B., Guzzella, L., Kurtcuoglu, V., 2012. Age-Specific Characteristics and Coupling of Cerebral Arterial Inflow and Cerebrospinal Fluid Dynamics. *PLoS One* 7. <https://doi.org/10.1371/journal.pone.0037502>

- [Darby 2014] Darby, S.A., 2014. Chapter 3 - General Anatomy of the Spinal Cord, in: Cramer, G.D., Darby, S.A. (Eds.), *Clinical Anatomy of the Spine, Spinal Cord, and Ans (Third Edition)*. Mosby, Saint Louis, pp. 65–97. <https://doi.org/10.1016/B978-0-323-07954-9.00003-7>
- [Datta et al. 2019] Datta, D., Conroy, A.L., Castelluccio, P.F., Ssenkusu, J.M., Park, G.S., Opoka, R.O., Bangirana, P., Idro, R., Saykin, A.J., John, C.C., 2020. Elevated Cerebrospinal Fluid Tau Protein Concentrations on Admission Are Associated With Long-term Neurologic and Cognitive Impairment in Ugandan Children With Cerebral Malaria. *Clin Infect Dis* 70, 1161–1168. <https://doi.org/10.1093/cid/ciz325>
- [Davies et al. 2018] Davies, B.M., Mowforth, O.D., Smith, E.K., Kotter, M.R., 2018. Degenerative cervical myelopathy. *BMJ* 360. <https://doi.org/10.1136/bmj.k186>
- [Ellingson et al. 2019] Ellingson, B.M., Woodworth, D.C., Leu, K., Salamon, N., Holly, L.T., 2019. Spinal Cord Perfusion MR Imaging Implicates Both Ischemia and Hypoxia in the Pathogenesis of Cervical Spondylosis. *World Neurosurgery* 128, e773–e781. <https://doi.org/10.1016/j.wneu.2019.04.253>
- [Fehlings et al. 2017] Fehlings, M.G., Tetreault, L.A., Riew, K.D., Middleton, J.W., Wang, J.C., 2017. A Clinical Practice Guideline for the Management of Degenerative Cervical Myelopathy: Introduction, Rationale, and Scope. *Global Spine J* 7, 21S-27S. <https://doi.org/10.1177/2192568217703088>
- [Fournely et al. 2020] Fournely, M., Petit, Y., Wagnac, E., Evin, M., Arnoux, P.-J., 2020. Effect of experimental, morphological and mechanical factors on the murine spinal cord subjected to transverse contusion: A finite element study. *PLOS ONE* 15, e0232975. <https://doi.org/10.1371/journal.pone.0232975>
- [Fowler et al. 2020] Fowler, M.J., Cotter, J.D., Knight, B.E., Sevick-Muraca, E.M., Sandberg, D.I., Sirianni, R.W., 2020. Intrathecal drug delivery in the era of nanomedicine. *Advanced Drug Delivery Reviews*. <https://doi.org/10.1016/j.addr.2020.02.006>
- [Fradet et al. 2014] Fradet L, Arnoux P-J, Ranjeva J-P, et al. Morphometrics of the entire human spinal cord and spinal canal measured from in vivo high-resolution anatomical magnetic resonance imaging. *Spine*. 2014;39(4):E262-269.
- [Fradet et al. 2016a] Fradet, L., Arnoux, P.-J., Callot, V., Petit, Y., 2016. Geometrical variations in white and gray matter affect the biomechanics of spinal cord injuries more than the arachnoid space. *Advances in Mechanical Engineering* 8, 1687814016664703. <https://doi.org/10.1177/1687814016664703>
- [Fradet et al. 2016b] Fradet, L., Cliche, F., Petit, Y., Mac-Thiong, J.-M., Arnoux, P.-J., 2016. Strain rate dependent behavior of the porcine spinal cord under transverse dynamic compression. *Proc Inst Mech Eng H* 230, 858–866. <https://doi.org/10.1177/0954411916655373>
- [Friese et al. 2004] Friese, S., Hamhaber, U., Erb, M., Kueker, W., Klose, U., 2004. The Influence of Pulse and Respiration on Spinal Cerebrospinal Fluid Pulsation. *Investigative Radiology* 39, 120–130. <https://doi.org/10.1097/01.rli.0000112089.66448.bd>
- [Ganau et al. 2019] Ganau, M., Zewude, R., Fehlings, M.G., 2019. Functional Anatomy of the Spinal Cord, in: Kaiser, M.G., Haid, R.W., Shaffrey, C.I., Fehlings, M.G. (Eds.), *Degenerative Cervical Myelopathy and Radiculopathy : Treatment Approaches and Options*. Springer International Publishing, Cham, pp. 3–12. https://doi.org/10.1007/978-3-319-97952-6_1
- [Garnotel et al. 2017] Garnotel, S., Salmon, S., Balédent, O., 2017. Numerical Modeling of the Intracranial Pressure using Windkessel Models. *MathematicS In Action* 8, 9–25. <https://doi.org/10.5802/msia.11>
- [Gassner et al. 2017] Grassner, L., Grillhösl, A., Griessenauer, C.J., Thomé, C., Bühren, V., Strowitzki, M., Winkler, P.A., 2017. Spinal Meninges and Their Role in Spinal Cord Injury: A Neuroanatomical Review. *Journal of Neurotrauma* 35, 403–410. <https://doi.org/10.1089/neu.2017.5215>
- [Gray's Anatomy for Students, 4th Edition (2020)] Gray's Anatomy for Students - 4th Edition [WWW Document], n.d. URL <https://www.elsevier.com/books/grays-anatomy-for-students/drake/978-0-323-39304-1>.
- [Hansson et al. 2019] Hansson, K., Dahlén, R., Hansson, O., Pernevik, E., Paterson, R., Schott, J.M., Magdalinou, N., Zetterberg, H., Blennow, K., Gobom, J., 2019. Use of the tau protein-to-peptide ratio in CSF to improve diagnostic classification of Alzheimer's disease. *Clinical Mass Spectrometry, Clinical Mass Spectrometry focusing on the Brain* 14, 74–82. <https://doi.org/10.1016/j.clinms.2019.07.002>
- [Hilton et al. 2018] Hilton, B., Tempest-Mitchell, J., Davies, B., Kotter, M., 2018. Assessment of degenerative cervical myelopathy differs between specialists and may influence time to diagnosis and clinical outcomes. *PLOS ONE* 13, e0207709. <https://doi.org/10.1371/journal.pone.0207709>
- [<https://cnx.org/>] <https://cnx.org/contents/voWXZkel@1.1:tbVb8yVc@1/Anatomical-Terminology>
- [Im et al. 2014] Im, V., Sm, M., El, M., B, M., Dk, L., A, R., T, V., V, V., Al, M., A, C., 2014. Increased spinal cord movements in cervical spondylotic myelopathy. *Spine J* 14, 2344–2354. <https://doi.org/10.1016/j.spinee.2014.01.036>
- [Jannesar et al. 2016] Jannesar, S., Nadler, B., Sparrey, C.J., 2016. The Transverse Isotropy of Spinal Cord White Matter Under Dynamic Load. *Journal of Biomechanical Engineering* 138. <https://doi.org/10.1115/1.4034171>
- [Jones 2011] Jones, C.F., 2011. Cerebrospinal fluid mechanics during and after experimental spinal cord injury.

- [Kalata et al. 2009] Kalata, W., Martin, B.A., Oshinski, J.N., Jerosch-Herold, M., Royston, T.J., Loth*, F., 2009. MR Measurement of Cerebrospinal Fluid Velocity Wave Speed in the Spinal Canal. *IEEE Transactions on Biomedical Engineering* 56, 1765–1768. <https://doi.org/10.1109/TBME.2008.2011647>
- [Kalsi-Ryan et al. 2013] Kalsi-Ryan, S., Karadimas, S.K., Fehlings, M.G., 2013. Cervical spondylotic myelopathy: the clinical phenomenon and the current pathobiology of an increasingly prevalent and devastating disorder. *Neuroscientist* 19, 409–421. <https://doi.org/10.1177/1073858412467377>
- [Karimi et al. 2017] Karimi, A., Shojaei, A., Tehrani, P., 2017. Mechanical properties of the human spinal cord under the compressive loading. *J. Chem. Neuroanat.* 86, 15–18. <https://doi.org/10.1016/j.jchemneu.2017.07.004>
- [Kato et al. 2015] Kato, S., Oshima, Y., Oka, H., Chikuda, H., Takeshita, Y., Miyoshi, K., Kawamura, N., Masuda, K., Kunogi, J., Okazaki, R., Azuma, S., Hara, N., Tanaka, S., Takeshita, K., 2015. Comparison of the Japanese Orthopaedic Association (JOA) Score and Modified JOA (mJOA) Score for the Assessment of Cervical Myelopathy: A Multicenter Observational Study. *PLOS ONE* 10, e0123022. <https://doi.org/10.1371/journal.pone.0123022>
- [Kato et al. 2016] Kato, S., Fehlings, M., 2016. Degenerative cervical myelopathy. *Curr Rev Musculoskelet Med* 9, 263–271. <https://doi.org/10.1007/s12178-016-9348-5>
- [Kato et al. 2018] Kato, S., Ganau, M., Fehlings, M.G., 2018. Surgical decision-making in degenerative cervical myelopathy – Anterior versus posterior approach. *Journal of Clinical Neuroscience* 58, 7–12. <https://doi.org/10.1016/j.jocn.2018.08.046>
- [Kim et al. 2019] Kim, K.-T., Streijger, F., So, K., Manouchehri, N., Shortt, K., Okon, E.B., Tigchelaar, S., Fong, A., Morrison, C., Keung, M., Sun, J., Liu, E., Cripton, P.A., Kwon, B.K., 2019. Differences in Morphometric Measures of the Uninjured Porcine Spinal Cord and Dural Sac Predict Histological and Behavioral Outcomes after Traumatic Spinal Cord Injury. *Journal of Neurotrauma* 36, 3005–3017. <https://doi.org/10.1089/neu.2018.5930>
- [Kinaci et al. 2020] Kinaci, A., Bergmann, W., Bleys, R.L., van der Zwan, A., van Doormaal, T.P., 2020. Histologic Comparison of the Dura Mater among Species. *Comparative Medicine* 70, 170–175. <https://doi.org/10.30802/AALAS-CM-19-000022>
- [Kiviniemi et al. 2016] Kiviniemi, V., Wang, X., Korhonen, V., Keinänen, T., Tuovinen, T., Autio, J., LeVan, P., Keilholz, S., Zang, Y.-F., Hennig, J., Nedergaard, M., 2016. Ultra-fast magnetic resonance encephalography of physiological brain activity – Glymphatic pulsation mechanisms? *J Cereb Blood Flow Metab* 36, 1033–1045. <https://doi.org/10.1177/0271678X15622047>
- [Korenczuk et al. 2017] Korenczuk, C.E., Votava, L.E., Dhume, R.Y., Kizilski, S.B., Brown, G.E., Narain, R., Barocas, V.H., 2017. Isotropic Failure Criteria Are Not Appropriate for Anisotropic Fibrous Biological Tissues. *J Biomech Eng* 139, 0710081–07100810. <https://doi.org/10.1115/1.4036316>
- [Kwon et al. 2016] Kwon, B.K., Streijger, F., Fallah, N., Noonan, V.K., Bélanger, L.M., Ritchie, L., Paquette, S.J., Ailon, T., Boyd, M.C., Street, J., Fisher, C.G., Dvorak, M.F., 2016. Cerebrospinal Fluid Biomarkers To Stratify Injury Severity and Predict Outcome in Human Traumatic Spinal Cord Injury. *Journal of Neurotrauma* 34, 567–580. <https://doi.org/10.1089/neu.2016.4435>
- [Laporte et al. 2017] Laporte, S., Van den Abbeele, M., Rohan, P.-Y., Adam, C., Rouch, P., Skalli, W., 2017. Chapter 22 - Spine, in: Payan, Y., Ohayon, J. (Eds.), *Biomechanics of Living Organs, Translational Epigenetics*. Academic Press, Oxford, pp. 471–495. <https://doi.org/10.1016/B978-0-12-804009-6.00022-5>
- [Lévy et al. 2020] Lévy, S., Baucher, G., Roche, P.-H., Evin, M., Callot, V., Arnoux, P.-J., 2020. Biomechanical comparison of spinal cord compression types occurring in Degenerative Cervical Myelopathy. *Clinical Biomechanics* 105174. <https://doi.org/10.1016/j.clinbiomech.2020.105174>
- [Liff and Simon 2019] Liff, J., Simon, M., 2019. The glymphatic system supports convective exchange of cerebrospinal fluid and brain interstitial fluid that is mediated by perivascular aquaporin-4. *J Physiol* 597, 4417–4419. <https://doi.org/10.1113/JP277635>
- [Liu et al. 2018] Liu, S., Lam, M.A., Sial, A., Hemley, S.J., Bilston, L.E., Stoodley, M.A., 2018. Fluid outflow in the rat spinal cord: the role of perivascular and paravascular pathways. *Fluids Barriers CNS* 15, 13. <https://doi.org/10.1186/s12987-018-0098-1>
- [Marmarou et al. 1975] Marmarou, A., Shulman, K., LaMorgese, J., 1975. Compartmental analysis of compliance and outflow resistance of the cerebrospinal fluid system. *J Neurosurg* 43, 523–534. <https://doi.org/10.3171/jns.1975.43.5.0523>
- [Martin and Pahlavian 2019] Martin, B.A., Heidari Pahlavian, S., 2019. Chapter 5 - Anatomy and Physiology of Cerebrospinal Fluid Dynamics, in: Lonser, R.R., Sarntinoranont, M., Bankiewicz, K. (Eds.), *Nervous System Drug Delivery*. Academic Press, pp. 73–89. <https://doi.org/10.1016/B978-0-12-813997-4.00005-0>
- [McCormick et al. 2019] McCormick, J.R., Sama, A.J., Schiller, N.C., Butler, A.J., Donnally, C.J., 2020. Cervical Spondylotic Myelopathy: A Guide to Diagnosis and Management. *J Am Board Fam Med* 33, 303–313. <https://doi.org/10.3122/jabfm.2020.02.190195>
- [McGregor et al. 2019] McGregor, S.M.K., Detombe, S.A., Goncalves, S., Doyle-Pettypiece, P., Bartha, R., Duggal, N., 2019. Does the Neurological Examination Correlate with Patient-Perceived Outcomes in Degenerative Cervical Myelopathy? *World Neurosurgery* 132, e885–e890. <https://doi.org/10.1016/j.wneu.2019.07.195>

- [Mortazavi et al. 2017] Mortazavi, M.M., Quadri, S.A., Khan, M.A., Gustin, A., Suriya, S.S., Hassanzadeh, T., Fahimdanesh, K.M., Adl, F.H., Fard, S.A., Taqi, M.A., Armstrong, I., Martin, B.A., Tubbs, R.S., 2018. Subarachnoid Trabeculae: A Comprehensive Review of Their Embryology, Histology, Morphology, and Surgical Significance. *World Neurosurgery* 111, 279–290. <https://doi.org/10.1016/j.wneu.2017.12.041>
- [Nam et al. 2019] Nam, D.C., Lee, H.J., Lee, C.J., Hwang, S.-C., 2019. Molecular Pathophysiology of Ossification of the Posterior Longitudinal Ligament (OPLL). *Biomol Ther (Seoul)* 27, 342–348. <https://doi.org/10.4062/biomolther.2019.043>
- [New et al. 2014] New, P.W., Cripps, R.A., Bonne Lee, B., 2014. Global maps of non-traumatic spinal cord injury epidemiology: towards a living data repository. *Spinal Cord* 52, 97–109. <https://doi.org/10.1038/sc.2012.165>
- [Northover et al. 2012] Northover, J.R., Wild, J.B., Braybrooke, J., Blanco, J., 2012. The epidemiology of cervical spondylotic myelopathy. *Skeletal Radiol* 41, 1543–1546. <https://doi.org/10.1007/s00256-012-1388-3>
- [Nouri et al. 2017] Nouri, A., Martin, A.R., Nater, A., Witiw, C.D., Kato, S., Tetreault, L., Reihani-Kermani, H., Santaguida, C., Fehlings, M.G., 2017. Influence of Magnetic Resonance Imaging Features on Surgical Decision-Making in Degenerative Cervical Myelopathy: Results from a Global Survey of AOSpine International Members. *World Neurosurgery* 105, 864–874. <https://doi.org/10.1016/j.wneu.2017.06.025>
- [OMS website] Spinal cord injury [WWW Document], n.d. URL <https://www.who.int/news-room/fact-sheets/detail/spinal-cord-injury> (accessed 12.11.20).
- [Panjabi and White 1998] Panjabi, M., White, A.I., 1988. Biomechanics of Nonacute Cervical Spinal Cord Trauma. *Spine* 13, 838–842.
- [Patin et al. 1993] Patin, D., Eckstein, E., Harum, K., Pallares, V., 1993. Anatomic and Biomechanical Properties of Human Lumbar Dura Mater. *Anesthesia & Analgesia* 76, 535–540.
- [Persson et al. 2011] Persson, C., Summers, J., Hall, R.M., 2011. The Effect of Cerebrospinal Fluid Thickness on Traumatic Spinal Cord Deformation. *Journal of Applied Biomechanics* 27, 330–335. <https://doi.org/10.1123/jab.27.4.330>
- [Polak et al. 2014] Polak, K., Czyż, M., Ścigała, K., Jarmundowicz, W., Będziński, R., 2014. Biomechanical characteristics of the porcine denticulate ligament in different vertebral levels of the cervical spine—Preliminary results of an experimental study. *Journal of the Mechanical Behavior of Biomedical Materials* 34, 165–170. <https://doi.org/10.1016/j.jmbbm.2014.02.010>
- [Polak et al. 2019] Polak-Kraśna K, Robak-Nawrocka S, Szotek S, et al. The denticulate ligament – Tensile characterisation and finite element micro-scale model of the structure stabilising spinal cord. *Journal of the Mechanical Behavior of Biomedical Materials*. 2019;91:10-17.
- [Ramo et al. 2018a] Ramo, N., Shetye, S.S., Puttlitz, C.M., 2018. Damage Accumulation Modeling and Rate Dependency of Spinal Dura Mater. *ASME J of Medical Diagnostics* 1. <https://doi.org/10.1115/1.4038261>
- [Ramo et al. 2018b] Ramo, N.L., Shetye, S.S., Streijger, F., Lee, J.H.T., Troyer, K.L., Kwon, B.K., Cripton, P., Puttlitz, C.M., 2018. Comparison of In-Vivo and Ex-Vivo Viscoelastic Behavior of the Spinal Cord. *Acta Biomater* 68, 78–89. <https://doi.org/10.1016/j.actbio.2017.12.024>
- [Ramo et al. 2018c] Ramo, N.L., Troyer, K.L., Puttlitz, C.M., 2018. Viscoelasticity of spinal cord and meningeal tissues. *Acta Biomaterialia* 75, 253–262. <https://doi.org/10.1016/j.actbio.2018.05.045>
- [Reina et al. 1997] Reina, M., Angel, Dittmann, M., Garcia, A.L., van Zundert, A., 1997. New perspectives in the microscopic structure of human dura mater in the dorsolumbar region. *Regional Anesthesia and Pain Medicine* 22, 161–166. [https://doi.org/10.1016/S1098-7339\(06\)80036-2](https://doi.org/10.1016/S1098-7339(06)80036-2)
- [Reina et al. 2002] Angel Reina, M., De Leon Casasola, O., López, A., Antonio De Andrés, J., Mora, M., Fernández, A., 2002. The Origin of the Spinal Subdural Space: Ultrastructure Findings. *Anesthesia & Analgesia* 94, 991–995. <https://doi.org/10.1097/0000539-200204000-00040>
- [Reina et al. 2008] Reina, M.A., Maches, F., López, A., De Andrés, J.A., 2008. The ultrastructure of the spinal arachnoid in humans and its impact on spinal anesthesia, cauda equina syndrome, and transient neurological syndrome. *Techniques in Regional Anesthesia and Pain Management, Anatomy in Regional Anesthesia* 12, 153–160. <https://doi.org/10.1053/j.trap.2008.03.002>
- [Reina et al. 2020] Reina, M.A., Boezaart, A., De Andres-Serrano, C., Rubio-Haro, R., De Andrés, J., 2020. Microanatomy Relevant to Intrathecal Drug Delivery, in: Jain, K.K. (Ed.), *Drug Delivery Systems, Methods in Molecular Biology*. Springer, New York, NY, pp. 109–120. https://doi.org/10.1007/978-1-4939-9798-5_4
- [Rey and Sarntinoranont 2018] Rey, J., Sarntinoranont, M., 2018. Pulsatile flow drivers in brain parenchyma and perivascular spaces: a resistance network model study. *Fluids and Barriers of the CNS* 15, 20. <https://doi.org/10.1186/s12987-018-0105-6>
- [Roisin T. Dolan et al. 2016] Roisin T Dolan, J.S.B., Byrne, A.R.P., 2016. Mechanical and cellular processes driving cervical myelopathy. *World Journal of Orthopedics* 7, 20–29. <https://doi.org/10.5312/wjo.v7.i1.20>
- [Sadasivan et al. 1993] Sadasivan, K.K., Reddy, R.P., Albright, J.A., 1993. The natural history of cervical spondylotic myelopathy. *Yale J Biol Med* 66, 235–242.
- [Sairyo et al. 2005] Sairyo, K., Biyani, A., Goel, V., Leaman, D., Booth, R.J., Thomas, J., Gehling, D., Vishnubhotla, L., Long, R., Ebraheim, N., 2005. Pathomechanism of Ligamentum Flavum Hypertrophy: A Multidisciplinary Investigation Based on Clinical, Biomechanical, Histologic, and Biologic Assessments. *Spine* 30, 2649–2656. <https://doi.org/10.1097/01.brs.0000188117.77657.ee>

- [Saker et al. 2016] Saker, E., Henry, B.M., Tomaszewski, K.A., Loukas, M., Iwanaga, J., Oskouian, R.J., Tubbs, R.S., n.d. The Human Central Canal of the Spinal Cord: A Comprehensive Review of its Anatomy, Embryology, Molecular Development, Variants, and Pathology. *Cureus* 8. <https://doi.org/10.7759/cureus.927>
- [Sakka et al. 2011] Sakka, L., Coll, G., Chazal, J., 2011. Anatomy and physiology of cerebrospinal fluid. *European Annals of Otorhinolaryngology, Head and Neck Diseases* 128, 309–316. <https://doi.org/10.1016/j.anorl.2011.03.002>
- [Sakka et al. 2016] Sakka, L., Gabrillargues, J., Coll, G., 2016. Anatomy of the Spinal Meninges. *Oper Neurosurg (Hagerstown)* 12, 168–188. <https://doi.org/10.1227/NEU.0000000000001048>
- [Schomberg et al. 2017] Schomberg, D.T., Miranpuri, G.S., Chopra, A., Patel, K., Meudt, J.J., Tellez, A., Resnick, D.K., Shanmuganayagam, D., 2017. Translational Relevance of Swine Models of Spinal Cord Injury. *J. Neurotrauma* 34, 541–551. <https://doi.org/10.1089/neu.2016.4567>
- [Shreiber et al. 2008] Shreiber, D.I., Hao, H., Elias, R.A., 2008. Probing the influence of myelin and glia on the tensile properties of the spinal cord. *Biomech Model Mechanobiol* 8, 311. <https://doi.org/10.1007/s10237-008-0137-y>
- [Simon and Iliff 2016] Simon, M.J., Iliff, J.J., 2016. Regulation of cerebrospinal fluid (CSF) flow in neurodegenerative, neurovascular and neuroinflammatory disease. *Biochimica et Biophysica Acta (BBA) - Molecular Basis of Disease, NEUROINFLAMMATION: A common denominator for stroke, multiple sclerosis and Alzheimer's disease* 1862, 442–451. <https://doi.org/10.1016/j.bbadis.2015.10.014>
- [Singh et al. 2006] Singh, A., Lu, Y., Chen, C., M Cavanaugh, J., 2006. Mechanical properties of spinal nerve roots subjected to tension at different strain rates. *Journal of Biomechanics* 39, 1669–1676. <https://doi.org/10.1016/j.jbiomech.2005.04.023>
- [Stoner et al. 2019] Stoner KE, Abode-Iyamah KO, Magnotta VA, et al. Measurement of in vivo spinal cord displacement and strain fields of healthy and myelopathic cervical spinal cord. *Journal of Neurosurgery: Spine*. 2019;31(1):53-59.
- [Stoner et al. 2020] Stoner, K.E., Abode-Iyamah, K.O., Fredericks, D.C., Viljoen, S., Howard, M.A., Grosland, N.M., 2020. A comprehensive finite element model of surgical treatment for cervical myelopathy. *Clinical Biomechanics* 74, 79–86. <https://doi.org/10.1016/j.clinbiomech.2020.02.009>
- [Swindle et al. 2013] Swindle, M.M., Smith, A.C., 2013. Best Practices for Performing Experimental Surgery in Swine. *Journal of Investigative Surgery* 26, 63–71. <https://doi.org/10.3109/08941939.2012.693149>
- Swine Resource Handbook for Market and Breeding Projects, page 3-15] Swine Resource Handbook for Market and Breeding Projects [WWW Document], n.d. . OSU Extension Publications. URL <https://extensionpubs.osu.edu/swine-resource-handbook-for-market-and-breeding-projects/>.
- [Thomas JH. 2019] Thomas, J.H., 2019. Fluid dynamics of cerebrospinal fluid flow in perivascular spaces. *Journal of The Royal Society Interface* 16, 20190572. <https://doi.org/10.1098/rsif.2019.0572>
- [Tortora, 14th edition] Tortora, Derrickson: Principles of Anatomy and Physiology, 14th Edition - Student Companion Site [WWW Document], n.d. URL <http://bcs.wiley.com/he-bcs/Books?action=index&bcsId=8680&itemId=1118345002>.
- [Tubbs et al. 2001] Tubbs, R.S., Salter, G., Grabb, P.A., Oakes, W.J., 2001. The denticulate ligament: anatomy and functional significance. *Journal of Neurosurgery: Spine* 94, 271–275. <https://doi.org/10.3171/spi.2001.94.2.0271>
- [Van Dogen et al. 2017] Van Dongen, R.M., Zielman, R., Noga, M., Dekkers, O.M., Hankemeier, T., van den Maagdenberg, A.M., Terwindt, G.M., Ferrari, M.D., 2017. Migraine biomarkers in cerebrospinal fluid: A systematic review and meta-analysis. *Cephalalgia* 37, 49–63. <https://doi.org/10.1177/0333102415625614>
- [Villar et al. 2014] Villar, L.M., Picón, C., Costa-Frossard, L., Alenda, R., García-Caldentey, J., Espiño, M., Muriel, A., Álvarez-Cermeño, J.C., 2015. Cerebrospinal fluid immunological biomarkers associated with axonal damage in multiple sclerosis. *European Journal of Neurology* 22, 1169–1175. <https://doi.org/10.1111/ene.12579>
- [Watabe et al. 1999] Watabe, N., Tominaga, T., Shimizu, H., Kosu, K., Yoshimoto, T., 1999. Quantitative analysis of cerebrospinal fluid flow in patients with cervical spondylosis using cine phase-contrast magnetic resonance imaging. *Neurosurgery* 44, 779–784. <https://doi.org/10.1097/00006123-199904000-00052>
- [White and Panjabi 1990] White, A.A., Panjabi, M.M., 1990. *Clinical Biomechanics of the Spine*. Lippincott.
- [Wilke et al. 2011] Wilke, H.-J., Geppert, J., Kienle, A., 2011. Biomechanical in vitro evaluation of the complete porcine spine in comparison with data of the human spine. *Eur Spine J* 20, 1859–1868. <https://doi.org/10.1007/s00586-011-1822-6>
- [Wu et al 2018] Wu, J.-C., Chen, Y.-C., Huang, W.-C., 2018. Ossification of the Posterior Longitudinal Ligament in Cervical Spine: Prevalence, Management, and Prognosis. *Neurospine* 15, 33–41. <https://doi.org/10.14245/ns.1836084.042>

Chapter 2

Literature Review

1. Studying cervical spinal canal morphometry	48
1.1. Healthy subjects	48
1.2. Cervical myelopathy	49
2. Studying mechanical properties of the mechanical properties of the CNS and the CSF	50
2.1. Cerebrospinal fluid	50
2.2. The spinal cord	52
2.3. The nerve roots	53
2.4. The denticulate ligaments	53
2.5. The meninges	53
3. Studying the CSF flow and the central nervous system modelling	56
3.1. Computational Fluid Dynamics models	56
3.2. Fluid-Structure Interaction models	60
4. Appendices	64
5. References	66

Abbreviations

ALE : arbitrary Lagrangian Eulerian
CFD : computational fluid dynamics
CNS : central nervous system
CT : computed tomography
CR : compression ratio
CSF : cerebrospinal fluid
CSS : cervical subarachnoid space
DMA : dynamic mechanical analysis
FSI : fluid-structure interactions
IVD : intervertebral disc
MRI : magnetic resonance image
OR : occupational ratio
PIV : particle image velocimetry
SAS : subarachnoid space
SC : spinal cord

1. Studying cervical spinal canal morphometry

Morphological characterization of healthy and symptomatic spinal canal is necessary for clinical diagnosis and prognosis as well as biomechanical modeling in terms of solid boundary conditions or partial validation of the morphometrics behavior.

1.1. Healthy subjects

All along the life, repetitive motion of the neck as well as durable posture such as office posture or long use of portable devices or activities leading to neck postural disorder create non-physiological strains and stresses on our spine but also within the vertebral canal. These changes in lifestyle and daily activities associated with repetitive cervical mobility can lead to chronic pain [Xie et al. 2019] which can be induced by musculoskeletal disorders. However, it cannot explain in all cases the origin of the neck pain. One of other hypothesis is that the structure and the morphometry of the vertebral canal is altered due to a repetitive neck mobility, could induce local alterations of the musculoskeletal structure of the cervical spine (intervertebral joint alteration for example), leading to canal stenosis. Thus, understanding the consequences of cervical subarachnoid space (CSS) morphological changes in healthy subjects and during the physiological motion of the neck could help to detect and to treat the pathology associated with medullar injuries.

First morphological studies were performed on human cadavers. Spinal cord was extracted and cutting by slice to allow 2D cross-sectional analysis in terms of area, transverse and sagittal diameters [Ko et al. 2004, Kameyama et al. 1994, Zhang et al. 1996]. Due to the advancements in medical imaging, *in vivo* 2D analysis became the gold standard [Table 1] to face the issues of *post mortem* characterization such as dried samples or the absence of pre-tension of the cord. Indeed, the *in vivo* physiological shape of spinal cord is maintained by the cerebrospinal fluid pressure and by the attachment of the brain and of the cauda equina.

Thus, the medical imaging such as CT-Scan or MRI allowed to measure new metrics. Indeed, Torg ratio i.e. the ratio of sagittal length of the mid-vertebra body over the canal length [Tierney et al. 2002], the length and the volume of the cord [Ko et al. 2004], Cobb angles to correlate the spinal curvature with the spinal canal morphological metrics [Kuwazawa et al. 2006], or occupational ratio of the spinal cord in the canal [Fradet et al. 2014, Kato et al. 2012].

Even if the MRI became a gold standard over the past years, the subarachnoid space is often simplified as dural tube or the space in the sagittal plane between the cord and the anterior and posterior parts of the canal due a limited spatial resolution reached on conventional MR systems (1.5T or 3T, against low-field at 0.5T and ultra-high field $\geq 7T$). Using this assumption, large database of *in vivo* morphological measurements was proposed showing the influence of the age and the sex on the occupation rate of the spinal cord in the dural tube on Japanese population. Indeed, the axial area of the spinal cord and the dural tube tended with age and to decrease faster in men [Kato et al. 2012].

However, operator dependency as well as time consumption associated with such manual definitions of morphological indices as well as relatively high inter and intra-operator errors between measurements need to be reported. In case of a subject follow-up, its position will vary in the MRI from an acquisition to another one which can induce an inter-session variability. Moreover, almost all the studies found in the literature performed discrete measurements, mostly at the mid-vertebra and the mid-IVD levels providing partial data on the cervical canal.

1.2.Cervical myelopathy

Due to ambiguous use of term, cervical spondylosis (meaning vertebra in ancient Greek) degenerative involving vertebra or disc degeneration is associated to a more general term, degenerative cervical myelopathy which includes all the processes leading to a pathological narrowed canal. The quantitative diagnosis and the prognosis of patient with a narrowed canal remains challenging for the clinician even if medical imaging, in particular MRI technology allowed to accurately visualize the *in vivo* anatomy. Local 2D analysis is a gold standard for the scientific and clinical community [Table 1]. Briefly, most used indices in literature were: the cross-sectional area (perpendicular to the centerline of the canal) of the canal, the SC and the CSF. The occupational ratio (OR) is derived from the ratio of these areas. Diameters of the canal, the CSF and the SC are also largely used in sagittal or axial planes. The compression ratio (CR) is derived from the large and small axial diameters of the canal or of the spinal cord are commonly used to quantify the level of flatness. Another common index used to quantify the canal stenosis is the Torg-Pavlov ratio (the sagittal spinal canal diameter divided by the sagittal vertebral body diameter). In most of the studies in Table 1, an operator has to manually perform the different measurements in a discretize way, i.e. plotting the segments or delineating the areas. The measurements are done at mid-vertebra as reference and mid-intervertebral discs because of structural changes appearing with aging or abnormal solicitations called spondylosis or hernia at the IVD levels and such as osteophytes at posterior vertebral plates. Only one study developed a 3D analysis of the spinal cord based on semi-manual 3D reconstruction of the cervical spinal cord. The 3D analysis allows to compute new metrics such as volume correlated to the cross-sectional area and the cord length [Smith et al. 2013].

Numerous limitations are already present in the morphometrics analysis of population with cervical myelopathy. First, such as for clinical studies on healthy population, the methodologies remain time-consuming and operator-dependent which is an important drawback in the data interpretation for the reasons mentioned in the above section. Moreover, such as the healthy populations, inter-session variability could induced additional errors in the metrics quantification. Finally, various morphometrics criteria are used in each study as depicted in the [Table 1] which jeopardize comparison.

2. Studying mechanical properties of the mechanical properties of the CNS and the CSF

The spinal central nervous system is a mechanical system made up of several tissues assembled and bathed in the cerebrospinal fluid, between which there are mechanical interplays. Each element has its own heterogeneous mechanical properties such as most living soft tissues. The mechanical properties of different structures in the spinal canal (cerebrospinal fluid, meninges, denticulate ligaments, spinal cord, nerve roots) are described separately. An overview of mechanical testing studies for each of spinal structures and fluid are respectively depicted in Table 2, 3, 4, 5 and Appendix - Table 6, 7. A brief description of the experimental protocols and results of the main studies presented in the tables were described in the following paragraphs.

2.1.Cerebrospinal fluid

As depicted in Table 2, the CSF is a colorless fluid with mechanical properties close to water at 37°C (body temperature) in term of :

- dynamic viscosity at body temperature [Bloomfield et al. 1998] : 0.8mPa.s

- density at body temperature : 1.0003 ± 0.0003 g.ml⁻¹ [[Levin et al. 1981](#)], 1.00059 ± 0.00020 g.mL⁻¹ [[Lui et al. 1998](#)], 1.00054 ± 0.00017 g.mL⁻¹ for male and 1.00049 ± 0.00011 g.mL⁻¹ [[Schiffer et al. 1999](#)]
- speed of sound in the fluid [[Palaniappan et al. 2004](#)] : 1508.2 – 1520.5 m.s⁻¹.

The CSF has its own pulsation driven by the cardiac and the respiratory pulsations; it is considered incompressible such as water, and it is modelled like a Newtonian fluid. This last property is described in details in Chapter 5.

Authors/Year	Journal	Population studied	Anatomical parts	Measured parameters	Measurement tool	Type of analysis
Healthy and asymptomatic cohorts						
Kameyama <i>et al.</i> 1996	Spine	12 healthy cadavers	Spinal cord C2 - S3	CSA, diameter	Computer-assisted image analysing system	2D
Zhang <i>et al.</i> 1996	The Showa University Journal of Medical Sciences	22 healthy cadavers	Spinal cord C6	Sagittal + Transverse diameters	Electronic optical planimeter	2D
Yuan <i>et al.</i> 1998	Spine	5 volunteers	spinal cord C1 - C7	Anterior and posterior cord, strain	1.5T MRI	2D
Malzac <i>et al.</i> 2002	Acta Ortopédica Brasileira	500 young military volunteers	Spinal canal C3 - C6	Sagittal diameter antero-posterior width	Radiography (X-ray)	2D
Tierney <i>et al.</i> 2002	Journal of Athletic Training	14 healthy subjects	CSF C3 - C7	Torg ratio - CSA CSF	1.5T MRI	2D
Dahlan <i>et al.</i> 2004	International Journal of Integrated Health Sciences	24 healthy subjects	Spinal canal C3-C7	Spinal canal diameter	CT-Scan	2D
Ko <i>et al.</i> 2004	Spinal cord	15 healthy cadavers	Spinal cord C3 - S5	Sagittal and transversal diameter + volume of spinal cord	x	2D
Kuwazawa <i>et al.</i> 2006	Spine	20 healthy volunteers	spinal cord and spine C1 - C7	Length of the cervical cord (anterior, middle, and posterior line), Cobb angle	0.6MRI	2D
Kato <i>et al.</i> 2012	Euro Spine Journal	1211 healthy subjects	Spinal cord and canal C2 - C7	Axial CSA of dural tube+ spinal cord, spinal cord diameter, occupational ratio	1.5T MRI	2D
Fradet <i>et al.</i> 2014	Spine	23 healthy subjects	Spinal cord C1 - S2	Spinal cord dimensions and position in spinal canal	3T MRI	2D
Symptomatic or patients populations with Cervical Spondylosis Degenerative						
Kawakami <i>et al.</i> 2002	Journal of Spinal Disorders and Techniques	113 patients with CSM	spinal cord C2 - T1	Cobb angle, convex index	MRI	2D
Zaaroor <i>et al.</i> 2006	Minimally Invasive Neurosurgery	42 patients	Spinal cord, subarachnoid space, dural sac C1 - L2	Sagittal + Transversal dimensions	0.5T MRI	2D
Muria <i>et al.</i> 2007	Journal of Spinal Disorders and Techniques	20 patients with CSM + 20 healthy control subjects	C3 - C7	the segmental forward-backward movement of the spinal cord, JOA score	1.5T MRI	2D
Morishita <i>et al.</i> 2009	European Spine Journal	295 symptomatic patients	Spinal cord and canal C3 - C7	Angle, sagittal diameters, compression	0.6T MRI	2D
Smith <i>et al.</i> 2013	Spine	56 preoperative subjects	C2 - C7	Spinal cord (CSA, volume, length) and spine dimensions (Cobb angle, SVA, C2-C7 plumbline)	MRI + radiography	2D+3D
Endo <i>et al.</i> 2014	Asian Spine Journal	62 asymptomatic subjects	spinal cord and canal C1 - C7	Length of cervical cord, anterior and posterior cervical canal lengths	MRI	2D
Kar <i>et al.</i> 2017	Journal of Clinical and Diagnostic Research	71 symptomatic subjects : neck pain, radiating, paresthesia neck + upper limb	Spinal cord and canal C3 - C7	Sagittal diameter of spinal cord and canal, Torg ratio	1.5T MRI	2D
Wolf <i>et al.</i> 2018	Spinal cord	12 gender-matched healthy control + 12 patients with cervical spondylotic myelopathy	Spinal cord and canal (C2 and C5)	CSF and SC displacement	3T MRI	2D
Kong <i>et al.</i> 2018	Therapeutics and Clinical Risk Management	317 patients with CSM	Spinal cord C4-C7 and spine C2 - C7	Anteroposterior diameter of canal, narrowed ratio, cobb angle		2D
Tykocki <i>et al.</i> 2018	Acta Neurochirurgica	63 patients (radiculopathy, myelopathy or myeloradiculopathy)	Spinal cord and canal C3 - C7	Length of cervical cord, spinal cord and canal (area, angles)	1.5T MRI	2D
Tykocki <i>et al.</i> 2018	World Neurosurgery	55 patients with CSM	Spinal cord, CSF (C3 - C7)	Spinal cord area, CSF area, CSF ratio)	1.5T MRI	2D
Pratali <i>et al.</i> 2019	Spine	18 patients with CSM	Spinal cord and canal	spinal canal diameter and the spinal cord width, the anterior and posterior length of the spinal cord	1.5T MRI	2D

Table 1. Overview of non-exhaustive studies of morphometrics analysis of the human spinal canal.

Authors/Year	Journal	Specie	Conservation method	Measurement tool	Physical measured variables	CSF properties	Water properties at 37°C
Levin <i>et al.</i> 1981	Anesthesia and Analgesia	15 human patints (none neurologic disease)	tested within 30 min of collection	Volumetry and balance	Density	1.0003 +/- 0.0003 g/mL (37°C)	0.9934 g/mL (37°C)
Bloomfield <i>et al.</i> 1998	Pediatric Neurosurgery	23 human patients	refrigerated at 4° C	Rotational viscometer	Viscosity	0.8 mPa.s (37°C)	0.692 mPa.s (37°C)
Lui <i>et al.</i> 1998	Canadian Journal of Anesthesia	131 preoperative patients	tested within 15 min of collection	Densitometer	Density	1.00059 (SD 0.00020) g/mL (37°C)	0.9934 g/mL (37°C)
Schiffer <i>et al.</i> 1999	British Journal of Anaesthesia	46 patients (without neurological disturbances)		Densitometer	Density	Male density : 1.00054 (SD 0.00017) g/mL Female density : 1.00049 (SD 0.00011) g/mL (37°C)	0.9934 g/mL (37°C)
Palaniappan & Velusamy 2004	Indian Journal of Pure & Applied Physics	10 samples	refrigerated at 4° C	Ultrasonic propagation velocity measurement - interferometer	Sound velocity	1508.2 - 1520.5 m/s	1523 m/s

Table 2. Overview of the experimental mechanical testing of the cerebrospinal fluid.

2.2. The spinal cord

The mechanical properties of spinal cord were investigated on several species such as the rats [Fifford and Bilston *et al.* 2005], mice [Koser *et al.* 2015], rabbit [Ozawa *et al.* 2004], sheep [Yang *et al.* 2019], cattle [Ichihara *et al.* 2003], porcine [Ramo *et al.* 2018 a,b , Fradet *et al.* 2016b], macaque [Jannesar *et al.* 2020], human [Karimi *et al.* 2017, Bilston *et al.* 1995, Mazuchowski and Thibault 2003] models [Appendix – Table 6].

The global mechanical testing of the spinal cord without differentiating the grey and white matters nor the pia mater were investigated by uniaxial and compressive tests. Due to the challenge to test *in vivo* tissues in terms of protocol, most of uniaxial tensile tests were performed on *ex vivo* specimens [Bilston *et al.* 1995, Mazuchowski and Thibault 2003, Ozawa *et al.* 2004, Fifford and Bilston 2005]. One study compared *in vivo* and *ex vivo* mechanical properties of the spinal cord in uniaxial test [Ramo *et al.* 2018a, b]. *In vivo* protocol consisted in surgery exposure of the thoracolumbar cord on which the pedicle screws were fixed on vertebrae for stabilization of the mechanical system. PVC tube sections were glued around the extremities of the tested cord and mechanical clamps were attached to the PVC supports. *Ex vivo* experiments followed the same protocol with an extraction of the cord. In addition, local compressive indentation tests on grey and white matters by a nano-indentation protocol [Zhang *et al.* 2016] and by a coupling approach between atomic-force microscopy and a nano-indentation approach [Koser *et al.* 2015] were performed. Additionally, macroscopic properties in compression of the cord (white and gray matters and pia mater) [Jannesar *et al.* 2018, Karimi *et al.* 2017, Fradet *et al.* 2014] were also tested. The local approach provides more detailed cartography of the mechanical properties but its implementation in numerical simulation is not clear and necessitates to elaborate a phenomenological model to be used. This approach could allow to develop multi-scale models of the spinal cord. The macroscopical approach provides mechanical properties more easily implementable in numerical models.

Due to the fast alteration of nervous tissues [Garo *et al.* 2007, Fountoulakis *et al.* 2001], the duration between the euthanasia or death of the model specimen have great effect on mechanical properties measurements and mechanical testing needs to be performed within 6h *post mortem*. Few studies described this duration [Ramo *et al.* 2018a, b].

Tensile linear elastic moduli provided by the literature were included in an interval between 2 kPa [Ozawa *et al.* 2004] and 47 kPa [Karimi *et al.* 2017] at quasi-static strain rate while hyperelastic [Jannesar *et al.* 2018, Karimi *et al.* 2017, Mazuchowski and Thibault 2003, Bilston *et al.* 1995] and viscoelastic [Ramo *et al.* 2018a,b, Jannesar *et al.* 2018, Fradet *et al.* 2016, Fifford and Bilston *et al.* 2003, Bilston *et al.* 1995] constitutive laws were fitted to stress/strain curves. Detailed description will be presented in

the “Introduction” sections of the chapter 4. Additionally, whose one dynamic mechanical analysis (DMA) of compressive test [Ramo et al. 2018 b, Fradet et al. 2016b] and two others DMA studies were investigated in tensile tests [Bilston et al. 1995].

2.3.The nerve roots

To the best of our knowledge, three studies investigated the tensile properties of the nerve roots with quasi-static [Beel et al. 1986, Singh et al. 2006] and dynamics strain rate [Tamura et al. 2018] on three different species being mice [Beel et al. 1986], rats [Singh et al. 2065], and porcine models [Tamura et al. 2018]. No clear data were found about the post mortem duration before testing.

Tensile linear moduli were measured at the lumbar level in quasi-static strain rate in the range between 0.88 MPa [Bell et al. 1986] and 2.1 MPa [Singh et al. 2005] on murine models. The inter-spinal levels variation of tensile linear moduli measured in dynamics strain rate on porcine models were described in Tamura et al. [2018] : 18.8 MPa at cervical, 25.1 MPa at thoracic and 15.3 MPa lumbar spinal levels.

2.4.The denticulate ligaments

To the best of our knowledge, two studies investigated the tensile mechanical properties of the cervical denticulate ligaments on porcine models at quasi-static strain. Tensile linear moduli were provided in the range in 1.31 MPa [Polak et al. 2014] and 6.69 MPa [Polak-Krasna et al. 2019].

2.5.The meninges

An overview of tensile mechanical tests of spinal meninges was provided in details in the introduction section of the chapter 4. A brief description of protocols and tensile linear moduli depicted Table 3 were provided in this section.

2.5.1.Dura mater and arachnoid mater

Regarding the tested dura and arachnoid mater, several specimen species were investigated on rat [Maikos et al. 2008], ovine [Shetye et al. 2014], dog [Patin et al. 1993], bovine [Runza et al. 1999, Persson et al. 2010], porcine [Mazgajczyk et al. 2012] and human [Patin et al. 1993, Zarzur et al. 1996, Runza et al. 1999, Chauvet et al. 2010] models.

Isotropic [Persson et al. 2010] and anisotropic [Shetye et al. 2014] hyperelastic constitutive laws were fitted to stress/strain measured curves in dynamics strain rate conditions. Others studies provided tensile linear moduli in longitudinal loading direction at quasi-static strain [Patin et al. 1993] ranging between 138 MPa and 265 MPa in longitudinal loading direction while ranging between 7.8 MPa and 76.4 MPa in circumferential loading direction for lumbar human specimens. The tensile linear moduli at dynamics strain rate were between 65 MPa and 102 MPa in longitudinal loading direction while were 5 MPa in circumferential loading direction on lumbar human specimens [Runza et al. 1999]. Complementary detailed description of protocol characteristics and linear moduli for different species are provided in the Table 3. Viscoelasticity were demonstrated in quasi-static, moderate and dynamic conditions, but on a small population of samples [Persson et al. 2010, Wilcox et al. 2003, Ramo et al. 2018a].

2.5.2.Pia mater

Few studies investigated the mechanical properties of pia mater including the parenchyma in tensile [[Ramo et al. 2018c](#), [Ozawa et 2004](#)] and compression uniaxial tests on rabbit [[Ozawa et 2004](#)] and ewe [[Ramo et al. 2018c](#)] models. The lack of data for these tissues could be explain by the challenging extraction and manipulations protocol without damaging the specimen. [Ramo et al. \[2018c\]](#) described a DMA and tensile linear modulus were measured at quasi-static strain for a value of 17 MPa and another study on rabbit provide a value of 2.4 MPa [[Ozawa et al. 2004](#)]. That showed a protective role of the pia mater which could also allow to maintain the oval transversal shape of spinal cord. Complementary detailed description of protocol characteristics and linear moduli for different species are provided in the [Table 3](#).

Authors/year	Journal	Specie	Tissue	Spinal level	Type of test	Strain rates	Conservation method	Maximum strain		Maximum stress		Elastic modulus	
								Longitudinal	Transverse	Longitudinal	Transverse	Longitudinal	Transverse
Dura mater													
Patin <i>et al.</i> 1993	Anesthesia & Analgesia	human dog	dura mater	lumbar	uniaxial tension	1.67 mm/s	Refrigerated in saline solution					human : 138 - 265 MPa dog : 58.8 - 73.5 MPa	human : 7.8 - 76.4 MPa dog : 54.9 - 58.8 MPa
Zarzur <i>et al.</i> 1996	Arq Neuropsiquiatr.	Human lumbar spine	dural sac		uniaxial tension		Preserved in formalin until 72h before testing					26.2 - 171.5 Mpa	4.5 - 26.9 MPa
Runza <i>et al.</i> 1999	Anesthesia & Analgesia	human bovin	dura mater	T12 - L4/L5	uniaxial tension	10 mm/min	In saline solution , frozen at 4°C for 24h and 120h	human : 0.20 - 0.62 bovin : 0.85 - 1.15	human : 0.38 - 0.58	human : 8 - 22 MPa bovin : 11 - 22 MPa	human : 3-4 MPa	human : 65 - 102 MPa bovin : 25 - 80 MPa	human : 5 MPa
Maikos <i>et al.</i> 2008	Journal of Neurotrauma	rat	dura mater	C1 - L1	uniaxial tension	19.4 sec-1, 0.0014 sec-1	2h after sacrifice	1.24		2.14 MPa			
Mazgajczyk <i>et al.</i> 2012	Acta of bioengineering and biomechanic	porcine	dura mater	C1 - C7	uniaxial tension	2 mm/min	Frozen	Dorsal : 0.17 - 0.28 Ventral : 0.15 - 0.24	Dorsal : 0.22 - 0.33 Ventral : 0.19 - 0.27	Dorsal : 7.4 - 22.3 MPa Ventral : 14.4 - 36.8 MPa	Dorsal : 14.2 - 24.8 MPa Ventral : 15.2 - 66.4 MPa		
Chauvet <i>et al.</i> 2010	Neurosurgical Review	human	dura mater	Cranio cervical junction	uniaxial tension		Fresh cadaver					entire dura : 44 - 91 MPa split dura : 19 - 25 MPa	
Persson <i>et al.</i> 2010	Annals of Biomedical Engineering	Bovine spinal cords	dura mater	full spine	uniaxial tension	- preconditioning cycles at 15 mm/min (1.5% of strain) - 3 strain rates (0.01, 0.1, 1s-1)	Frozen at -20°C and stabilized at room temperature before testing	Hyperelastic (Ogden) constitutive models fitting					
Shetye <i>et al.</i> 2014	Journal of Mechanical Behavior and Biomedical Material	Ovine spinal cords	dura mater	C1 - C6	biaxial tension	- 3 loading protocols (1, 2:1 and 1:2)	In a saline solution	GOH [Gasser et al. 2006]constitutive continuum model fitting					
Pia Mater													
Yang <i>et al.</i> 2019	Zhongguo Xiu Fu Chong Jian Wai Ke Za Zhi	sheep	dura mater	C6, C7, T11, T12, L4, and L5	uniaxial tension								
Ozawa <i>et al.</i> 2011	Journal of Neurosurgery	rabbit	pia mater	C5 - C6	uniaxial tension	0.02 N/s	In saline solution					2.4 MPa	
Ramo <i>et al.</i> 2018	Acta Biomaterialia	cervical ewe spinal cords	pia-arachnoid complex	C0 - C7	uniaxial tension	0.05Sec-1	fresh after sacrifice					17 MPa	

Table 3. Overview of mechanical test and properties of the spinal meninges.

3. Studying the CSF flow and the central nervous system modelling

3.1. Computational Fluid Dynamics models

3.1.1. General considerations

Fluid flow simulation models called "Computational Fluid Dynamics" (CFD) models are numerical tools that exclusively analyze the behavior and phenomena of the flow of fluids or gases. They are very well known in engineering in many fields of application (aeronautics, automotive, meteorology, biomedical in particular) which involve problems in mainly fluid mechanics and / or thermodynamics. CFD is actually a specialized field of mathematics and fluid mechanics that focuses on solving Navier-Stokes equations by numerical methods. These methods are also based on a discretization strategy following the same general philosophy as the one used for finite element models in a preprocessing point of view.

3.1.2. Advantages and drawbacks

The advantage of modelling the cerebrospinal system with a CFD approach is that modelling is a robust and accurate way to model a velocity field conditioned by coherent bio-reliable fluid initial and boundaries conditions as well as fluid assumptions. The additional interest is that CFD is also able to provide the data of the 3d velocity field and the pressure field over time. From the first type of CFD output (velocity field), it is often interesting to compute the wall shear stress (i.e. the shear stress acting orthogonally to the wall of the cavity) along the wall of the fluid domain. That could provide a quantification of the effect of this fluid index on the wall such as the meninges, the nerves or the spinal cord. The main drawback of this numerical approach is that the walls are considered as rigid and mostly model by a no-slip condition [Jacobson et al. 1996, Yiallourou et al. 2012, Helgeland et al. 2014, Clarke et al. 2017, Holmlund et al. 2019, Khani et al. 2020] even if some deformable wall conditions can eventually be modeled with a qualitative estimation of the wall displacement [Khani et al. 2017, Tangen et al. 2015]. Indeed, the structures in contact with the CSF have only a geometrical effect on the fluid flow without taking into account the material behavior.

3.1.3. Fluid boundary conditions

Several studies performed simulations of cerebrospinal flow in the subarachnoid space [Table 4]. These modelling vary in terms of boundaries conditions; in particular about the geometry and inflow conditions. The first study investigating the cerebrospinal flow in the cerebral aqueduct was performed on an idealized geometry [Jacobson et al. 1996]. Most of studies currently modeled subject -specific geometries such as the brain SAS [Bardan et al. 2012], cervical SAS [Yiallourou et al. 2012, Helgeland et al. 2013, Clark et al. 2013, Pahlavian et al. 2014] and the full spinal SAS [Tangen et al. 2015, Sass et al. 2014, Khani et al. 2020]. These subject-specific models reconstructed the patient geometry by segmentation of anatomical MRI scans. This step is still time-consuming due to the lack of segmentation automatization of the spinal cord and the SAS.

It requires a specific definition of the SAS anatomy and structures definition which mostly has been performed using a MRI-based semi-manual segmentation approach with mandatory manual correction by the operator. This definition is MRI-resolution-dependent and varies between each paper [Table 4]. This dependance to segmentation and smoothing techniques seems to not have been quantified in the literature to the best of my knowledge.

Regarding the smaller structures such as the denticulate ligaments, the nerves and the subarachnoid trabeculae, such geometrical details were modeled as idealized such as trabeculae were modeled by a random generation of thin cylinder extrude from the fluid mesh [Sweetman & Lininger 2011]. Due to the MRI resolution insufficiency to reconstruct the smaller anatomical structures, the denticulate ligaments and the nerves were modeled based on anatomical photography and on literature measurements [Pahlavian et al. 2015] and the nerves were modeled with subject-specific locations of nerve insertions from medical images and as idealized sheaths of the bundle of nerves [Tangen et al. 2015, Pahlavian et al. 2015] or such as each individual nerve [Sass et al. 2017]. The geometrical modeling of structures inside the SAS still remains challenging due to the lack of anatomical knowledge in particular regarding the spinal subarachnoid space and due to the resolution limitation of the current medical imaging approach. This limitation will be partially face in the future with more powerful technology such as for example the 7T MR system.

3.1.4. Boundary layers

In Fluid mechanics, thin layers of fluid in which viscosity effects are significant, are formed along the solid walls called boundary layers. As the velocity gradient tends rapidly to zero near the wall, these boundary layers can significantly affect the entire flow field. Thus, a particular modelling is required. In literature, the CFD modelling of the CSF tends to agree on the transitional [Tangen et al. 2015] or at least laminar flow regime [Pahlavian et al. 2014, Clarke et al. 2013, Helgeland et al. 2012] among the three described regimes (laminar, transitional, turbulence). The definition of the regime is often associated to the quantification of the dimensionless Reynolds number (ratio of inertial forces to viscous forces) but it remains quite ambiguous to theoretically describe the transition between each regime. Nevertheless, another dimensionless number is more commonly used for complex flow patterns such as the CSF pulsatile flow pattern: the Womersley number. It describes the relationship between the pulsatile flow frequency (i.e. the instationary inertial forces) and the viscous effects. Peak Reynolds number (relative to peak velocity) was computed around 300-400 [Pahlavian et al. 2014] and the Womersley number ranges from 5 to 17 [Loth et al. 2001].

3.1.5. Fluid initial and boundary conditions

Initial definition of boundary conditions of the CSF flow is still challenging to model due to the difficulty to directly measure the flow of the patient by a non-invasive sensor. Measurements of pressure or velocity can be performed during a surgery of the brain or during lumbar puncture exclusively around the L3/L4 lumbar level where the spinal cord is not present. Fortunately, recent MRI technologies advancements allow to measure *in vivo* the CSF flow in any part of the SAS. In CFD models, the initial inflow condition was modelled in two ways. The first way is to model the inlet profile as an average velocity or pressure signal or an idealized sinusoidal signal applied orthogonally to the inlet surface [Jacobson et al. 1996, Helgeland et al. 2014]. More recently, the subject-specific CSF flow conditions were applied from *in vivo* phase-contrast *cine* MRI (MRI flux imaging throughout the cardiac cycle) [Yiallourou et al. 2012, Cheng et al. 2014, Pahlavian et al. 2015, Tangen et al. 2015, Sass et al. 2017, Khani et al. 2020] enabling to model specificities between patients. The CSF flow was computed by integrating the pixel velocities within the region of interest at a given axial location. In most of the studies, the outflow condition was set to a zero pressure condition. Indeed, the average pressure at a given point of the fluid is close to zero due to the cycling pulsation of the CSF in the caudal (diastole), in the cranial (systole) and then again in the caudal (diastole) direction for an average ventricular cardiac cycle (800-900 ms).

3.1.6.Applications

Regarding the cerebrospinal flow simulations, three main applications are described in the literature. First, hydrocephalus models [Holmlund et al. 2019, Jacobson 1996] describing the cerebrospinal flow in the cerebral ventricles pathologically enlarged. Second application of models were used to describe the pathological mechanisms of syringomyelia, a CSF fluid cavity growing in the spinal CNS and the Chiari I Malformation [Pahlavian et al. 2014, Helgeland et al. 2014, Cheng et al. 2014], a structural congenital anomaly of the cerebellum falling in the foramen magnum and disturbing the CSF flow. A third type of therapeutic application consisting in an intrathecal drug delivery [Tangen et al. 2015] or blood filtrated drain [Khani et al. 2020]. The intrathecal drug delivery describes the way to bypass the blood brain barrier (BBB) which filters the molecule exchanges between the brain and the vascular system. To bypass the BBB, a catheter is inserted in the subarachnoid space. Such sensitive manipulation has to take into account the CSF volume in the SAS, the detailed subject-specific cerebrospinal flow pattern to predict the drug quantity injected and the drug particle motion in the SAS. To the best of my knowledge, no CFD study was found about the CSF flow modelling in a cervical canal with a myelopathy or stenosis.

3.1.7.Validation

The validation of the CFD models was described in literature in two ways. A pure numerical validation is necessary to ensure the reliability of the solution. For that, two categories of numerical validation are advised : the spatial one and the temporal one. The first category consists in performing a convergence study which quantify the convergence of the simulation solution in terms of mesh size (the more the mesh size is small the more the solution has to converge). The second category consists in performed a convergence study on the number of simulated cycles to ensure the establishment of the fluid flow as well as on the time step (to reduce the propagation of residual numerical error along the simulation). An experimental validation is also essential to quantify the limits of a model. As explain in a previous paragraph, *in vivo* PC MRI allows to perform a cartography of the velocity within a region of interest at a given time t in 2D, 3D or even in 4D (i.e. 3D + t , spatial and time components). A pressure field can eventually be computed from the velocity field by numerical resolution of Navier-Stokes equations. The second way to validate a model of cerebrospinal system is to reproduce *in vitro* the subject-specific patient anatomy and boundary conditions. It consists in 3D printing of the subject-specific patient reconstructed anatomy and in reproducing the physiological CSF flow by a hydraulic pump [Pahlavian et al. 2016], a drain system [Khani et al. 2020] or a pump associated to an injection system [Tangen et al. 2017]. Regarding the measurement of the velocity field of the CSF, the test bench was positioned in an MRI to be acquired by a 4D flow MRI protocol [Pahlavian et al. 2016], or coupled to a particle image velocimetry (PIV) system [Khani et al. 2020, Tangen et al. 2017]. The PIV system can be described in a simplistic way such as a particle tracking approach in an Eulerian grid to associate velocities to each part of the fluid domain while based on particles tracking within the considered fluid. Current limitation of the MRI flow sequence (phase contrast 4D or 3D+t) require the comparison with the PIV.

Author/Year	Journal	Anatomical part	Detailed anatomical parts	Geometry source	Initial boundaries conditions	Boundaries conditions	CSF formulation	Flow assumption	CSF properties	Solver	Type of elements	Number of elements	Convergence study	Pathology/Situation modeled	Validation	Related studies
Jacobson <i>et al.</i> 1996	Pediatric Neurosurgery	Brain	SAS (aqueduc of Sylvius)	Idealized	Case 1 : constant pressure inlet + 0 Pa outlet Case 2 : constant velocity profile as inlet + 0 Pa outlet Case 3 : sinusoidal pressure drop as inlet + zero pressure outlet	no-slip boundary condition for the walls	Continuity and Navier-Stokes equations using finite volume method	laminar flow	$\rho = 1000 \text{ kg.m}^{-3}$ $\mu = 0.001 \text{ Pa.s}$	CFDS-FLOW3D		2500-7520		Hydrocephalus		
Yiallourou <i>et al.</i> 2012	PLOS One	Human cervical (FM to C7)	SAS	Subject-specific geometry based on anatomical 1.5T MRI	Inlet : velocity profile from 4D PC MRI Outlet : zero pressure condition	no-slip boundary condition for the walls	Continuity and Navier-Stokes equations	laminar flow	$\rho = 1000 \text{ kg.m}^{-3}$ $\mu = 0.001 \text{ Pa.s}$	ANSYS CFX 13.0	tetrahedral element	~2 million	Yes	CSF flow dynamics pattern	<i>in vivo</i> (1.5T 4D PCMRI)	
Helgeland <i>et al.</i> 2013	Journal of Biomechanics	Human cervical (FM to C7)	SAS	Subject-specific geometry based on anatomical MRI	Inlet/Outlet : idealized velocity profile derived from []	no-slip boundary condition for the walls	Continuity and Navier-Stokes equation resolved by direct numerical simulations	laminar/transitional flow	$\rho = 1000 \text{ kg.m}^{-3}$ $\nu = 0.7 \times 10^{-6} \text{ m}^2/\text{s}$			~46.5 million		Syringomyelia/Chiari I Malformation	Literature values comparison	
Clarke <i>et al.</i> 2013	Journal of Biomechanics	Human cranial/cervical part	SAS ; cerebellum	Subject-specific geometry based on anatomical 3T PC-MRI	Inlet : velocity profile from 3D PC MRI Outlet : zero pressure condition	no-slip boundary condition for the walls	Continuity and Navier-Stokes equations using finite volume method	laminar flow	$\rho = 1000 \text{ kg.m}^{-3}$ $\nu = 0.8 \times 10^{-6} \text{ m}^2/\text{s}$ []	ANSYS CFX 13.0	tetrahedral element			Syringomyelia/Chiari I Malformation	Velocity field by MRI	
Pahlavian <i>et al.</i> 2014	PLOS One	Human cervical (FM to C7)	SAS ; NR (idealized) ; DL (idealized)	Subject-specific geometry based on anatomical MRI	Inlet : velocity profile from 4D PC MRI Outlet : zero pressure condition		Navier-Stokes equations using finite volume method	laminar flow		ANSYS Fluent 14.0	tetrahedral element	~5.5 - 7.4 million	Yes	Syringomyelia/Chiari I Malformation	<i>in vivo</i> (1.5T 4D PCMRI)	
Tangen <i>et al.</i> 2015	Journal of Biomechanics	Human full spine	SAS ; NR (idealized) ; arachnoid trabeculae (idealized)	Subject-specific geometry based on anatomical MRI	Inlet : velocity profile from 3D PC MRI	mid-sagittal symmetry + explicit deformable boundaries	Continuity and Navier-Stokes equations							CSF flow dynamics pattern with intrathecal drug delivery	<i>in vivo</i> MRI flow measurement	
Sass <i>et al.</i> 2017	Fluids and Barriers of the CNS	Human full spine	SAS ; NR (half-idealized)	Subject-specific geometry based on anatomical 3T MRI			Continuity and Navier-Stokes equations using finite volume method	laminar flow		ANSYS Fluent 18.1	quad & tria elements	124,935 quadrangles & 325,855 triangles		CSF flow dynamics pattern	<i>in vivo</i> (4D PCMRI)	
Holmlund <i>et al.</i> 2019	Fluids and Barriers of the CNS	Brain	SAS - Cerebral ventricular system	Subject-specific geometry based on anatomical 3T MRI	Inlet : laminar parabolic inflow	no-slip boundary condition for the walls	Continuity and Navier-Stokes equations using finite volume method	laminar flow	$\rho = 1000 \text{ kg.m}^{-3}$ $\nu = 0.9 \times 10^{-6} \text{ m}^2/\text{s}$ []	COMSOL 5.3a	tetrahedral element	550.000	Yes	Hydrocephalus	<i>in vivo</i> PC MRI comparison	
Khani <i>et al.</i> 2020	Fluids and Barriers of the CNS	Brain and spine	SAS ; NR (half-idealized) ; DL (idealized) + dual-lumen Neurophoresis catheter	Subject-specific geometry based on anatomical MRI	Inlet : constant CSF flow rate (CSF production at choroid plexus) + C2/C3 oscillatory velocity from PC MRI Outlet : constant fluid flow rate (drain under Neurophoresis therapy) + zero pressure at the foramen magnum	no-slip boundary condition for the walls	Continuity and Navier-Stokes equations using finite volume method	laminar flow	$\rho = 998.3 \text{ kg.m}^{-3}$ $\mu = 0.89 \text{ mPa.s}$	ANSYS Fluent 19.2	Tetrahedral & tria elements	16.8 million	Yes	Blood removal from CSF with lumbar drain	<i>in vivo</i> anatomical MRI, <i>in vitro</i> model	

Table 4. Non-exhaustive overview of the frequently cited CFD models of the cerebrospinal system.

3.2.Fluid-Structure Interaction models

3.2.1.General considerations

The fluid-structure interaction (FSI) approach allows to model a multi-physics problem, in particular the scientific problems coupling Structural Mechanics and Fluid Mechanics. The coupling of physical laws of Fluid Mechanics and Solid Mechanics describes the interactions between one or more deformable/moving structures and a fluid flowing around or inside the structure by Continuum Mechanics. The FSI modeling is challenging because the solid deformed boundaries change the fluid flow and the fluid deforms the solid boundaries simultaneously.

FSI modeling have already been applied in the field of cardiovascular biomechanics [Bavo et al. 2016]. However, for the study of the interaction of CSF and the central nervous system, very few models take into account these numerical approaches which are now applicable due to the increase and optimization of the computing power.

3.2.2.Categories of FSI approaches and advantages

Two resolution approaches are described in the literature which are the monolithic or the partitioned resolution. The first one consists in the resolution of fluid and solid equations in the same mathematical framework to form a single system of equations. One solver algorithm is necessary to resolve the system as a single matrix while the partitioned approach considered two computational domains. It consists in the sequential resolution of fluid and solid equations, and the coupling is reached by an iterative process necessitating two appropriated solver algorithms respectively to the fluid and the solid equations. The two solvers algorithms need a third algorithm which manages the force and displacements exchanges between the fluid and the solid. In addition to the resolution method, an appropriate kinematical description of the continuous media is necessary to accurately model a problem. A FSI problem can classically be described by a Lagrangian description for the solids and by an Eulerian description for the fluid. This approach is called Immersed Boundary method [Peskin 1972] and requires a non-conforming mesh method to treat the interface modeling. The interface boundary constraints are imposed directly in the model equations and the respective meshes do not need to match [Hou et al. 2012]. A second well known kinematical description called Arbitrary Lagrangian-Eulerian (ALE) description. For a FSI problem, it faces the drawbacks of the Lagrangian description which can hardly handle the large deformations of the solid and the Eulerian description which loses accuracy when applied to solids. ALE methods allow the mesh to move in arbitrary way to handle greater distortions of the full computational domain which would be allowed by a Lagrangian description and to offer more resolution which would allow by the Eulerian description. The most appropriate interface modeling for ALE method is to use a conforming mesh method. The method considers the interface boundary constraints as physical boundary constraints which means that the solid mesh domain and the fluid mesh domain require the same interface [Hou et al. 2012].

3.2.3.Drawbacks

Due to the high computational cost of partitioned FSI simulation compared to the monolithic simulations, the central nervous system need be simplified, only considering the meninges or simulating CNS as structure mimicking its global behavior. It is the reason why no substructures such as denticulate ligaments, nerves or arachnoid trabeculae were not represented in the literature. The initial boundaries conditions (inflow and outflow) are modeled as in CFD models of the cerebrospinal system, mostly in using PC MRI flow measurements.

3.2.4.Applications

According to the scientific problem, the FSI approach varies. In comparison to previously cerebrospinal system CFD models which described long phenomena (several seconds), FSI models considering the CNS and the CSF can be categorized in two types of applications: the short high-energy traumatism and the degenerative or idiopathic pathologies such as degenerative cervical myelopathy, syringomyelia or Chiari I Malformation.

As depicted in [Table 5](#), simplified 2d geometry were used to create more phenomenological model. It allows to describe more qualitatively a physiological or a pathological mechanism. [Bertram et al. \[2016\]](#) demonstrated the effect of the CSF on the spinal subarachnoid space/pia mater interface by a FSI poroelastic model of stenosis of the canal with the presence of a syrinx in the cord. Indeed, it shows a radial pulsatile CSF flow was shunted through the interface without significative effect on the syrinx. [Garnotel et al. \[2018\]](#) used a simplify 2D geometry based on volume ratio of the different parts of the cerebrospinal system : the brain, the intracranial SAS, the ventricles and the spinal SAS. This model showed a high robustness to describe the CSF by part of the cerebrospinal system with only 2.7 % of maximum error compared to the flow measured by MRI. The type of model is easily adaptable to any subject but it is limited in term of output variable such as velocity or pressure fields. Compared to the 2D CSF model, most of the models described in the literature preferred to develop and use 3D detailed geometrical FSI models. These descriptive models allow to reach the most complete and accurate representation of the cerebrospinal system. Due to the high computational cost of this type of model, only a part of the cerebrospinal system is modeled in particular the brain and the cervical SAS compartments [[Cheng et al 2014](#), [Fradet et al. 2016a](#), [Gholampour et al. 2018](#)]. Only one study described a full 3D geometrical SAS model without mentioning the computational time [[Sweetman and Linninger 2011](#)].

In [table 3.2](#), a majority of partitioned FSI models are represented. They are mostly used to reproduce the biomechanics of the CSF flow and its interaction with surrounding structures as accurately as possible. The partitioned approach allows to use a previous developed CFD model and to add a structural modeling without developing from scratch. Indeed, [Sweetman and Linninger \[2011\]](#) showed a highly accurate prediction of normal CSF flow compared to PC MRI acquisition in terms of pressure, the velocity magnitude over a cardiac cycle using a hyperelastic Neo-Hookean constitutive law for the structural domain and a classical Navier-Stokes formulation. [Gholampour et al. \[2018\]](#) shows a vortex intensification and location changes, an increase of CSF pulsation for patients with post shunt surgery hydrocephalus compared to normal subjects with a high accurate poroelastic brain CSS model. It recommended the pressure indicator as pathological biomarker for prognostic of a hydrocephalus patient. Concerning the study of cervical stenosis, only one study was developed a 3D subject specific FSI model of a non-existing stenose derived from a normal geometry in comparing FSI and CFD models. The study demonstrated that the rigid wall assumption in CFD model had not a significant effect on the CSF flow and FSI modeling had a small impact on CSF pressure for both normal and stenosis models [[Cheng et al. 2014](#)]. In opposition of partitioned FSI modeling, monolithic resolution is essentially used to reproduce and predict the effect of brain or spinal traumatism. Indeed, the CSF is modeled such as a fluid with no exchange, i.e. CSF pulsation is not simulated. It allows to model short and high energy impact. Then, a protective role of the CSF for the whole central nervous system was highlighted in traumatic conditions [[Persson et al. 2011](#), [Fradet et al 2016a](#), [Toma and Nguyen 2018](#)].

3.2.5.Validation

As for the approach considered, the validation of the FSI model highly depend on the application of this FSI model. Concerning the FSI model which are focusing on CFS flow analysis. The validation is done by comparison between the numerical model and an *in vivo* phase-contrast MRI where the pressure and the velocity fields, and the flow rate are the reference output parameters [[Garnotel et al. 2018](#), [Sweetman and Linninger 2011](#)]. To the best of our knowledge, only one traumatic model of a compression case has been validated by an experimental compressive mechanical test. The maximum deformation and the time to maximum deformation were compared [[Persson et al. 2010](#)].

Continuum mechanical formulation of a basic FSI problem as well as different FSI modelling approaches were detailed in the chapter 5.

Author/Year	Journal	Anatomical part	Dimensions of the problem	Geometry source	FSI approach	Solver	Type of elements	Number of elements	Pathology / Situation modeled	Convergence study	Validation	Related studies
Sweetman and Linninger 2011	Annals of Biomedical Engineering	Brain + upper spinal cervical SAS	3D	Cine-MRI-based subject-specific anatomy	Coupled FSI approach for flow formulation	ADINA-FSI 8.6	Tetrahedral and tria elements	871 358	Normal and Hydrocephalic Brain Dynamics	Yes	Cine-MRI (CSF velocity and flow rates)	
Persson <i>et al.</i> 2011	Journal of Neurotrauma	Bovine spinal cord model	3D	Idealized geometry	Coupled FSI approach for no exchange fluid formulation	ADINA 8.5	Quad and Hexahedral elements	22776	Spinal cord traumatic injury	Yes	In vitro model validation	
Cheng <i>et al.</i> 2014	Journal of Biomechanics	Human cervical Spinal SAS	3D	MRI-based subject-specific anatomy	Coupled FSI approach (Navier-Stokes formulation)	ANSYS Mechanical/ ANSYS CFX	Tri and Tetrahedral elements	x	Cervical stenosis		x	
Fradet <i>et al.</i> 2016	Advances in Mechanical Engineering	Human cervical Spinal SAS	3D	MRI-based subject-specific anatomy	Monolithics FSI approach (ALE formulation for no fluid exchange)	RADIOSS	Structure : tetrahedral and tri elements Fluid : hexahedral elements	779 034	Spinal cord traumatic injury	Yes	x	
Bertram <i>et al.</i> 2017	Journal of Biomechanical Engineering	Human spinal model	2D	Idealized geometry	Coupled FSI approach (Navier-Stokes & Darcy's law)	OOMPHELIB/ADINA	Tria elements	x	Syringomyelia		x	
Garnotel <i>et al.</i> 2017	Acta Neurochirurgica Supplement	Cerebrospinal system	2D	Idealized geometry	Coupled FSI approach (Navier-Stokes formulation)	FreeFem++			Normal cerebrospinal system		Numerical validation + flow MRI comparison	
Gholampour <i>et al.</i> 2018	PLOS One	Brain SAS	3D	MRI-based subject-specific anatomy + PC-MRI (flux)	Coupled FSI (Navier-Stokes & Darcy's law) ALE formulation with no fluid exchange	ADINA 8.3		x	Normal and Hydrocephalic Brain Dynamics	Yes	x	
Toma and Nguyen 2018	Brain Injury	Brain SAS	3D	MRI-based subject-specific anatomy	Monolithics FSI approach (SPH formulation)	RADIOSS	Tetrahedral and SPH elements	156 137	Head acceleration & deceleration	Yes	x	

Table 5. Non-exhaustive overview of the frequently cited FSI models of the cerebrospinal system.

4. Appendices

Authors/Year	Journal	Specie	Conservation method	Type of tests	Test characteristics	Physical measured variables
Ramo <i>et al.</i> 2018	Acta Biomaterialia	6 thoracolumbar porcine spine	Immersed in a room temperature saline bath during testing	<i>In vivo</i> and <i>ex vivo</i> uniaxial tensile test	- preconditioning cycles (3 % of engineering strain at 1 Hz) - stress-relaxation tests (1%, 2%, 3%, 4%, and 5% engineering strain) - dynamic cyclic test (2% engineering strain at 1Hz).	Uniaxial non-linear viscoelastic model fitting
Jannesar <i>et al.</i> 2018	Acta Biomaterialia	9 cervical spines of macaque (Macaca mulatta) (75 samples)	tested within one-hour post-mortem	<i>Ex vivo</i> compressive test	Samples compressed for 1mm in 4 pre-set deformation velocities (0.5mm/sec, 5.0mm/sec, 50.0mm/sec and 150.0mm/sec)	incompressible isotropic hyperelastic and viscoelastic constitutive model fitting
Zhang <i>et al.</i> 2016	Conference Proceedings of the Society for Experimental Mechanics Series	1 sheep spinal cord with meninges		<i>In vivo</i> uniaxial compressive indentation test	velocity test of 0.05 in/s to displacements (2mm, 3mm and 4mm)	Equivalent <i>in vivo</i> elastic modulus
Karimi <i>et al.</i> 2017	Journal of Chemical Neuroanatomy	24 human cervical spinal cords	Refregerided at 4°C	<i>Ex vivo</i> uniaxial compressive test	- 5 load-unload cycles to 50% nominal strain at rates of 1 to minimize the viscoelastic effect of the spinal cord tissue - 5 mm/min up to the failure point	incompressible isotropic linear and hyperelastic constitutive models fitting
Fradet <i>et al.</i> 2014	Journal of Engineering in Medicine	16 pigs (C1 - L6)	Immersed in saline solution	<i>Ex vivo</i> uniaxial DMA compressive test	- 3 loading ramps (0.5s-1, 5s-1, 50s-1) - 3 cyclic loading (1Hz, 10Hz, 20Hz)	Viscoelastic model fitting
Bilston <i>et al.</i> 1996	Annals of Biomedical Engineering	Cervical and thoracic human spinal cord	Samples hydrated by a saline solution	<i>Ex vivo</i> uniaxial DMA tensile test	- preload of 0.5N (3-5% of strain) - test velocity : 5mm/min	Quasilinear viscoelastic and hyperelastic models fitting
Fiford and Bilston 2005	Journal of Biomechanics	Rat spinal cords (C1 - L4)	Hydrated with a saline solution	<i>Ex vivo</i> tensile test	- sample fullyhydrated by re-circulating physiological saline at 37 °C - preload of 0.02N at a speed of 2.5 mm/min (0.001s-1) - strain rate (0.002, 0.02, 0.2 s-1) to a given strain (0.02, 0.035, 0.05)	Non linear viscoelastic model fitting
Koser <i>et al.</i> 2015	Biophysical Journal	21 mices	ice conservation	<i>Ex vivo</i> compressive indentation test	- 10 micrometer/s - indentation depth (2, 2.5, 3, and 3.5mm)	Apparent elastic modulus
Mazuchowski and Thibault 2003	Summer Bioengineering Conference	18 samples of human spinal cords	Refregerided at 4°C in a saline solution	<i>Ex vivo</i> tensile test	- stretch ratio of 1.5 - strain rates of .1s-1, 1s-1, 10s-1	Neo-Hookean model fitting
Ichihara <i>et al.</i> 2003	Journal of Neurosurgery	6 spinal cords of catlles	Humidified	<i>Ex vivo</i> tensile test	- strain rate (0.5 to 0.005 mm/s) to a given strain (0.02, 0.035, 0.05)	Tangent elastic modulus
Ozawa <i>et al.</i> 2004	Journal of Neurosurgery	9 white rabbits C5 - C6 segments	In a physiological saline solution at room temperature (16°C)	<i>Ex vivo</i> tensile test	- A tensile load of 4.8N applied to the sample	Elastic modulus

Table 6. Overview of the mechanical tests and properties characteristics of the spinal cord.

Authors/year	Journal	Specie	Tissue	Spinal level	Type of test	Strain rates	Conservation method	Maximum strain	Maximum stress	Elastic modulus
Nerve and nerve roots										
Bell <i>et al.</i> 1986	Experimental neurology	mices	Nerve roots	Lumbar	Uniaxial tension	1mm/s	In a saline solution at 22-24°C	0.46 (SD 0.03)	3.03 (SD 0.16) MPa	Apparent elastic modulus : 1.19 (SD 0.31) MPa
Singh <i>et al.</i> 2005	Journal of Biomechanics	rats	Nerve roots	Lumbar	Uniaxial tension	quasistatic : 0.01 mm/s dynamic : 15 mm/s	In a saline solution	quasistatic : 0.29 (SD 0.09) dynamic : 0.30 (SD 0.08)	quasistatic : 257.9 (SD 111.3) kPa dynamic : 624.9 (SD 306.8) kPa	quasistatic : 1.3 (SD 0.8) MPa dynamic : 2.9 (SD 1.5) MPa
Tamura <i>et al.</i> 2018	Journal of Engineering and Science in Medical Diagnostics and Therapy	porcins spinal cords	Nerve roots	Full spinal cord	Uniaxial tension	testing velocity of 0.2mm/s, (0.01 s ⁻¹), 2 mm/s (0.11 s ⁻¹), or 20mm/s (1.11 s ⁻¹),	Refrigerated (12h) at 4°C in a saline solution	Non linear viscoelastic tensile beahvior		cervical : 18.8 MPa thoracic : 25.1 MPa lumbar : 15.3 MPa
Denticulate ligaments										
Polak <i>et al.</i> 2014	Journal of the mechanical behavior of biomedical material	porcins	denticulate ligaments	cervical	Uniaxial tension	2 mm/min until rupture	In 10°C saline solution for less than 24h	1.02 (SD 0.37) - 1.28 (SD 0.65)	1.22 (SD 0.25) MPa - 2.31 (SD 1.45) MPa	1.31 MPa - 2.46 MPa
Polak-Krašna <i>et al.</i> 2018	Journal of the mechanical behavior of biomedical material	porcins	denticulate ligaments	cervical C1 - C7	Uniaxial tension	2 mm/min until rupture	In a saline solution	0.39 (SD 0.16) - 0.67 (SD 0.27)	1.03 (SD 0.43) MPa - 1.51 (SD 0.89) MPa	3.26 (SD 1.45) MPa - 4.42 (SD 2.27) MPa

Table 7. Overview of the mechanical tests and properties characteristics of the nerves and nerve roots

5. References

- [Bardan et al. 2012] Bardan, G., Plouraboue, F., Zagzoule, M., Baledent, O., 2012. Simple Patient-Based Transmantle Pressure and Shear Estimate From Cine Phase-Contrast MRI in Cerebral Aqueduct. *IEEE Transactions on Biomedical Engineering* 59, 2874–2883. <https://doi.org/10.1109/TBME.2012.2210716>
- [Bavo et al. 2016] Bavo, A.M., Rocatello, G., Iannaccone, F., Degroote, J., Vierendeels, J., Segers, P., 2016. Fluid-Structure Interaction Simulation of Prosthetic Aortic Valves: Comparison between Immersed Boundary and Arbitrary Lagrangian-Eulerian Techniques for the Mesh Representation. *PLoS One* 11. <https://doi.org/10.1371/journal.pone.0154517>
- [Beel et al. 1986] Beel, J.A., Stodieck, L.S., Luttges, M.W., 1986. Structural properties of spinal nerve roots: Biomechanics. *Experimental Neurology* 91, 30–40. [https://doi.org/10.1016/0014-4886\(86\)90023-3](https://doi.org/10.1016/0014-4886(86)90023-3)
- [Bertram et al. 2016] Bertram, C.D., Heil, M., 2016. A Poroelastic Fluid/Structure-Interaction Model of Cerebrospinal Fluid Dynamics in the Cord With Syringomyelia and Adjacent Subarachnoid-Space Stenosis. *J Biomech Eng* 139, 011001-011001–10. <https://doi.org/10.1115/1.4034657>
- [Bilston et al. 1995] Bilston, L.E., Thibault, L.E., 1995. The mechanical properties of the human cervical spinal cord In Vitro. *Ann Biomed Eng* 24, 67–74. <https://doi.org/10.1007/BF02770996>
- [Bloomfield et al. 1998] Bloomfield, I.G., Johnston, I.H., Bilston, L.E., 1998. Effects of Proteins, Blood Cells and Glucose on the Viscosity of Cerebrospinal Fluid. *PNE* 28, 246–251. <https://doi.org/10.1159/000028659>
- [Chauvet et al. 2010] Chauvet, D., Carpentier, A., Allain, J.-M., Polivka, M., Crépin, J., George, B., 2010. Histological and biomechanical study of dura mater applied to the technique of dura splitting decompression in Chiari type I malformation. *Neurosurg Rev* 33, 287–295. <https://doi.org/10.1007/s10143-010-0261-x>
- [Cheng et al. 2014] Cheng, S., Fletcher, D., Hemley, S., Stoodley, M., Bilston, L., 2014. Effects of fluid structure interaction in a three dimensional model of the spinal subarachnoid space. *Journal of Biomechanics* 47, 2826–2830. <https://doi.org/10.1016/j.jbiomech.2014.04.027>
- [Clarke et al. 2017] Clarke, E.C., Fletcher, D.F., Bilston, L.E., 2017. Sustained high-pressure in the spinal subarachnoid space while arterial expansion is low may be linked to syrinx development. *Computer Methods in Biomechanics and Biomedical Engineering* 20, 457–467. <https://doi.org/10.1080/10255842.2016.1243665>
- [Dahlan et al. 2014] Dahlan, R.H., Saputra, P.A.E., Yudoyono, F.F., Ompusunggu, S.E., Arifin, M.Z., Sutiono, A.B., Faried, A., 2014. Morphometric Analysis of the Corpus, Spinal Canal and Torg Ratio Using Midsagittal Cervical Vertebrae Computed Tomography Scan: Indonesian Population. *International Journal of Integrated Health Sciences* 2, 36–39.
- [Endo et al. 2014] Endo, K., Suzuki, H., Nishimura, H., Tanaka, H., Shishido, T., Yamamoto, K., 2014. Kinematic Analysis of the Cervical Cord and Cervical Canal by Dynamic Neck Motion. *Asian Spine J* 8, 747–752. <https://doi.org/10.4184/asj.2014.8.6.747>
- [Fifford and Bilston et al. 2005] Fifford, R.J., Bilston, L.E., 2005. The mechanical properties of rat spinal cord in vitro. *Journal of Biomechanics* 38, 1509–1515. <https://doi.org/10.1016/j.jbiomech.2004.07.009>
- [Fountoulakis et al. 2001] Fountoulakis, M., Hardmeier, R., Höger, H., Lubec, G., 2001. Postmortem Changes in the Level of Brain Proteins. *Experimental Neurology* 167, 86–94. <https://doi.org/10.1006/exnr.2000.7529>
- [Fradet et al. 2014] Fradet, L., Arnoux, P.-J., Ranjeva, J.-P., Petit, Y., Callot, V., 2014. Morphometrics of the entire human spinal cord and spinal canal measured from in vivo high-resolution anatomical magnetic resonance imaging. *Spine* 39, E262-269. <https://doi.org/10.1097/BRS.0000000000000125>
- [Fradet et al. 2016a] Fradet, L., Arnoux, P.-J., Callot, V., Petit, Y., 2016a. Geometrical variations in white and gray matter affect the biomechanics of spinal cord injuries more than the arachnoid space. *Advances in Mechanical Engineering* 8, 1687814016664703. <https://doi.org/10.1177/1687814016664703>
- [Fradet et al. 2016b] Fradet, L., Cliche, F., Petit, Y., Mac-Thiong, J.-M., Arnoux, P.-J., 2016b. Strain rate dependent behavior of the porcine spinal cord under transverse dynamic compression. *Proc Inst Mech Eng H* 230, 858–866. <https://doi.org/10.1177/0954411916655373>
- [Garnotel et al. 2018] Garnotel, S., Salmon, S., Balédent, O., 2018. Numerical Cerebrospinal System Modeling in Fluid-Structure Interaction, in: Heldt, T. (Ed.), *Intracranial Pressure & Neuromonitoring XVI*, Acta Neurochirurgica Supplement. Springer International Publishing, Cham, pp. 255–259. https://doi.org/10.1007/978-3-319-65798-1_51
- [Garo et al. 2007] Garo, A., Hrapko, M., van Dommelen, J. a. W., Peters, G.W.M., 2007. Towards a reliable characterisation of the mechanical behaviour of brain tissue: The effects of post-mortem time and sample preparation. *Biorheology* 44, 51–58.
- [Gholampour et al. 2018] S, G., 2018. FSI simulation of CSF hydrodynamic changes in a large population of non-communicating hydrocephalus patients during treatment process with regard to their clinical symptoms [WWW Document]. *PLoS one*. <https://doi.org/10.1371/journal.pone.0196216>
- [Helgeland et al. 2014] Helgeland, A., Mardal, K.-A., Haughton, V., Reif, B.A.P., 2014. Numerical simulations of the pulsating flow of cerebrospinal fluid flow in the cervical spinal canal of a Chiari patient. *Journal of Biomechanics* 47, 1082–1090. <https://doi.org/10.1016/j.jbiomech.2013.12.023>

- [Holmlund et al. 2019] Holmlund, P., Qvarlander, S., Malm, J., Eklund, A., 2019. Can pulsatile CSF flow across the cerebral aqueduct cause ventriculomegaly? A prospective study of patients with communicating hydrocephalus. *Fluids and Barriers of the CNS* 16, 40. <https://doi.org/10.1186/s12987-019-0159-0>
- [Hou et al. 2012] Hou, G., Wang, J., Layton, A., 2012. Numerical Methods for Fluid-Structure Interaction — A Review. *Communications in Computational Physics* 12, 337–377. <https://doi.org/10.4208/cicp.291210.290411s>
- [Ichihara et al. 2003] Ichihara, K., Taguchi, T., Sakuramoto, I., Kawano, S., Kawai, S., 2003. Mechanism of the spinal cord injury and the cervical spondylotic myelopathy: new approach based on the mechanical features of the spinal cord white and gray matter. *Journal of Neurosurgery: Spine* 99, 278–285. <https://doi.org/10.3171/spi.2003.99.3.0278>
- [Jacobson et al. 1996] Jacobson, E.E., Fletcher, D.F., Morgan, M.K., Johnston, I.H., 1996. Fluid Dynamics of the Cerebral Aqueduct. *PNE* 24, 229–236. <https://doi.org/10.1159/000121044>
- [Jannesar et al. 2020] Jannesar, S., Salegio, E., Beattie, M.S., Bresnahan, J.C., Sparrey, C.J., 2020. Correlating tissue mechanics and spinal cord injury: patient-specific finite element models of unilateral cervical contusion spinal cord injury in non-human primates. *Journal of Neurotrauma*. <https://doi.org/10.1089/neu.2019.6840>
- [Kameyama et al. 1994] Kameyama, T., Hashizume, Y., Ando, T., Takahashi, A., 1994. Morphometry of the normal cadaveric cervical spinal cord. *Spine* 19, 2077–2081.
- [Kar et al. 2017] Kar, M., Bhaumik, D., Ishore, K., Saha, P.K., 2017. MRI Study on Spinal Canal Morphometry: An Indian Study. *J Clin Diagn Res* 11, AC08-AC11. <https://doi.org/10.7860/JCDR/2017/25981.9899>
- [Karimi et al. 2017] Karimi, A., Shojaei, A., Tehrani, P., 2017. Mechanical properties of the human spinal cord under the compressive loading. *J. Chem. Neuroanat.* 86, 15–18. <https://doi.org/10.1016/j.jchemneu.2017.07.004>
- [Kato et al. 2012] Kato, F., Yukawa, Y., Suda, K., Yamagata, M., Ueta, T., 2012. Normal morphology, age-related changes and abnormal findings of the cervical spine. Part II: magnetic resonance imaging of over 1,200 asymptomatic subjects. *Eur Spine J* 21, 1499–1507. <https://doi.org/10.1007/s00586-012-2176-4>
- [Kawakami et al. 2002] Kawakami, M., Tamaki, T., Ando, M., Yamada, H., Yoshida, M., 2002. Relationships Between Sagittal Alignment of the Cervical Spine and Morphology of the Spinal Cord and Clinical Outcomes in Patients With Cervical Spondylotic Myelopathy Treated With Expansive Laminoplasty. *Clinical Spine Surgery* 15, 391.
- [Khani et al. 2017] Khani, M., Xing, T., Gibbs, C., Oshinski, J.N., Stewart, G.R., Zeller, J.R., Martin, B.A., 2017. Nonuniform Moving Boundary Method for Computational Fluid Dynamics Simulation of Intrathecal Cerebrospinal Flow Distribution in a Cynomolgus Monkey. *Journal of Biomechanical Engineering* 139. <https://doi.org/10.1115/1.4036608>
- [Khani et al. 2020] Khani, M., Sass, L.R., Xing, T., Keith Sharp, M., Balédent, O., Martin, B.A., 2018. Anthropomorphic Model of Intrathecal Cerebrospinal Fluid Dynamics Within the Spinal Subarachnoid Space: Spinal Cord Nerve Roots Increase Steady-Streaming. *J Biomech Eng* 140. <https://doi.org/10.1115/1.4040401>
- [Ko et al. 2004] Ko, H.-Y., Park, J.H., Shin, Y.B., Baek, S.Y., 2004. Gross quantitative measurements of spinal cord segments in human. *Spinal Cord* 42, 3101538. <https://doi.org/10.1038/sj.sc.3101538>
- [Koser et al. 2015] Koser, D.E., Moeendarbary, E., Hanne, J., Kuerten, S., Franze, K., 2015. CNS Cell Distribution and Axon Orientation Determine Local Spinal Cord Mechanical Properties. *Biophysical Journal* 108, 2137–2147. <https://doi.org/10.1016/j.bpj.2015.03.039>
- [Kuwasawa et al. 2006] Kuwasawa, Y., Pope, M.H., Bashir, W., Takahashi, K., Smith, F.W., 2006. The Length of the Cervical Cord: Effects of Postural Changes in Healthy Volunteers Using Positional Magnetic Resonance Imaging. *Spine* 31, E579. <https://doi.org/10.1097/01.brs.0000229228.62627.75>
- [Levin et al. 1981] Levin, E., Muravchick, S., Gold, M.I., 1981. Density of normal human cerebrospinal fluid and tetracaine solutions. *Anesth. Analg.* 60, 814–817.
- [Loth et al. 2001] Loth, F., Yardimci, M.A., Alperin, N., 2001. Hydrodynamic Modeling of Cerebrospinal Fluid Motion Within the Spinal Cavity. *J Biomech Eng* 123, 71–79. <https://doi.org/10.1115/1.1336144>
- [Lui et al. 1998] Lui, A.C., Polis, T.Z., Cicutti, N.J., 1998. Densities of cerebrospinal fluid and spinal anaesthetic solutions in surgical patients at body temperature. *Can J Anaesth* 45, 297–303. <https://doi.org/10.1007/BF03012018>
- [Maikos et al. 2008] Maikos, J.T., Elias, R.A.I., Shreiber, D.I., 2008. Mechanical Properties of Dura Mater from the Rat Brain and Spinal Cord. *Journal of Neurotrauma* 25, 38–51. <https://doi.org/10.1089/neu.2007.0348>
- [Malzac et al. 2002] Malzac, A., Filho, B., De, T.E.P., 2002. Morphometry of the spinal canal at cervical region in asymptomatic military young men. *Acta Ortopédica Brasileira* 10, 40–51. <https://doi.org/10.1590/S1413-78522002000400006>
- [Mazgajczyk et al. 2012] Mazgajczyk, E., Ściagała, K., Czyż, M., Jarmundowicz, W., Będziński, R., 2012. Mechanical properties of cervical dura mater. *Acta Bioeng Biomech* 14, 51–58.
- [Mazuchowski and Thibault 2003] Mazuchowski, E.L., Thibault, L.E., 2003. BIOMECHANICAL PROPERTIES OF THE HUMAN SPINAL CORD AND PIA MATER 2.

- [Miura et al. 2009] Miura, J., Doita, M., Miyata, K., Marui, T., Nishida, K., Fujii, M., Kurosaka, M., 2009. Dynamic Evaluation of the Spinal Cord in Patients With Cervical Spondylotic Myelopathy Using a Kinematic Magnetic Resonance Imaging Technique. *Clinical Spine Surgery* 22, 8–13. <https://doi.org/10.1097/BSD.0b013e31815f2556>
- [Morishita et al. 2009] Morishita, Y., Naito, M., Hymanson, H., Miyazaki, M., Wu, G., Wang, J.C., 2009. The relationship between the cervical spinal canal diameter and the pathological changes in the cervical spine. *Eur Spine J* 18, 877–883. <https://doi.org/10.1007/s00586-009-0968-y>
- [Ozawa et al. 2004] Ozawa, H., Matsumoto, T., Ohashi, T., Sato, M., Kokubun, S., 2004. Mechanical properties and function of the spinal pia mater. *Journal of Neurosurgery: Spine* 1, 122–127. <https://doi.org/10.3171/spi.2004.1.1.0122>
- [Pahlavian et al. 2014] Pahlavian, S.H., Yiallourou, T., Tubbs, R.S., Bunck, A.C., Loth, F., Goodin, M., Raisee, M., Martin, B.A., 2014. The Impact of Spinal Cord Nerve Roots and Denticulate Ligaments on Cerebrospinal Fluid Dynamics in the Cervical Spine. *PLOS ONE* 9, e91888. <https://doi.org/10.1371/journal.pone.0091888>
- [Pahlavian et al. 2015] Pahlavian, S.H., Loth, F., Luciano, M., Oshinski, J., Martin, B.A., 2015. Neural tissue motion impacts cerebrospinal fluid dynamics at the cervical medullary junction: a patient-specific moving-boundary computational model. *Ann Biomed Eng* 43, 2911–2923. <https://doi.org/10.1007/s10439-015-1355-y>
- [Pahlavian et al. 2016] Heidari Pahlavian, S., Bunck, A.C., Thyagaraj, S., Giese, D., Loth, F., Hedderich, D.M., Kröger, J.R., Martin, B.A., 2016. Accuracy of 4D Flow Measurement of Cerebrospinal Fluid Dynamics in the Cervical Spine: An In Vitro Verification Against Numerical Simulation. *Ann Biomed Eng* 44, 3202–3214. <https://doi.org/10.1007/s10439-016-1602-x>
- [Palaniappan et al. 2004] Palaniappan, L., Velusamy, V., 2004. Ultrasonic study of human cerebrospinal fluid. *IJPAP Vol.42(08)* [August 2004].
- [Patin et al. 1993] Patin, D., Eckstein, E., Harum, K., Pallares, V., 1993. Anatomic and Biomechanical Properties of Human Lumbar Dura Mater. *Anesthesia & Analgesia* 76, 535–540.
- [Persson et al. 2010] Persson, C., Evans, S., Marsh, R., Summers, J.L., Hall, R.M., 2010. Poisson's Ratio and Strain Rate Dependency of the Constitutive Behavior of Spinal Dura Mater. *Ann Biomed Eng* 38, 975–983. <https://doi.org/10.1007/s10439-010-9924-6>
- [Persson et al. 2011] Persson, C., Summers, J., Hall, R.M., 2011. The Effect of Cerebrospinal Fluid Thickness on Traumatic Spinal Cord Deformation. *Journal of Applied Biomechanics* 27, 330–335. <https://doi.org/10.1123/jab.27.4.330>
- [Peskin 1972] Peskin, C.S., 1972. Flow patterns around heart valves: A numerical method. *Journal of Computational Physics* 10, 252–271. [https://doi.org/10.1016/0021-9991\(72\)90065-4](https://doi.org/10.1016/0021-9991(72)90065-4)
- [Polak et al. 2014] Polak, K., Czyż, M., Ścigała, K., Jarmundowicz, W., Będziński, R., 2014. Biomechanical characteristics of the porcine denticulate ligament in different vertebral levels of the cervical spine—Preliminary results of an experimental study. *Journal of the Mechanical Behavior of Biomedical Materials* 34, 165–170. <https://doi.org/10.1016/j.jmbbm.2014.02.010>
- [Polak-Krasna et al. 2019] Polak-Krasna, K., Robak-Nawrocka, S., Szotek, S., Czyż, M., Gheek, D., Pezowicz, C., 2019. The denticulate ligament – Tensile characterisation and finite element micro-scale model of the structure stabilising spinal cord. *Journal of the Mechanical Behavior of Biomedical Materials* 91, 10–17. <https://doi.org/10.1016/j.jmbbm.2018.11.017>
- [Pratali et al. 2019] Pratali, R.R., Smith, J.S., Ancheschi, B.C., Maranhão, D.A., Savarese, A., Nogueira-Barbosa, M.H., Herrero, C.F.P.S., 2019. A Technique for Dynamic Cervical Magnetic Resonance Imaging Applied to Cervical Spondylotic Myelopathy: A Reliability Study. *Spine* 44, E26. <https://doi.org/10.1097/BRS.0000000000002765>
- [Ramo et al. 2018 a] Ramo, N., Shetye, S.S., Puttlitz, C.M., 2018. Damage Accumulation Modeling and Rate Dependency of Spinal Dura Mater. *ASME J of Medical Diagnostics* 1. <https://doi.org/10.1115/1.4038261>
- [Ramo et al. 2018 b] Ramo, N.L., Shetye, S.S., Streijger, F., Lee, J.H.T., Troyer, K.L., Kwon, B.K., Crompton, P., Puttlitz, C.M., 2018a. Comparison of In-Vivo and Ex-Vivo Viscoelastic Behavior of the Spinal Cord. *Acta Biomater* 68, 78–89. <https://doi.org/10.1016/j.actbio.2017.12.024>
- [Ramo et al. 2018 c] Ramo, N.L., Troyer, K.L., Puttlitz, C.M., 2018b. Viscoelasticity of spinal cord and meningeal tissues. *Acta Biomaterialia* 75, 253–262. <https://doi.org/10.1016/j.actbio.2018.05.045>
- [Runza et al. 1999] Runza, M., Pietrabissa, R., Mantero, S., Albani, A., Quaglini, V., Contro, R., 1999. Lumbar Dura Mater Biomechanics: Experimental Characterization and Scanning Electron Microscopy Observations. *Anesthesia & Analgesia* 88, 1317–1321. <https://doi.org/10.1213/0000539-199906000-00022>
- [Sass et al. 2017] Sass, L.R., Khani, M., Natividad, G.C., Tubbs, R.S., Baledent, O., Martin, B.A., 2017. A 3D subject-specific model of the spinal subarachnoid space with anatomically realistic ventral and dorsal spinal cord nerve rootlets. *Fluids Barriers CNS* 14, 36. <https://doi.org/10.1186/s12987-017-0085-y>
- [Schiffer et al. 1999] Schiffer, E., van Gessel, E., Gamulin, Z., 1999. Influence of sex on cerebrospinal fluid density in adults. *British Journal of Anaesthesia* 83, 943–944. <https://doi.org/10.1093/bja/83.6.943>
- [Shetye et al. 2014] Shetye, S.S., Deault, M., Puttlitz, C.M., 2014. Biaxial Response of Ovine Spinal Cord Dura Mater. *J Mech Behav Biomed Mater* 34, 146–153. <https://doi.org/10.1016/j.jmbbm.2014.02.014>
- [Singh et al. 2006] Singh, A., Lu, Y., Chen, C., M Cavanaugh, J., 2006. Mechanical properties of spinal nerve roots subjected to tension at different strain rates. *Journal of Biomechanics* 39, 1669–1676. <https://doi.org/10.1016/j.jbiomech.2005.04.023>

- [Smith et al. 2013] Smith, J.S., Lafage, V., Ryan, D.J., Shaffrey, C.I., Schwab, F.J., Patel, A.A., Brodke, D.S., Arnold, P.M., Riew, K.D., Traynelis, V.C., Radcliff, K., Vaccaro, A.R., Fehlings, M.G., Ames, C.P., 2013. Association of myelopathy scores with cervical sagittal balance and normalized spinal cord volume: analysis of 56 preoperative cases from the AOSpine North America Myelopathy study. *SPINE* 38.
- [Sweetman and Linninger 2011] Sweetman, B., Linninger, A.A., 2011. Cerebrospinal Fluid Flow Dynamics in the Central Nervous System. *Ann Biomed Eng* 39, 484–496. <https://doi.org/10.1007/s10439-010-0141-0>
- [Tamura et al. 2018] Tamura, A., Sakaya, M., 2018. Dynamic Tensile Behavior of Fiber Bundles Isolated From Spinal Nerve Roots: Effects of Anatomical Site and Loading Rate on Mechanical Strength. *ASME J of Medical Diagnostics* 1, 031001-031001-6. <https://doi.org/10.1115/1.4039560>
- [Tangen et al. 2015] Tangen, K.M., Hsu, Y., Zhu, D.C., Linninger, A.A., 2015. CNS wide simulation of flow resistance and drug transport due to spinal microanatomy. *Journal of Biomechanics* 48, 2144–2154. <https://doi.org/10.1016/j.jbiomech.2015.02.018>
- [Tierney et al. 2002] Tierney, R.T., Maldjian, C., Mattacola, C.G., Straub, S.J., Sittler, M.R., 2002. Cervical Spine Stenosis Measures in Normal Subjects. *J Athl Train* 37, 190–193.
- [Toma and Nguyen 2018] Toma, M., Nguyen, P.D.H., 2018. Fluid–structure interaction analysis of cerebrospinal fluid with a comprehensive head model subject to a rapid acceleration and deceleration. *Brain Injury* 32, 1576–1584. <https://doi.org/10.1080/02699052.2018.1502470>
- [Wilcox et al. 2003] Wilcox, R.K., Bilston, L.E., Barton, D.C., Hall, R.M., 2003. Mathematical model for the viscoelastic properties of dura mater. *Journal of Orthopaedic Science* 8, 432–434. <https://doi.org/10.1007/s10776-003-0644-9>
- [Wolf et al. 2018] Wolf, K., Hupp, M., Friedl, S., Sutter, R., Klarhöfer, M., Grabher, P., Freund, P., Curt, A., 2018. In cervical spondylotic myelopathy spinal cord motion is focally increased at the level of stenosis: a controlled cross-sectional study. *Spinal Cord* 56, 769–776. <https://doi.org/10.1038/s41393-018-0075-1>
- [Xie et al 2019] Xie, Y.M., Zheng, Y.C., Qiu, S.J., Gong, K.Q., Duan, Y., 2019. The appropriate hybrid surgical strategy in three-level cervical degenerative disc disease: a finite element analysis. *J Orthop Surg Res* 14, 444. <https://doi.org/10.1186/s13018-019-1502-5>
- [Yang et al. 2019] Yang, C., Yang, X., Lan, X., Zhang, H., Wang, M., Zhang, Y., Xu, Y., Zhen, P., 2019. [Structure and mechanical characteristics of spinal dura mater in different segments of sheep's spine]. *Zhongguo Xiu Fu Chong Jian Wai Ke Za Zhi* 33, 232–238. <https://doi.org/10.7507/1002-1892.201807085>
- [Yiallourou et al. 2012] Yiallourou, T.I., Kröger, J.R., Stergiopoulos, N., Maintz, D., Martin, B.A., Bunck, A.C., 2012. Comparison of 4D Phase-Contrast MRI Flow Measurements to Computational Fluid Dynamics Simulations of Cerebrospinal Fluid Motion in the Cervical Spine. *PLoS One* 7. <https://doi.org/10.1371/journal.pone.0052284>
- [Yuan et al. 1998] Yuan, Q., Dougherty, L., Margulies, S.S., 1998. In vivo human cervical spinal cord deformation and displacement in flexion. *SPINE* 23, 1677–1683. <https://doi.org/10.1097/00007632-199808010-00012>
- [Zaaroor et al. 2006] Zaaroor, M., Kósa, G., Peri-Eran, A., Maharil, I., Shoham, M., Goldsher, D., 2006. Morphological Study of the Spinal Canal Content for Subarachnoid Endoscopy. *Minim Invasive Neurosurg* 49, 220–226. <https://doi.org/10.1055/s-2006-948000>
- [Zarzur et al. 1996] Zarzur, E., 1996. Mechanical properties of the human lumbar dura mater. *Arquivos de Neuro-Psiquiatria* 54, 455–460. <https://doi.org/10.1590/S0004-282X1996000300015>
- [Zhang et al. 1996] Zhang, C., Goto, N., Suzuki, M., Ke, M., 1996. Age-related Reductions in Number and Size of Anterior Horn Cells at C6 Level of the Human Spinal Cord. *Okajimas Folia Anatomica Japonica* 73, 171–177. https://doi.org/10.2535/ofaj1936.73.4_171
- [Zhang et al. 2016] Zhang, H., Falkner, P., Cai, C., 2016. In-Vivo Indentation Testing of Sheep Spinal Cord with Meninges, in: Tekalur, S.A., Zavattieri, P., Korach, C.S. (Eds.), *Mechanics of Biological Systems and Materials*, Volume 6, Conference Proceedings of the Society for Experimental Mechanics Series. Springer International Publishing, Cham, pp. 99–103. https://doi.org/10.1007/978-3-319-21455-9_11

Chapter summary

Section 1 summary

In a context of cervical canal alteration, a state-of-the-art of morphometrical analysis highlighted that MRI and 2D time-consuming and operator-dependent manual morphometric analysis remain the gold standard to quantify geometrical changes in the cervical canal. Then, the main morphological metrics in clinical research are the cross-sectional areas of the spinal cord (SC) and the cerebrospinal fluid, the occupational ratio, the diameter of the SC and the cervical canal in axial and sagittal planes, the Torg-Pavlov ratio derived from sagittal diameters of the canal and the vertebral body, and the compression ratio. Finally, the “DCM” term was preferred to the “cervical spondylosis degenerative” term.

Section 2 summary

In this PhD context of biomechanical modelling, the necessity to understand and measure the mechanical properties of the CSF and the central nervous structures is crucial. The main descriptions of the different anatomical elements presented in the section 2 are:

- the CSF is similar to water, acting as shock absorber and protecting the spinal cord.
- the SC was demonstrated incompressible, non-linear elastic (hyperelastic) and viscoelastic, anisotropic with significant differences between white and gray matter properties.
- various studies showed different properties of the spinal meninges: elastic, non-linear elastic (hyperelastic), anisotropic, viscoelastic in different conditions (quasi-static to dynamic) and in various animal species.
- the nerve, nerve roots were only studied from an elastic point of view in quasi-static and in dynamic conditions.
- the denticulate ligaments were only studied from an elastic point of view in quasi-static condition.

Section 3 summary

To model the cerebrospinal fluid flow, two main branches in computer science were presented: the computational fluid dynamics (CFD) and the fluid-structure interactions (FSI) modellings. The CFD approach is a robust and accurate way to model a 3D velocity field conditioned by coherent bio-reliable fluid initial and boundaries conditions as well as fluid assumptions. The main drawback is that the walls (i.e. the geometrical boundary conditions) are considered as rigid. The fluid-structure interaction (FSI) approach allows to model the deformation of the solid boundaries induced by the fluid flow and conversely. Among them, partitioned approach are dependent to the algorithm modelling the exchanges at the fluid-structure boundaries between two numerical solvers while the monolithic approach necessitates a special pre-processing approach on only one solver. Both techniques are highly time-consuming.

Chapter 3

Morphometry of the human cervical canal

1.Cervical canal morphology : effects of neck flexion in normal conditions – New elements for Biomechanical simulations and surgical management	72
1.1. Introduction.....	72
1.2. Material and Methods.	73
1.3.Results.....	75
1.4.Discussion	81
1.5.Conclusion	83
1.6.Appendices	84
2.Degenerative cervical myelopathy morphology : effects of decompressive surgery by laminectomy - New elements for patient follow-up.....	87
2.1.Introduction.....	87
2.2.Material and Methods	91
2.3.Results.....	94
2.4.Discussion	106
2.5.Conclusion	108
2.6.Appendices	109
3.References.....	112

The aims of this chapter were :

- 1) to provide a methodology allowing to measure as accurately as possible the morphometry of the cervical canal of a healthy population for further clinical and numerical applications.
- 2) To study the morphometrics link between the neutral and the neck-flexion effects on the canal morphometry.
- 3) To apply the previous methodology to study three pathological cases of cervical myelopathy in order to provide a new morphometrical description in a clinical point of view.

1. Cervical canal morphology : effects of neck flexion in normal conditions – New elements for Biomechanical simulations and surgical management

Patrice Sudres (1,4), Morgane Evin (1,4), Pierre-Jean Arnoux (1,4), Virginie Callot (2,3,4)

1. Laboratoire de Biomécanique Appliquée, UMRT24 AMU/IFSTTAR, Marseille, France;
2. Aix-Marseille Université, CNRS, CRMBM, Marseille, France;
3. APHM, Hôpital Universitaire Timone, CEMEREM, Marseille, France ;
4. iLab-Spine – Laboratoire International en Imagerie et Biomécanique du Rachis, Marseille, France & Montréal, Canada.

Article published in Spine [[Sudres et al. 2020](#)].

Abbreviations

AP : antero-posterior
AVD VERT : spatial averaged value (over the whole vertebra)
CP : compression ratio
CSA : cross-sectional area
CSM : cervical spondylotic myelopathy
CSS : cervical subarachnoïd space
LAC : length of anterior column
LPC : length of posterior column
LR : left-right
LSC : length of spinal cord
MID-IVD : spatial value for cross-sectional plane located at the middle of the intervertebral disc
MID-VERT : spatial value for a cross-sectional plane mid-vertebra
MRI : magnetic resonance imaging
kMRI : kinematic magnetic resonance imaging
OR : occupational ratio
SC : spinal cord

Keywords :

cervical ; subarachnoid space ; spinal cord ; kinematical ; magnetic resonance imaging ; morphology ; anatomy ; spine ; absolute metrics ; cross-sectional area ; neck-flexion ; 3D reconstruction ; continuous description.

1.1.Introduction

Magnetic Resonance Imaging (MRI) has become a gold standard to understand different physiological mechanisms of the spine. In the context of degenerative process, Kinematic MRI (kMRI), or postural MRI, which refers to imaging of the spine at different neck positions, is largely used to diagnosis position-dependent alterations that could not be detected in normal posture. It is mostly applied qualitatively to visualize cervical canal narrowing, however little is known concerning the changes occurring at the level of the healthy cervical subarachnoid space(CSS) and spinal cord (SC) tissues for both positions.

Considering the limited spatial resolution that could be reached on conventional MR system (1.5 or 3T), the subarachnoid space is often simplified as a dural tube or the space in the sagittal plane between the spinal cord and the anterior and posterior parts of the canal. Using this assumption, large database of *in vivo* morphological measurements was proposed and showing the influence of the age and the gender on the occupation rate of the spinal cord in the dural tube [Kato et al. 2012]. Dahlan et al. [2014] established normal values of cervical canal diameters for young military subjects. Others studies focused on the SC location in the canal based on two-dimensional (2D) visualization analysis for healthy subjects [Fradet et al. 2014] and for symptomatic subjects [Kar et al.2017]. CSS and SC characterizations at specific locations (mid-vertebrae, discs) can also be found, with different parameters such as compression ratio, cross-sectional area or spinal cord displacement that have been used in clinical research [Malzac et al. 2002, Tykocki et al. 2018 a, b]. In patients with Cervical Spondylotic Myelopathy (CSM), area of the SC, as well as antero-posterior and left-right diameters were described [Stoner et al. 2019, Yuan et al. 2018] so as to evaluate the cord compression.

When characterizing changes in posture, some articles considered a quantification of the strain of cord while others considered displacement measurements. Indeed, longitudinal strain of human cervical cord can reach a magnitude of 5% and 20% for, respectively, flexion and extension [Smith et al. 2013, Hu et al. 2019, Bilston and Thibault 1997, Bilston 1994], respectively.

In this study, based on 3D MR acquisitions in healthy subjects in both neutral supine and flexion, we propose a new methodology to characterize and to quantify the morphology of the CSS and the cervical SC in 3D for healthy subjects in both neutral supine and flexion. This approach aims at providing accurate and detailed morphological data (cross-sectional area, eccentricity indices, and displacements of the cord and canal) in order to quantify the impact of the flexion in the cervical canal.

1.2. Material and methods

1.2.1. MRI acquisition

Eleven european healthy subjects (5 females and 6 males, mean age : 30 +/- 6y, BMI : 23.86 +/- 1.78 kg/m²) were scanned using a 3T MR system (Siemens Healthineers, Erlangen, France) equipped with head, neck and spine coils. Subjects were first examined with the neck in neutral and flexion positions, using a dedicated homemade device (device flexion up to 40°). Images were acquired using a sagittal 3D T₂-SPACE sequence (Sampling Perfection with Application optimized Contrasts using different flip angle Evolution) with the following parameters: voxel size (1x1x1 mm³), field-of-view (256x256 mm²), echo time (TE : 124 ms), repetition time (TR : 1500 ms), total acquisition time (6 min). The MR protocol was approved by the institutional ethics committee and all subjects signed the informed consents. The cohort was chosen excluding history, presence of cervical pathologies or deformations.

1.2.2. Segmentation and anatomical markers

The SC was first segmented in 3D by a semi-automatic approach using the Spinal Cord Toolbox (SCT, 3.1.1) [De Leener et al. 2017] and providing SC centerline. The outer canal border, assumed as the dura mater, was then segmented by a semi-automatic approach from ITK-SNAP software [Yushkevich et al. 2006]. The 3D CSS was defined as the space between the canal segmentation and the SC segmentation [Fig. 21-a,b]. Eleven landmarks [Fig. 21-b] were selected, by one operator on the middle slice of the sagittal view, using 3DSlicer 4.8.1 [Kikinis et al. 2014] for the delimitation of the segment of interest:

- 1) "Reference landmarks": at the top of the dens of C2 (axis) and at the posterior extremity of C7 inferior endplate.
- 2) "Cervical vertebral landmarks", at the posterior extremities of each endplate (superior and inferior, C2 to C6).

1.2.3. Data preparation, indices and lengths computation

The post-processing steps performed using in-house Matlab codes (R2018a version, Matlab®MathWorks,1984) are summarized in [Fig.21] and were performed for both neutral and flexion positions. Both 3D segmentations (dural tube and SC raw surface meshes) were smoothed using ($\lambda : 1, \sigma : 0$) [Desbrun et al. 1999]. Morphological parameters were computed from anatomical markers and centerline coordinates in less than 10 s per subject (Dell Latitude 7480, Intel® Core™ i7-7600U CPU – 2.80GHz/2.90GHz, RAM : 8Go). The boundaries of the SC and the canal were interpolated as the intersection [Tropp and al. 2006] of the surface meshes and meshed planes orthogonal to the centerline [Fig.21-c] using 3D splines. Then, the CSA of the SC, canal and CSS ($CSA_{SC}, CSA_{canal}, CSA_{CSS}$, respectively) were computed. Seven others absolute metrics were also computed ($AP_{eccentricity}, LR_{eccentricity}, CR, OR, LSC, LAC, LPC$) (Text – Supplemental Digital Content 1, describing the all metrics).

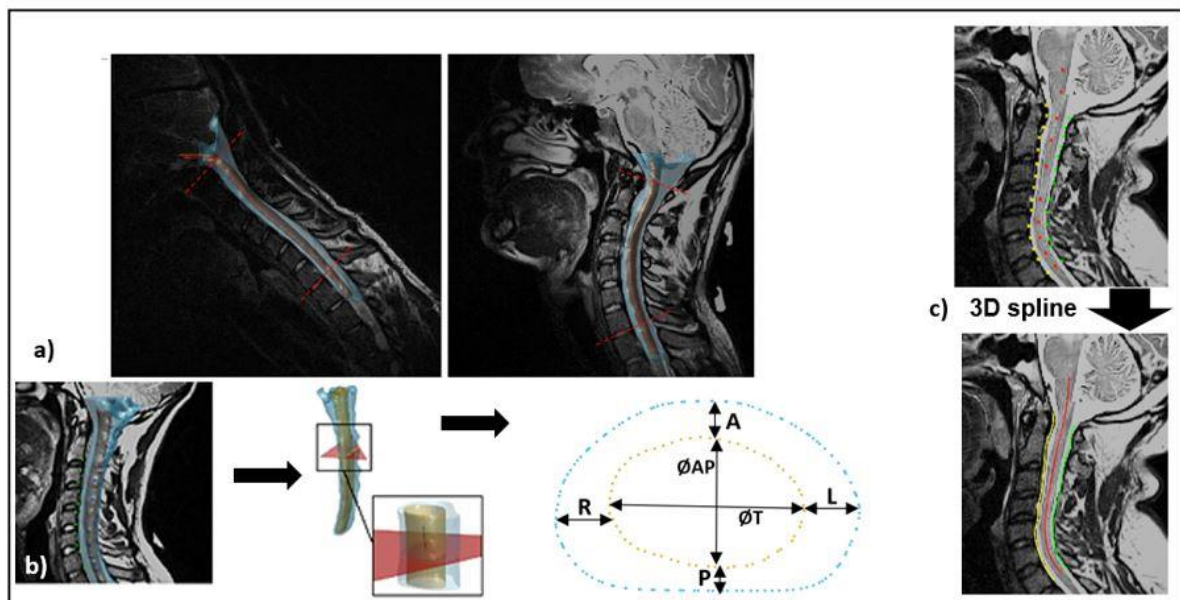


Figure 21. **a)** Sagittal view with superimposed 3D reconstruction of the SC (gold color) and the CSS (blue color) in flexion (left), and neutral (right) neck positions. The red dotted lines indicates the delimitation of the cervical segment (C1-C7) considered in this study. **b)** Main postprocessing steps, 3D reconstruction and 3D landmarks (left), orthogonal planes to the centerline all along the cervical segment (middle), boundaries points (zoom x5) extracted from the intersection between 3D reconstruction and the plane, with distance representations of eccentricity indices (A, P, L, R, \varnothing_{AP} , \varnothing_T) (right). **c)** As in Jha et al.²⁰, main steps to compute the length of the cervical spinal cord (LSC) attached to the caudal side of the pons in red, length of the cervical spinal anterior column (LAC) in yellow and length of the cervical spinal posterior column (LPC) in green (top : manual inputs, bottom : 3D-spline interpolation).

1.2.4. Inter-operator variability, intra-operator variability and statistical analyses process

The intra-operator variability was quantified in 5 subjects randomly selected to assess the accuracy of the semi-automatic segmentation [Table 8]. Additional information on the reliability of the SC

segmentation can be found in literature [De Leener et al. 2017]. Inter (by 2 raters) and intra-operator (at 2 different time points by operator 1) variabilities of 3D reconstruction and landmarks positioning were also assessed reporting the Euclidian distance [Table 10], mean relative error of the CSA (CSS, SC) and of the eccentricity indices (AP, LR) [Table 9]. A summary table describing three sub-metrics by absolute metrics statistically analyzed was provided [Text - Supplemental Digital Content 2, describing the sub-metrics, Table 12 - Supplemental Digital Content 3].

Statistical comparisons between neutral and flexion measurements were performed using RStudio (© 2009-2018 RStudio, Inc. – Version 1.1.463). Due to the small number of samples, paired samples Wilcoxon tests (non-parametric test) were used. Significant differences were defined for p-values < 0.05.

1.3. Results

1.3.1. Segmentation and inter-operator reliability

The maximum error value between manual and automatic canal CSA measurements was found for the C2 dens reaching 25.06% while for the others cervical levels, the canal CSA relative errors reminded lower than 18% [Table 8].

The maximal distance, when considering inter-operator differences, was found of 2.29 mm (ie. 2 voxels) in neutral position and 4.29 mm (ie. 4 voxels) in neutral position and 3.62 mm (ie. 4 voxels) in flexion.

Consequences of inter/intra-operator differences in landmarks positioning show for the first tenth of the cervical segment (C1-C2 functional unit) high variability (gray zone [Table 9]), whereas mean differences were less than 5% of the measured values otherwise, except for the CSA_{CSS} (relative error of 7.5%).

Vertebral level	CSA relative error (manual VS automatic) [%] [Mean ± STD]
C1 (odontoid)	25.06 ± 15.06
C2 inferior endplate	14.69 ± 17.37
C3 middle vertebra	15.7 ± 16.81
C4 middle vertebra	14.12 ± 15.85
C5 middle vertebra	15.42 ± 16.51
C6 middle vertebra	13.32 ± 17.18
C7 middle vertebra	17.43 ± 14.46

Table 8. CSA relative error between manual and automatic CSA measurements for 5 subjects randomly selected. Mean and standard deviation were computed by averaging all subjects for seven levels along the cervical spine.

Intra-operator differences	CSA SC [mm²]	CSA CSS [mm²]	AP Eccentricity [%]	LR Eccentricity [%]
Neutral	1.36±0.85 ; 0/2.69	16.42±7.32 ; 0.01/29.98	3.13±2.02 ; 0/6.56	3.85±4.66 ; 0.01/18.18
	2.36±0.97 ; 0.5/4.57	2.26±2.17 ; 0.02/11.27	2.11±2.15 ; 0.01/10.08	2.15±2.03 ; 0.02/11.58
Flexion	3.49±1.79 ; 0/6.92	32.28±22.38 ; 0.06/72.69	6.62±3 ; 0.05/11.79	3.58±2.42 ; 0.12/8.98
	1.1±1.26 ; 0.01/11.35	4.81±4.56 ; 0.03/24.68	3.54±3.11 ; 0.03/15.13	2.93±2.78 ; 0.01/14.53

Table 9. Intra-operator relative errors for spinal cord (SC) and Cervical Subarachnoid Space (CSS) CSA and Antero-posterior (AP) and Left – Right (LR) eccentricity indices, due to the positioning of landmarks by the same operator. The averaged value, standard deviation, minimum and maximum averaged value on the 5 subjects randomly selected are described as : [Mean ± STD ; Min/Max]. The grey zones represent the first tenth of the measures along the cervical cord and the white zones represent the rest.

1.3.2. Cervical subarachnoid space (CSS) and spinal cord (SC) in the canal

Cross-sectional areas and occupational ratio

The mean CSA_{CSS} evolution along the canal after normalization in abscissa is depicted [Fig.22-Top]. The abscissa represents the averaged distances of each “cervical vertebral landmarks” from the top “reference landmarks” projected on the centerline for all the subjects normalized as (1) :

$$Y = \frac{X - \min(X)}{\max(X) - \min(X)} \quad (1)$$

with **Y** : the normalized vector of the abscissa. **X** : the vector of mean values of the distances on the centerline from the top projected “reference landmark” to the projected “cervical vertebral landmarks”.

CSA_{CSS} rapidly decreased from C2 dens to C2 inferior endplate (from 481.6 mm² to 177.5 mm² in neutral position ; 379.8 mm² to 157.9 mm² in flexion), with minimal values around C3. Oscillations can be observed along the segment [Fig.22-Top].

In flexion, the mean of CSA_{SC} [Fig. 25 – Supplemental Digital Content 4] was systematically lower than in neutral position.

After the superior C3 endplate (0.33 – neutral ; 0.35 – flexion), the flexion OR decreases faster than in neutral position with an oscillating behavior until the C7 inferior vertebrate endplate (0.31 – neutral ; 0.22 - flexion). Large standard deviations could be noticed (± 8-30% - neutral ; ± 13-45% - flexion) [Fig.22-Bottom].

Eccentricity indices and compression ratio.

The first tenth of the presented curves (0 to 0.1 in abscissa) will not be considered in further analysis because of the difficulty of the post-processing algorithm to be efficient with the small complex geometry of the subarachnoid space (*cisterna magna/pontis/interpeduncularis, medulla oblongata*) between the foramen magnum and the C2 dens.

After the C3 superior endplate, mean $AP_{eccentricity}$ index in neutral was systematically lower than in flexion position. [Fig.23-Top].

The $LR_{eccentricity}$ index constantly oscillated around 0% and 8% respectively in neutral and flexion neck postures respectively [Fig.23-Middle].

The CR for the flexion case was systematically lower than in neutral position, except along the C3 vertebra [Fig.23-Bottom].

Anterior/Posterior columns and of the spinal cord length

The mean length values were measured equal to 118 ± 5 mm and 120.3 ± 7.6 mm for LAC, 107 ± 6 and 120.4 ± 6.4 mm for LPC, 142 ± 7 mm and 159.4 ± 11.5 mm for LSC in neutral and flexion neck postures, respectively [Fig.24].

Statistical differences were found between both postures for CSA_{CSS} , OR, $AP_{eccentricity}$ ($p < 0.05$) for C1-C2, C5, C6, C7, and were found for all local locations for CSA_{SC} . No significant difference in $LR_{eccentricity}$ index between the postures was found ($0.08 < p < 0.97$) except for the vertebral level C1-C2. Statistical differences for the CR index between neutral and flexion neck postures were found ($p < 0.05$) locally for the vertebral levels C4, C5, C6 and for the mid-levels of intervertebral discs values of C4/C5 to C6/C7. Statistical differences between both the postures were found for each characteristic lengths ($p < 0.05$) [Table 12 - Supplemental Digital Content 3].

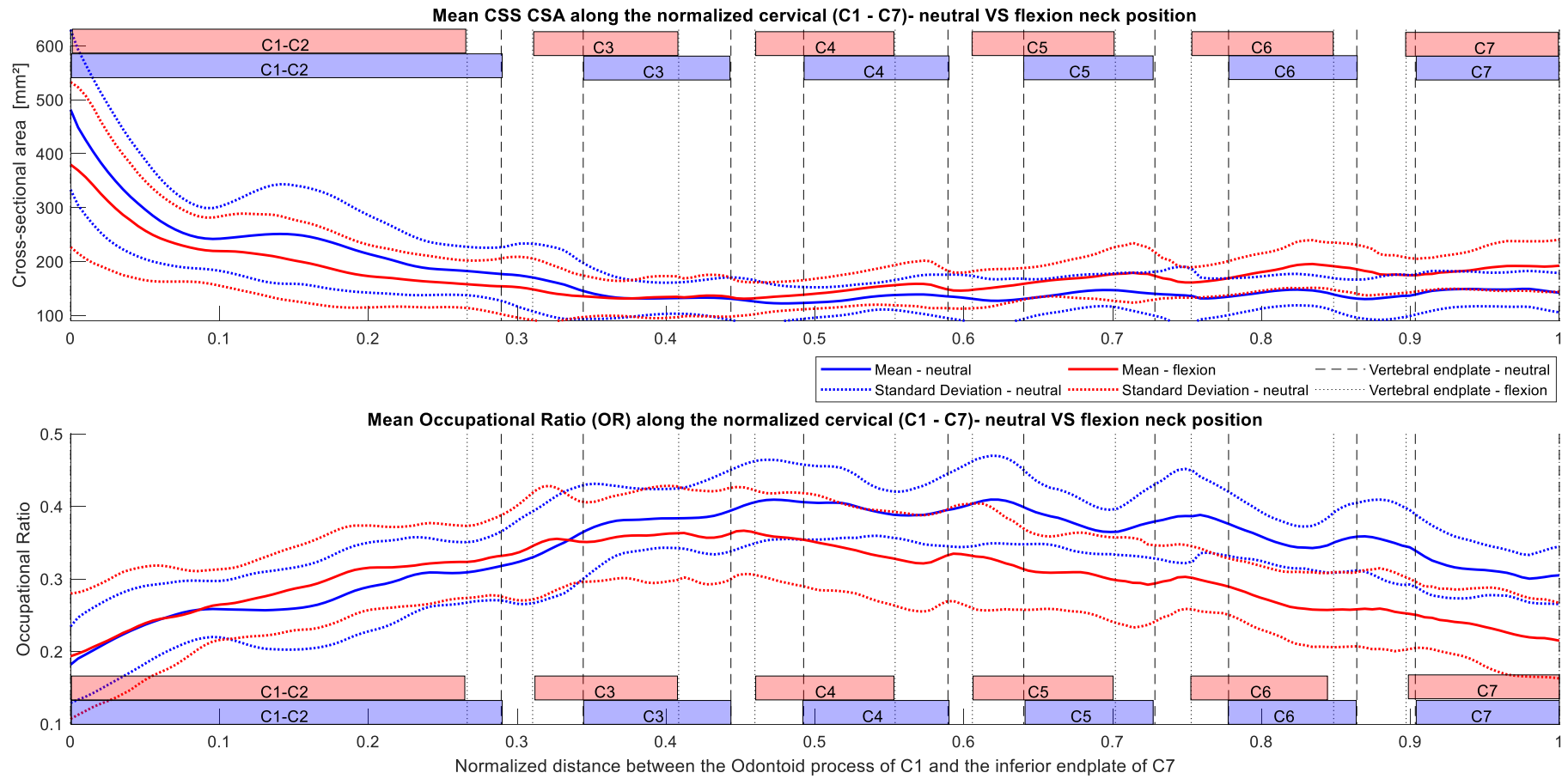


Figure 22. (Top) Mean Cross-Sectional Area of the cervical subarachnoid space (mm^2) along the normalized cervical spinal normalized (formula 1 for normalization process) segment of interest length, (bottom) Mean Occupation Ratio (% defined as SC CSA over total canal CSA (SC CSA + CSS CSA)). For each subplot figure, the mean value of the neutral (blue continuous curve) and flexion (red continuous curve) cases are indicated with their standard deviations (dot curve). Mean normalized positions of the vertebral endplates (computed as the mean position of each vertebral endplates between all the subjects) are indicated with color boxes and as vertical lines (small dots in flexion and bigger dots in neutral).

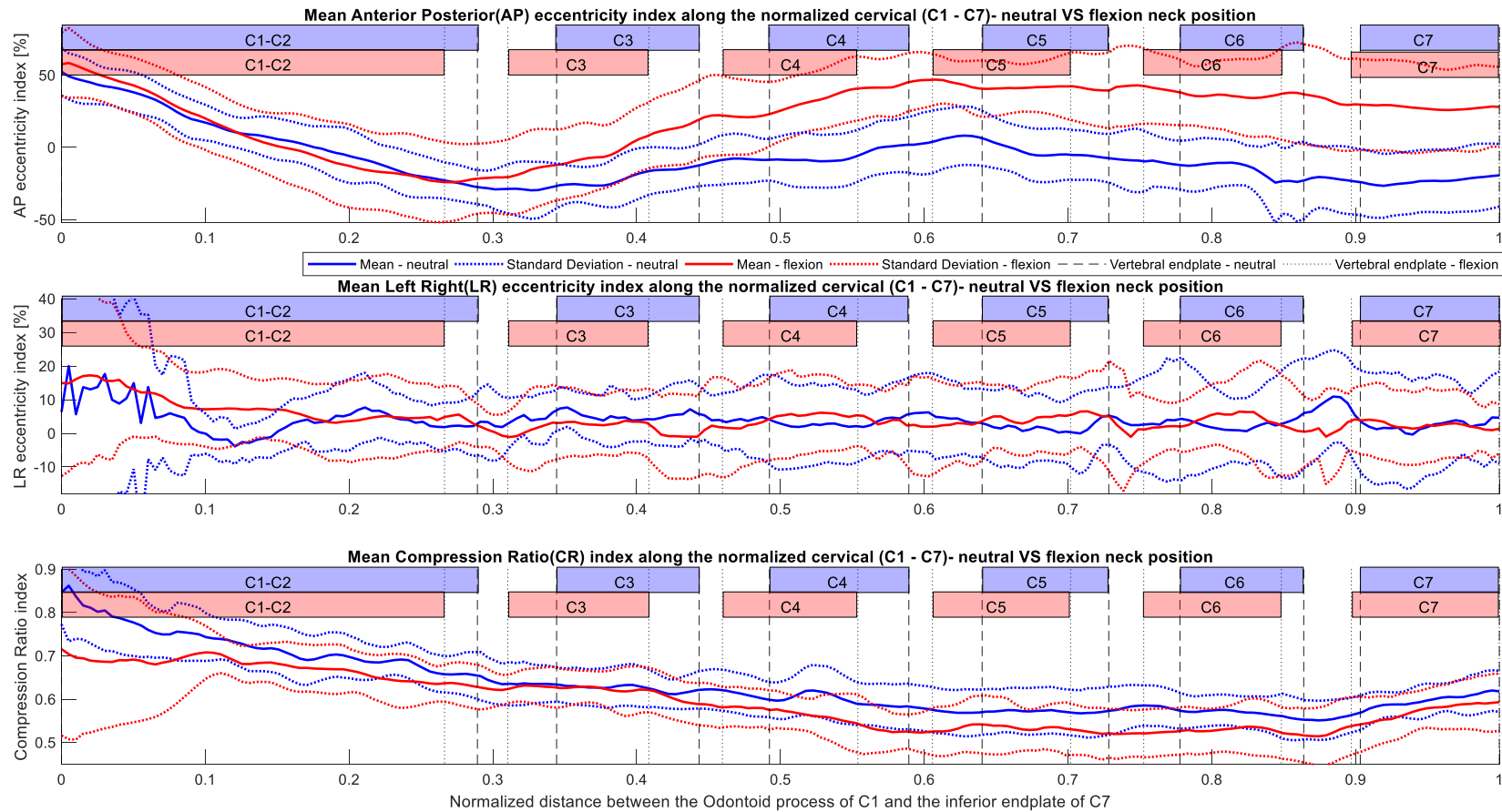


Figure 23. AP (top) and LR (middle) eccentricity indices along the normalized cervical cord, together with the Compression Ratio index (bottom). For each subplot figure, the mean value of the neutral (blue continuous curve) and flexion (red continuous curve) cases are indicated with their standard deviations (dotted curves). Mean normalized positions of the vertebral endplates are indicated as well, standard deviations are not indicated on the figure for a sake of clarity.

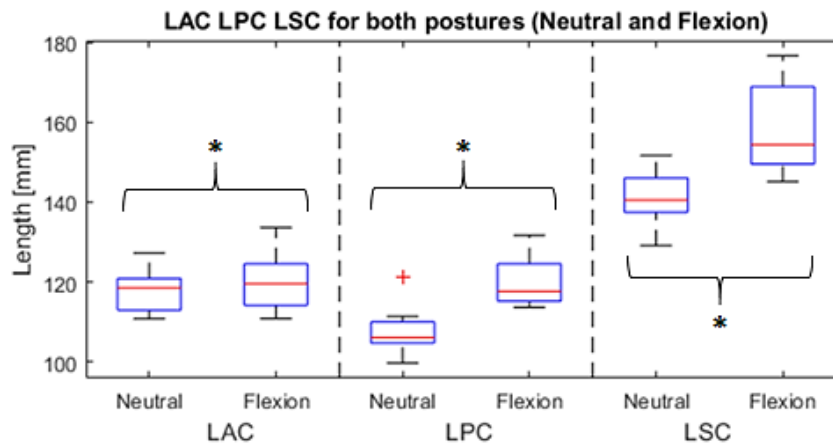


Figure 24. Boxplots of characteristics lengths in the cervical segment, a) Length of the Anterior Column (LAC), b) Length of the Posterior Column (LPC) c) Length of the Spinal Cord (LSC). On each box, the central mark indicates the median (red line), and the bottom and top edges of the box indicate the 25th and 75th percentiles (horizontal blue lines), respectively. The whiskers extend to the most extreme data points not considered outliers, and the outliers are plotted individually using the red '+' symbol (* $p < 0.05$).

	Inter-operator		Intra-operator	
	Neutral	Flexion	Neutral	Flexion
C1 odontoid (ref pt)	1.72 ; 0.52/4.26	4.29 ; 1.47/6.19	2.12 ; 0.56/4.02	3.62 ; 2.36/6.22
C2 inf	2.03 ; 0.31/3.51	6.4 ; 1.27/29.75	1.44 ; 0.36/3.2	2.64 ; 1.13/6.09
C3 sup	2.29 ; 1.13/3.82	2.37 ; 0.37/3.37	1.53 ; 0.87/3.83	2.51 ; 0.86/5.67
C3 inf	2.05 ; 0.98/4.07	2.61 ; 1.33/4.87	2.02 ; 1/3.61	2.49 ; 1.01/5.58
C4 sup	1.62 ; 0.27/3.01	2.77 ; 1.77/3.4	1.29 ; 0.42/2.37	2.65 ; 1.36/5.07
C4 inf	2.03 ; 0.36/3.73	2.61 ; 1.3/3.51	1.63 ; 0.32/2.53	2.6 ; 1.12/5.08
C5 sup	1.96 ; 0.74/3.52	3.69 ; 1.32/12.06	1.43 ; 0.72/2.77	2.43 ; 1.2/5.01
C5 inf	2.12 ; 0.89/4.25	2.99 ; 1.26/5.35	1.29 ; 0.08/2.57	2.85 ; 1.53/6.31
C6 sup	1.69 ; 0.9/2.73	3.84 ; 1.54/14.01	1.65 ; 1.03/2.4	2.44 ; 0.73/5.02
C6 inf	1.61 ; 0.4/3.43	2.84 ; 1.27/5.13	1.31 ; 0.29/2.5	2.49 ; 0.17/6.75
C7 sup	1.32 ; 0.38/2.39	3.76 ; 1.3/14.49	1.42 ; 0.5/2.62	2.19 ; 0.67/5.05
C7 inf (ref pt)	1.32 ; 0.11/2.72	2.51 ; 1.01/4.81	1.47 ; 0.71/2.28	2.43 ; 1.43/5.44

Table 10. Distance errors (L2-norm in mm) per vertebra landmarks between operator 1 and the operator 2 (inter-operator variability), as well as between 2-measurements sessions by operator 1 (intra-operator variability). For each cell, the results are presented as follow : [Mean ; Min/Max].

1.4. Discussion

Morphological parameters	Main position-dependent evolution
CSS CSA	Significant decrease from C1 to C3 superior endplate. From C3 to C7, low variation and oscillating phase around 157 mm ² in neutral and 162 mm ² in flexion positions.
SC CSA	Significantly lower in flexion than in neutral supine position.
OR	After the superior C3 endplate (0.33 – neutral ; 0.35 - flexion), the flexion OR decreases faster than in neutral position.
CR	The CR index decreased steadily between C2 dens and to C7 inferior endplate for both posture. The CR for the flexion case is systematically lower.
AP eccentricity index	Same location for the both postures before C3 vertebra. After C3, in flexion the SC is more anteriorly positioned with respect to the center of the canal.
LR eccentricity index	Spinal cord centered (shift of 3% from the center of the canal) in the canal for the both postures.
Characteristics lengths	Significantly different in neck flexion than in neutral supine position (+2 mm, 13mm and 18mm for the anterior column (LAC), posterior column (LPC) and spinal cord, respectively).

Table 11. Summary table of the main results for each index.

Using MRI segmented 3D geometrical reconstructions, it was possible to investigate the morphological changes induced by the neck-flexion. Different geometrical metrics (CSA, eccentricity, indices, ratios) related to the SC and the CSS could be derived. The most noticeable results are summarized in [Table 11].

Cord and CSS kinematical description

Firstly, the low oscillating behavior of CSA_{CSS} and OR indices in [Fig.22] describes the geometry of dura mater at each spine level : nerve root funnel-shaped lateral extensions of sheaths leave the dura mater as spinal ganglions toward the peripheral nervous system [Polak-Krasna et al. 2019].

Secondly, the kinematic of the cord is not only induced by the flexion itself but also by the surrounding structures. The spinal cord being fixed to the superior anatomical structures (pons, *medulla*) on one hand and to the *filum terminale* on the other hand, it is subject to tensile forces applied in both cranio-caudal and antero-posterior directions when flexed. Here a “stretching” phenomenon occurs while the SC is pull through the anterior side of the spine column, as reflected by the $AP_{eccentricity}$ and $LR_{eccentricity}$ [Fig.23]. The nerve roots attached in the dural sheaths could be limiting the longitudinal motion and allow an elongation that follows the spinal motion. The SC lateral position stays globally centered (slight shift on the left : 2-3% from the center of the canal), in line with the literature [Fradet et al. 2014], and similar in neutral and in flexion. Indeed, both denticulate ligaments [Nightingale et al. 2002, Johnson et al. 1975] between the arachnoid (assumed to be stick to the dura mater) and the pia mater, and nerve roots leaving the SC dorsal and ventral side by pairs and exiting the CSS by the dural sheath, insure coronal stabilization of the SC.

Thirdly, the high reduction of CSA_{CSS} from C2 dens to C3 vertebra in flexion position compared to the neutral one appears to be induced by the high mobility of the upper cervical segment [Holmes et al. 1996]. After the C3 vertebra, the CSA_{SC} was globally steady while the CSA_{CSS} decreased. In addition,

the action of the yellow and posterior longitudinal ligaments inside the vertebral should be noticed [Kuwazawa et al. 2006] while explaining the CSS modification [Endo et al. 2014].

Toward cord and spine biomechanical description

The geometrical evolution described by the CR index was intrinsically linked to the mechanical properties of the spinal cord. Indeed, the decrease of the CR from C4 to C6 observed in flexion depicts a significant strain of the SC from 3% to 7%. Such results underline the “stretching” phenomenon previously mentioned. This is further confirmed by the 13% increase of the LSC in flexion, in line with literature [Bilston 1994, Bilston and Thibault 1997, Jha et al. 2018, Ceylan et al. 2012].

The “stretching” phenomenon results from the Poisson effect described as the amount of lateral contraction against the amount of axial elongation experienced by a material under the action of a force. The three OR, CP, and LSC metrics could overcome the current lack of mechanical characterization and could be used for biomechanical modeling validation. Such Poisson effect can induce some local stresses or damages in the structure near the zone where the cord is attached, namely nerve roots and denticulate ligaments [Frykholm et al. 1947].

The LAC and LPC values (respectively +2% and +12% in flexion) are also in line with literature [Jha et al. 2018, Bilston 1994]. The LSC metric in comparison to LAC and LPC ones shows that the SC follows the motion of the canal in freeing more space posteriorly in flexion ($-22\% < AP_{eccentricity} < 47\%$) than in neutral position ($-22\% < AP_{eccentricity} < 7\%$) after C2 vertebra. Validation and further use of finite element spine models require advanced knowledges as spinal cord deformation and length variations. Hence the data related to the location of the cord and its space distribution obtained in this study could provide a strong added value for model design. Altogether, our study provide the necessary measurements in a healthy adult population in physiologically conditions for such validation.

Clinical aspects

In this study, we presented nine morphological parameters were used to describe the postural modifications occurring in the canal. These parameters were chosen in relation to their use in a clinical research context. Indeed, transverse area criteria corresponding to our CSA_{SC} , CSA_{CSS} , CSA_{canal} , $\emptyset T_{SC}$, $\emptyset AP_{SC}$ and CR, are used for CSM description [Yuan et al. 2018, Stoner et al. 2019]. CSM, disc herniation, osteophytes can also cause reduction of the canal and an occupation ratio (sagittal diameters ratio of spinal cord over canal, or ratio of spinal cord over canal area corresponding to our OR index) could be useful to quantify the degree of compression [Pratali et al. 2019, Sun et al. 2019]. Moreover, additional parameters related to the location of the spinal cord in the canal ($AP_{eccentricity}$ and $LR_{eccentricity}$ indices) and the characteristic lengths (LSC, LAC, LPC) complete this physiological database of healthy subjects that could now be used to compare with injured or symptomatic subjects. This methodology and database open the perspective of more accurate clinical indices.

Limitations

The first limitation of our methodology is that the MR acquisitions were performed in supine position, which is not a position corresponding to the active phase of a day as working. A previous study showed no significant difference of the spinal cord length between erect and supine position [Kuwazawa et al. 2006]. However, with cervical lordosis changes, a slight difference between erect and supine position is expected for SC position in the CSS and eccentricity indices. Nonetheless, as the cerebrospinal fluid mechanical properties are similar to water properties [Schiffer et al.1999, Bloomfield et al. 1998] (incompressibility), the fluid limits the effect of gravity in supine position.

The second limitation is the ambiguous difference between displacements and elongation of the SC in the CSS, which will be confirmed in the future by refine MR acquisition of head neck at 7T in order to

enable a more precise localization of the nerve roots along the CSS, in complement to description already provided at 3T [Cadotte et al. 2015].

The last limitation of our methodological work is the small amount of subjects currently included and the lack of symptomatic subjects. Future investigations and multicentric studies could complete this work to turn it into normative database adapted to a clinical routine.

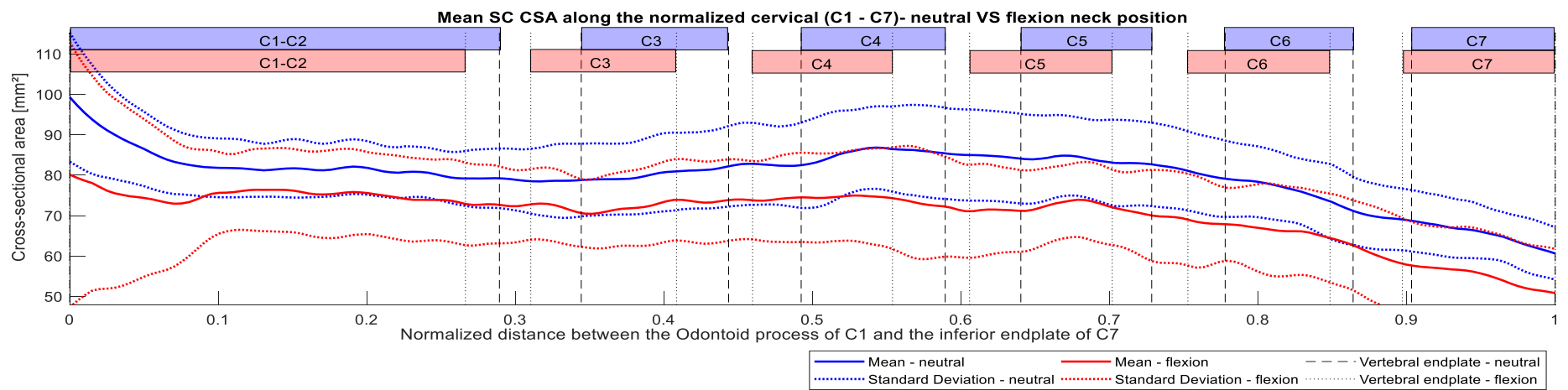
1.5. Conclusion

A new methodology allowing a detailed description of the vertebral canal morphology thanks to high resolution 3T-kMRI was developed. Reference values in healthy population allowing to characterize the CSS behavior with nine absolute metrics are provided. The mechanical roles of the different structures inside the vertebral canal in flexion were also confirmed through geometric measurements changes : 1) left-right stability (described by the LR eccentricity index) ensured by the denticulate ligaments and the nerve roots attached to the dural sheaths, 2) a Poisson effect of the SC was partially notified through its axial (AP diameter, OR, CR) and its longitudinal geometrical description (LSC). Such morphological data can be useful for geometrical finite element modeling of the canal (boundaries or initial conditions) or for an optimization of the mechanical properties by geometrical sensitivity analysis. Confronting this methodology and these results in a further study with a pathological cohort (CSM, post-traumatic population) is crucial to refine these clinical criteria in the medico-surgical management.

1.6.Appendices

Posture	Level	Cross-Sectional Area - SC [mm2]			Cross-Sectional Area - CSS [mm2]			Occupational Ratio (OR)			Eccentricity Indices - Anterior/Posterior (AP) [%]			Eccentricity Indices - Left/Right (LR) [%]			Eccentricity Indices - Compression Ratio (CR)		
		AVD VERT	MID VERT	MID IVD	AVD VERT	MID VERT	MID IVD	AVD VERT	MID VERT	MID IVD	AVD VERT	MID VERT	MID IVD	AVD VERT	MID VERT	MID IVD	AVD VERT	MID VERT	MID IVD
Neutral	C1C2	83.2±7.46	81.8±6.85	78.55±8.42	247.28±70.37	249.43±91.46	157.83±55.75	0.27±0.05	0.26±0.06	0.34±0.06	7.27±9.92	4.67±15.07	-28.47±16.68	4.92±7.96	-0.15±5.54	4.01±8.71	0.72±0.05	0.71±0.06	0.63±0.05
		(71.46/91.32)*	(71.62/89.88)*	(66.02/91.41)*	(164.11/398.1)*	(156.11/473.57)*	(107.84/297.66)*	(0.18/0.35)*	(0.15/0.36)*	(0.21/0.42)	(-10.25/20.78)*	(-24/24.53)	(-49.5/-1.13)	(-5.94/19.11)*	(-8.51/9.25)*	(-10.77/18.58)	(0.63/0.82)	(0.6/0.8)*	0.55/0.7)
Neutral	C3	80.22±9.54	79.73±9.11	82.26±10.15	131.9±33.67	133.43±30.97	118.67±33.16	0.38±0.04	0.38±0.04	0.42±0.06	-20.44±13.77	-19.53±14.95	-6.19±14.68	5.01±6.52	2.91±8.46	6.68±8.78	0.62±0.04	0.62±0.04	0.6±0.05
		(64.31/95.33)*	(63.72/93.83)*	(64.86/98.11)*	(91.18/205.42)	(96.61/195.41)	(84.76/193.89)*	(0.28/0.44)	(0.29/0.43)	(0.3/0.49)*	(-39/9.23)	(-32.89/20.77)	(-29.94/14.92)*	(-4.69/17.91)	(-9.25/19.65)	(-4.81/23.43)	(0.54/0.67)	(0.53/0.65)	0.52/0.68)
Neutral	C4	85.2±10.83	85.92±9.89	83.13±11.89	132.87±31.44	137.5±29.2	127.81±40.29	0.4±0.04	0.39±0.03	0.4±0.06	-6.99±16.99	-7.26±20.2	6.66±20.87	3.02±10.62	1.64±10.87	2.9±12.2	0.6±0.05	0.61±0.06	0.57±0.05
		(68.34/102.14)*	(70.7/100.74)*	(68.05/99.92)*	(99.82/198.25)	(105.16/193.52)	(81.78/207.08)*	(0.31/0.44)*	(0.31/0.42)	(0.32/0.51)*	(-37.58/16.84)*	(-43.71/17.87)*	(-28.44/34.33)*	(-13.5/24.34)	(-15.51/22.15)	(-14.54/19.8)	(0.5/0.66)*	(0.5/0.69)*	0.46/0.64)*
Neutral	C5	83.75±9.98	84.24±9.45	79.76±9.84	142.32±33.28	147.76±30.18	129.3±36.48	0.38±0.04	0.37±0.03	0.39±0.05	-3.56±17.92	-5.3±17.64	-10.01±19.63	1.64±8.79	2.5±11.05	1.04±14.62	0.58±0.05	0.58±0.06	0.57±0.05
		(71.93/98.73)*	(73.82/98.66)*	(66.72/94.56)*	(105.32/203.7)*	(108.62/206.87)*	(81.49/195.56)*	(0.3/0.42)*	(0.31/0.4)*	(0.31/0.46)*	(-29.47/21.63)*	(-31.63/17.15)*	(-38.2/16.21)*	(-10.57/18.92)	(-11.28/23.11)	(-20.91/23)	(0.48/0.63)*	(0.46/0.65)*	0.49/0.63)*
Neutral	C6	76.17±8.57	76.35±8.32	69.91±7.63	141.92±30.82	147.02±30.32	132.89±38.69	0.35±0.04	0.35±0.03	0.35±0.05	-16.27±18.66	-13.63±16.38	-21.22±23.35	2.95±10.82	2.74±10.96	6.32±15.28	0.57±0.04	0.57±0.04	0.56±0.05
		(65.1/88.25)*	(64.69/89.35)*	(60.3/80.45)*	(106.79/206.64)*	(114.26/213.4)*	(84.99/199.08)*	(0.29/0.39)*	(0.29/0.38)*	(0.28/0.44)*	(-51.95/4.25)*	(-38.6/3.86)*	(-53.18/26.03)*	17.59/19.47)	(-18.04/20.83)	(-10.96/34.75)	(0.49/0.61)*	(0.5/0.62)*	0.45/0.6)*
Neutral	C7	65.16±6.71	65.88±6.67	146.6±32.78	148.47±30.67	148.47±30.67	0.31±0.04	0.31±0.03	0.31±0.04	-23.01±21.82	(-23.33±21.84)	(-44.37/31.53)*	(-49.96/30.57)*	3.14±12.05	2.28±13.35	0.6±0.04	0.6±0.04	0.6±0.04	0.6±0.04
		(56.21/74.7)*	(56.19/76.15)*	(103.87/213.71)*	(109.67/209.99)*	(109.67/209.99)*	(0.25/0.38)*	(0.26/0.36)*	(0.26/0.36)*	(-44.37/31.53)*	(-49.96/30.57)*	(-44.37/31.53)*	(-49.96/30.57)*	10.44/31.16)	(-13.94/27.36)	(-13.94/27.36)	(0.51/0.63)	(0.52/0.66)	(0.52/0.66)
Flexion	C1C2	75.5±10.51	76.67±10.25	71.8±8.83	215.46±64.37	208.65±73.66	152.6±52.21	0.28±0.05	0.28±0.05	0.33±0.06	10.42±20.08	5.12±19.76	-23.8±23.73	8.2±9.88	8.61±11.57	2.59±7.11	0.68±0.06	0.68±0.04	0.63±0.06
		(63.17/93.22)*	(63.92/92.03)*	(59.58/85.17)*	(140.69/351.29)*	(130.57/394.59)*	(99.14/269.91)*	(0.19/0.35)*	(0.17/0.36)*	(0.22/0.41)	(-21.01/40.63)*	(-19.36/31.8)	(-60.5/12.77)	(-1.72/30.81)*	(-2.97/30.66)*	(-9.78/14.45)	(0.54/0.74)	(0.61/0.75)*	0.56/0.73)
Flexion	C3	71.61±9.14	70.75±9.44	72.28±10.1	133.6±35.89	133.38±38.12	131.29±32.63	0.36±0.06	0.36±0.06	0.36±0.06	-7.86±24.5	-9.75±20.69	18.42±25.36	0.9±9.14	2.96±9.25	2.72±14.94	0.62±0.04	0.62±0.04	0.59±0.06
		(56.48/82.39)*	(56.05/81.98)*	(55.53/83.27)*	(94.75/192.99)	(92.48/219.92)	(95.12/186.04)*	(0.24/0.44)	(0.21/0.45)	(0.24/0.44)*	(-48.97/26.37)	(-37.29/25.93)	(-24.29/63.84)*	7.87/24.63)	(-5.16/25.5)	(-19.27/32.55)	(0.58/0.68)	(0.56/0.68)	0.47/0.72)
Flexion	C4	74.02±11.46	74.03±12.1	72.65±12.73	142.67±32.09	142.91±30.85	149.26±38.44	0.35±0.07	0.35±0.07	0.34±0.08	27.12±22.34	24.53±20.77	44.7±21.39	4.1±10.48	4.77±12.22	3.22±13.56	0.57±0.05	0.57±0.06	0.52±0.05
		(49.76/84.29)*	(48.35/86.21)*	(47.11/83.23)*	(101.21/202.18)	(99.48/202.03)	(89.44/200.56)*	(0.22/0.44)*	(0.22/0.46)	(0.19/0.47)*	(-22.78/55.21)	(-23.44/52.22)*	(3.8/82.09)*	6.83/31)	(-9.49/34.42)	(-18.59/29.29)	(0.48/0.65)*	(0.47/0.67)*	0.44/0.6)*
Flexion	C5	72.81±9.47	72.97±8.9	70.18±10.05	163.95±35.95	166.03±33.87	166.91±36.67	0.31±0.05	0.31±0.05	0.3±0.04	40.68±20.41	39.02±16.71	41.84±25.88	3.9±9.51	4.11±8.3	6.93±16.66	0.53±0.05	0.53±0.05	0.52±0.06
		(55.22/81.5)*	(58.61/83.33)*	(51.92/83.89)*	(112.6/223.36)*	(109.13/218.74)*	(107.72/227.6)*	(0.22/0.41)*	(0.23/0.43)*	(0.25/0.4)*	(-9.04/61.23)*	(3.29/58.23)*	(-26.86/65.44)*	(-6.35/18.87)	(-5.14/18.56)	(-7.86/49.85)	(0.44/0.61)*	(0.45/0.62)*	0.41/0.62)*
Flexion	C6	67.24±10.31	67.35±10.36	60.86±10.81	181.04±34.25	181.87±34.9	175.28±36.37	0.28±0.04	0.27±0.04	0.26±0.05	35.77±24.29	(-28.79/55.98)*	(-28.01/52.79)*	3.64±8.66	5.39±8.88	-0.09±12.24	0.53±0.05	0.52±0.05	0.52±0.06
		(48.83/79.04)*	(48.84/79.56)*	(42.06/73.15)*	(116.39/233.92)*	(121.32/238.34)*	(115.31/217.69)*	(0.22/0.34)*	(0.22/0.33)*	(0.19/0.33)*	27.85±29.27	26.95±30.1	(-37.91/75.26)*	(-12.58/17)	(-10.39/18.99)	(-26.49/15.44)	(0.46/0.61)*	(0.44/0.61)*	0.41/0.64)*
Flexion	C7	54.99±10.54	55.54±10.52	185.41±37.42	187.96±40.73	187.96±40.73	0.23±0.05	0.23±0.05	0.23±0.05	27.85±29.27	26.95±30.1	(-21.65/57.9)*	(-26.32/54.33)*	2.11±9.26	1.98±11.13	0.57±0.05	0.58±0.04	0.58±0.04	0.58±0.04
		(39.35/69.53)*	(40.19/71.33)*	(121.2/245.82)*	(117.55/245.38)*	(117.55/245.38)*	(0.15/0.3)*	(0.16/0.3)*	(0.16/0.3)*	(-21.65/57.9)*	(-26.32/54.33)*	(-21.65/57.9)*	(-26.32/54.33)*	(-13.17/14.24)	(-15.84/19.58)	(0.48/0.68)	(0.49/0.66)	(0.49/0.66)	
Canal lengths [mm]		Neutral		Flexion															
LAC		118.01±5.21	120.29±7.61	(110.81/127.25)*															
LPC		107.6±5.57	120.35±6.38	(99.74/127.25)*															
LSC		141.56±6.77	159.35±11.48	(129.1/151.7)*															

Supplemental Digital Content 3 - Table 12. Statistical summary [Mean ± std (min/max)] of each measured parameter (SC and CSS CSA, OR, AP/LR eccentricity and CR) for both position (neutral in white, flexion in gray). For each one, three sub-values are given, corresponding to a spatial vertebral average of measures (AVD VERT, with C1 and C2 vertebrae merged : the C2 dens passing through the ring of C1 vertebra), value picked up at the middle of the vertebra in the middle sagittal plan (MID VERT) and value picked up at the middle of the intervertebral disc in the middle sagittal plan (MID IVD) , considering the disc below the mentioned vertebral level). The LAC, LPC and LSC parameters correspond to the lengths of the anterior canal, posterior canal and the spinal cord, along the whole cervical segment, respectively. *indicates p<0.05 (Paired samples Wilcoxon test).



Supplemental Digital Content 4 - Figure 25. Spinal cord cross-sectional area (SC CSA) mean along the cervical. The mean value of the neutral (blue continuous curve) and flexion (red continuous curve) cases are indicated with their standard deviations (dotted curves). Mean normalized positions of the vertebral endplates are indicated as well standard deviations are not indicated on the figure for a sake of clarity

Supplemental Digital Content 1

Description of absolute metrics

The cord transverse and antero-posterior diameters ($\emptyset T_{SC}$, $\emptyset AP_{SC}$ respectively), as well as distance between the SC and the canal in anterior (A), posterior (P), right (R) and left (L) directions were computed from the most eccentrical points in AP (4) and LR (5) directions. Compression (CR – (2)) and occupation (OR – (3)) ratios, as well as eccentricity indices were then derived from these metrics⁷ (see (2) to (5)).

$$CSA_{CSS} = CSA_{canal} - CSA_{SC} \quad (1)$$

$$CR = \frac{\emptyset AP_{SC}}{\emptyset T_{SC}} \quad (2)$$

$$OR = \frac{CSA_{SC}}{CSA_{canal}} \quad (3)$$

$$AP_{eccentricity} = \left(\frac{P-A}{P+A} \right) * 100 \quad (4)$$

$$LR_{eccentricity} = \left(\frac{L-R}{L+R} \right) * 100 \quad (5)$$

An $AP_{eccentricity} > 0$ (<0) indicates that the SC is anteriorly (posteriorly) positioned. Similarly, a $LR_{eccentricity} > 0$ (<0) indicates that the SC is located on the right (left) side of the canal. Three specific lengths were also computed in both positions^{20, 21}: the length of the cervical spinal cord (LSC), length of the cervical spinal anterior column (LAC) and length of the cervical spinal posterior column (LPC). They were respectively delimited by the caudal side of the pons to C7 inferior endplate, the C2 dens process to C7 inferior endplate, and the top of C1 posterior arch to C7 inferior endplate. Three 3D splines passing through the points positioned manually by an operator to define each curvature were computed to get more accurate lengths.

Supplemental Digital Content 2

Description of summary table : absolute and sub metrics

Three sub-metric values were calculated at each vertebral level : spatial averaged value (over the whole vertebra) (AVD VERT), spatial value for a cross-sectional plane mid-vertebra (MID-VERT) and spatial value for cross-sectional plane located at the middle of the intervertebral disc (MID-IVD) (vertebral levels defined as the “cervical vertebral landmarks” projected onto the centerline). For both postures (neutral and flexion), all values are reported as averaged value with standard deviation by vertebra and disc on all subjects. Mean vertebral level positions across all subjects were computed from : the position of each vertebra according to the “Reference landmarks” and “Cervical vertebral points” positions projected to the centerline.

2. Degenerative cervical myelopathy morphology : effects of decompressive surgery by laminectomy - New elements for patient follow-up

Patrice Sudres (1,5), Guillaume Frébourg (1,5), , Pierre-Jean Arnoux (1,5), Guillaume Baucher (4,5), Pierre-Hugues Roche(4,5), Virginie Callot (2,3,5), Morgane Evin (1,5)

1. Laboratoire de Biomécanique Appliquée, UMRT24 AMU/IFSTTAR, Marseille, France
2. Aix-Marseille Université, CNRS, CRMBM, Marseille, France
3. APHM, Hôpital Universitaire Timone, CEMEREM, Marseille, France
4. Neurosurgery Department, APHM, Hopital Nord, Marseille, France
5. iLab-Spine – Laboratoire International en Imagerie et Biomécanique du Rachis, Marseille, France & Montréal, Canada

In this second subchapter, an improved methodology of the morphometrical measurement was proposed and a preliminary application to three clinical cases was performed.

Abbreviations

DCM: degenerative cervical myelopathy
SCI: spinal cord injury
IVD: inter-vertebral disc
IVJ: inter-vertebral joint
SC: spinal cord
CSF: cerebrospinal fluid
OR: occupational ratio
CR: compression ratio
QAS: quasi-automatic segmentation
SMS: semi-automatic segmentation
CSS: cervical subarachnoid space
SPL: spondylosis
CSM: cervical spondylosis myelopathy
ROI: region of interest
GVF: ground vector field
CSA: cross-sectional area
HSD: Hausdorff Distance
MSD: mean surface distance

Keywords

degenerative cervical myelopathy, morphometry, MRI, 3D visualization, cervical canal

2.1.Introduction

Degenerative cervical myelopathy (DCM) is a chronic degenerative disease occurring in the cervical vertebral canal. The rapid or slow degenerative process of stenosis development may lead to a compression of the spinal cord with a risk of damaging the neuronal pathway. It remains challenging to establish a complete and non-equivocal diagnosis before surgery. This disease is a common cause of SCI

for elderly population aged over 55 years. [Northover et al. \[2012\]](#) showed a correlation between the age and the number of affected cervical levels and between age and the degree of antero-posterior stenosis. Moreover, women are affected earlier than men (57.0 y against 66.5 y) but with less affected levels (2 against 3) and a degree of stenosis inferior in the antero-posterior direction. Abnormalities in the cervical canal were detected in 14%, and disk herniation in 28% of people under 40 years. These percentage doubled for people over 40 years. Spatially, the C5/C6 IVD is the most common impacted level, followed by the C6/C7 and the C4/C5 levels. Then, single-level DCM represents 92.5 % of cases while multi-level disease represents 80.5% of cases [[Northover et al. 2012](#)].

All previously described difficulties inherent to DCM diagnosis lead to a problematic delay in diagnosis [[Hilton et al. 2018](#)]. A mean time delay in diagnosis of DCM was estimated at 2.2 ± 2.3 years [[Behrbalk et al. 2013](#)] while an older study highlighted an average time delay of 6.3 years with a decrease up to the 4th Nurick grade (assistance for walking) [[Sadasivan et al. 1993](#)].

Local 2D analysis is a gold standard for the scientific and clinical community [[Table 13](#)]. Briefly, most used indices in literature were: the cross-sectional area (perpendicular to the centerline of the canal) of the canal, the SC and the CSF. The occupational ratio (OR) is derived from the ratio of these areas. Diameters of the canal, the CSF and the SC are also largely used in sagittal or axial planes. The compression ratio (CR) is derived from the large and small axial diameters of the canal or of the spinal cord are commonly used to quantify the level of flatness. Another common index used to quantify the canal stenosis is the Torg-Pavlov ratio (the sagittal spinal canal diameter divided by the sagittal vertebral body diameter). In most of the studies in [Table 13](#), an operator has to manually perform the different measurements in a discretize way, i.e. plotting the segments or delineating the areas. The measurements are done at mid-vertebra as reference and mid-intervertebral discs because of structural changes appear at the discs levels called spondylosis or hernia and at vertebral plates such as osteophytes. To the best of our knowledge, only one study developed a 3D analysis of the spinal cord based on semi-manual 3D reconstruction of the cervical spinal cord. The 3D analysis allows to compute new metrics such as volume correlated to the cross-sectional area and the cord length. [[Smith et al. 2013](#)].

It remains difficult to establish pathological criteria to detect a potential narrowing of the canal due to the inter-individual variability as well as the posture-dependent diagnosis. Indeed, some narrowed canal can be detected in neutral, in flexion or in extension neck position in terms of morphometrical changes but also neuro-senso motor scores.

The aim of the study is to propose a quasi-automatic morphometric tool which provide detailed description and visualization of the cervical canal based on clinical research and routine indices to measure the effect of a decompressive surgery on patients with degenerative cervical myelopathy.

Authors/Year	Journal	Population studied	Anatomical parts	Measured parameters	Measurement tool	Type of analysis
Kawakami <i>et al.</i> 2002	Journal of Spinal Disorders and Techniques	113 patients with CSM	spinal cord C2 - T1	Cobb angle, convex index	MRI	2D
Zaaroor <i>et al.</i> 2006	Minimally Invasive Neurosurgery	42 patients	Spinal cord, subarachnoid space, dural sac C1 - L2	Sagittal + Transversal dimensions	0.5T MRI	2D
Miura <i>et al.</i> 2009	Journal of Spinal Disorders and Techniques	20 patients with CSM + 20 healthy control subjects	C3 - C7	the segmental forward-backward movement of the spinal cord, JOA score	1.5T MRI	2D
Morishita <i>et al.</i> 2009	European Spine Journal	295 symptomatic patients	Spinal cord and canal C3 - C7	Angle, sagittal diameters, compression	0.6T MRI	2D
Smith <i>et al.</i> 2013	Spine	56 preoperative subjects	C2 - C7	Spinal cord (CSA, volume, length) and spine dimensions (Cobb angle, SVA, C2-C7 plumbline)	MRI + radiography	2D+3D
Endo <i>et al.</i> 2014	Asian Spine Journal	62 asymptomatic subjects	spinal cord and canal C1 - C7	Length of cervical cord, anterior and posterior cervical canal lengths	MRI	2D
Kar <i>et al.</i> 2017	Journal of Clinical and Diagnostic Research	71 symptomatic subjects : neck pain, radiating, paresthesia neck + upper limb	Spinal cord and canal C3 - C7	Sagittal diameter of spinal cord and canal, Torg ratio	1.5T MRI	2D
Wolf <i>et al.</i> 2018	Spinal cord	12 gender-matched healthy control + 12 patients with cervical spondylotic myelopathy	Spinal cord and canal (C2 and C5)	CSF and SC displacement	3T MRI	2D
Kong <i>et al.</i> 2018	Therapeutics and Clinical Risk Management	317 patients with CSM	Spinal cord C4-C7 and spine C2 - C7	Anteroposterior diameter of canal, narrowed ratio, Cobb angle		2D
Tykocki <i>et al.</i> 2018	Acta Neurochirurgica	63 patients (radiculopathy, myelopathy or myeloradiculopathy)	Spinal cord and canal C3 - C7	Length of cervical cord, spinal cord and canal (area, angles)	1.5T MRI	2D
Tykocki <i>et al.</i> 2018	World Neurosurgery	55 patients with CSM	Spinal cord, CSF (C3 - C7)	Spinal cord area, CSF area, CSF ratio)	1.5T MRI	2D
Pratali <i>et al.</i> 2019	Spine	18 patients with CSM	Spinal cord and canal	spinal canal diameter and the spinal cord width, the anterior and posterior length of the spinal cord	1.5T MRI	2D

Table 13. Review table of morphological studies of DCM patients. CSM : cervical spondylosis myelopathy.

Patient	State of patient	Gender	Size [m]	Age [y]	Masse [kg]	BMI	Symptoms	Follow-up time	Surgery solution	
1	Pre-operative	Male	1.79	37	86	26.84	Tetra pyramidal syndrome ; Positive Hoffman		Decompressive surgery (Laminectomy)	
	Post-operative 1		1.79	38	86	26.84				+ 6 months
	Post-operative 2		1.79	38	83	25.90				+ 5.5 months
2	Pre-operative	Male	1.69	72	80	28.01	Sensorimotor symptomatology of 4 limbs ; Positive Hoffman ; Myelopathy		Decompressive surgery (Laminectomy)	
	Post-operative 1		1.69	72	80	28.01				+ 3 months
	Post-operative 2		1.69	73	80	28.01				+ 8.5 months
3	Pre-operative	Female	1.60	69	63	24.61	Narrowed cervical canal (C4-C6)		Decompressive surgery (Laminectomy) C6-C7 canal recalibration supplement on restenosis at a level not initially affected	
	Post-operative 1		1.60	70	66	25.78				+ 4 months
	Post-operative 2		1.60	70	65	25.39				+ 8 months

Table 14. Demographic characteristics of suspicious DCM population (N=3)

2.2. Material and methods

2.2.1. MRI acquisition

The cohort composed of three European patients with three follow-up cases by patient [Table 14]. They were scanned using a 3T MR system (Siemens Healthineers, Erlangen, France). The pathological study sample here consisted of a retrospective cohort of subjects who had been referred to the "Hôpital Timone and Hôpital Nord, Neurosurgery service (Marseille, France)" between April 2017 and December 2019 with clinical signs [Table 15].

Each subject was equipped with head, neck and spine coils. Images were acquired using a sagittal 3D T₂-SPACE sequence (Sampling Perfection with Application optimized Contrasts using different flip angle Evolution) with the following parameters: voxel size (1x1x1 mm³), field-of-view (256x256 mm²), echo time (TE : 124 ms), repetition time (TR : 1500 ms), total acquisition time (6 min). The MR protocol was approved by the institutional ethics committee and all subjects signed the informed consents. The control cohort was chosen excluding history, presence of cervical pathologies or deformations.

2.2.2. Clinical scores

For each patient, clinical scores were computed which have been set by a neurosurgeon. The types of scores are:

- the overall stenosis score (OSS), sum of the single stenosis scores, from 0 to 3, for each discal level from C2-C3 to C6-C7.
- modified Japanese Orthopaedic Association (mJOA) score

In addition, the type of compression had established for each discal level according to the classification proposed by Lévy et al. [2020], Fig. 26.

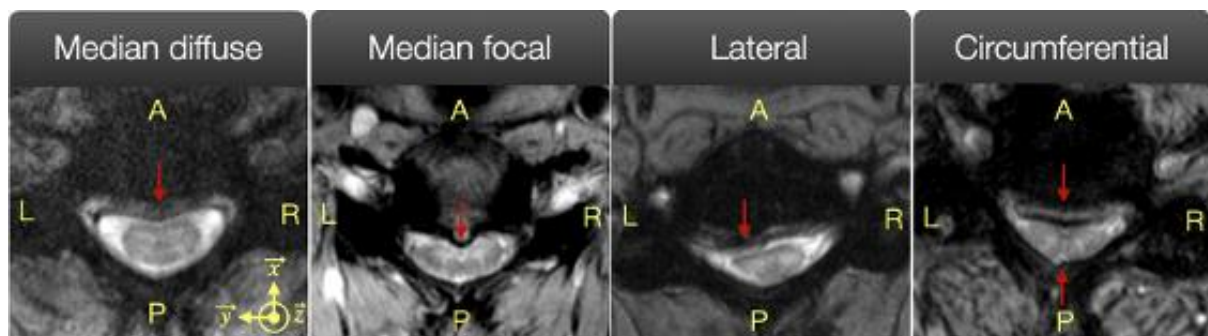


Figure 26. Classification of main compression types observed in DCM [Lévy et al. 2020].

Patient	Compression type	Onset	Radiologic		mJOA(/17)		
			DCM type	OSS [0-15]	M0	Pass1	Pass2
1	C4-C5 : left lateral ; C6 : right lateral ; C7 : left lateral	C5- C6- Chronic	SPL	9 (moderate)	14	15	15/16
2	C4-C5 : circumferential ; C5-C6 : left lateral ; C7 : median diffuse	C6- Chronic	SPL	7 (moderate)	13		13
3	C3-C4 : median diffuse; C4-C5 : circumferential ; C5-C6 : circumferential ; C6-C7 : circumferential	Chronic	SPL	12 (severe)	13	14	14

Table 15. Clinical scores and compression type classification of each patient. SPL: Spondylosis

2.2.3. Segmentation and anatomical landmarks positioning

The global methodology was based on a previous study [Sudres et al. 2020] with specific improvements. Briefly, the SC was first segmented in 3D by a quasi-automatic deep-learning approach using the Spinal Cord Toolbox (“deepseg” function; SCT ver 4.1.1) [De Leener et al. 2017] with manual corrections done on ITK SNAP ver 3.8.0 [Yushkevich et al. 2006]. The outer canal border, assumed as the dura mater, was then segmented by a quasi-automatic approach from an in-house Matlab (R2018a version, Matlab®MathWorks,1984 – Image Processing Toolbox) pipeline [Fig.27].

The quasi-automatic segmentation (QAS) of the cervical spinal canal (CSS) and the landmarks positioning through the entire MR volume, composed of n MR images ($I_i, i \in [1, n]$) were performed in six steps using an active contour approach [Xu and Prince 1998]:

- **Step 1.** Cervical canal cropping by setting up a rectangle on the mid-sagittal MRI slice with the maximum and minimum height given by two morphometric landmarks: the odontoid process of C1 and C7 inferior endplate [Fig.27-2-A]. Then the smallest rectangular ROI containing the cervical canal is set to extract the mask of the canal contour by a threshold from the axial view of I_1 [Fig.27-2-C].
- **Step 2.** Two reference and ten complementary anatomical landmarks are positioned on the same mid-sagittal MRI slice [Fig.27-2-B]. The two reference landmarks (odontoid and posterior corner of the inferior C7 endplate) were used to delimit the ROI once the 3D reconstruction done for further post-processing. The complementary landmarks were positioned on the posterior corners of each vertebra from the odontoid to C7 inferior endplate and used to identify the vertebrae location with respect to morphometrical measurements.
- **Step 3.** To obtain a refined segmentation of the canal contour of I_1 , the parametric active contour GVF snake [Xu and Prince 1997] is initialized as the contour of the mask found in step 1, fixing $\alpha=0.09$, $\beta=1$ and $\mu=0.2$, where α and β specify the flexibility and smoothness of the contour and μ is a regularization parameter. The snake moves under the influence of two main constraints. The internal constraint tries to keep the smoothness of the contour whereas the external one attracts contour to edges of the object to be segmented.
- **Step 4.** A pre-processing of I_{i+1} is performed, the brightest pixels inside the contour of I_i is retained to threshold I_{i+1} . The centroid of the contour of I_i is retained and the anteroposterior axis of symmetry of I_{i+1} is determined in order to align the contour_i along left-right axis on I_{i+1} . Maximum similarity between the ROI of I_i and the image I_{i+1} along the axis found is determined to set the contour_i along right-left axis on I_{i+1} to determine contour_{i+1} . Gaussian filter with standard deviation of $\sigma=1$ is applied to homogenize pixel values around the ROI [Fig.27-2-D].
- **Step 5.** Steps 2 and 3 are repeated ($n - 1$) times.
- **Step 6.** The point cloud of SC and CSS MRI-based segmentations were interpolated by 3D splines and surfaces are meshed by Delaunay triangulation to provide a 3D meshed surface canal [Fig.27-3].

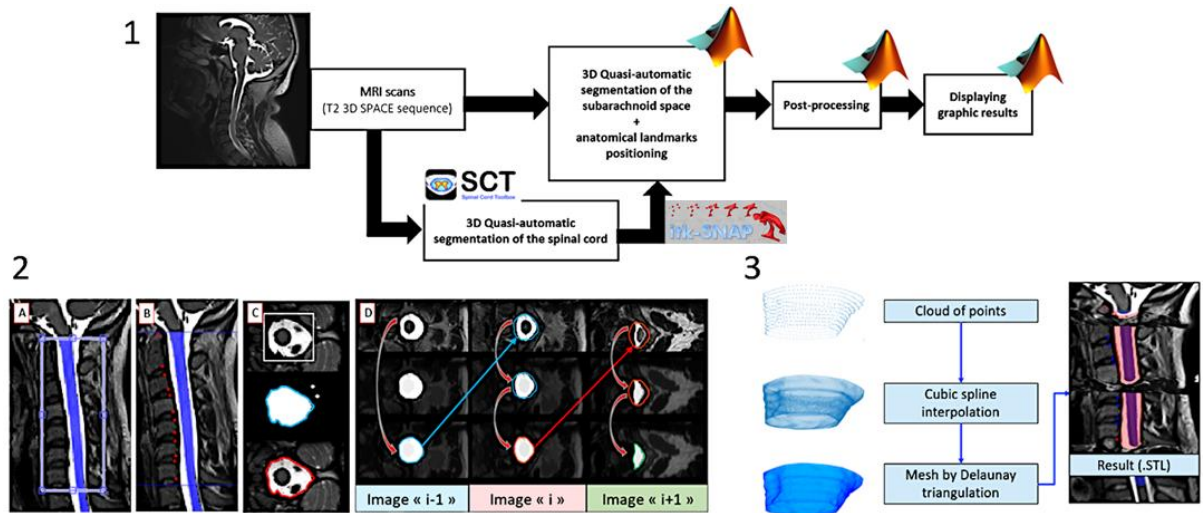


Figure 27. Global schema of the 3D reconstruction methodology. 2-Active contouring methodology, A-ROI selection by the operator on the mid-sagittal view (rectangle) with the spinal cord segmentation from SCT (blue), B-anatomical landmarks (red) positioning, C-ROI selection by the operator on the first chosen axial image, contour detection and thresholding and final contour, D-active contour iterations. 3-Contour interpolation along the canal and mesh reconstruction with a surface mesh of the CSS.

2.2.4. Evaluation of the segmentation

To evaluate the performance of the CSS segmentation method, segmentations derived from the GVF QAS approach were compared to reference segmentations obtained with the semi-automatic segmentation (SMS) method [Sudres and al. 2020] using two overlap-based and two distance-based metrics. Dice (1), Jaccard (2), Mean Surface Distance (3) and Hausdorff Distance (4) were thus calculated for each axial slice of the MR volume:

$$Dice = 2 \times \frac{QAS \cap SMS}{QAS + SMS} \quad (1)$$

$$Jaccard \text{ index} = \frac{AS \cap MS}{AS + MS - (AS \cap MS)} \quad (2)$$

$$MSD = \frac{1}{2} (d_{mean}^{MS \rightarrow AS} + d_{mean}^{AS \rightarrow MS}) \quad (3)$$

$$HSD = \max(\max(d_{SMS \rightarrow QAS}), \max(d_{QAS \rightarrow SMS})) \quad (4)$$

Where d is the Euclidian distance between QAS and SMS.

2.2.5. Data preparation and metrics computation

The post-processing steps was based on a previous study [Sudres et al. 2020]. The boundaries of the SC and the canal were interpolated using 3D splines as the intersection of the surface meshes and meshed planes orthogonal to the centerline. Then, 15 metrics were computed : $\frac{SC_radius}{Canal_radius}$ which was plotted in 3D map representing the patient's canal. The red regions (close to 1) means that the CSF radius tends to zero (meaning the fluid is absent) compared to the blue regions meaning that the fluid is present. Others metrics which are AP and LR eccentricity indices, compression ratio, occupational ration and cross-sectional area of the canal and the SC called global CSA were defined in [Fradet et al. 2014]. New local metrics were also proposed. Each cross-sectional slice considered along the centerline were virtually divided in 8 zones in which the CSA was computed for the canal.

All the calculation were performed on Dell Latitude 7480, Intel® Core™ i7-7600U CPU – 2.80GHz/2.90GHz, RAM : 8Go.

2.2.6. Statistical analysis

Statistical comparisons between pre-operative, post-operative 1 and post-operative 2 measurements were not performed due to the limited size of population.

2.3. Results

The methodology (segmentation, reconstruction and post-processing) is performed less than 30 min.

Morphological parameters were computed from anatomical markers and centerline coordinates in less than 5 min. The QAS segmentation of the CSS were evaluated on a healthy population and compared to the semi-manual segmentation with a mean dice value of 0.935 ± 0.007 and a mean HSD value of 1.690 ± 0.157 mm. The QAS segmentations of DCM population were evaluated between a semi-manual segmentation performed by an operator. A mean dice value of 0.934 ± 0.008 and a mean HSD value of 1.305 mm were measured [Table 16].

Similarity indices	Healthy population (n=11)	DCM population (n=9)
Dice	0.935 ± 0.007	0.934 ± 0.008
Jaccard	0.878 ± 0.012	0.877 ± 0.014
HSD (mm)	1.690 ± 0.308	1.305 ± 0.157
MSD (mm)	1.073 ± 0.036	1.033 ± 0.022

Table 16. Similarity indices evaluating the quality of the QAS segmentation of the healthy population (neutral neck position) [Sudres et al. 2020] and the DCM population.

2.3.1. Segmentation evaluation

The measurement of the similarity indices by patient were depicted in [Supplementary data](#).

Patient 1. A decrease of the Dice and Jaccard indices were observed at the C4/C5 IVJ (0.82 and 0.7 respectively) for the pre-operative MR images whereas an increase of the Hausdorff distance (HD) and of the MSD (2 and 1.2 mm respectively) were measured. The same observations were done for the post-operative 1 and 2 MR images at the C6/C7 IVJ (Dice: 0.89 and 0.91, Jaccard: 0.89, HSD: 2.8 mm and 1.8, MSD: 1.2 and 1.08 mm).

Patient 2. A decrease of the Dice and Jaccard indices (0.87 and 0.78) at the C4/C5 IVJ and an increase of the HSD and MSD indices (1.5 and 1.08 mm) at the C4/C5 IVJ and at the C5/C6 IVJ (1.5 and 1.08 mm) were measured for the pre-operative case. A slight increase of the mean HD and mean MSD indices associated with high variation of the SD at the C2/C3 IVJ and C5/C6 IVJ whereas a slight decrease of the Dice and Jaccard indices (0.93 and 0.87, respectively) were measured at the C4/C5 IVJ, C4, C6 vertebral levels for the post-operative 1 case. A slight decrease of the Dice and Jaccard indices and an increase of the HD and MSD were measured at the C6/C7 IVJ (Dice: 0.91, Jaccard: 0.83, HSD: 1.8 mm, MSD: 1.08 mm) for the post-operative 2 case.

Patient 3. A decrease of the Dice and Jaccard indices were measured at the C4/C5 and C5/C6 IVJ (Dice : 0.92 and 0.89, Jaccard: 0.86 and 0.8) whereas an increase of the HD and MSD were observed at the C4/C5 IVJ (1.4 and 1.05 mm) for the pre-operative case.

2.3.2. Patient 1

Common clinical research morphometrical metrics.

The CR of the pre-operative case is inferior (flatter) to the CR of the post-operative 2 case at the first half of C3 vertebra (0.5 and 0.6, respectively) and the second half of C4 vertebra (0.4 and 0.55, respectively). The AP index of the pre-operative case is superior (more antero-posteriorly central) to the AP value of the post-operative 2 case at the second half of C4 vertebra (-5% against -25% respectively) and inferior (less anterior) at the C6/C7 IVJ (41% against 62% respectively). The LR index of the pre-operative case is inferior (more on the right of the center) to the LR index of the post-operative 2 case at the C4/C5 IVJ (-12% against -2%) and C5/C6 IVJ (-29% against -4.5%). This index for the pre-operative case is superior (more on the left) at the C6 vertebra and inferior (close to the center) at the C7 cervical compared to the post-operative 2 case one (C6: 40% against 2%; C7: 4% against 43%). The OR for the pre-operative case is superior to the post-operative 2 at the first half of C5 vertebra and the superior endplate of C5/C6 IVJ (0.5 against 0.35 respectively between the cases). Finally, the global SC CSA of the pre-operative case is superior to this index for the post-operative 1 and 2 at the end of C5 vertebra (53 mm², 22 mm², 40 mm² respectively) [Fig. 29].

New local morphometrical metrics.

The CSA of the Z2 pre-operative case is superior to the CSA of the post-operative 1,2 cases at the C5 vertebral level (51 mm² and 28 mm² respectively) and at the C7 vertebra level (43 mm² and 30 mm²). The CSA of the Z7 pre-operative case is inferior to the CSA of the post-operative 1,2 cases at the C5 vertebral level (18 mm² and 34 mm² respectively) as well as for the CSA of Z8 at the C3 vertebral level (14 mm² and 21 mm² respectively) and at the C5 vertebral level (7 mm² and 13 mm² respectively) [Fig. 30].

3D visualization and volume quantification.

The volume from the superior C3 endplate to the superior C7 endplate of the SC, the CSF and the canal increase of -6%, 3% and 0% respectively between the pre-operative and the post-operative 2 cases. The SC over canal radius ratio is close to 1 (in red) on the dorsal left side from the C3 vertebral level to the C6 vertebra for the pre-operative case. This index is close to 1 with spatial attenuations compared to the pre-operative case 2 on the dorsal sides from the C4 vertebra the C5 vertebra for the post-operative 1 and 2 cases [Fig. 28].

2.3.3. Patient 2

Common clinical research morphometrical metrics.

The CR of the pre-operative case is inferior (flatter) to the CR of the post-operative 2 case between the C2/C3 IVJ and the end of C5/C6 IVJ with a peak at the C4/C5 IVJ (0.56 against 0.85, respectively). The AP index of the pre-operative case is superior (more posterior) to the AP value of the post-operative 2 case between the end of C2 vertebra and the C5 vertebra (approximately +25%) and two peaks occur at C5/C6 IVJ (61% against -10% respectively) and at the C6/C7 IVJ (46% against 15% respectively). Two peaks were observed for the LR index of the pre-operative case compared to the index of the post-operative 2 case at the C5 vertebra (-31% against 9% respectively) and the C5/C6 IVJ (57% against 11% respectively). The OR for the pre-operative case increase between the C3/C4 IVJ and the C6 vertebra compared to the post-operative 2, with two peaks at the C4/C5 IVJ (0.56 against 0.28 respectively) and the C5/C6 IVJ (0.53 against 0.28 respectively). Finally, two peaks of the global canal CSA were observed for the pre-operative case compared to the post-operative 2 case at C4/C5 (81 mm² against 201 mm², respectively) and at the C5/C6 IVJ (90 mm² against 180 mm², respectively) [Fig. 32].

New local morphometrical metrics.

The CSA of Z1 and Z8 of the pre-operative case were strongly inferior to those of the post-operative 1 and 2 cases between the end of C2 vertebra and C6 vertebra (Z1 maximum peak: 7 mm² and 36 mm²

respectively at 0.5 for abscissa ; Z8 maximum peak: 6.8 mm² and 30 mm² respectively at 0.6 for abscissa) [Fig. 33].

3D visualization and volume quantification.

The volume from the superior C3 endplate to the superior C7 endplate of the SC, the CSF and the canal increase of -5%, 43% and 25% respectively between the pre-operative and the post-operative 2 cases. The SC over canal radius ratio is close to 1 (in red) on the dorsal left side of the C2/C3, C5/C6 and C6/C7 IVJ as well as the C4 vertebra for the pre-operative case. This index is close to 1 on the lateral sides from the C2/C3 IVJ to the C7 vertebra for the post-operative 1 and 2 cases with an attenuation for this latter [Fig. 31].

2.3.4. Patient 3

Common clinical research morphometrical metrics.

The CR of the pre-operative case is close to 0.4 (flatter than the post-operative cases) between the C4 vertebra and the beginning of the C7 vertebra. Four peaks were observed for the AP index between the pre-operative and the post-operative 2 cases at the beginning of the C4 vertebra (44.6% against 4.6% respectively), at the end of the C4/C5 IVJ (41.9% against -3.3% respectively), at the C5/C6 IVJ (54.1% against 9.1% respectively) and the C6/C7 IVJ (51.3% against 9.1%). A peak was observed for the LR index of the pre-operative case compared to the index of the post-operative 2 case at the beginning of C6 vertebra (40% against 1%). The OR for the pre-operative case is superior to those of the post-operative 2 between the C3/C4 IVJ and the C7 vertebra (a gap between +0.1 and +0.2 compared to the post-operative 2 case). Finally, a decrease of the global SC CSA up to 60mm² (around 0.75 of abscissa) and the global canal CSA up to 21 mm² (0.72 of abscissa) of the pre-operative case compared to those of the post-operative 2 were measured [Fig. 35].

New local morphometrical metrics.

The CSA of Z1 and Z8 of the pre-operative case were strongly inferior to those of the post-operative 1 and 2 cases between the end of C3 vertebra and the end of C7 vertebra (Z1 maximum peak: 7.5 mm² and 36.2 mm² respectively at 0.8 for abscissa ; Z8 maximum peak: 4.9 mm² and 36.0 mm² respectively at 0.8 for abscissa) [Fig. 36].

3D visualization and volume quantification.

The volume from the superior C3 endplate to the superior C7 endplate of the SC, the CSF and the canal increase of 13%, 77% and 54% respectively between the pre-operative and the post-operative 2 cases. The SC over canal radius ratio is close to 1 (in red) on the dorsal left side of the C4/C5 IVJ and the C6 vertebra whereas it is the C5/C6 IVJ and the C6/C7 IVJ for the ventral side of the pre-operative case. This index is close to 1 on the left lateral side (ventral view) from the C3/C4 IVJ to the C5/C6 IVJ for the post-operative 1 and 2 cases with an attenuation for this latter [Fig. 34].

Patient 1

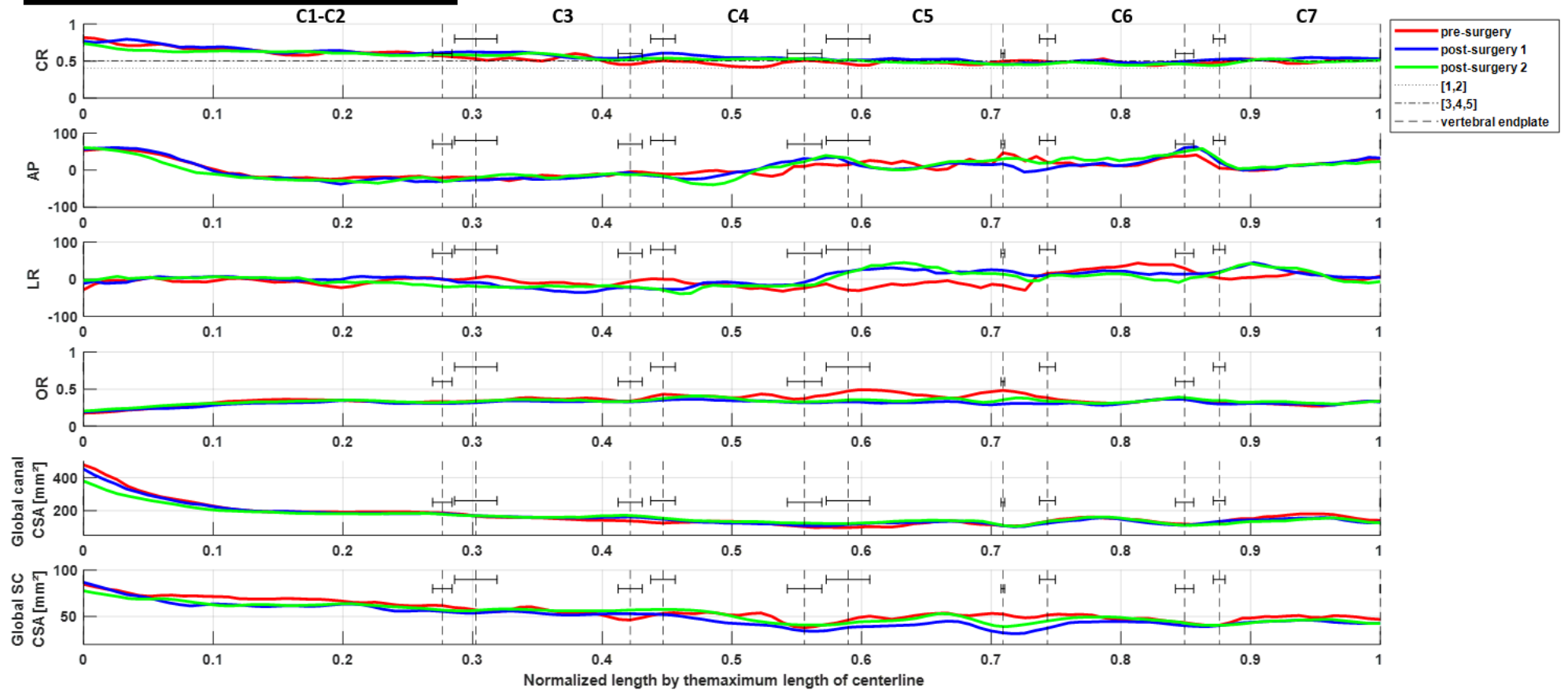


Figure 28. **Patient 1.** Quantification of morphometrics metrics along the normalized centerline of the SC. **CR**: Compression Ratio, **AP**: Antero-Posterior eccentricity, **LR** : Left-Right eccentricity, **OR** : Occupational Ratio, **Global canal CSA** : canal area of each slice, **Global SC CSA** : spinal cord area. All the indices were computed along the normalized centerline. On each subplot, the pre-surgery case (in red), the post-surgery 1 (in blue) and the post-surgery 2 (in green). The vertical dashed lines represent the mean location of the vertebral endplates with the standard deviations associated (error bars). On the CR subplot, the horizontal dotted and dash-dot lines represent pathological threshold identified by the literature: [1] Kovalova et al. 2015 (0.4), [2] Kadanka et al. 2017 (0.4), [3] Abudouaini et al. 2020 (0.5), [4] Chen et al. 2016 (0.5), [5] Nagai et al. 2018 (0.5).

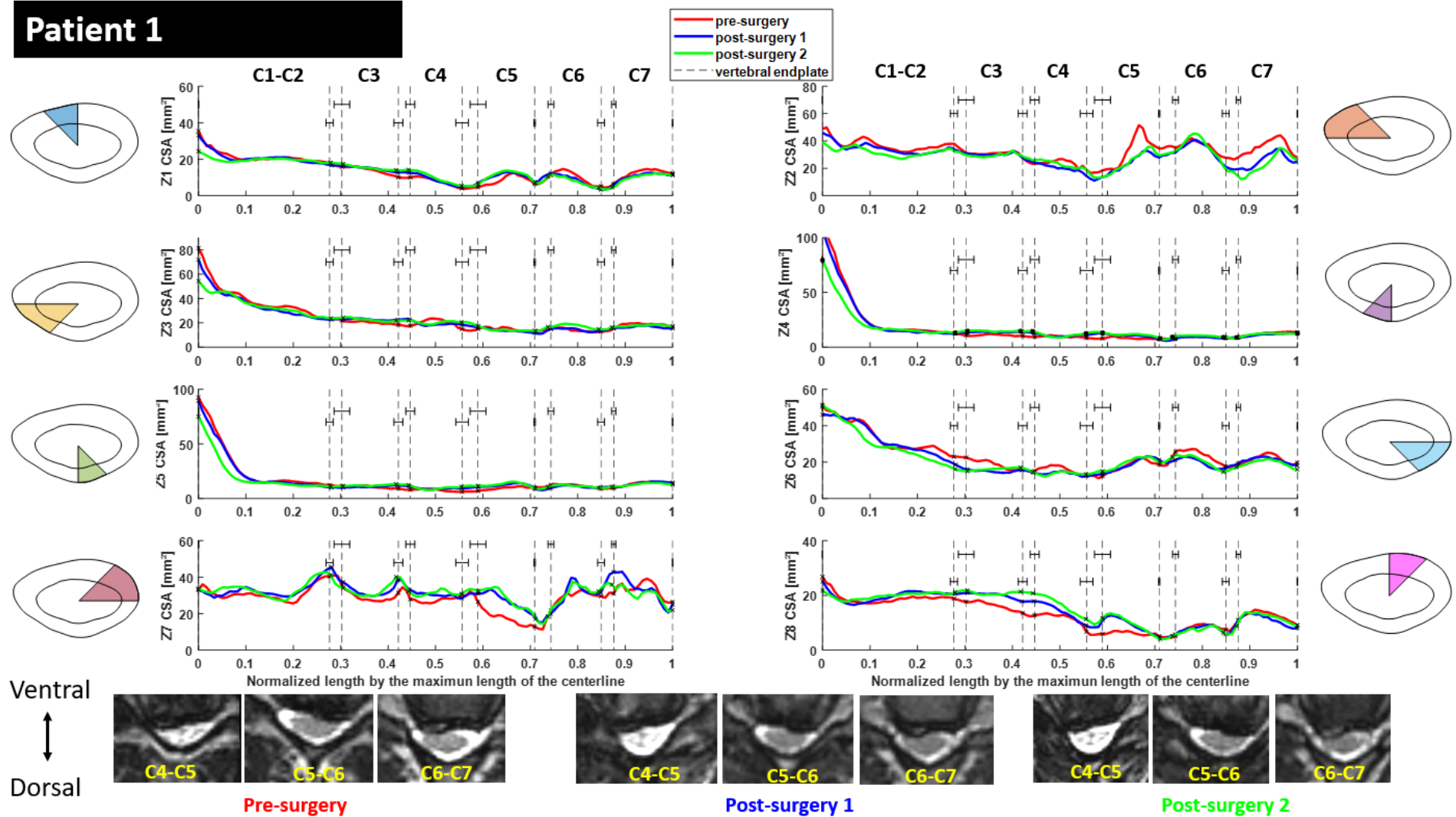


Figure 29. **Patient 1.** Quantification of a **local canal area** by slice along the normalized spinal cord centerline. Each local zone Z_i is represented by a schema next to the associated subplot. The axial slices where the canal is the most narrowed are depicted under the subplot. C_x-C_y represents the intervertebral level. The vertical dashed lines represent the mean location of the vertebral endplates with the standard deviations associated (error bars).

Patient 1

Pre-surgery
 SC volume = 4181 mm³
 CSF volume = 7166 mm³
 Canal volume = 11347 mm³

Post-surgery 1
 SC volume = 3828 mm³
 CSF volume = 7996 mm³
 Canal volume = 11824 mm³

Post-surgery 2
 SC volume = 3917 mm³
 CSF volume = 7414 mm³
 Canal volume = 11331 mm³

Volume gains
 SC (1->2) = -8 %
 SC (1->3) = -6 %
 SC (2->3) = 2 %
 CSF (1->2) = 12 %
 CSF (1->3) = 3 %
 CSF (2->3) = -7 %
 Canal (1->2) = 4 %
 Canal (1->3) = 0 %
 Canal (2->3) = -4 %

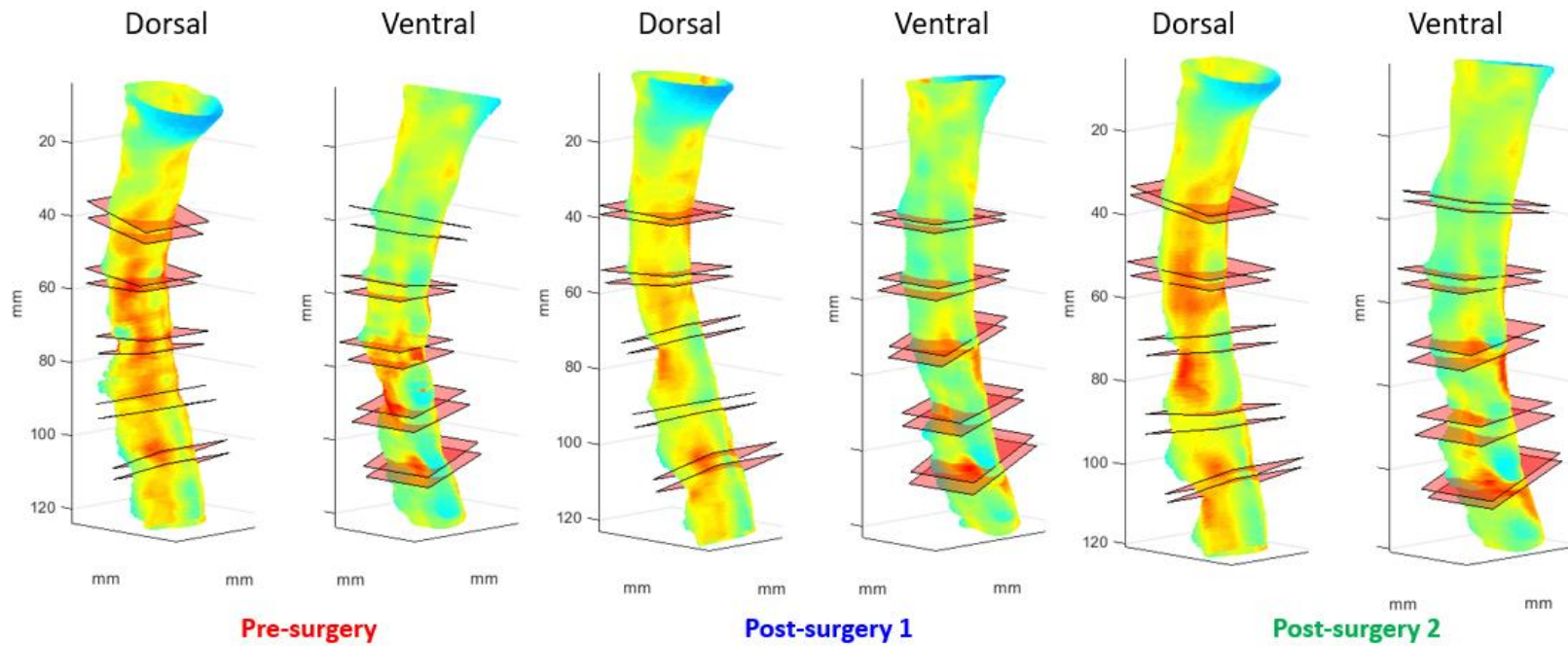
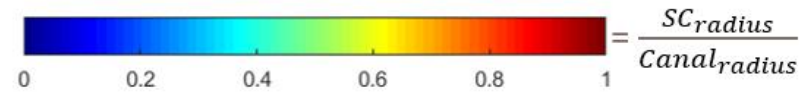


Figure 30. **Patient 1.** 3D cartography of the SC radius over canal radius ratio computed for each point of slice along the spinal cord centerline. The textbox in upper left describes the volume of each anatomical part (CS, CSF and canal) in pre-surgery phase (in red), in post-surgery phase 1 (in blue) and in post-surgery phase 2 (in green). In the left, the volume gains (in black) before each phase were computed in percentage. For each phase, the 3D cartography is displayed in the right lateral dorsal orientation (Dorsal) and in the left lateral ventral orientation (Ventral).

Patient 2

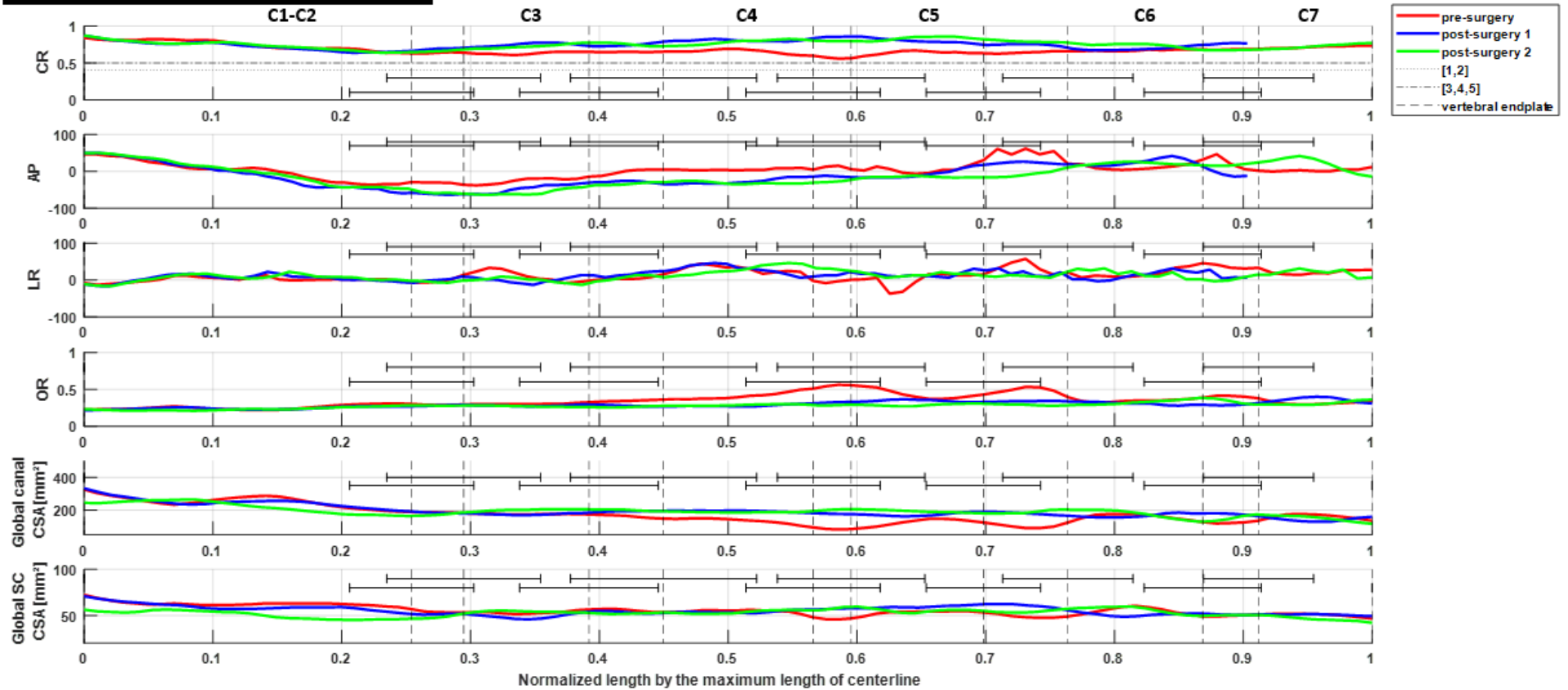


Figure 31. **Patient 2.** Quantification of morphometrics metrics along the normalized centerline of the SC. **CR**: Compression Ratio, **AP**: Antero-Posterior eccentricity, **LR** : Left-Right eccentricity, **OR** : Occupational Ratio, **Global canal CSA** : canal area of each slice, **Global SC CSA** : spinal cord area. All the indices were computed along the normalized centerline. On each subplot, the pre-surgery case (in red), the post-surgery 1 (in blue) and the post-surgery 2 (in green). The vertical dashed lines represent the mean location of the vertebral endplates with the standard deviations associated (error bars). On the CR subplot, the horizontal dotted and dash-dot lines represent pathological threshold identified by the literature : [1]: Kovalova et al. 2015, [2]: Kadanka et al. 2017, [3]: Abudouaini et al. 2020, [4]: Chen et al. 2016, [5]: Nagai et al. 2018.

Patient 2

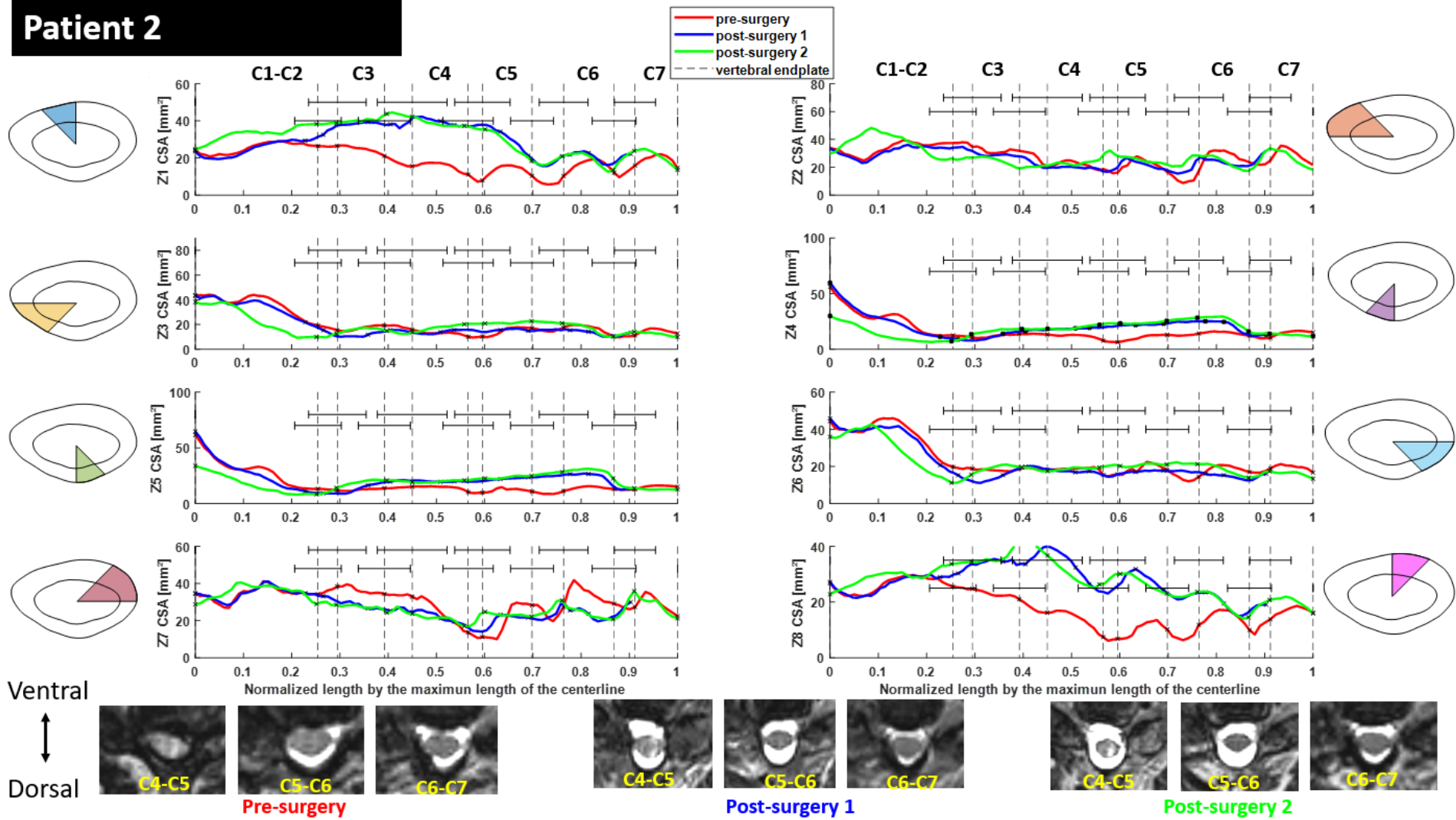


Figure 32. **Patient 2.** Quantification of a **local canal area** by slice along the normalized spinal cord centerline. Each local zone Z_i is represented by a schema next to the associated subplot. The axial slices where the canal is the most narrowed are depicted under the subplot. C_x-C_y represents the intervertebral level. The vertical dashed lines represent the mean location of the vertebral endplates with the standard deviations associated (error bars).

Patient 2

Pre-surgery
 SC volume = 3408 mm³
 CSF volume = 5568 mm³
 Canal volume = 8976 mm³

Post-surgery 1
 SC volume = 3181 mm³
 CSF volume = 7311 mm³
 Canal volume = 10491 mm³

Post-surgery 2
 SC volume = 3247 mm³
 CSF volume = 7954 mm³
 Canal volume = 11201 mm³

Volume gains
 SC (1->2) = -7 %
 SC (1->3) = -5 %
 SC (2->3) = 2 %
 CSF (1->2) = 31 %
 CSF (1->3) = 43 %
 CSF (2->3) = 9 %
 Canal (1->2) = 17 %
 Canal (1->3) = 25 %
 Canal (2->3) = 7 %

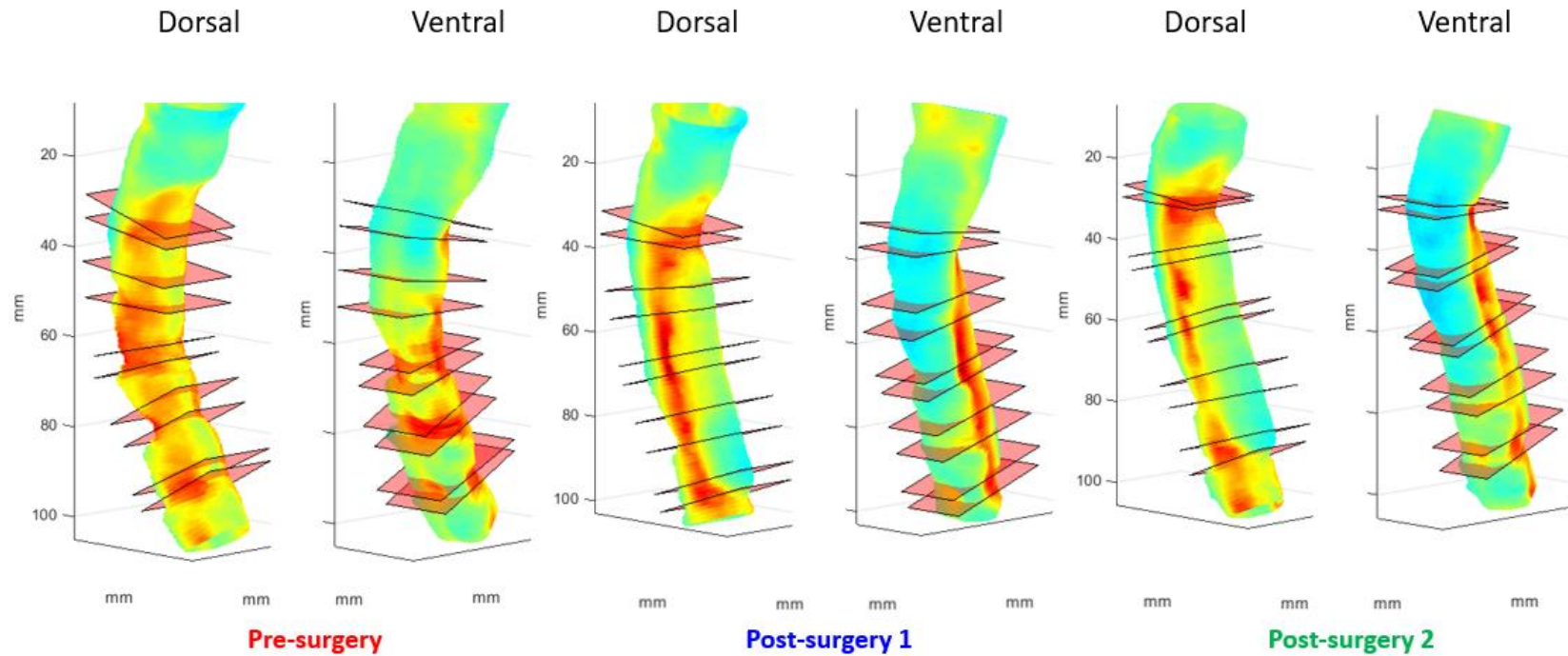
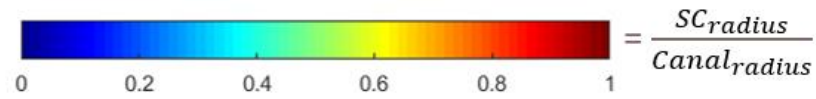


Figure 33. **Patient 2.** 3D cartography of the SC radius over canal radius ratio computed for each point of slice along the spinal cord centerline. The textbox in upper left describes the volume (from the C3 superior endplate to the C7 inferior endplate) of each anatomical part (CS, CSF and canal) in pre-surgery phase (in red), in post-surgery phase 1 (in blue) and in post-surgery phase 2 (in green). In the left, the volume gains (in black) before each phase were computed in percentage. For each phase, the 3D cartography is displayed in the right lateral dorsal orientation (Dorsal) and in the left lateral ventral orientation (Ventral).

Patient 3

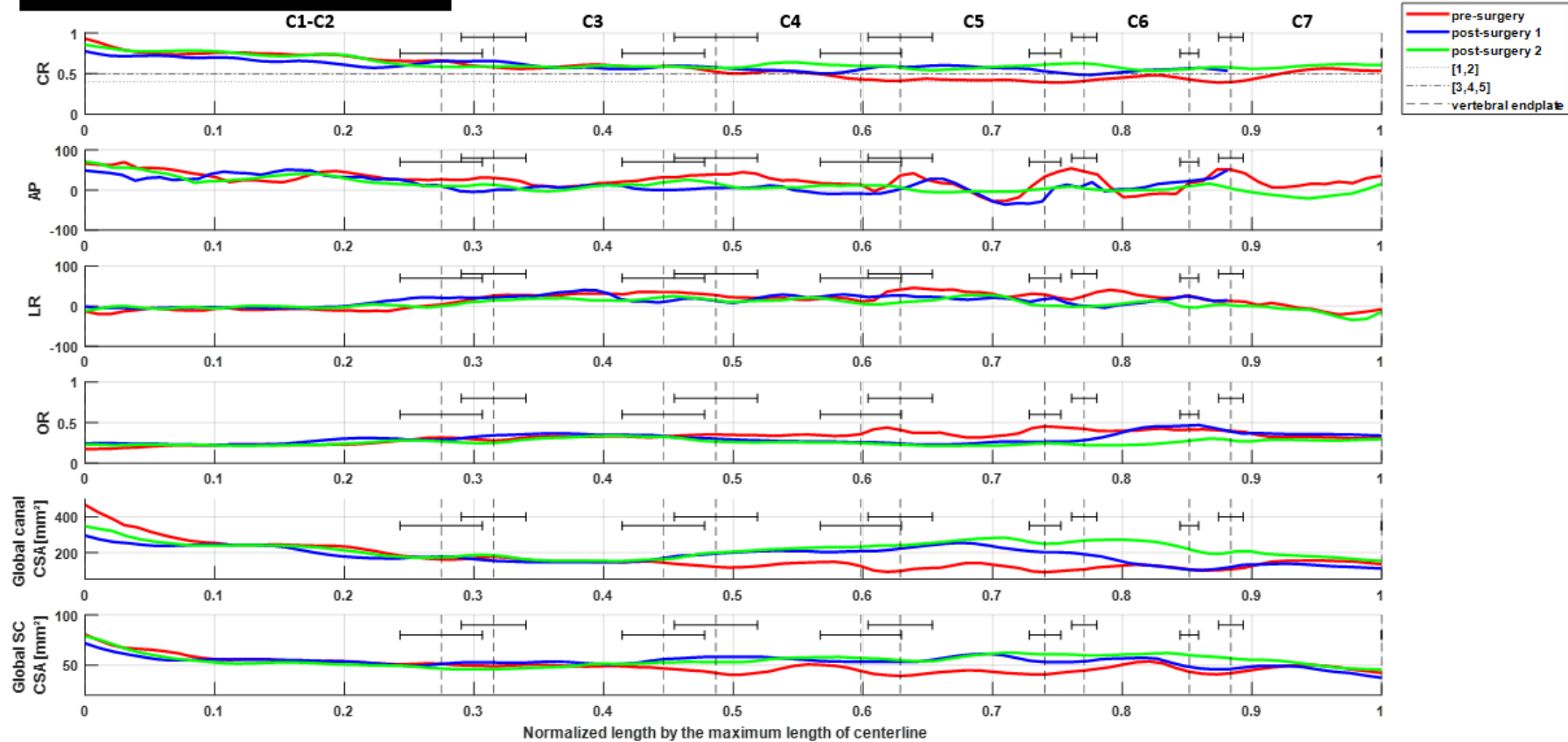


Figure 34. **Patient 3.** Quantification of morphometric metrics along the normalized centerline of the SC. **CR**: Compression Ratio, **AP**: Antero-Posterior eccentricity, **LR**: Left-Right eccentricity, **OR**: Occupational Ratio, **Global canal CSA**: canal area of each slice, **Global SC CSA**: spinal cord area. All the indices were computed along the normalized centerline. On each subplot, the pre-surgery case (in red), the post-surgery 1 (in blue) and the post-surgery 2 (in green). The vertical dashed lines represent the mean location of the vertebral endplates with the standard deviations associated (error bars). On the CR subplot, the horizontal dotted and dash-dot lines represent pathological threshold identified by the literature: [1]: Kovalova et al. 2015, [2]: Kadanka et al. 2017, [3]: Abudouaini et al. 2020, [4]: Chen et al. 2016, [5]: Nagai et al. 2018.

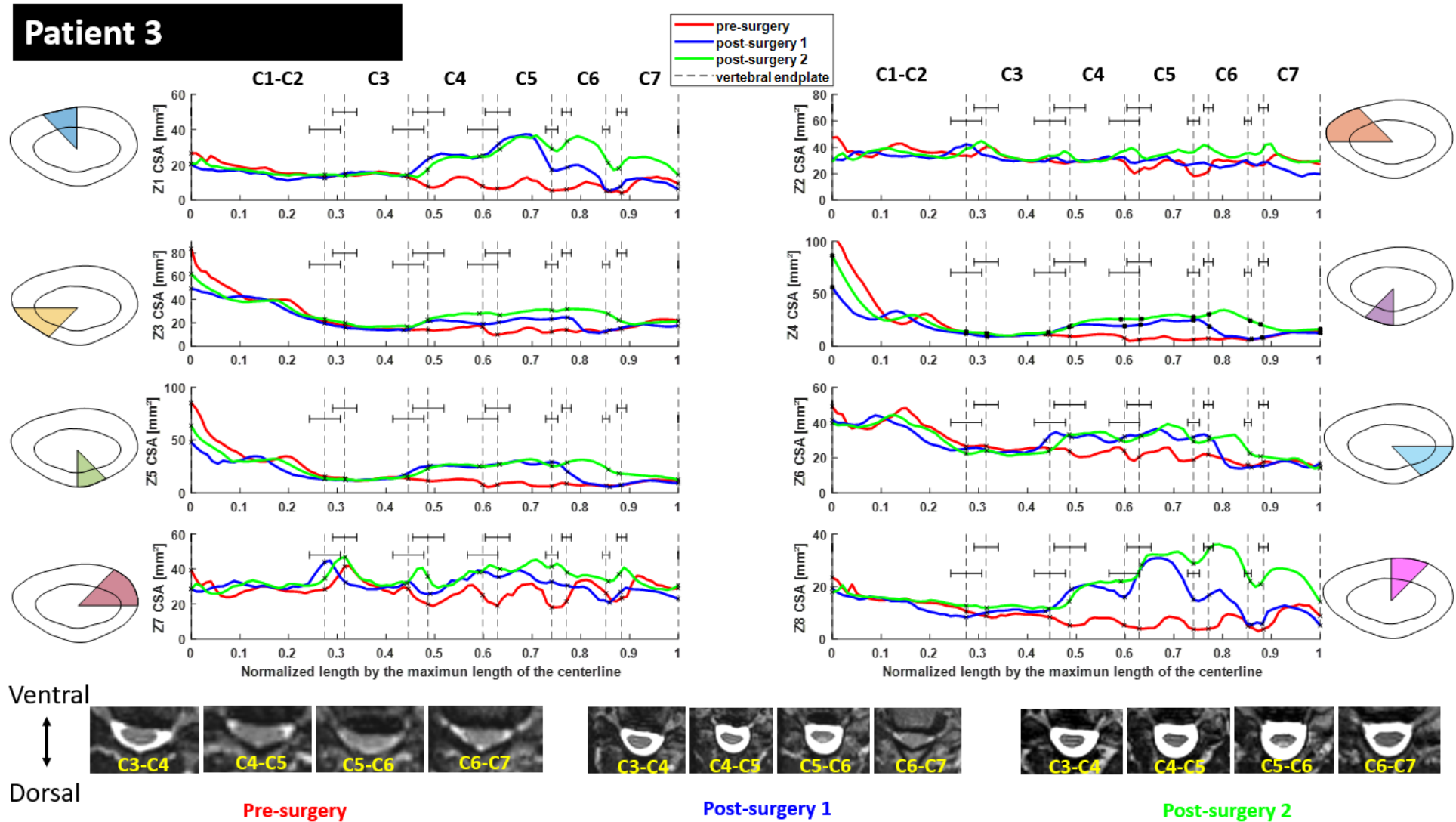


Figure 35. **Patient 3.** Quantification of a **local canal area** by slice along the normalized spinal cord centerline. Each local zone Z_i is represented by a schema next to the associated subplot. The axial slices where the canal is the most narrowed are depicted under the subplot. C_x-C_y represents the intervertebral level. The vertical dashed lines represent the mean location of the vertebral endplates with the standard deviations associated (error bars)

Patient 3

Pre-surgery

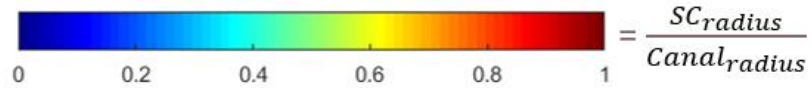
SC volume = 3129 mm³
 CSF volume = 5738 mm³
 Canal volume = 8867 mm³

Post-surgery 1

SC volume = 3256 mm³
 CSF volume = 7347 mm³
 Canal volume = 10603 mm³

Post-surgery 2

SC volume = 3547 mm³
 CSF volume = 10133 mm³
 Canal volume = 13680 mm³



Volume gains
 SC (1->2) = 4 %
 SC (1->3) = 13 %
 SC (2->3) = 9 %
 CSF (1->2) = 28 %
 CSF (1->3) = 77 %
 CSF (2->3) = 38 %
 Canal (1->2) = 20 %
 Canal (1->3) = 54 %
 Canal (2->3) = 29 %

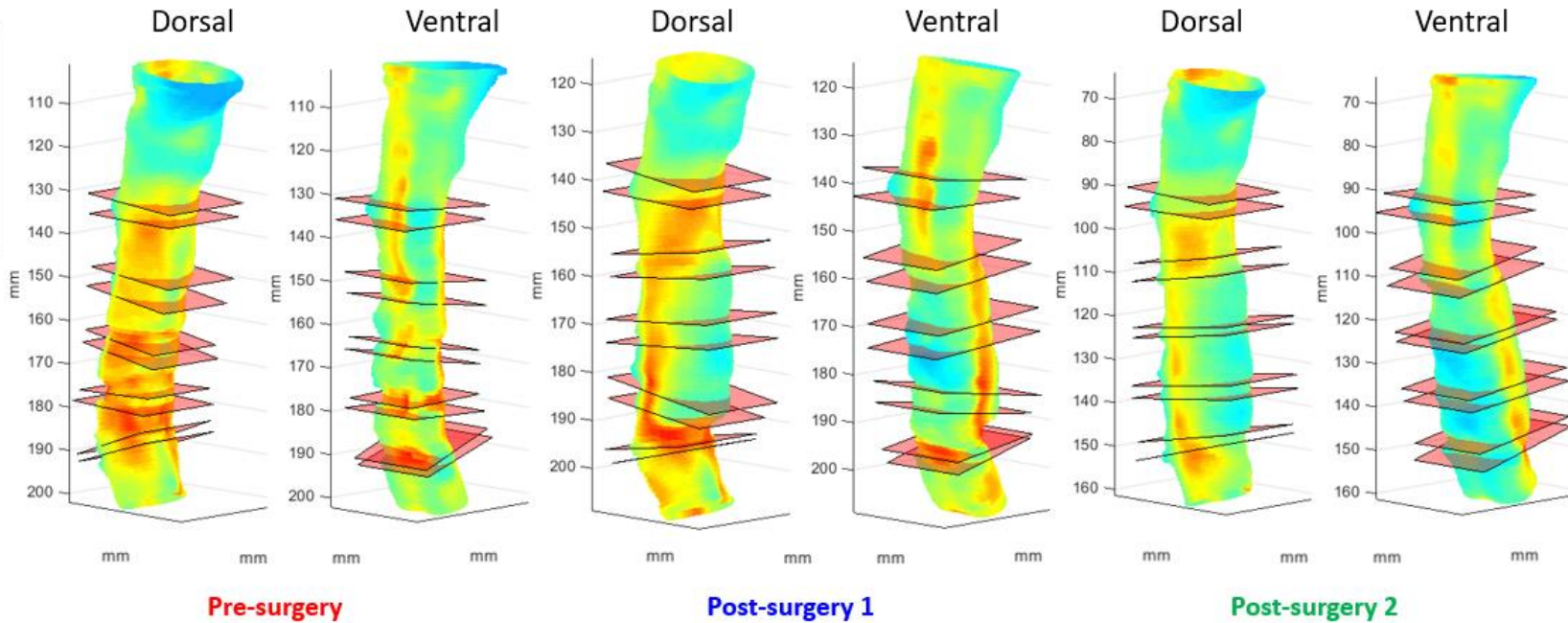


Figure 36. **Patient 3.** 3D cartography of the SC radius over canal radius ratio computed for each point of slice along the spinal cord centerline. The textbox in upper left describes the volume of each anatomical part (CS, CSF and canal) in pre-surgery phase (in red), in post-surgery phase 1 (in blue) and in post-surgery phase 2 (in green). In the left, the volume gains (in black) before each phase were computed in percentage. For each phase, the 3D cartography is displayed in the right lateral dorsal orientation (Dorsal) and in the left lateral ventral orientation (Ventral).

2.4. Discussion

The segmentation evaluation of the healthy population by the dice index was superior and in coherence with the literature : 0.70 ± 0.05 [Koh et al. 2010], 0.85 ± 0.03 [Chen et al. 2013] and 0.91 ± 0.02 [De Leener et al. 2015].

Using segmented MRI 3D geometrical reconstructions, it was possible to describe the morphological changes induced by decompressive surgical procedures for myelopathy cases. Common clinical research indices (CR, AP and LR eccentricities, OR and global CSA of the spinal cord and canal) as well as new local morphological indices divided in axial zones (from 1 to 8) and a 3D visualization of the spinal cord radius over canal radius ratio were provided in this study for each case (pre-operative, post-operative 1 and post-operative 2) of each subject (from 1 to 3). Thresholds of 0.4 and 0.5 for the compression ratio (CR) (plotted on the Fig. 3, 6 and 9) were considered as pathological thresholds in case of cervical stenosis. The SC volumes provided in the Fig. 2, 5 and 8 were in coherence with Smith et al. [2013] using a similar methodology of computation.

Patient1.

This patient suffered from chronic spondylosis with longitudinal spatial canal narrowing at the C4/C5, C5/C6 and C6/C7 IVJ while the canal compression was located on the left, the right and the left lateral sides in the axial spatiality. The spinal cord is flatter at these spinal levels [axial MRI – Fig. 30] and the CR ratio of the three cases were measured below 0.5 and below 0.4 for the pre-operative cases. This index allows to show that the spinal cord is also flatter around the more impacted spinal level (from C3 to C7 vertebra). The OR index shows that decompressive surgery (post-surgery 1 and 2) of the dorsal side (consisting in the C3, C4 and C5 spinous processes resection) release more the canal CSA and more specifically the CSF CSA than the SC CSA [Fig. 29]. The observation was supported by the increase of volume gain of CSF (1->2: 31%; 1->3: 43%) and canal (1->2: 17%; 1->3: 25%) compared to the SC volume (1->2: -7%; 1->3: -5%) [Fig. 28]. The negative volume gains of the spinal cord can be explained by an inter-session variation of the subject during the MRI acquisition. It is probable that the neck position changed having a displacement effect on the spinal cord. Thus, the segment of spinal cord on each case seems to not be exactly the same leading to negative volume variation not physiological. However the spinal cord volume variation should be found closed to 0% between the cases.

The spatial axial compression were quantified with the local canal area zones [Fig. 30]. The surgery released the more canal space at the C5 vertebra level on the left and right ventral side where the spinal cord moved posteriorly [LR index – Fig. 29]. This local apparent difference has to be taken with caution because assessment of the segmentation in this specific area shows a decrease of the HD and MSD (Supplementary data - Fig. 37). Nevertheless, the oscillations in the canal zones Z1, Z2, Z7 and Z8 corresponding to the axial compressions were identified at the corresponding IVJ [Fig. 30].

Clinical aspects

The 3D visualization of the SC over canal radius ratio (a local form of the OR) [Fig. 29] shows more variations on the dorsal side than the ventral side even if the ventral compression observed on the axial MRI slices [Fig. 30] were identified.

Patient2.

The thresholds on CR index seem to visually identify the compressions at the C4/C5, C5/C6 and the C6/C7 IVJ. Indeed, the index values of the three cases are above the thresholds. However, an increase of the index value can be observed between the pre-operative and the two others post-operative cases between the C2/C3 IVJ and the end of C5/C6 IVJ. The AP index shows that the spinal cord is more antero-posteriorly centered for the pre-operative case than the spinal cords of post-operative 1 and 2 with two peaks at the C4 vertebra and at the C5/C6 IVJ where the spinal cord of the pre-operative case is more posterior positioned. On one side this observation can be corroborated with the values of the OR of the pre-operative case at the same locations. Indeed, two superior peaks observed for the pre-operative case at the C4/C5 IVJ and at the C5/C6 IVJ mean that these superior values are induced by the

superior decrease of the global canal CSA compared to the decrease of the global SC CSA. In regard of the AP eccentricity inferior values (more posterior position compared to the post-operative cases) between the C2/C3 IVJ and the C6/C7 IVJ for the pre-operative case, the local canal CSA of Z1, Z8 (anterior zones) shows a superior decrease of the areas compared to the decrease of the local canal CSA of Z4, Z5, and Z7 (posterior and lateral zones). These spatial variations could be explained by the local displacement of the cerebrospinal fluid from the anterior side of the canal to the posterior side and possibly to the cranio-caudal directions. This local ventral shunt would lead to a decrease of velocity on the opposite sides of C5/C6 left lateral and C6/C7 median diffuse compressions locations [Bae et al. 2017, Im et al. 2014, Watabe et al. 1999] and creating a spatial wall shear stress gradient increasing from the level stenosis to the around regions [Ahmed et al. 1984].

The 3D visualization of the spinal cord over canal radius ratio of the pre-operative highlights the decrease of the spatial locations of the compressions in the ventral and dorsal side. The red regions (close to 1) means that the CSF radius tends to zero (meaning the fluid is absent) compared to the blue regions meaning that the fluid is present. Thus, the C4/C5 circumferential compression is represented by red patches all around this IVJ level. The left lateral compression (on the ventral side on the [Figure 31](#) and on the axial MRI slices [Fig. 33](#)) is also identifiable as well as the lateral median diffuse compression on the dorsal view [[Fig. 31](#)] for the pre-operative case. The remaining lateral compression from the C3/C4 IVJ to the C7 vertebra (in red) is in coherence with the absence of CSF (in white) on the MRI axial slices on the [Figure 31](#) for the post-operative 1 and 2 cases. The release of space due to the decompressive surgery is represented by the blue regions due to the increase of the CSF space. The red zone which appears at the C3/C4 IVJ for the post-operative case 2 would show a pinch effect induced by the resection of the spinous process and creating a spatial post-stenosis increase of CSF space. Thus, during neck extension, this morphological variation leads to a shunt effect. A biomechanical modeling of this case could be identified if this pinch effect leads to a local stress increase.

Patient3.

This subject shows a comparable case with a ventral median diffuse compression at the C3/C4 IVJ whereas the compressions are circumferential at the C4/C5, C5/C6 and C6/C7 IVJ. The decrease of the global and local (from Z1 to Z8) canal CSA as well as the increase of the OR at the same levels are corroborated with the red patches displayed on the dorsal and ventral sides. In addition, the dorsal pinch effect already observed for the subject 2 for the post-operative 1 and 2 is also present for the post-operative 1 and largely attenuated for the post-operative 2 case. This observation is validated by the sagittal MRI slice in [Fig. 39 \(Supplementary data\)](#). The variation of pinch effect could be due to the variation of the neck flexion between the sessions. As discussed above, it could also lead to replicate stress concentration along daily activities.

Several limitations were reported. Firstly, vertebral endplate location variations were observed for the three subjects (horizontal error bars on each graph). Strong variations of location between each case were measured for the patient 2. No error concerning the landmarks positioning were noticed. An inter-session variability could be explained these variations. Indeed, the neck position of the subject at each acquisition could enough change enough to create a variation of vertebra location regarding the spinal cord location. In addition, the spinal cord could also move between each session. These potential displacements of the spinal cord could explain the negative volume gain measured for the patient 1. Inter-sessions error will be quantified in future work in comparing the morphometrics indices between two MR acquisitions.

Secondly, potential error associated with segmentation could be reported at the stenosis level due to a strong decrease of contrast ratio signal between the cerebrospinal fluid (in white) and the spinal cord (in gray). These particular regions required a specific reading by a clinician on both MR images and 3D reconstructed surfaces in order to validate the new quasi-automatic segmentation process. In addition, the effect of smoothing should be furtherly investigated to provide a complete validation of the segmentation process and to quantify the biomechanical effects on the cerebrospinal fluid flow.

To finish, I would highlight the fact that MR system has a strong potential in future years to investigate *in vivo* properties of the body. However, such imaging modality do not provide an absolute anatomical description of the body structure. Indeed, the accuracy of all the metrics proposed in literature is directly linked to multiple MRI-driven factors such as the MRI magnet power (1.5T vs 3T vs 7T), the resolution of the images, motion of the subject in the machine, position and uniformity of the radio frequency field between receptors and transmitter leading to an alteration of the image contrast are factors which could lead to an increase of the error of segmentation and of the metrics quantification. Indeed, all these residual errors could have high effect in biomechanical modelling, in particular in fluid mechanics considering a potential correlation between variation of topology/morphology of the structures in which flows the cerebrospinal fluid and the temporal and spatial wall shear stress distributions. A quantification of these errors and of their effects on the segmentation and the metrics should be studied in measuring the propagation of uncertainties by a Monte-Carlo methodology [[JCGM 101:2008](#)] as used in the Chapter 4, section 1.6.

2.5.Conclusion

A detailed semi-automatic subject-specific morphological description of Degenerative Cervical Myelopathy canal of three cases were provided. Not only common clinical indices were presented but also new local area indices as well as a 3D visualizations of the SC over canal radius ration showing preliminary high visual relationship with the MRI spatial identification of the compressive regions. Finally, the 3D segmented surfaces as well as the morphological data could be used to further biomechanical quantification of the stress effects due to the post-operative pinch effect at the C3/C4 IVJ and the wall sear stress quantification into and around the stenosis regions.

2.6.Appendices

Supplementary data – Similarity quantification by vertebral and IVJ level along the CSS

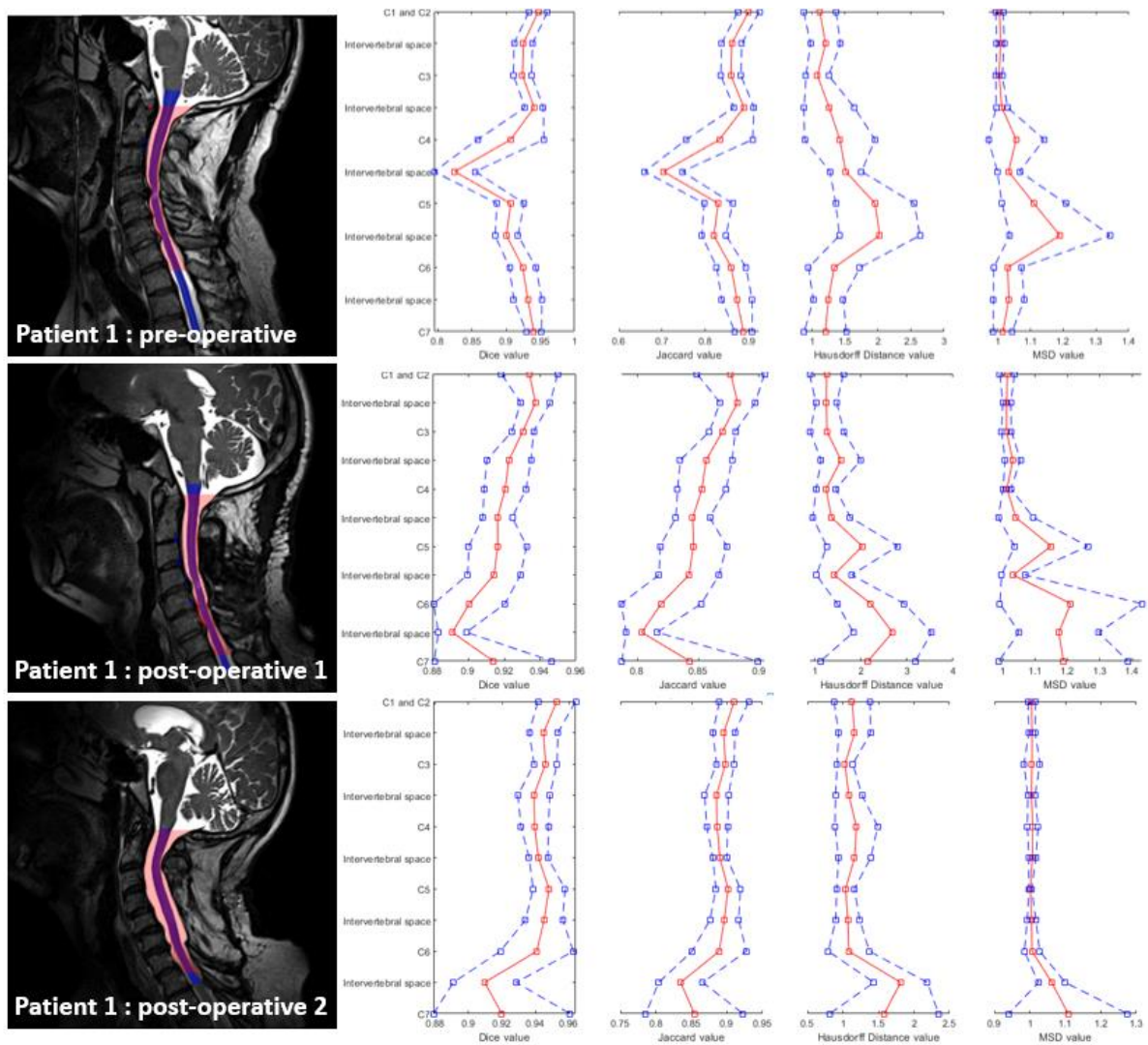


Figure 37. Patient 1. Evaluation of the 4 similarity indices (Dice, Jaccard, Hausdorff and MSD) along the canal. Each value (square markers) corresponds to a mean (in red) with the associated standard deviation (in blue).

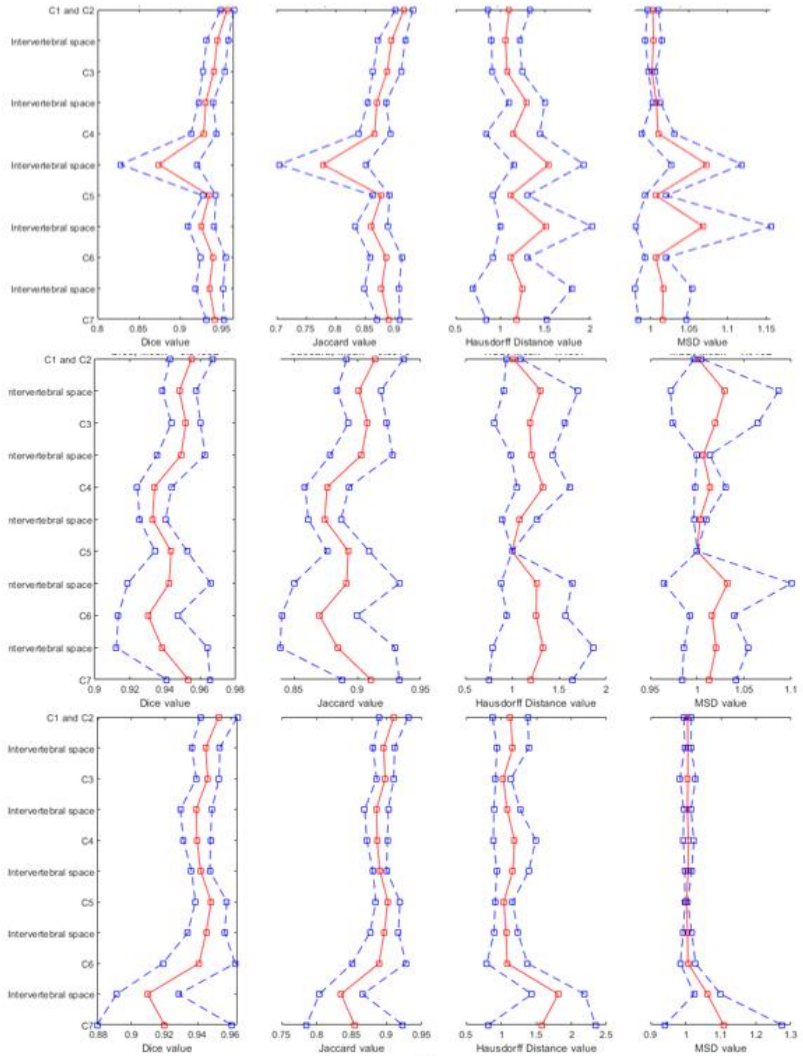
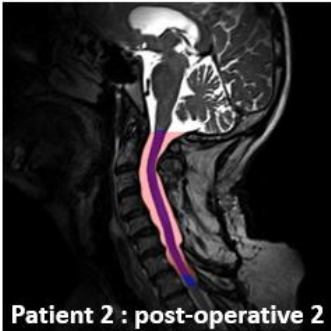
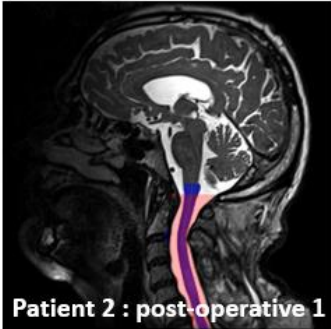
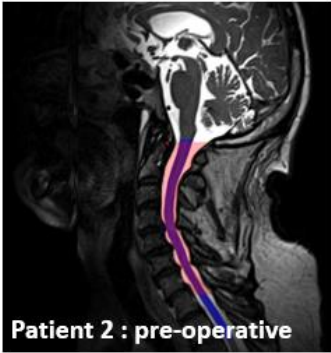


Figure 38. Patient 2. Evaluation of the 4 similarity indices (Dice, Jaccard, Hausdorff and MSD) along the canal. Each value (square markers) corresponds to a mean (in red) with the associated standard deviation (in blue).

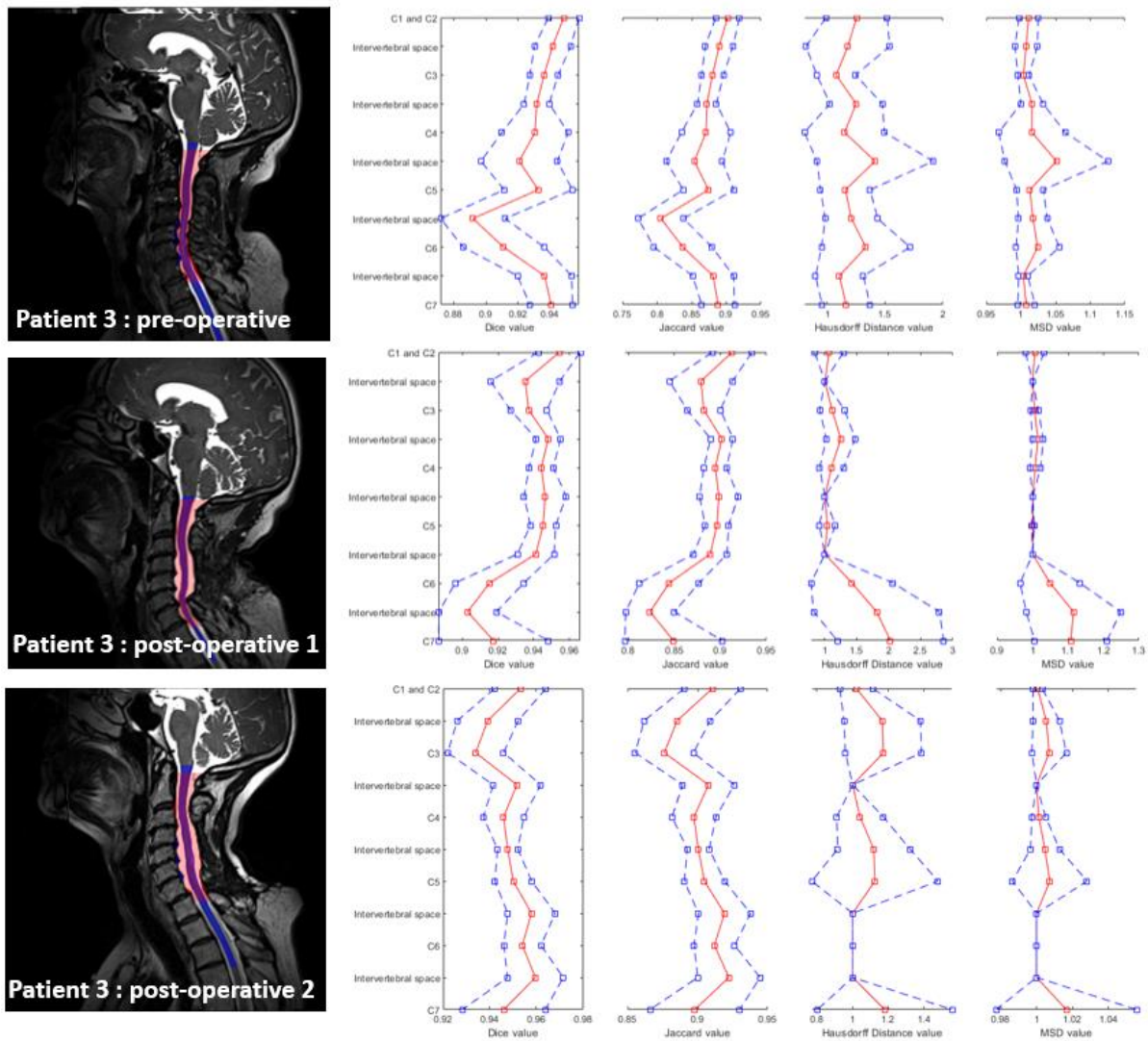


Figure 39. Patient 3. Evaluation of the 4 similarity indices (Dice, Jaccard, Hausdorff and MSD) along the canal. Each value (square markers) corresponds to a mean (in red) with the associated standard deviation (in blue).

3. References

- [Abudouaini et al. 2020] Abudouaini, H., Liu, H., Wang, B., Meng, Y., Yang, Y., Ding, C., Wu, T., Huang, C., 2020. Outcome and predictive factors in rapid progressive cervical spondylotic myelopathy: A retrospective case-control study. *Clinical Neurology and Neurosurgery* 198, 106226. <https://doi.org/10.1016/j.clineuro.2020.106226>
- [Ahmed et al. 1984] Ahmed, S.A., Giddens, D.P., 1984. Pulsatile poststenotic flow studies with laser Doppler anemometry. *J Biomech* 17, 695–705. [https://doi.org/10.1016/0021-9290\(84\)90123-4](https://doi.org/10.1016/0021-9290(84)90123-4)
- [Bae et al. 2017] Bae, Y.J., Lee, J.W., Lee, E., Yeom, J.S., Kim, K.-J., Kang, H.S., 2017. Cervical compressive myelopathy: flow analysis of cerebrospinal fluid using phase-contrast magnetic resonance imaging. *Eur Spine J* 26, 40–48. <https://doi.org/10.1007/s00586-016-4874-9>
- [Behrbalk et al. 2013] Behrbalk, E., Salame, K., Regev, G.J., Keynan, O., Boszczyk, B., Lidar, Z., 2013. Delayed diagnosis of cervical spondylotic myelopathy by primary care physicians. *Neurosurgical Focus* 35, E1. <https://doi.org/10.3171/2013.3.FOCUS1374>
- [Bilston 1994] Bilston LE. *The Biomechanics of the Spinal Cord During Traumatic Spinal Cord Injury*; 1994. Available at: <https://core.ac.uk/display/76367966>. Accessed March 22, 2019.
- [Bilston and Thibault 1997] Bilston LE, Thibault LE. Biomechanics of cervical spinal cord injury in flexion and extension: a physical model to estimate spinal cord deformations. *Int J Crashworth* 1997;2:207–18.
- [Bloomfield et al. 1998] Bloomfield IG, Johnston IH, Bilston LE. Effects of proteins, blood cells and glucose on the viscosity of cerebrospinal fluid. *Pediatr Neurosurg* 1998;28:246–51.
- [Cadotte et al. 2015] Cadotte DW, Cadotte A, Cohen-Adad J, et al. Characterizing the location of spinal and vertebral levels in the human cervical spinal cord. *AJNR Am J Neuroradiol* 2015;36:803–10.
- [Ceylan et al. 2012] Ceylan D, Tatarlı N, Abdullaev T, et al. The denticulate ligament: anatomical properties, functional and clinical significance. *Acta Neurochir (Wien)* 2012;154:1229–34.
- [Chen et al. 2013] Chen, M., Carass, A., Oh, J., Nair, G., Pham, D.L., Reich, D.S., Prince, J.L., 2013. Automatic magnetic resonance spinal cord segmentation with topology constraints for variable fields of view. *NeuroImage* 83, 1051–1062. <https://doi.org/10.1016/j.neuroimage.2013.07.060>
- [Chen et al. 2016] Chen, G.-D., Lu, Q., Sun, J.-J., Yuan, Q., Luo, Z.-P., Yang, H.-L., 2016. Effect and Prognostic Factors of Laminoplasty for Cervical Myelopathy With an Occupying Ratio Greater Than 50%. *Spine* 41, 378–383. <https://doi.org/10.1097/BRS.0000000000001289>
- [Dahlan et al. 2014] Dahlan RH, Saputra PAE, Yudoyono FF, et al. Morphometric analysis of the corpus, spinal canal and torg ratio using midsagittal cervical vertebrae computed tomography scan: Indonesian Population. *Int J Integr Health Sci* 2014;2:36–9.
- [De Leener et al. 2015] De Leener, B., Cohen-Adad, J., Kadoury, S., 2015. Automatic Segmentation of the Spinal Cord and Spinal Canal Coupled With Vertebral Labeling. *IEEE Trans Med Imaging* 34, 1705–1718. <https://doi.org/10.1109/TMI.2015.2437192>
- [De Leener et al. 2017] De Leener, B., Lévy, S., Dupont, S.M., Fonov, V.S., Stikov, N., Louis Collins, D., Callot, V., Cohen-Adad, J., 2017. SCT: Spinal Cord Toolbox, an open-source software for processing spinal cord MRI data. *Neuroimage* 145, 24–43. <https://doi.org/10.1016/j.neuroimage.2016.10.009>
- [Desbrun et al. 1999] Desbrun M, Meyer M, Schröder P, Barr AH. Implicit Fairing of Irregular Meshes Using Diffusion and Curvature Flow. In: *Proceedings of the 26th Annual Conference on Computer Graphics and Interactive Techniques. SIGGRAPH '99*. New York, NY, USA: ACM Press/Addison-Wesley Publishing Co.; 1999:317–324.
- [Endo et al. 2014] Endo, K., Suzuki, H., Nishimura, H., Tanaka, H., Shishido, T., Yamamoto, K., 2014. Kinematic Analysis of the Cervical Cord and Cervical Canal by Dynamic Neck Motion. *Asian Spine J* 8, 747–752. <https://doi.org/10.4184/asj.2014.8.6.747>
- [Fradet et al. 2014] Fradet L, Arnoux P-J, Ranjeva J-P, et al. Morphometrics of the entire human spinal cord and spinal canal measured from in vivo high-resolution anatomical magnetic resonance imaging. *Spine (Phila Pa 1976)* 2014;39:E262–9.
- [Frykholm et al. 1947] Frykholm R. Deformities of dural pouches and strictures of dural sheaths in the cervical region producing nerve-root compression: a contribution to the etiology and operative treatment of brachial neuralgia. *J Neurosurg* 1947;4:403–13.
- [Hilton et al. 2018] Hilton, B., Tempest-Mitchell, J., Davies, B., Kotter, M., 2018. Assessment of degenerative cervical myelopathy differs between specialists and may influence time to diagnosis and clinical outcomes. *PLOS ONE* 13, e0207709. <https://doi.org/10.1371/journal.pone.0207709>
- [Holmes et al. 1996] Holmes A, Han ZH, Dang GT, et al. Changes in cervical canal spinal volume during in vitro flexion-extension. *Spine (Phila Pa 1976)* 1996;21:1313–9.
- [Hu et al. 2019] Hu P, He Z, Cui J, et al. Pathological changes of cervical spinal canal in cervical spondylotic myelopathy: a retrospective study on 39 cases. *Clin Neurol Neurosurg* 2019;181:133–7.

- [Im et al. 2014] Im, V., Sm, M., El, M., B, M., Dk, L., A, R., T, V., V, V., Al, M., A, C., 2014. Increased spinal cord movements in cervical spondylotic myelopathy. *Spine J* 14, 2344–2354. <https://doi.org/10.1016/j.spinee.2014.01.036>
- [ISO 98:1995 GUM] ISO 98:1995 Guide to the expression of Uncertainty in Measurement 2nd edn (1995) International Organization for Standardization, Geneva
- [Jha et al. 2018] Jha SC, Miyazaki M, Tsumura H. Kinetic change of spinal cord compression on flexion-extension magnetic resonance imaging in cervical spine. *Clin Neurol Neurosurg* 2018;174:86–91.
- [Johnson et al. 1975] Johnson RM, Crelin ES, White AA, et al. Some new observations on the functional anatomy of the lower cervical spine. *Clin Orthop Relat Res* 1975;192–200.
- [Kadanka et al. 2017] Kadanka, Z., Adamova, B., Kerkovsky, M., Kadanka, Z., Dusek, L., Jurova, B., Vlckova, E., Bednarik, J., 2017. Predictors of symptomatic myelopathy in degenerative cervical spinal cord compression. *Brain and Behavior* 7, e00797. <https://doi.org/10.1002/brb3.797>
- [Kar et al. 2017] Kar, M., Bhaumik, D., Ishore, K., Saha, P.K., 2017. MRI Study on Spinal Canal Morphometry: An Indian Study. *J Clin Diagn Res* 11, AC08-AC11. <https://doi.org/10.7860/JCDR/2017/25981.9899>
- [Kato et al. 2012] Kato F, Yukawa Y, Suda K, et al. Normal morphology, age-related changes and abnormal findings of the cervical spine. Part II: magnetic resonance imaging of over 1,200 asymptomatic subjects. *Eur Spine J* 2012;21:1499–507.
- [Kawakami et al. 2002] Kawakami, M., Tamaki, T., Ando, M., Yamada, H., Yoshida, M., 2002. Relationships Between Sagittal Alignment of the Cervical Spine and Morphology of the Spinal Cord and Clinical Outcomes in Patients With Cervical Spondylotic Myelopathy Treated With Expansive Laminoplasty. *Clinical Spine Surgery* 15, 391.
- [Kikinis et al. 2014] Kikinis R, Pieper SD, Vosburgh KG. 3D Slicer: a platform for subject-specific image analysis, visualization, and clinical support. *Intraoperative Imaging and Image-Guided Therapy*. New York, NY: Springer New York; 2014. pp. 277–89.
- [Koh et al. 2011] J., Scott, P.D., Chaudhary, V., Dhillon, G., 2011. An automatic segmentation method of the spinal canal from clinical MR images based on an attention model and an active contour model. <https://doi.org/10.1109/ISBI.2011.5872677>
- [Kong et al. 2018] Kong, L., Bai, J., Zhang, B., Shen, Y., Tian, D., 2018. Predictive factors of symptomatic lumbar canal stenosis in patients after surgery for cervical spondylotic myelopathy [WWW Document]. *Therapeutics and Clinical Risk Management*. <https://doi.org/10.2147/TCRM.S156364>
- [Kovalova et al. 2016] Kovalova, I., Kerkovsky, M., Kadanka, Z., Kadanka, Z.J., Nemeč, M., Jurova, B., Dusek, L., Jarkovsky, J., Bednarik, J., 2016. Prevalence and Imaging Characteristics of Nonmyelopathic and Myelopathic Spondylotic Cervical Cord Compression. *Spine* 41, 1908–1916. <https://doi.org/10.1097/BRS.0000000000001842>
- [Kuuzawa et al. 2006] Kuuzawa Y, Pope MH, Bashir W, et al. The length of the cervical cord: effects of postural changes in healthy volunteers using positional magnetic resonance imaging. *Spine (Phila Pa 1976)* 2006;31:E579–83.
- [Lévy et al. 2020] Lévy, S., Baucher, G., Roche, P.-H., Evin, M., Callot, V., Arnoux, P.-J., 2020. Biomechanical comparison of spinal cord compression types occurring in Degenerative Cervical Myelopathy. *Clinical Biomechanics* 105174. <https://doi.org/10.1016/j.clinbiomech.2020.105174>
- [Malzac et al. 2002] Malzac A, Barros F, Tarcísio E P D., et al. Morphometry of the spinal canal at cervical region in asymptomatic military young men. *Acta Ortopédica Brasileira* 2002;10:40–51.
- [Miura et al. 2009] Miura, J., Doita, M., Miyata, K., Marui, T., Nishida, K., Fujii, M., Kurosaka, M., 2009. Dynamic Evaluation of the Spinal Cord in Patients With Cervical Spondylotic Myelopathy Using a Kinematic Magnetic Resonance Imaging Technique. *Clinical Spine Surgery* 22, 8–13. <https://doi.org/10.1097/BSD.0b013e31815f2556>
- [Morishita et al. 2009] Morishita, Y., Naito, M., Hymanson, H., Miyazaki, M., Wu, G., Wang, J.C., 2009. The relationship between the cervical spinal canal diameter and the pathological changes in the cervical spine. *Eur Spine J* 18, 877–883. <https://doi.org/10.1007/s00586-009-0968-y>
- [Nagai et al. 2018] Nagai, T., Takahashi, Y., Endo, K., Ikegami, R., Ueno, R., Yamamoto, K., 2018. Analysis of spastic gait in cervical myelopathy: Linking compression ratio to spatiotemporal and pedobarographic parameters. *Gait & Posture* 59, 152–156. <https://doi.org/10.1016/j.gaitpost.2017.10.013>
- [Nightingale et al. 2002] Nightingale RW, Winkelstein BA, Knaub KE, et al. Comparative strengths and structural properties of the upper and lower cervical spine in flexion and extension. *J Biomech* 2002;35:725–32.
- [Northover et al. 2012] Northover, J.R., Wild, J.B., Braybrooke, J., Blanco, J., 2012. The epidemiology of cervical spondylotic myelopathy. *Skeletal Radiol* 41, 1543–1546. <https://doi.org/10.1007/s00256-012-1388-3>
- [Polak-Krasna et al. 2019] Polak-Krasna K, Robak-Nawrocka S, Szotek S, et al. The denticulate ligament – Tensile characterisation and finite element microscale model of the structure stabilising spinal cord. *J Mech Behav Biomed Mater* 2019;91:10–7.

- [Pratali et al. 2019] Pratali, R.R., Smith, J.S., Ancheschi, B.C., Maranhó, D.A., Savarese, A., Nogueira-Barbosa, M.H., Herrero, C.F.P.S., 2019. A Technique for Dynamic Cervical Magnetic Resonance Imaging Applied to Cervical Spondylotic Myelopathy: A Reliability Study. *Spine* 44, E26. <https://doi.org/10.1097/BRS.0000000000002765>
- [Sadasivan et al. 1993] Sadasivan, K.K., Reddy, R.P., Albright, J.A., 1993. The natural history of cervical spondylotic myelopathy. *Yale J Biol Med* 66, 235–242.
- [Schiffer et al.1999] Schiffer E, van Gessel E, Gamulin Z. Influence of sex on cerebrospinal fluid density in adults. *Br J Anaesth* 1999;83:943–4.
- [Smith et al. 2013] Smith, J.S., Lafage, V., Ryan, D.J., Shaffrey, C.I., Schwab, F.J., Patel, A.A., Brodke, D.S., Arnold, P.M., Riew, K.D., Traynelis, V.C., Radcliff, K., Vaccaro, A.R., Fehlings, M.G., Ames, C.P., 2013. Association of myelopathy scores with cervical sagittal balance and normalized spinal cord volume: analysis of 56 preoperative cases from the AOSpine North America Myelopathy study. *SPINE* 38.
- [Stoner et al . 2019] Stoner KE, Abode-iyamah KO, Magnotta VA, et al. Measurement of in vivo spinal cord displacement and strain fields of healthy and myelopathic cervical spinal cord. *J Neurosurg Spine* 2019; 31:53–9.
- [Sudres et al. 2020] Sudres, P., Evin, M., Arnoux, P.-J., Callot, V., 2020. Cervical Canal Morphology: Effects of Neck Flexion in Normal Condition: New Elements for Biomechanical Simulations and Surgical Management. *Spine* 45, 1102–1109. <https://doi.org/10.1097/BRS.0000000000003496>
- [Sun et al. 2019] Sun K, Wang S, Sun J, et al. Analysis of the correlation between cerebrospinal fluid space and outcomes of anterior controllable antedisplacement and fusion for cervical myelopathy due to ossification of the posterior longitudinal ligament. *World Neurosurg* 2019;122:e358–66.
- [Tropp and al. 2006] Tropp O, Tal A, Shimshoni I. A fast triangle to triangle intersection test for collision detection. *J Visual Comput Anim* 2006;17:527–35.
- [Tykocki et al. 2018 a] Tykocki, T., du Plessis, J., Wynne-Jones, G., 2018a. Correlation between the severity of myelopathy and cervical morphometric parameters on dynamic magnetic resonance imaging. *Acta Neurochir* 160, 1251–1258. <https://doi.org/10.1007/s00701-018-3540-x>
- [Tykocki et al. 2018 b] Tykocki, T., du Plessis, J., Wynne-Jones, G., 2018b. Analysis of Morphometric Parameters in Cervical Canal Stenosis on Neutral and Dynamic Magnetic Resonance Imaging. *World Neurosurgery* 114, e317–e322. <https://doi.org/10.1016/j.wneu.2018.02.179>
- [Watabe et al. 1999] Watabe, N., Tominaga, T., Shimizu, H., Kosu, K., Yoshimoto, T., 1999. Quantitative analysis of cerebrospinal fluid flow in patients with cervical spondylosis using cine phase-contrast magnetic resonance imaging. *Neurosurgery* 44, 779–784. <https://doi.org/10.1097/00006123-199904000-00052>
- [Wolf et al. 2018] Wolf, K., Hupp, M., Friedl, S., Sutter, R., Klarhöfer, M., Grabher, P., Freund, P., Curt, A., 2018. In cervical spondylotic myelopathy spinal cord motion is focally increased at the level of stenosis: a controlled cross-sectional study. *Spinal Cord* 56, 769–776. <https://doi.org/10.1038/s41393-018-0075-1>
- [Xu and Prince 1997] Chenyang Xu, Prince, J.L., 1997. Gradient vector flow: a new external force for snakes, in: *Proceedings of IEEE Computer Society Conference on Computer Vision and Pattern Recognition*. Presented at the Proceedings of IEEE Computer Society Conference on Computer Vision and Pattern Recognition, pp. 66–71. <https://doi.org/10.1109/CVPR.1997.609299>
- [Xu and Prince 1998] Xu, C., Prince, J.L., 1998. Snakes, shapes, and gradient vector flow. *Trans. Img. Proc.* 7, 359–369. <https://doi.org/10.1109/83.661186>
- [Yuan et al. 2018] Yuan Q, Dougherty L, Margulies SS. In vivo human cervical spinal cord deformation and displacement in flexion. *Spine (Phila Pa1976)* 1998;23:1677–83.
- [Yushkevich et al. 2006] Yushkevich, P.A., Piven, J., Hazlett, H.C., Smith, R.G., Ho, S., Gee, J.C., Gerig, G., 2006. User-guided 3D active contour segmentation of anatomical structures: Significantly improved efficiency and reliability. *NeuroImage* 31, 1116–1128. <https://doi.org/10.1016/j.neuroimage.2006.01.015>
- [Zaaroor et al. 2006] Zaaroor, M., Kósa, G., Peri-Eran, A., Maharil, I., Shoham, M., Goldsher, D., 2006. Morphological Study of the Spinal Canal Content for Subarachnoid Endoscopy. *Minim Invasive Neurosurg* 49, 220–226. <https://doi.org/10.1055/s-2006-948000>

Chapter summary

Section 1 summary

A first published study on the development of a methodology allowing the quantification of morphometrical indices along the cervical canal was performed. This approach aimed at providing accurate and detailed morphological data (cross-sectional area, eccentricity indices, and displacements of the cord and canal) in order to quantify the impact of the flexion in the cervical canal. Indeed, absolute morphological indices describing the spinal cord (cross-sectional area, compression ratio, position in the canal, length) and of the cervical subarachnoid canal (cross section, occupational ratio, lengths) were calculated from semi-automatic reconstructions of *in vivo* high resolution MRI (3D T2-SPACE sequence, on 11 healthy volunteers, for two postures: neutral position and flexion of the neck). The two main results of this study are: (1) the left-right stability described by the left-right eccentricity index and is ensured by the denticulate ligaments and nerve roots attached to the dural sheaths, (2) an effect of Poisson (decrease in axial section and lengthening of the cord in flexion) of the spinal cord has been partially shown in the axial plane (anteroposterior diameter, occupational ratio, compression ratio) and by its longitudinal geometric descriptions (length of the cord spinal). This methodology can now be used for comparison with patients affected by degenerative cervical myelopathy (DCM), as well as in the context of biomechanical modeling.

Section 2 summary

In the study described in this section, we are interested in the morphology of the cervical canal for 3 DCM patients, treated surgically (1 preoperative and 2 postoperative follow-ups). Indeed, decompression surgery strongly modifies the morphology of the patient's cervical canal. Then, it remains difficult to establish pathological morphological criteria for detecting potential canal narrowing both for the diagnostic stage and for the follow-up or even prognostic stage. In this context, we propose a methodology based on our previous work described above to morphologically quantify these modifications and provide additional information to neurosurgeons in the follow-up of the DCM patient. Not only common clinical indices were presented but also new local area indices as well as a 3D visualization of the SC over canal radius ration showing preliminary high visual relationship with the MRI spatial identification of the compressed regions. Finally, the 3D segmented surfaces as well as the morphological data could be used to further biomechanical quantification of the stress effects induced by the post-operative pinch effect at the C3/C4 IVJ and the wall shear stress quantification into and around the stenosis regions before surgery.

Chapter 4

Mechanical properties of spinal porcine meninges

1. Tensile Mechanical Properties of the Cervical, Thoracic and Lumbar Porcine Spinal Meninges	117
1.1. Introduction.....	117
1.2. Material and Methods.....	119
1.3. Results.....	124
1.4. Discussion.....	130
1.5. Conclusion.....	134
1.6. Appendices.....	135
2. Experimental Bi-axial Tensile Tests of Meningeal Tissues and Constitutive Models Comparison.....	144
2.1. Introduction.....	144
2.2. Material and Methods.....	148
2.3. Results.....	152
2.4. Discussion.....	162
2.5. Conclusion.....	164
3. References.....	165

In the previous chapter, the morphometry of a healthy and a pathological population was provided and reconstructed in 3D for the purpose of future simulation in FSI. However, as explained in the chapter 2, the accurate definition of the solid domain is equally important as the fluid domain. In this context, the study and the quantification of the material properties of tissue in contact with the CSF is required.

The aims of this chapter were :

- 1) to provide a preliminary hyperelastic as well as a detailed elastic description of the uniaxial tensile properties of the spinal porcine meninges in a moderate condition.
- 2) to provide a characterization of biaxial tensile properties of the spinal porcine meninges.
- 3) based on the 2nd objective, to propose an isotropic and anisotropic hyper-elastic description of the spinal porcine meninges.

1. Tensile Mechanical Properties of the Cervical, Thoracic and Lumbar Porcine Spinal Meninges

Patrice SUDRES (1,4), Morgane EVIN (1,4), Eric WAGNAC (2,3,4), Nicolas BAILLY (2,3,4), Lucien DIOTALEVI (2,3,4), Anthony MELOT (1,4,5), Pierre-Jean ARNOUX (1,4), Yvan PETIT (2,3,4)

1. Laboratoire de Biomécanique Appliquée, UMRT24 AMU/IFSTTAR, Marseille, France.
2. Department of Mechanical Engineering, École de Technologie Supérieure, 1100 Notre-Dame Street West, Montréal, Québec H3C 1K3, Canada
3. Research Center, Hôpital du Sacré-Coeur de Montréal, 5400 Gouin blvd, Montréal H4J 1C5, Québec, Canada
4. iLab-Spine – Laboratoire International en Imagerie et Biomécanique du Rachis, Marseille, France & Montréal, Canada.
5. Hôpital privé Clairval, Marseille, France.

Article published in Journal of the Mechanical Behavior of Biomedical Materials [[Sudres et al. 2021](#)].

Abbreviations

DAC: dura-arachnoid mater complex
PM: pia mater
ROI: region of interest
DIC: digital image correlation
CSA: cross-sectional area
GUM: Guide to the expression of Uncertainty in Measurement
SE : standard error
SD: standard deviation
RMSE: Root Mean Square Error
ROM: range of motion
CSF: cerebrospinal fluid

Keywords:

meninges, mechanical properties, biomechanics, spine, elasticity

1.1.Introduction

The spinal meninges composed of the dura mater, the arachnoid mater and the pia mater, play a mechanical protective role for the spinal cord [[Sakka et al. 2016](#)]. The dura mater is a fibrous, white, thick, and resistant membrane formed by a dense connective tissue poorly vascularized with a ratio of collagen I fibers to elastin fibers varying radially. The arachnoid mater can be described as an outer layer, consisting of a thin transparent membrane mainly composed of collagen and elastin fibers, attached to the dura mater by thin strands of collagen. The pia mater is mainly composed of predominantly longitudinally orientated collagen fibers, which carry larger branches of the spinal vasculature [[Reina et al. 1997, 2020](#)].

As any biological soft tissue, meningeal mechanical properties are altered *post mortem* due to drying and the interruption of blood supply, thus leading to tissue degeneration [Garo et al. 2007, Fountoulakis et al. 2001]. In consequence, the experimental testing methodology needs an thorough management of time and manipulation to provide reliable mechanical measurements in order to highlight the specificities of such biological soft tissues. Better knowledge of the mechanical behavior of these tissues wrapping the cord is required to accurately model the stress and strain fields of the spinal cord during physiological or traumatic motions [Bertram and Heil 2016, Fradet et al. 2016a, Sparrey and Keaveny 2009, Kimpara et al. 2006, Khuyagbaatar et al. 2014]. Such modeling tools allowed the correlation of the stresses fields in the spinal cord with clinical analyses [Lévy et al. 2020, Czyż et al. 2012], and the assessment of the effect of a specific surgery on these tissues [Henao et al. 2016].

The spinal dura mater was mainly tested in tension at different locations of the spine. A porcine cervical cartography of the mechanical properties showed differences between the dorsal and the ventral side of the dura mater [Mazgajczyk et al. 2012]. A significant variability of properties was found between species, such as rats [Maikos et al. 2008], dogs [Patin et al. 1993], sheeps [Shetye et al. 2014], swines [Mazgajczyk et al. 2012], cattle [Runza et al. 1999] and humans [Runza et al. 1999, Chauvet et al. 2010]. Due to ethical and logistical complications related to human species, the high similarity of porcine model to the human species on the genetic, anatomical, physiological, pathophysiological [Schomberg et al. 2017], and biomechanical [Wilke et al. 2011] levels, the swine model appears as the best transversal human models, next to non-human primates [Schomberg et al. 2017], and is increasingly used in spine research [Kim et al. 2019, Ramo et al. 2018b, Brummund et al. 2017, Fradet et al. 2016b, Swindel et al. 2013]. In addition, similarities between human and porcine models were highlighted histologically for the dura mater (3 dural layers structure) [Kinaci et al. 2020].

An anisotropic behavior (in longitudinal or cranio-caudal direction and in circumferential direction) was also reported in most of the species except for the dog. One biaxial study confirmed this difference between these two mechanical orientations on ovine samples [Shetye et al. 2014]. The anisotropic behavior was corroborated by histological studies describing, in particular, the longitudinal direction of fibers along the cord [Maikos et al. 2008, Chauvet et al. 2010]. Among these studies, the spinal arachnoid mater was considered as a part of the spinal dura mater, excepted for two of them which assumed its adherence to the spinal pia mater [Fabris et al. 2019, Ramo et al. 2018c]. The spinal arachnoid-dura tissue continuity assumption was validated by others histological quantification, showing the arachnoid mater to be the inner layer of the dura mater. The relative thickness of dura-to-arachnoid mater however suggested a limited role of the arachnoid to the mechanical properties of the dura mater [Vandenabeele et al. 1996, Reina et al. 1997]. Then, quantification of the mechanical properties of pia and dura-arachnoid mater complex (DAC) mechanical properties is not fully described along the whole spinal cord in the literature. One study compared biomechanical properties of the ovine dura mater at six spinal levels (C₆, C₇, T₁₁, T₁₂, L₄, and L₅). No significant difference of elastic moduli values between longitudinal and circumferential directions at the cervical levels were notified, but this study showed that the ratio between the longitudinal and circumferential elastic moduli were significantly smaller at the cervical and thoracic levels [Yang et al. 2019]. In addition, Mazgajczyk et al. [2012] highlighted a significative variability of DAC mechanical properties along the porcine cervical segment between the dorsal and the ventral sides on porcine models. Our hypothesis is that the elastic mechanical properties, which vary between the ventral and dorsal sides, could also vary along the whole longitudinal spinal cord from the spinal cervical to the spinal lumbar levels.

The effect of conservation methods on mechanical characteristics is not systematically quantified. Freezing method at -4°C was shown to modify the mechanical properties variability of the human dura

mater through time, while the mechanical properties of the bovine dura mater decreases independently of the time [Runza et al. 1999].

Concerning the spinal pia mater, two studies provided indirect measurements of the cervical compressive and tensile mechanical properties on rabbits [Ozawa et al. 2004] and on human spinal cord [Mazuchowski and Thibault 2003]. More recently, quasi-static tensile tests and a dynamics mechanical analysis were performed on cervical ewe pia mater assumed as an integrally laminated structure composed of the arachnoid and the pia maters. This study highlighted the non-linear viscoelasticity of the ewe pia-arachnoid structure [Ramo et al. 2018c].

The aim of this study is to quantify the elastic meningeal mechanical properties along the porcine spinal cord in the longitudinal (cranio-caudal) direction and in the circumferential (surrounding the spinal cord) directions for the DAC, and solely in longitudinal direction for the PM. A quasi-static loading close to physiological solicitations was considered. In addition, the effect of the conservation method effect was assessed by comparing flash frozen (at -80°C) [Sparrey and Keaveny 2009] (different from a classical freezing at -4°C) and fresh samples properties.

1.2. Material and methods

1.2.1. Sample preparation

Two tissue structures were characterized in this study: the dura-arachnoid mater complex (DAC) and the pia mater (PM). Six complete spines (C0 – L5) were harvested from pigs (race: crossbreeding Yorkshire x Landrace, age: 2-3 months, weight: 43 +/- 13 kg, gender: 4 males and 2 females) one to two hours following euthanasia. The animals were euthanatized for reasons unrelated to this study. The spine was firstly extracted by a dissection on the dorsal side using scalpels and oscillating saw. This step was performed less than 35 minutes after euthanasia. The spine was then sectioned in three levels: cervical level (from the foramen magnum to the T1-T2 joint), thoracic level (from the T1-T2 joint to the T13-T14 joint, and lumbar level (from the T13-T14 joint to the L6-S1 joint). The spinal cord-meningeal complex, including the DAC, was carefully removed from the spinal canal through fine dissection with scalpels and gouge clamps, and small clamps (duration of 1 hour). The nerve roots and the denticulate ligaments were resected along the DAC. The spinal cord-meningeal complex from two spinal levels over three were stored in PBS at 4°C. The DAC and PM samples were prepared and tested within a 12 hours and 30 minutes after euthanasia. The remaining one third of spinal cord-meningeal complex was saved using flash-freezing (FF) method at -80°C [Sparrey and Keaveny 2009] and thawed at 4°C and prepared and tested at 20°C. For all samples, the DAC was longitudinally incised on the lateral side of the spinal cord-meningeal complex and was removed from the cord. The same operation was done for the PM, which was also taken apart from the white and grey matters. All the fresh and FF samples were stored in PBS at 20°C to keep them moist after preparation and tested at room laboratory temperature of 20°C. The samples were placed between two pieces of sandpaper into which a window was cut, and a stochastic pattern of dots was applied using an oil-based black paint spray (Ptouch 2x + sspr 6pk flat black, Rust-Oleum Corporation, USA), [Fig 40 – A]. This step was used to measure the length and the width of the sample as well as to perform strain and stress fields analyses. The support was then inserted and fastened into the clamps of the testing machine (GRIP ASST, T/C, 3200, Bose Corporation, Framingham, Massachusetts, US). The lateral side of the sandpaper support was cut before testing to allow traction with the clamps [Fig 40 – B]. Two different orientations of clamping were used, leading to 2 different loading directions for the DAC: longitudinal and circumferential. PM samples were only tested in the longitudinal direction.

The length (L_0) of the samples was defined as the minimum distance between the clamps at the initial position before testing. The width (w) was defined as the lateral distance of the clamped sample at the initial time position before the mechanical test. Samples not fully attached samples to the clamps [Fig. C.4] or with a visible deterioration after attachment were excluded from the study. The reference thicknesses (t) of the DAC and PM were measured at 3 spinal levels (cervical, thoracic and lumbar) on an additional porcine subject to avoid damaging the samples due to supplementary manipulations. The DAC and PM samples were sectioned to a width of 1mm and a length corresponding to the longitudinal distance between two nerves roots. They were positioned on a black 120g paper. The samples' side with the largest area were glued on with the black paper by a transparent agar substrate. Then, the samples were positioned on the edge on a graph paper. A Micro C110 camera (Vision Research, 8GB) with a 105 macro lens (Nikon F2.8), as well as two light systems (LED EFFILUX) were used to acquire high resolution images of the samples' thickness. Three samples were sectioned in three sub-samples at each spinal level as defined in the first paragraph of this section. Calibration of the camera was performed using three measurements of the graph paper. Ten measurements were performed on each sub-sample. A total of 30 measurements by tissue (DAC and PM) and by spinal level (cervical, thoracic and lumbar) were performed. The cross-section area (CSA) of the sample was assumed to be rectangular and defined as the product of the width (w) by the thickness (t).

1.2.2. Tensile testing

Both types of sample were submitted to the same testing protocol with specific preload and threshold values for the pre-cycling phase [Fig. 41]. A preload of 0.5 N was applied for the pia mater and of 2 N for the DAC samples followed by 30 preconditioning cycles (frequency varies with the time to reach the preload, the magnitude: 1 N). They were performed to compensate the retraction of the sample and remove any buckling of the sample before testing. The amplitude of preloading was based in the literature [Shetye et al. 2014, Ramo et al. 2018a,b,c]. A moderate tensile ramp at 0.2 mm/s was chosen in accordance with *in vivo* experiment of porcine spinal-cord-pia-arachnoid construct [Ramo et al. 2018b] and reported by the literature for ex vivo ovine dura mater and pia-arachnoid complex [Ramo et al. 2018a, c].

The tests were stopped at failure or when the maximum displacement was reached [Fig. 46, Table 23 - Appendix B].

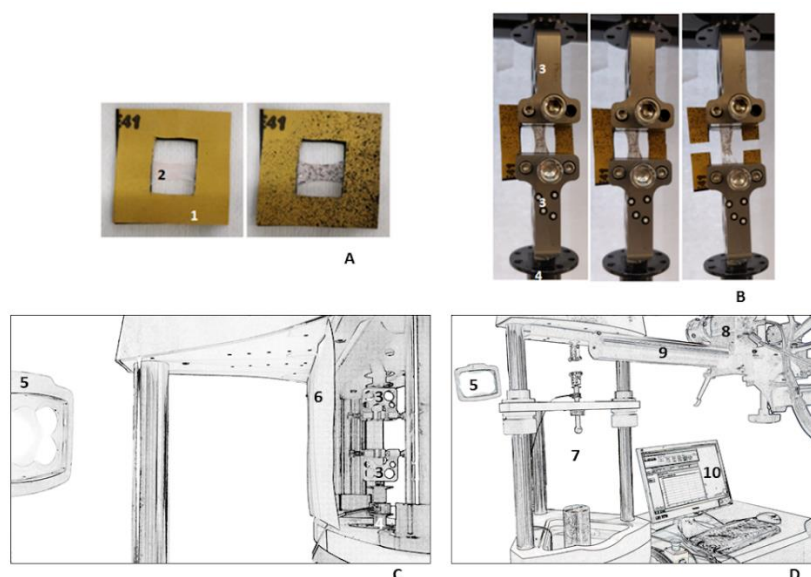


Figure 40. Mechanical testing set up: **A/** (1) Sandpaper support with (2) fastened sample (left), with stochastic pattern (right) ; **B/** Ramp test to-failure. (3) Clamps, (4) load cell ; **C/** Lateral view of the setup with (5) a spotlight, (6) a white filter for indirect lightening of the sample ; **D/** Front view including the (7) mechanical testing machine, (8) a high-definition camera, (9) a sliding support to adjust the location of the camera and (10) a computer to control and to record the measurement.

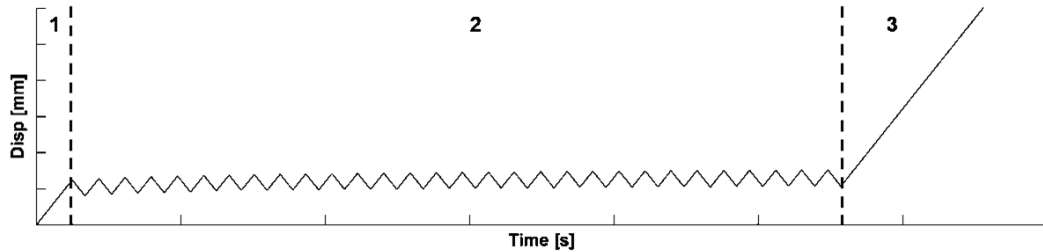


Figure 41. Typical imposed displacement over time for each mechanical tensile test. 1) Initial pre-load, 2) 30 preconditioning cycles, 3) ramp to failure.

1.2.3. Data acquisition

A testing machine Bose© ElectroForce 3200 Series (Bose Corporation, Framingham, Massachusetts, US) was used to perform tensile tests [Fig.40]. The loads data were acquired with a 22 N load cell (reliability manufacturer error of 0.11 % and a repeatability error of 0.19 %) at a sampling rate of 100 Hz. Dimensions (length and width) as well as the displacements of the samples. Complementary displacement and strain fields were measured by 2D digital image correlation (DIC) (ARAMIS 5 M, GOM mbH, Germany) at 15 frames per second.

1.2.4. Data analysis

Linear elasticity

The force/displacement curves were zeroed for comparison by subtracting the minimum measured displacement to the initial measured displacement. Each engineering stress-strain curve was computed from the measured force/displacement curves as follows:

$$\sigma = F/CSA \quad (1)$$

$$CSA = t * w \quad (2)$$

$$\varepsilon = \Delta L/L_0 \quad (3)$$

where equation (1) defines the engineering stress (σ) as the ratio of the tensile force (F) over the initial the cross-sectional area (CSA) on which the force is applied. The initial cross-sectional area (2) of the sample is the product of its thickness (t) by its width (w) in his undeformed state. Equation (3) allows computing the engineering strain (ε) as the ratio of the measured displacement (ΔL) over the initial length (L_0) of the sample.

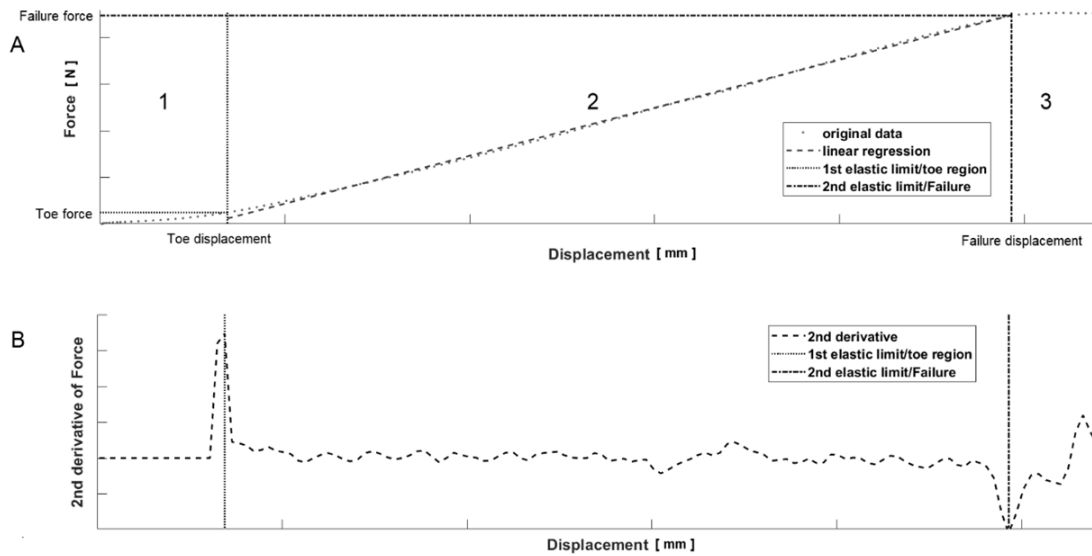


Figure 42. Identification of the linear elastic region of interest. A- force/displacement responses with two elastic limits delimiting the three regions (1 - toe region ending by the toe force and the toe displacement, 2 – linear elastic region, 3 – failure region starting by the failure force and the failure displacement) and the linear regression, B) 2nd derivative of the force/displacement curve identifying the elastic limits points.

Three regions of interest (ROI) were identified on force/displacement curves to performed the post-processing of the stress/strain curves. The toe region (ROI 1 in Fig. 42) corresponds to a non-linear region before the linear region (region 2 in Fig. 42). The elastic limit is defined as the maximum stress point in the linear region. The third region follows the elastic limit and corresponds to a non-linear region called damage region (ROI 2 in Fig. 42). The beginning of the damage region was defined by the first observed macroscopic drop in the force-displacement curve even if fiber ruptures could be present before this non-linear ROI. Several others local damage sub-regions describing a progressive, in stages, load loss linked with the progressive in stages rupture. To determine the range of the linear region, the second derivative of each force/displacement curve was computed and the maximum and the minimum inflection points were identified. The maximum and the minimum values of the second derivative were found and projected on the force/displacement curves to establish the elasticity region by two points corresponding to the stress/strain curve as follows. The toe stress (σ_{toe}) and strain (ϵ_{toe}) represent the values of the first elastic limit point and the damage stress (σ_{damage}) and strain (ϵ_{damage}) represent the values of the second elastic limit point [Fig. 42]. A linear regression was computed between the elastic limits ($R^2 > 0.99$ for 111 over 119 fresh samples, and 21 over 22 flash freezing samples). The elastic moduli were computed from the linear regression defining equations (1), (2) and (3). A comparison of elastic moduli between the fresh and flash-frozen samples was performed only for the thoracic spinal samples. This choice was made to avoid the inter-level spinal variability of the samples.

Hyperelasticity

An isotropic hyperelastic one-degree Ogden model was fitted on each experimental curve depicted on Fig. 43. The uniaxial stress-stretch Ogden function (4) is expressed as :

$$\sigma = \frac{2\mu}{b} \left(\lambda^{b-1} + \lambda^{\frac{-b}{2}-1} \right) \quad (4)$$

Where μ is the shear modulus and b is a material constant and the stretch ratio defined as $\lambda = \epsilon + 1$.

The curve fitting was performed with the nonlinear least squares method using the fit function in Matlab R2018b (MatWorks, Natick, MA, USA) and evaluated by a R^2 and RMSE (Root Mean Square Error).

1.2.5. Statistical analysis

The uncertainty of samples' CSA, and its effect on the linear modulus, due to the use of a sample thickness estimated from a different animal, was evaluated. This uncertainty evaluation was based on the ISO 98:1995 Guide to the Expression of Uncertainty in Measurement (GUM) [ISO 98:1995 GUM] and used the Monte-Carlo simulation approach described in the GUM supplement 1 [JCGM 101:2008].

The model of surface uncertainty is defined as presented in equation (5), where u_S is the uncertainty of the surface value, $u_{w_{rep}}$ is the uncertainty induced by the repeatability of width measurements, $u_{w_{resolution}}$ is the uncertainty induced by the DIC resolution to measure the width, and $u_{th_{rep}}$ is the uncertainty induced by the repeatability of thickness measurement.

$$u_S = (u_{w_{rep}} + u_{w_{resolution}}) * u_{th_{rep}} \quad (5)$$

An algorithm [Solaguren-Beascoa Fernandez et al. 2009] was used with the following input distributions: $u_{w_{rep}}$ was defined as a normal distribution from the mean of and the standard deviation (SD) of $w_{measures}$.

$u_{w_{resolution}}$ was defined as a uniform distribution from $-DIC_{resolution}$ to $+DIC_{resolution}$.

$u_{th_{rep}}$ was defined as a normal distribution from the mean of and the standard deviation (SD) of $th_{measures}$.

$w_{measures}$ represents all the width measurements by type of tissue and by spinal level, $w_{resolution}$ represents the resolution of the DIC, and th_{rep} represents all the thickness measurements by type of tissue and by spinal level.

Then, a probabilistic range of linear modulus is provided based on the 32th and the 68th percentile values of the measurement CSA distribution for each sample, corresponding to the most likely physical confidence interval. Then the 32th and the 68th probabilistic value of elastic modulus were calculated from the 32th and the 68th probabilistic value of the CSA. The Monte-Carlo GUM methodology is described in [appendix A](#).

All data were statistically analyzed as follows. The normality of each distribution was verified using Shapiro-Wilk normality tests. Due to the heterogeneity of normal distribution and the unequal distribution size, Wilcoxon rank sum test was performed to quantify the significant difference of all variables (force, stress, displacement, strain, elastic modulus) with respect to the spinal levels, the orientation of loading for the DAC as well as the conservation methods. The significance level was set to $p < 0.05$. Data analysis was performed using Matlab software (R2018a version, Matlab®MathWorks,1984). Additionally, Bayesian linear mixed models (blme package - <https://github.com/vdorie/blme>) were fitted with R [R Core Team 2018] to assess the dependency of our result to the subjects and computed the standard errors (SE) of the elastic modulus taking into account the between-subjects and within-subjects variabilities [Tirrell et al. 2018].

1.3.Results

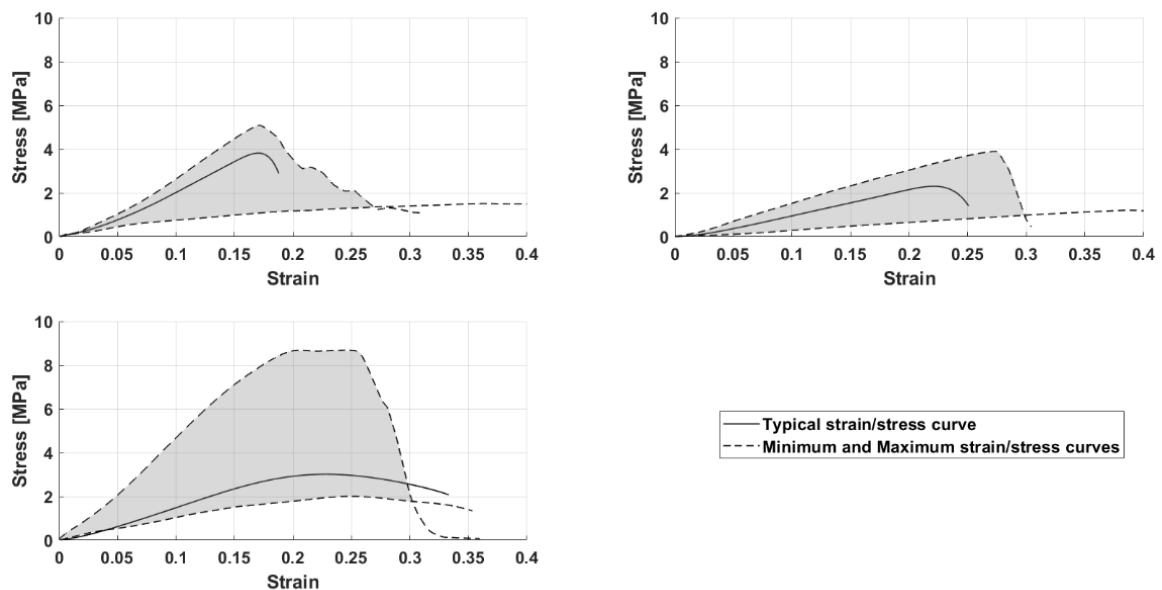


Figure 43. Mechanical of the tissue samples (shaded and curves): A - longitudinal DAC ; B - circumferential DAC ; C - longitudinal PM). Dotted lines represent the maximum and the minimum stress/strain curves delineating the experimental corridor (shaded area) and the continuous lines represent the typical stress/strain curves for A, B and C.

The description of fresh and flash-frozen samples which were tested, excluded and analyzed is summarized in Table 17. The exclusion criteria are the following: sample damaged before being fastened into the clamps, sample not well fastened in the clamps, issue due to an operator error with the control command of the computer. Ten fresh samples (0 from longitudinal DAC, 6 from circumferential DAC, 4 from longitudinal pia mater) and 3 flash-frozen samples (0 from longitudinal DAC, 2 from circumferential DAC, 1 from longitudinal pia mater) tore at the middle of their length. All experimental tests were completed less than 12 hours and 30 min after euthanasia of the animal (mean: 7 h 26 min; max: 12 h 23 min).

The dimension of samples from the experimental measured are depicted in Table 18. The samples' range of length is between 8.33 mm and 15.49 mm for the longitudinal DAC while it is between 6.36 mm and 18.51 mm for the circumferential DAC. The range of length is between 6.23 mm and 13.91 mm for the longitudinal PM samples. The DAC sample harvested at the thoracic level are the thickest (0.28 mm) while it is the cervical level for the PM (0.22 mm). The sample's CSA is the greatest at the thoracic levels for the longitudinal and circumferential DAC and the longitudinal PM (with a mean value of 3.77 mm², 4.84 mm² and 2.44 mm² respectively).

Figure 43 reports the corridor of mechanical properties of the fresh samples: the DAC and the PM behavior in longitudinal direction and the DAC behavior in the circumferential direction. The lower and upper curves describe the experimental corridor (shaded area) defining the range from minimum and maximum engineering stress/strain curves. Solid curves represent the typical stress/strain curve.

The elastic modulus of DAC in the longitudinal direction was found to be significantly different between the cervical level (22.35 ± 10.0 MPa) and the two others levels, thoracic (38.1 ± 12.6 MPa) and lumbar (36.6 ± 12.6 MPa). The elastic limit or damage stress/strain point of the cervical samples (0.25 ± 0.09) is

1.7 times superior when compared to the thoracic samples (0.15 ± 0.09), and 1.4 times inferior than the lumbar samples (0.18 ± 0.09). The elastic limit (damage strain) of the circumferential lumbar samples (0.32 ± 0.14) is 1.5 times superior than for the thoracic samples (0.21 ± 0.08) and 1.4 times superior than the cervical samples (0.23 ± 0.1). Elastic modulus of the thoracic samples (21.2 ± 3.0 MPa) is 1.7 times superior than lumbar samples (12.2 ± 4.4 MPa) and slightly superior than cervical samples (20.6 ± 8.1 MPa). Significant differences were found between longitudinal and circumferential elastic moduli between the thoracic (38.1 ± 12.6 MPa against 21.2 ± 3.0 MPa respectively) and lumbar spine (36.6 ± 12.6 MPa against 12.2 ± 4.4 respectively) samples, but not with the cervical samples [Table 19]. No significant difference was found between the fresh samples and the flash frozen samples for the DAC [Table 19].

No significant difference was noticed between the levels for the elastic modulus. The elastic modulus of longitudinal PM was significantly different between fresh and flash frozen samples (17.2 ± 9 MPa against 21.3 ± 9.1 MPa respectively) [Table 19].

The CSA were used to choose the most likely CSA of tested samples from the probabilistic distribution computed from a Monte-Carlo approach of uncertainties quantification. Then the probabilistic range of elastic moduli computed from the 38th (E_38) and 62th (E_62) percentile probabilistic values of CSA is depicted in the Table 19. The range of probabilistic values of elastic modulus differ from the standard deviation range. Indeed, the probabilistic elastic moduli range (E_32 – E_68) was greater than the range of SD experimental elastic moduli (E) for DAC samples in circumferential direction. In longitudinal direction, the inferior value of probabilistic range (E_62) was greater than the SD inferior value of DAC samples. For the PM samples in longitudinal direction, E_38 and E_62 values were respectively always greater to the superior and the inferior SD values.

Ogden coefficient presented in Table 23 were computed for curves (min, max and typical) of the Fig. 4 and were represented in Figure 46 [Appendix B].

Typical stress and strain fields were depicted in Figure 47, 48 and 49 (Appendix C) as well as the maximum deformations to failure in Table 23 [Appendix B]. The maximum stresses and strains are not located in the same part of the sample describing the heterogeneous behavior of the DAC and PM tissues.

Level	Tissue	Fresh samples			Flash Frozen samples		
		Nb of tested samples	Nb of excluded	Nb of analyzed	Nb of tested samples	Nb of excluded	Nb of analyzed
Cervical	LONG DAC	15	1	14		X	
	CIRC DAC	20	3	17		X	
	LONG PM	14	0	14		X	
Thoracic	LONG DAC	15	3	12	9	3	6
	CIRC DAC	8	0	8	11	0	11
	LONG PM	18	1	17	13	5	8
Lumbar	LONG DAC	10	0	10		X	
	CIRC DAC	12	1	11		X	
	LONG PM	16	0	16		X	
Total	LONG DAC	40	4	36	9	3	6
	CIRC DAC	40	4	36	11	0	11
	LONG PM	48	1	47	13	5	8
Total		128	9	119	33	8	25

Table 17. Summarized description of number of samples

Level	Tissue	Length [mm]	Width [mm]	Thickness [mm]	Cross-sectional area [mm ²]
Cervical	LONG DAC	9.65 (0.96) [8.33-12.06]	11.35 (2.22) [8.1-15.73]	0.28 (0.05) [0.22-0.37]	3.18 (0.62) [2.27-4.40]
	CIRC DAC	10.61 (1.95) [8.19-15.92]	11.16 (2.75) [7.2-15.02]	0.28 (0.05) [0.22-0.37]	3.12 (0.77) [2.02-4.21]
	LONG PM	9.1 (1.7) [6.99-12.7]	8.09 (1.93) [3.96-10.92]	0.22 (0.04) [0.16-0.28]	1.78 (0.42) [0.87-2.40]
Thoracic	LONG DAC	11.7 (1.81) [9.23-15.36]	11.79 (4.6) [7.66-22.44]	0.32 (0.05) [0.19-0.49]	3.77 (1.47) [2.45-7.18]
	CIRC DAC	11.18 (2.22) [9.14-15.6]	15.12 (3.62) [9.34-20.98]	0.32 (0.05) [0.19-0.49]	4.84 (1.16) [2.99-6.71]
	LONG PM	10.65 (1.61) [8.1-13.75]	12.13 (3.75) [4.5-16.21]	0.2 (0.05) [0.11-0.29]	2.44 (0.76) [0.90-3.24]
Lumbar	LONG DAC	12.35 (1.92) [10.08-15.49]	9.64 (1.69) [7.94-12.57]	0.28 (0.05) [0.21-0.37]	2.7 (0.47) [2.22-3.52]
	CIRC DAC	11.36 (3.44) [6.36-18.51]	12.03 (3.01) [6.88-6.69]	0.28 (0.05) [0.21-0.37]	3.37 (0.84) [1.93-4.67]
	LONG PM	11.13 (2.14) [6.23-13.91]	8.88 (2.35) [4.79-12.55]	0.2 (0.04) [0.14-0.28]	1.78 (0.47) [0.96-2.51]

Table 18. Summary of sample dimensions. Each quantity is described as the mean value, the standard deviation between parenthesis and the min and max respectively, between brackets.

Level	Tissue	Elastic Modulus [MPa]	
		Fresh samples	Flash Frozen samples
Thoracic	LONG DAC	38.1 (12.6) n=12	39.3 (19.3) n=6
	CIRC DAC	21.2 (3) n=8	17.4 (4.4) n=11
	LONG PM	17.2 (9) n=17	21.3 (9.1) n=5

Table 19. Comparison table of samples's elastic modulus between fresh and flash-freezing conservation methods. **Bold*** stands for a significant difference between the fresh and the flash-freezing samples for the thoracic level and a given tissue ($p < 0.05$).

Level	Tissue	Toe strain (ϵ_{toe})	Toe stress (σ_{toe}) [MPa]	Failure strain ($\epsilon_{failure}$)	Failure stress ($\sigma_{failure}$) [MPa]	Elastic modulus (E) [MPa]	E_0.32 [MPa]	E_0.68 [MPa]
	LONG DAC (n=14)	0.04 (0,03)*T	0.5 (0.21)	0.25 (0.09)*T,L	5.08 (2.97)	22.3 (10.0)*T,L (SE: 23.0)	30.3	17.4
Cervical	CIRC DAC (n=17)	0.04 (0.02)	0.49 (0.37)	0.23 (0.1)*L	4.1 (2.23)	20.6 (8.1)*L (SE: 6.6)	49.5	25.8
	LONG PM (n=14)	0.03 (0.01)*T,L	0.64 (0.27)*T,L	0.23 (0.08)	3.85 (1.88)	18.4 (8.0) (SE: 14.4)	30.4	16.0
	LONG DAC (n=12)	0.02 (0.01)*C	0.49 (0.33)	0.15 (0.09)*C	4.98 (2.7)	38.1 (12.6)*C, \S (SE: 23.3)	69.1	27.4
Thoracic	CIRC DAC (n=8)	0.03 (0.01)	0.27 (0.07)	0.21 (0.08)*L	3.94 (1.38)*L	21.2 (3.0)*L,\S (SE: 6.7)	30.4	16.6
	LONG PM (n=17)	0.02 (0.02)*C	0.34 (0.18)*C	0.2 (0.05)	3.07 (1.73)	17.2 (9) (SE: 13.7)	28.4	11.6
	LONG DAC (n=10)	0.03 (0.01)	0.73 (0.41)	0.18 (0.09)*C	5.3 (1.62)	36.6 (12.6)*C, \S (SE: 23.8)	45.2	26.8
Lumbar	CIRC DAC (n=11)	0.03 (0.01)	0.3 (0.11)	0.32 (0.14)*C,T	3.26 (0.89)*T	12.2 (4.4)*C,T,\S (SE: 6.6)	17.2	8.9
	LONG PM (n=16)	0.02 (0.01)*C	0.43 (0.2)*C	0.18 (0.03)	3.17 (0.91)	19.6 (6.8) (SE: 13.5)	31.1	15.2
	LONG DAC (n=36)	0.03 (0,02)	0.56 (0.32)	0.2 (0.1)	5.11 (2.5)	32.3 (13.5) (SE: 21.7)		
Total	CIRC DAC (n=36)	0.03 (0,02)	0.38 (0.28)	0.25 (0.12)	3.81 (1.74)	18.0 (7.3) (SE: 6.53)		
	LONG PM (n=47)	0.02 (0,01)	0.46 (0.25)	0.2 (0.06)	3.34 (1.56)	18.4 (7.9) (SE: 10.2)		

Table 20. Summary of post-processed quantities by spinal segment (stress, strain, elastic moduli and probabilistic elastic moduli) for toe region, quasi-linear region and damage region. Mean with standard deviation in parenthesis values as well as reported standard error (SE).

Bold*C,T,L stand for a significant difference between the spinal level and the level given by the letters C (cervical), T (thoracic) or L (lumbar) for a given tissue and a given variable ($p < 0.05$). **Bold \S** stands for a significant difference between the DAC longitudinal and circumferential for a given spinal level ($p < 0.05$).

Authors	Journal	Number of specimen ; samples	Specie	Tissue	Spinal level	Type of test	Strain rates	Conservation method	Elastic modulus	
									Longitudinal	Transverse
Patin <i>et al.</i> 1993	Anesthesia & Analgesia	9 specimens ; 7 samples by specie	human dog	dura mater	lumbar	uniaxial tension	1.67 mm/s	Refrigerated in saline solution	human : 138 - 265 MPa dog : 58.8 - 73.5 MPa	human : 7.8 - 76.4 MPa dog : 54.9 - 58.8 MPa
Runza <i>et al.</i> 1999	Anesthesia & Analgesia	6 cadavers	human bovin	dura mater	T12 - L4/L5	uniaxial tension	10 mm/min	In saline solution , frozen at 4°C for 24h and 120h	human : 65 - 102 MPa bovin : 25 - 80 MPa	human : 5 MPa
Maikos <i>et al.</i> 2008	Journal of Neurotrauma	23 spinal samples	rat	dura mater	C1 - L1	uniaxial tension	19.4 sec-1; 0.0014 sec-1	2h after sacrifice		
Mazgajczyk <i>et al.</i> 2012	Acta of bioengineering and biomechanic	9 specimens ; 250 samples	porcine	dura mater	C1 - C7	uniaxial tension	2 mm/min	Frozen		
Chauvet <i>et al.</i> 2010	Neurosurgical Review	10 specimens; 22 samples	human	dura mater	Craniocervical junction	uniaxial tension		Fresh cadaver	entire dura : 44 - 91 MPa split dura : 19 - 25 MPa	
Yang <i>et al.</i> 2019	Zhongguo Xiu Fu Chong Jian Wai Ke Za Zhi	5 specimens	sheep	dura mater	C6, C7, T11, T12, L4, and L5	uniaxial tension	0.016 mm/s	in saline solution	cervical : 15.97±2.52 MPa thoracic : 12.39±1.88 MPa lumbar : 8.33 ±3.10 MPa	cervical : 14.38±2.68 MPa thoracic : 8.78±1.01 MPa lumbar : 3.46±1.24 MPa
Ozawa <i>et al.</i> 2011	Journal of Neurosurgery	9 specimens	rabbit	pia mater	C5 - C6	uniaxial tension and compression	0.02 N/s	In saline solution	2.4 MPa	
Ramo <i>et al.</i> 2018c	Acta Biomaterialia	8 specimens	ewe	pia-arachnoid complex	C0 - C7	uniaxial tension	0.05sec-1	fresh after sacrifice	17 MPa	

Table 21. Comparative literature table of mechanical characterization of spinal meninges

Loading direction/ Tissue	μ	b	R^2	RMSE
Longitudinal DAC				
Curve 1 (superior limit of the corridor)	6.619 (6.452, 6.787)	11.8 (11.36, 12.24)	0.9974	0.0739
Curve 2 (typical curve)	5.02 (4.882, 5.158)	11.93 (11.45, 12.41)	0.9966	0.0613
Curve 3 (inferior limit of the corridor)	3.286 (2.966, 3.606)	-7.291 (-16.47, 1.888)	0.9916	0.0292
Circumferential DAC				
Curve 1 (superior limit of the corridor)	4.684 (4.562, 4.806)	6.955 (6.379, 7.531)	0.9973	0.0396
Curve 2 (typical curve)	2.499 (2.397, 2.6)	10.5 (9.761, 11.24)	0.9942	0.0377
Curve 3 (inferior limit of the corridor)	0.765 (0.74, 0.79)	10.77 (10.18, 11.36)	0.9946	0.0109
Longitudinal PM				
Curve 1 (superior limit of the corridor)	14.12 (13.88, 14.36)	7.342 (6.972, 7.712)	0.9984	0.0885
Curve 2 (typical curve)	4.184 (4.04, 4.329)	9.01 (8.338, 9.683)	0.9966	0.0437
Curve 3 (inferior limit of the corridor)	3.763 (3.684, 3.842)	2.549 (1.927, 3.172)	0.9977	0.0235

Table 22. One degree Ogden model material constants b and μ the shear modulus of the curves depicted in Fig. 4 and Fig. B (Appendix B). A 95% confidence interval is provided between parenthesis for each couple of the material constants.

1.4. Discussion

The elastic mechanical properties of meninges along the porcine spinal cord were quantified and tested in the longitudinal and the circumferential directions. While assuming a linear elastic behavior only provides a macroscopic mechanical description of only the linear part of the stress/stress curve. The results showed that the cervical DAC linear modulus is the lowest in longitudinal loading direction while the lumbar DAC linear modulus is the highest in circumferential loading direction. The effect of conservation method between fresh and flash frozen (at -80°C) samples at the thoracic level showed suggest the reliability of the flash frozen conservative approach for DAC tissues. To the best of our knowledge, such comparison of mechanical properties between the cervical, thoracic and lumbar spinal levels as well as of the behavior of flash frozen with fresh samples is an addition to the current literature. A probabilistic quantification of CSA was performed to estimate the effect of measurement variabilities reported for the thickness and the width, resulting in a probabilistic elastic moduli per tissue and loading direction.

For the next paragraphs, the literature comparisons were solely focused on spinal meninges mechanical properties, without any comparison with the brain meninges properties. This choice was done due to the difference of structural tissue alignments.

1.4.1. Spinal levels

Dura-Arachnoid Complex (DAC).

The significant mechanical difference between the porcine DAC elastic moduli tested in longitudinal and circumferential loading directions matched the mechanical spinal dura mater behavior previously reported in literature. However, the magnitude of our elastic moduli was lower. Our mean longitudinal elastic modulus of DAC was 1.8 times significantly superior to the circumferential elastic modulus at the thoracic spinal level while the longitudinal elastic modulus was three times significantly superior to the circumferential elastic modulus at the lumbar spinal level which is lower than literature measurements. The longitudinal over circumferential elastic moduli ratio is still coherent [Patin et al. 1996, Zarzur 1996, Runza et al. 1999, Yang et al. 2019]. Then, our results in terms of elastic modulus support a longitudinal fiber alignment for the pigs, in accordance with the literature for the rat [Maikos et al. 2008], the dog [Patin et al. 1996], for the pig [Kinaci et al. 2020] and for the human [Chauvet et al. 2010]. We showed elasticity variations along the canal for the DAC in longitudinal and in circumferential loading directions. The greatest elasticity in longitudinal loading direction was measured at the cervical spinal level whereas the greatest elasticity in the circumferential loading direction was measured at the lumbar level.

In longitudinal loading direction for DAC samples, significant differences were highlighted in our study between each spinal level of elastic moduli. The reported longitudinal elastic modulus at the lumbar level of human cadavers varied between 65 and 102 MPa for fresh samples [Runza et al. 1999] whereas it was 36.6 ± 12.6 MPa in our study in similar testing conditions. A similar difference is observed between the frozen samples of human cadavers varying between 42 and 142 MPa [Runza et al. 1999] whereas it was 39.3 ± 19.3 MPa for flash frozen samples in our study. In circumferential loading direction, the DAC elastic modulus was found significantly lower at the lumbar level in this study when compared to cervical and thoracic levels. These differences of elasticity could be due to local structural changes at the cervical and lumbar levels in order to respectively support the longitudinal and the circumferential loading. Indeed, the particular local geometry around the foramen magnum and around the cauda equina would induce these local structural changes, locally modifying the mechanical properties. A loss of a longitudinal alignment at the cervical and the lumbar spinal levels could explain a loss of cervical longitudinal and lumbar circumferential elasticity.

Firstly, a potential link between the tissue stiffness variation and the range of motion of each spinal segment could explain such findings. Indeed, the absence of significant difference between the longitudinal and the circumferential loading orientation at the cervical level of DAC could be explained by the variation of range of motion (ROM) between the spinal segments (cervical, thoracic, lumbar). Indeed, the ROM in flexion/extension, lateral bending angles are greater at the cervical level [Wilke et al. 2011, Persson et al. 2010]. The capacity to flex and to bend of the neck do not induce any significant difference of elastic mechanical properties in longitudinal and in circumferential directions. Then, the lower ROM in the thoracic and lumbar spinal levels bringing a greater stability [Wilke et al. 2011] limits the circumferential the stresses and the strains in the canal. For the dura mater, this could result in a higher capacity to be stressed in the longitudinal orientation.

Secondly, the higher values of circumferential stiffness of the DAC were found at the cervical and thoracic levels. The high or reasonable presence of cerebrospinal fluid (CSF) vortices and the higher CSF pulsatile pressure in the canal of the cervical and thoracic segments compared to the lumbar segment [Tangen et al. 2015, Khani et al. 2018] could explain such observations. Indeed, these potential stresses applied by the fluid vortices (orthogonally to the longitudinal flow direction) on the DAC in the upper spinal levels could create a tissue densification driving to a greater circumferential rigidity. This assumption takes its source from the Davis 'law (the corollary of Wolff's law for soft tissue) [Davis 1867] and from others mechanobiological theories [Liedekerke et al. 2019, Cyron and Humphrey 2017].

Pia mater

In PM samples, no significant difference was observed between the elastic moduli of each spinal level. There is a limited number of studies on the PM tissue material properties compared to the dura mater. Accordingly, no comparative data was found. However, two studies investigating pia mater properties performed on ewe and rabbit model were used as partial comparative data. Our results show a significantly higher value of elastic modulus (18.4 ± 8 MPa) compared to the elastic modulus of cervical rabbit (2.4 MPa) tested with a ramp of 0.02 N/s [Ozawa et al. 2004]. This difference can be explain by the inter-specie ROM, the motion strategy and the morphology between the rabbit and the porcine model. However, our values are coherent with the modulus (17 MPa) of the cervical ewe PM samples tested at strain rate of 0.05/s [Ramo et al. 2018c]. Ozawa et al. [2004] showed that the rabbit pia mater increased the stiffness of the spinal cord and enhanced its shape recovery after releasing the compression on the spinal cord. The porcine PM sheath seems also maintain the oval spinal cord shape with a similar elasticity. Then the Poisson's effect of the human spinal cord [Breig and Braxton 1960, Sudres et al. 2020] could be limited by the PM mechanical properties. The PM would mitigate the stresses and strains into the spinal cord during posture changes.

1.4.2. Protocol aspects

Testing model

Due to morphological, feasibility, housing, ethical in term of accessibility to human cadavers, histological [Kinaci et al. 2020] and biomechanical considerations in term of the cervical and thoracic ROM in lateral bending and in flexion/extension [Wilke et al. 2011], this quadruped makes the most appropriate transversal models human, next to non-human primates [Schomberg et al. 2017].

Failure pattern aspects

One of the limitations of our protocol is the method used to cut our samples. That could generate high damaging risks, making it difficult to homogenize the dimensions of each samples. The consequence of that is a random control of the failure location with failures located at the level of clamps in a majority

of samples, induced by stress concentration by the jaws [Figure 51 - Appendix C]. When the failure occurred in the center of samples [Figure 52 -Appendix C], we observed a difference of failure pattern between the DAC in circumferential loading and the PM in longitudinal loading. Indeed, PM appeared to be more heterogeneous with vessels more apparent while the DAC appeared more homogeneous macroscopically with an assumed longitudinal fiber organization.

Additional stress and strain fields analyses were proposed on typical samples [Fig. 47, 48 and 49]. Two solutions could solve this protocol issue: cutting using the sample with a steel mechanical cutting piece [Chauvet et al. 2010] and the fastening of the sample to the clamps with a pressure sensor, thus ensuring symmetrical boundary conditions. In addition, working in an environmental chamber with CSF-like fluid could maintain moisture conditions of the sample and reproduce a more biofidelic test environment. However, those solutions would certainly induce longer protocols, worsening the *post mortem* degradation of tissues.

Conservative approaches

Regarding conservative method aspect, our value of elastic moduli as well as our values of damage stresses are lower than the mechanical properties provided in the literature [Runza et al. 1999]. This difference could be due to the time and the choice of conservation (mean time after euthanasia: mean of 7h26 against between less than 24h and 120h of low temperature freezing). The classical freezing at -4°C seems to result in a drying of the sample and to finally increase the stiffness of the samples. Mazgajczyk et al. [2012] showed cervical stress and strain values greater than our measurements. The difference of damage or maximum stresses could be explained by the porcine species used (Yorkshire X Landrace against no detailed porcine animals), the maximum time used to perform the experiments (12h23 against 24h) and the conservation method (flash freezing at -80°C against a classical freezing method below 0°C without detail).

No significant difference was mechanically observed between the fresh and flash-frozen DAC samples' elastic moduli. This could be explained by a denser fiber of the DAC structure compared to the PM structure [Reina et al. 2020]. This higher density of fibers could limit the effect of freezing at very low temperature, in limiting the shrinkage of the matter caused by H₂O presence and in limiting the quantity of fluid available in the tissue. The flash-freezing conservative approach allowed to reduce the importance of the time variable in an experimental protocol, as well as to mitigate the mechanical behavior between the flash frozen and the fresh samples. In addition, both tissues have viscoelastic properties due to their direct contact with the cerebrospinal fluid. A further study investigating the viscoelastic properties differences between fresh and flash frozen samples could highlight the effect of fluids with respect to the tissue structure in the mechanical behavior of spinal meninges. Then, the flash freezing increased the stiffness of PM samples with respect to the fresh samples. A further study could investigate this effect potentially induced by a limited number of flash-frozen PM thoracic samples.

Thickness uncertainty analysis

The measurements of force/displacement of the samples remain a challenge, particularly due to uncertainty errors induced by the protocol. The thickness measurements were not performed on the tested samples but on one specific porcine subject not included in the mechanical testing protocol due to the high damaging risk induces by tissue manipulation. Measurement errors from the tools as well as the difference of sample thickness measurement (with a different pig to avoid damaging the sample) could lead to non-linear result uncertainties [Fig. 45- Appendix A]. A propagation uncertainty analysis is not frequently used for soft tissue characterization, but it brings a more complete and comparable range of mechanical properties. The GUM uncertainty analysis [ISO 98:1995 GUM] provided the uncertainty distribution [Fig. 44- Appendix A] of CSA as an output and from input uncertainty distributions of

thickness and width repeatability and width resolution. Such output CSA uncertainty distribution is then used to the probabilistic elastic moduli calculations. The more the input uncertainty is clearly defined, the more the output uncertainty distribution will be accurate. As depicted in [Table 19](#), differences between the probabilistic moduli (E_32 and E_68) and the experimental elastic modulus (E) varied with respect to the type of tissue (DAC and PM) and with respect to the loading direction (longitudinal or circumferential). When focusing on the existing available elastic moduli values in the literature, no uncertainties are provided and the provided SD ranges of experimental elastic moduli should then be taken carefully.

To experimentally face the thickness measurement challenge, the implementation of a non-contact measurement method (laser) during the tensile test could be investigated. Otherwise, a combined approach between geometrical and biomechanical experiments would allow to establish potential correlation between geometrical and biomechanical behavior of the meninges as proposed by [Yoganandan et al. \[2000\]](#) for the cervical human ligaments.

Strain rate and elasticity approximation

Only one moderate strain rate (0.2 mm/s) was used to describe the mechanical properties of the spinal meninges along the spinal cord which would correspond to a value lower than those occurring during injury [[Ramo et al. 2018b](#)].

Previously reported uniaxial tensile tests showed no significant strain rate dependency at low strain rate and moderate strain rates (0.01s⁻¹, 0.1s⁻¹ and 1s⁻¹) for dura mater [[Persson et al.2010](#)]. The same finding was reported for the pia-arachnoid complex at 0.016 and 0.16 s⁻¹ [[Ramo et al. 2018c](#)]. However, strain dependency of the meninges should be investigated more in details in future work. In addition, the elastic properties are easily comparable with the existing literature [[Zwirner et al. 2019](#), [Runza et al. 1999](#), [Ramo et al. 2018c](#), [Ozawa et al. 2004](#)]. A potential correlation between “the higher nonlinearity observed in the circumferential direction as compared to longitudinal direction” due to the deformation of the toe region and the low deformations of the spinal cord in physiological conditions. gradual to region due to the toe region during physiological motion of the spinal cord was discussed in literature [[Shetye et al. 2014](#)]. We assumed the linear part would be a transitional phase (between the physiological behavior of the tissue and a beginning failure phase) in which the tissue is not yet injured. We additionally provided a range of isotropic hyperelastic (one term Ogden model) coefficients to provide a better description of the tissue behavior in all test loadings direction for the first 15% of strain [[Table 22](#)].

The μ Ogden coefficients of the typical curves were found superior to those provided for spinal bovine dura mater at 0.01 s⁻¹ (5.0 MPa against almost null in the longitudinal direction and 2.4 MPa against 2.2 MPa in the circumferential direction respectively). The b Ogden coefficients were found inferior to those provided in the same study (11.9 against almost 24.0 in the longitudinal direction and 10.5 against 18.0 in the circumferential direction respectively) [[Persson et al. 2010](#)]. No equivalent data was found to compare the Ogden coefficients of PM.

Trends reported in inter-segmental spinal level variation (cervical, thoracic and lumbar) of elastic properties in DAC and PM need to be confirmed due to high standard error induced by within-subject and between-subject variability. Thus a larger population of samples by levels and by subject will be tested. Anisotropic hyperelastic models [[De Keghel et al. 2018](#), [Shetye et al. 2014](#)] as well as dorsal and ventral locations of samples along the spine [[Mazgajczyk et al. 2012](#)] could be investigated in future work. Finally, our mechanical properties could be used in spine FE models such as stenotic scenarios [[Bailly et al. 2020](#)] or post-surgery analysis [[Stoner et al. 2020](#)] for a better description of tissues in longitudinal and circumferential loading direction of DAC and in longitudinal PM.

1.5.Conclusion

The porcine model is an appropriate alternative to study the mechanical properties of meninges compared to human cadavers. In addition, this study provided isotropic hyperelastic properties and showed the negligible effect of a flash freezing conservative method to provide comparable results on DAC tissues, thus limiting the effect of the time factor in such experimental protocol.

The following mean values were proposed for the elastic moduli of the spinal meninges :

- Longitudinal DAC elastic moduli : **22.4 MPa** (SE: 23.0) in cervical, **38.1 MPa** (SE: 23.3) in thoracic and **36.6 MPa** (SE: 23.81) in lumbar spinal levels.
- Circumferential DAC elastic moduli : **20.6 MPa** (SE: 6.6) in cervical, **21.2 MPa** (SE: 6.7) in thoracic and **12.2 MPa** (SE: 6.6) in lumbar spinal levels.
- Longitudinal PM elastic moduli : **18.4 MPa** (SE: 14.4) in cervical, **17.2 MPa** (SE: 13.7) in thoracic and **19.6 MPa** (SE: 13.5) in lumbar spinal levels.

This variety of mechanical properties of the meninges suggests that it cannot be regarded as a homogenous structure along the whole length of the spinal cord. Furthermore, a spatial personalization along the spinal cord of this biological soft elastic behavior should be taken into account when building a numerical model of the central nervous system.

Acknowledgements

The authors wish to thank Elisabeth Laroche for the technical assistance during the experiments.

Funding

This research was funded by Aix-Marseille University PhD scholarship and by the Franco-Quebec research grant "Samuel-De Champlain".

1.6.Appendices

Appendix A : Monte-Carlo method for the evaluation of measurement uncertainties

In sciences and engineering, the estimation of measurement uncertainties is a fundamental process for the quality of every measurement. In order to harmonize this process for every laboratory, the ISO 98:1995 Guide to the Expression of Uncertainty in Measurement established an analytical approach [ISO 98:1995 GUM].

The Monte Carlo methodology (MCM) as presented by the GUM Supplement 1 [JCGM 101:2008] is an alternative to the analytical process. The MCM does not require the validation of the next assumptions for application : an insignificant non-linearity in the model and the validity of the central limit theorem. The propagation of uncertainties through the distributions of the input sources using an uncertainty model provides a probabilistic distribution of the estimated quantity called a measurand. The process is illustrated in Figure 44.

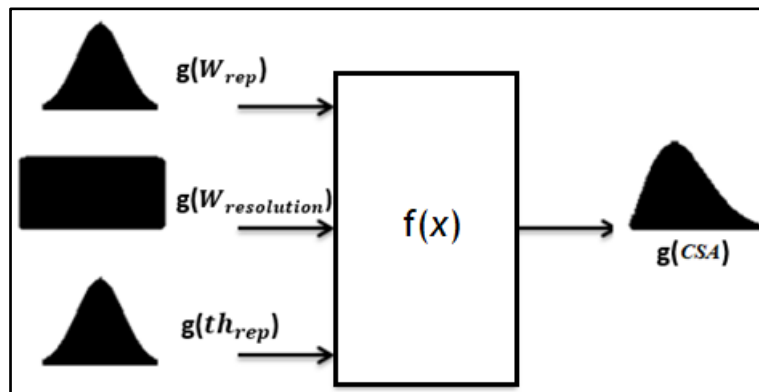


Figure 44. Schema of propagation of distributions, where $g(W_{rep})$, $g(W_{resolution})$ and $g(th_{rep})$ are the distribution functions of the input sources and $g(u_{CSA})$ is the distribution of the measurand, the quantity intended to be measured.

Methodology :

Definition of the measurand and input sources

The measurand is a final quantity dependent on the measurements. It is denoted Y and it is expressed in function input quantities X_i as:

$$Y = f(X_1, X_2, \dots, X_n) \quad A.1$$

In the article, the measurand is the surface S expressed as :

$$Y = f(W_{rep}, W_{resolution}, th_{rep}) \quad A.2$$

Modeling

In this step, the measurement quantities should be modeled to get the measurand as a result of all the input quantities. The modeling can be help by a cause-effect diagram (Fig. 45). Then, each input quantities is categorized among two types of uncertainties : type A and type B. The type A represent the uncertainties from repeatability measurement, while type B are determined from any other sources of data (resolution, calibration or not well known value).

To model the uncertainty induced by the surface computation, the equation (A.3) was proposed :

$$CSA = (w_{rep} + w_{resolution}) * th_{rep} \quad A.3$$

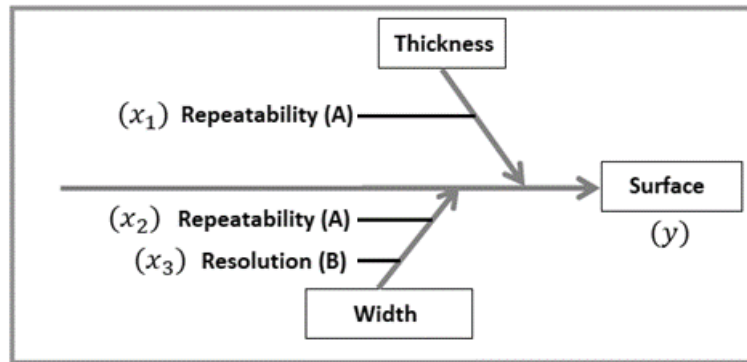


Figure 45. Cause-effect diagram for the surface of the sample uncertainty estimation. (A) and (B) represent the type of uncertainties

Estimation of the probability density function (PDFs) for the input sources

This step consists in the choice of the most appropriate probability density function for each input sources. Type B uncertainty was modeled as an uniform distribution while the type A uncertainties were modeled as Gaussian distribution after a normality test validation.

Setup and running the Monte-Carlo simulation

At this step, a number of Monte-Carlo has to be fixed, the GUM Supplement 1 recommends the selection of a number M of trials :

$$M > 10^4 / (1 - p) \quad A.4$$

Where $100 * p\%$ is the selected coverage probability. In the article, p was chose to be equal to 0.68 as proposed in the algorithm used [Solaguren-Beascoa Fernandez et al. 2009], to limit the computation cost and to guaranty a reliability of the uncertainty estimation. For the simulation, M was equal to $2 * 10^7$ trials.

The stabilization criterion for the results was fixed according a numerical tolerance proposed by the GUM supplement 1 [JCGM 101:2008]. The numerical tolerance is defined as the semi-width of the shortest interval containing all numbers that can be expressed to a specified number of significant decimal digits [Solaguren-Beascoa Fernandez et al. 2009]. The algorithm used proposed a number of decimal digits equal to 1 and a numerical tolerance equal to 5.

Computation of the linear modulus range

To compute a range of linear modulus, two values of the output probabilistic distribution of the surface quantity were used, the 32th ($CSA_{32th_percentile}$) and the 68th percentile ($CSA_{68th_percentile}$). Then, these values were injected in the formula of linear modulus as :

$$E_{32th_percentile} = \frac{mean(\Delta F_i) * mean(l_{o_i})}{mean(\Delta L_i) * CSA_{32th_percentile}} \quad A.5$$

$$E_{68th_percentile} = \frac{mean(\Delta F_i) * mean(l_{o_i})}{mean(\Delta L_i) * CSA_{68th_percentile}} \quad A.6$$

Where,

ΔF_i is the difference of each sample between the two force values of the force/displacement curve used to compute the mean value of the linear modulus.

l_{0i} is the initial length of each sample used to compute the mean value of the linear modulus.

ΔL_i is the difference of each sample between the two displacement values of the force/displacement curve used to compute the mean value of the linear modulus.

Appendix B : measurements by spinal segment of force and deformation, Ogden fit comparison with experimental curves

Level	Tissue	Toe displacement [mm]	Toe force [N]	Failure force [N]	Maximum deformation to failure [mm]
Cervical	LONG DAC (n=14)	0.36 (0.24)	1.52 (0.63)	15.24 (7.79)	2.8 (0.7)
	CIRC DAC (n=17)	0.38 (0.18)*T	1.38 (0.79)	13.32 (6.86)*T	3.2 (1.0)
	LONG PM (n=14)	0.29 (0.08)*L	1.12 (0.53)*L	7.01 (3.68)	2.5 (0.5)
Thoracic	LONG DAC (n=12)	0.28 (0.03)*L	1.64 (0.9)	18.62 (11.62)	2.1 (0.8)
	CIRC DAC (n=8)	0.28 (0.04)*C	1.28 (0.3)	19.24 (7.35)*C,L	2.5 (0.4)
	LONG PM (n=17)	0.25 (0.2)	0.78 (0.38)	6.78 (2.59)	2.9 (0.5)
Lumbar	LONG DAC (n=10)	0.39 (0.22)*T	1.98 (1.17)	14.3 (5.12)	2.6 (0.7)
	CIRC DAC (n=11)	0.34 (0.06)	0.97 (0.38)	10.42 (1.67)*T	3.9 (1.0)
	LONG PM (n=16)	0.19 (0.09)*C	0.7 (0.26)*C	5.57 (2.23)	2.3 (0.4)
Total	LONG DAC (n=36)	0.34 (0.19)	1.69 (0.89)	16.11 (8.67)	2.5 (0.8)
	CIRC DAC (n=36)	0.34 (0.14)	1.23 (0.62)	13.75 (6.6)	3.2 (1.0)
	LONG PM (n=47)	0.24 (0.14)	0.85 (0.43)	6.43 (2.86)	2.6 (0.5)

Table 23. Summary of pre-processed measurements by spinal segment (force, deformation) for toe region, quasi-linear region, damage region and maximum deformation to failure. Mean with standard deviation in parenthesis values reported. **Bold*C,T,L** stand for a significant difference between the spinal level and the level given by the letters C (cervical), T (thoracic) or L (lumbar) for a given tissue and a given variable. ($p < 0.05$).

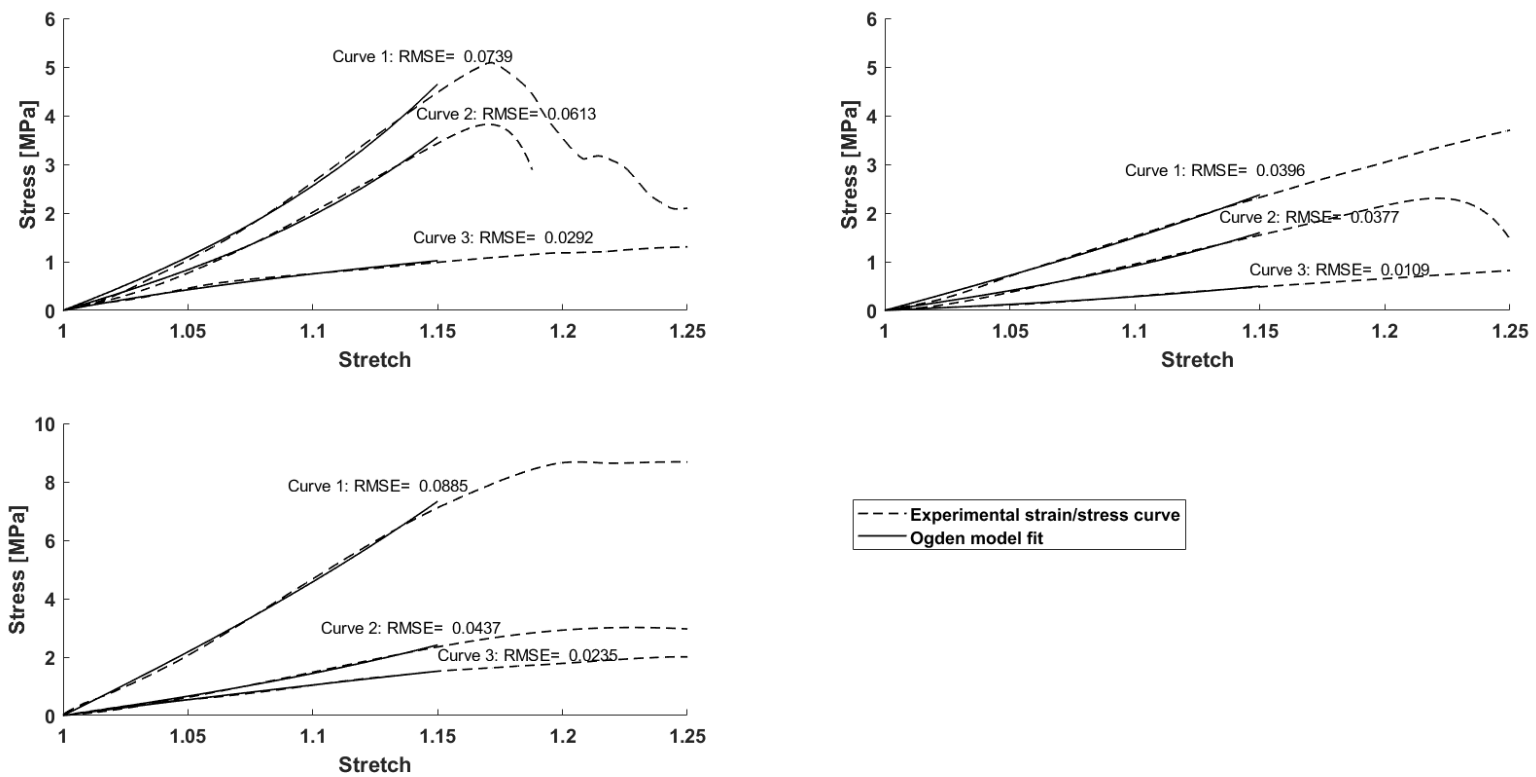


Figure 46. Comparison of experimental curves (dashed) with Ogden fitted curves (continuous). RMSE was displayed for each curve. These curves are the same than the curves in Fig. 4.

Appendix C - Preliminary analysis of digital image correlation and video records.

- pia mater sample tested in tensile longitudinal loading direction

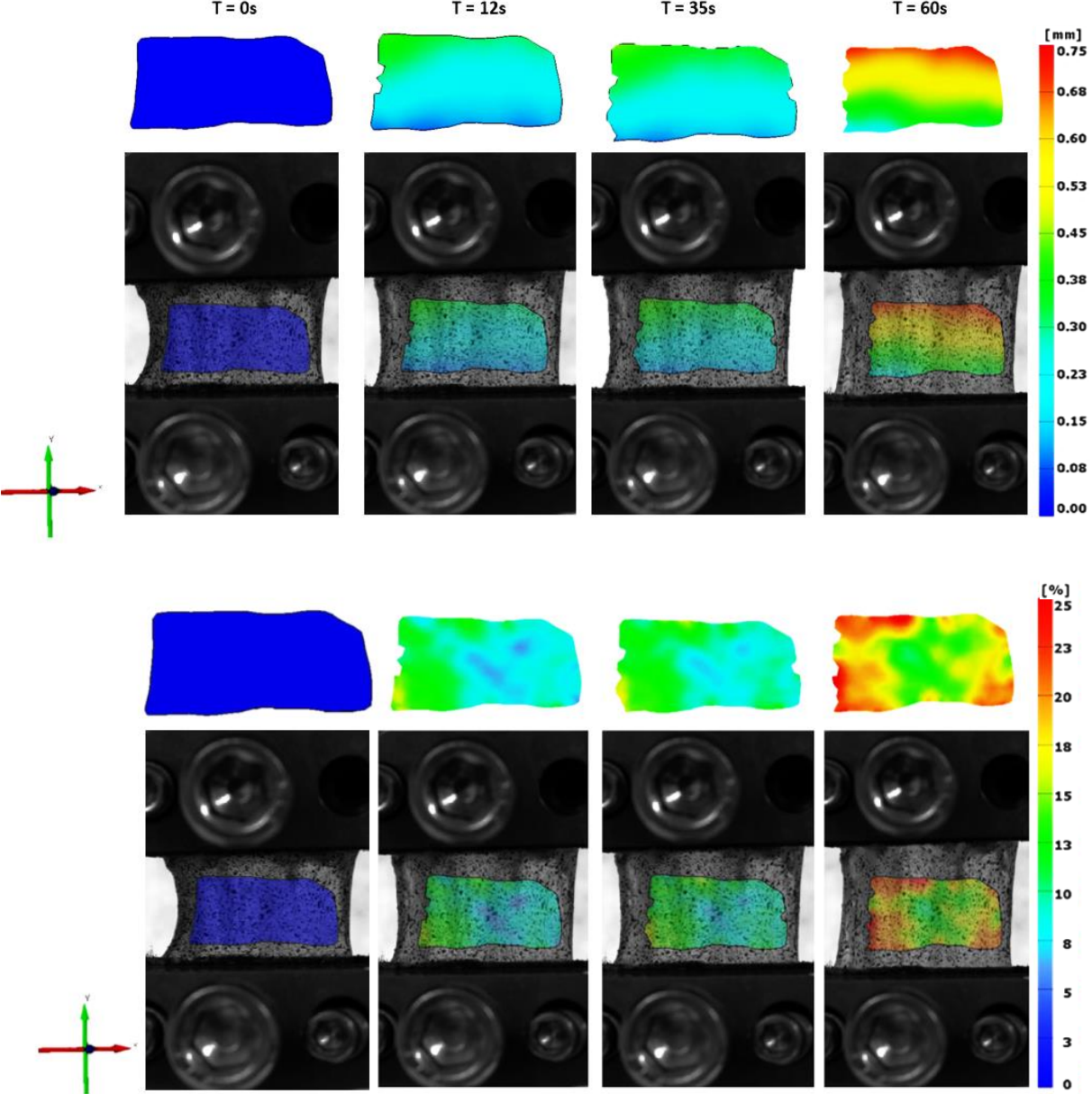


Figure 47. Typical pia mater sample DIC patterns tested in the longitudinal loading direction at time steps 0, 12, 35, 60 s. Upper image depicted the Y displacement field while the lower image depicted the Y strain.

- *dura-arachnoid mater complex sample tested in tensile circumferential loading direction*

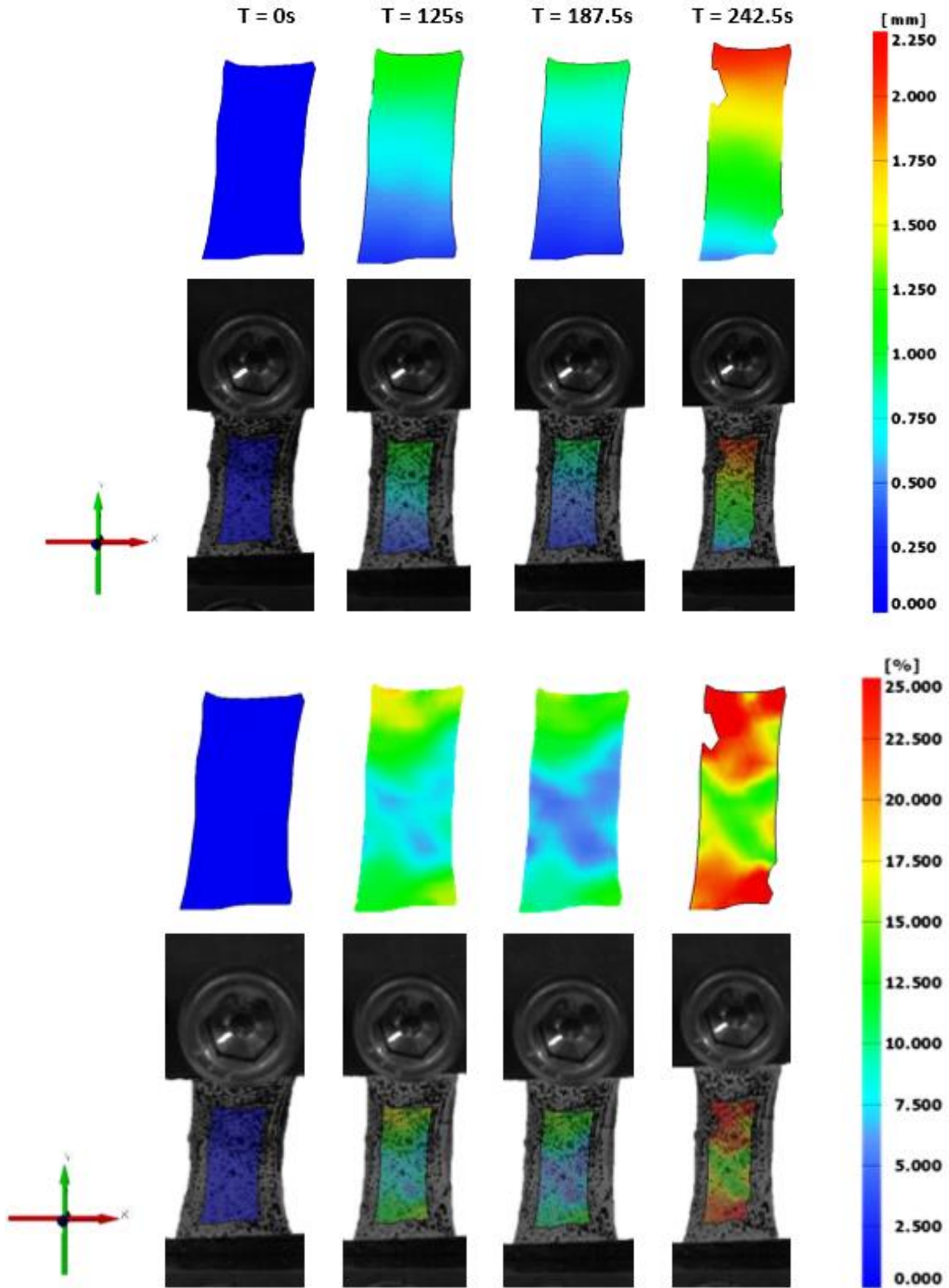


Figure 48. Typical DAC sample DIC patterns tested in the circumferential loading direction at time steps 0, 125, 187.5, 242.5 s. Upper image depicted the Y displacement field while the lower image depicted the Y strain.

- *dura-arachnoid mater complex sample tested in tensile longitudinal loading direction*

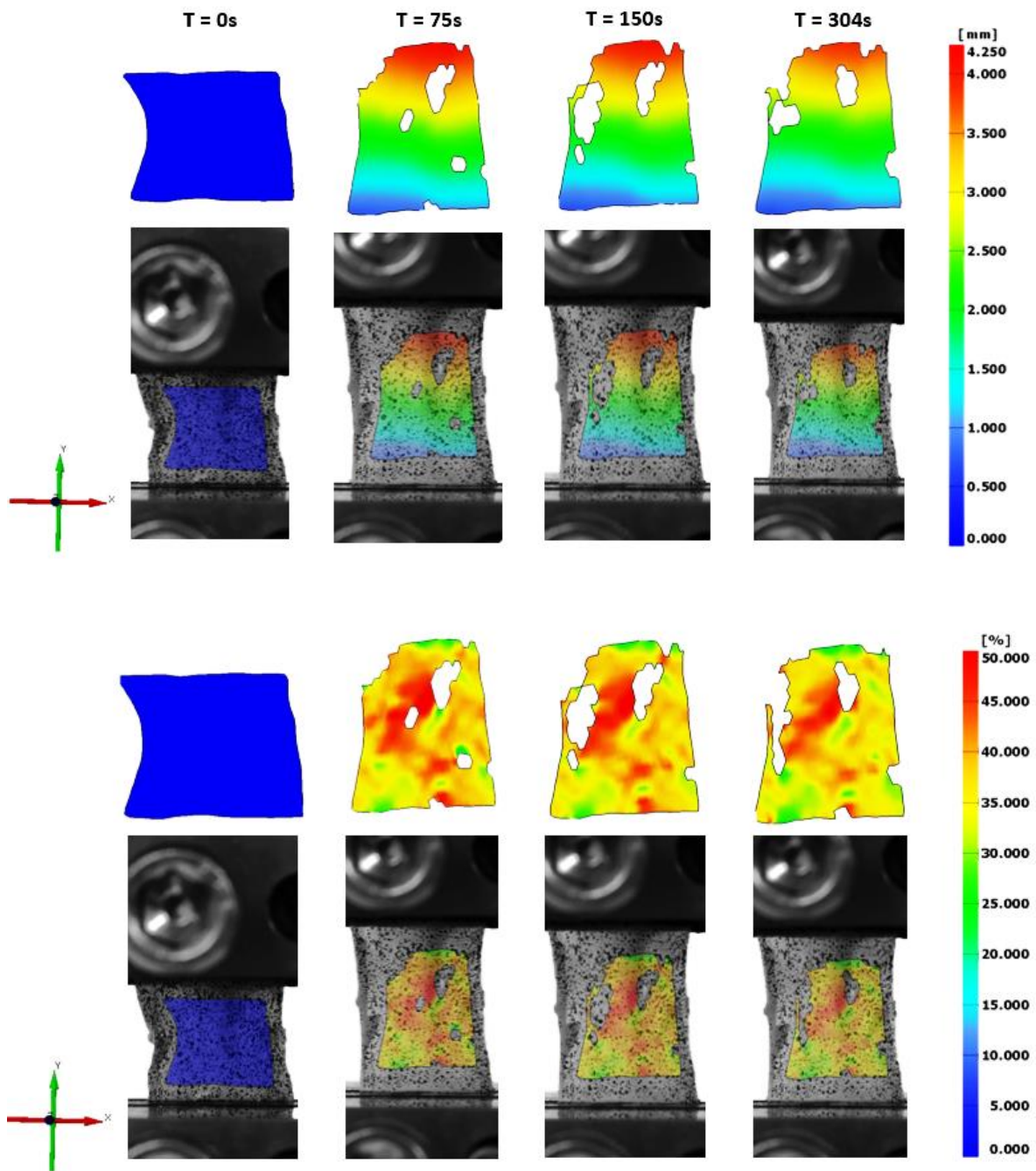


Figure 49. Typical DAC sample DIC patterns tested in the longitudinal loading direction at time steps 0, 75, 150, 304 s. Upper image depicted the Y displacement field while the lower image depicted the Y strain.

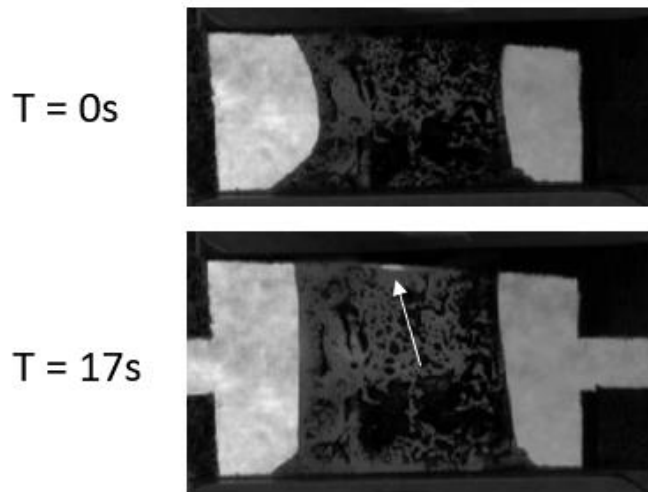


Figure 50. **C.4.** Typical example of not fully attached sample by a lack of tissue clamped in the jaws, creating a space notified by the white arrow.

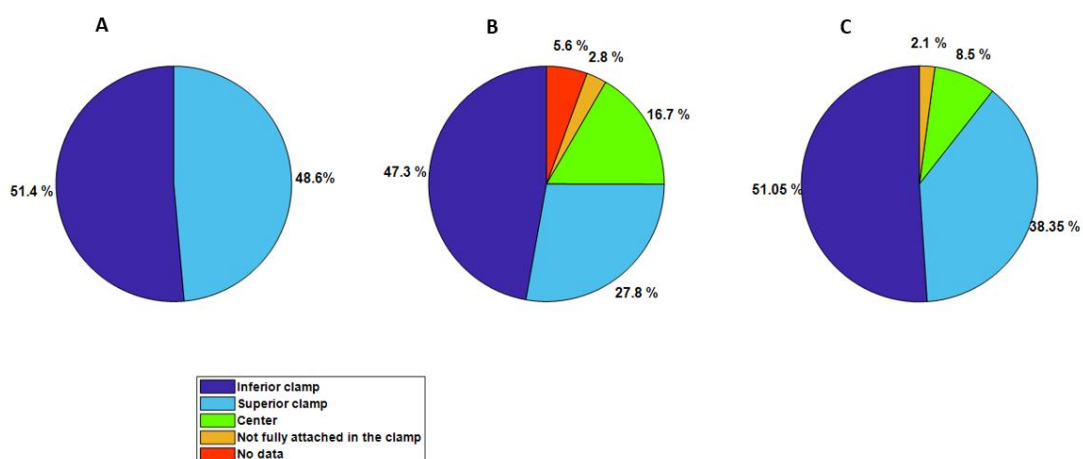


Figure 51. preliminary analysis of failure location on the samples by type of tissue. A. DAC in longitudinal loading; B. DAC in circumferential loading; C. PM in longitudinal loading. "No data" referred an absence of video recording.

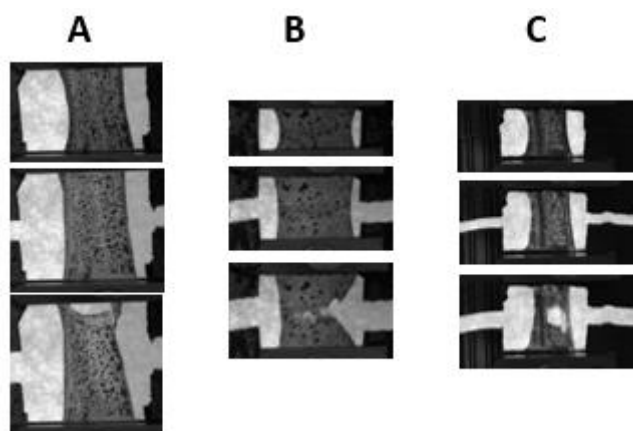


Figure 52. Typical failure patterns of samples. A. Failure at the superior clamp induced by stress concentration of the jaws (DAC in longitudinal loading). B. Failure at the center of the sample (DAC in circumferential loading). C. Failure at the center of the sample (PM in longitudinal loading).

2. Experimental Bi-axial Tensile Tests of Meningeal Tissues and Constitutive Models Comparison

Morgane Evin^{1,4}, Patrice Sudres^{1,4}, Pascal Weber⁵, Yves Godio-Raboutet^{1,4}, Pierre-Jean Arnoux^{1,4}, Eric Wagnac^{2,3,4}, Yvan Petit^{2,3,4} PhD, Yannick Thillier⁶ PhD

1. Laboratoire de Biomécanique Appliquée, UMRT24 AMU/IFSTTAR, Marseille, France.
2. Department of Mechanical Engineering, École de Technologie Supérieure, 1100 Notre-Dame Street West, Montréal, Québec H3C 1K3, Canada
3. Research Center, Hôpital du Sacré-Coeur de Montréal, 5400 Gouin blvd, Montréal H4J 1C5, Québec, Canada
4. iLab-Spine – Laboratoire International en Imagerie et Biomécanique du Rachis, Marseille, France & Montréal, Canada.
4. Institut de Neurosciences de la Timone, CNRS, AMU, Marseille, France
5. CEMEF Centre de Mise En Forme des Matériaux MINES ParisTech, PSL Research University CNRS UMR, 7635, CS10 207 06904, Sophia Antipolis Cedex, France

For this study, I contributed to develop the testing protocol, to perform the pre-tests, to provide an understanding of constitutive laws and to participate to the interpretation of data and to the writing and reading parts.

Abbreviations

CSF: cerebrospinal fluid
PM: pia mater
PAC: pia-arachnoid complex
DAC: dura-arachnoid complex
GOH: Gasser, Ogden and Holzapfel
RMSE: root mean square error

Keywords: bi-axial testing, meningeal tissue, bi-photon microscopy, hyperelasticity.

2.1. Introduction

The required understanding of physiopathology mechanisms involving meningeal tissue have been previously highlighted. Interest in dura mater mechanical behaviour was risen by the post-subdural and epidural anesthesia-puncture headaches as well as in Chiari malformation [Chauvet et al. 2010]. The dura mater integrity contributes to cerebro-spinal fluid (CSF) resorption and to the balance of intracranial pressure in human [Protasoni et al. 2011] and daily cranial volume expansion leads to the mechanical strain on dura mater growth [Fong et al. 2003]. Additionally, pia mater (PM) and arachnoid mater has been reported to change mechanical behaviour of the spinal cord [Ramo et al. 2018c]. Finite element modelling has intended to address the question of injured spinal cord in traumatic events and more recently included fluid structure interaction modelling of CSF to simulate physiology [Bertram 2010, Bertram and Heil 2017]. Such modelling requires specific material properties. In addition,

prosthetic biomaterial scaffold engineering has also been questioning structure and material properties of the meningeal tissues [Sacks and Sun 2003]. However, little is known on the mechanical properties of this meningeal tissue. Association between meningeal tissue micro-structure and mechanical properties of these tissues under physiological conditions is still unclear.

2.1.1.Meningeal micro-structure

The characterization of the micro-structure and collagen fibres of the meningeal tissues requires specific imaging technics, including histology [Reina et al. 2004], two photon microscopy or scanning electron microscopy stereo images [Reina et al. 2004]. To the best to our knowledge, few studies address the relation between structure composition and mechanical properties. The elastic modulus has been shown to be influenced by the protein content of the cranial porcine region of the dura mater analysed by immunoblot according to its locations [Walsh et al. 2018]. Microstructure of the porcine dura mater is reported to be relatively similarly to human dura mater [Kinaci et al. 2020].

At its cranial location, human dura mater was shown to be divided into three layers with different fibres organization and thickness:

The bone surface layer: a 2µm thick outermost layer with fibroblast, collagen and elastin fibres. The outer part is a structure in which the collagen fibres are disorganized while the collagen fibres are organized parallel to each other in the inner part,

a fibrous dura layer then divided into three layers with their own organisation. The external layer has one direction of collagen fibres, the vascular layer has holes and interstitial compartments and the internal layer has collagen fibres organized in bundles transversally oriented like the upper layer, and then an arachnoid layer with disorganized collagen bundles [Protasoni et al. 2011].

The arachnoid layer in the subarachnoid canal has been described as inner layer of dura mater [Reina et al. 2020] with trabeculae inserted in the pia mater and with similar cells that this latest structure [Reina et al. 2004]. It has been previously associated with PM in mechanical testing while no clear evidence supported such assumption. In the following work, arachnoid was chosen to be associated with dura mater as described in [Reina et al. 2020].

Pia structure has been described with fenestration in human cadaver's lumbar spine using histology and microscopy technics. A large amount of collagen fibres as well as few elastin fibres were identified using staining. An amorphous intracellular substance, small vessels fibroblasts and macrophages were also identified. PM has several layers: subpial tissues with collagen fibre, pial cellular layers from neuroglial cells surrounding the spinal cord [Reina et al. 2004, Machés et al. 2015].

2.1.2.Meningeal mechanical characterization

To define material properties, the experimental testing of the dura mater reported in the literature highly differ depending on the studied species and anatomical segments as well as on the objectives of the characterization protocol (description of quasi-static or dynamic behaviours of the tissue). Tensile test experimental protocols were mainly quasi-static and uniaxial. They were carried out on both brain and spinal dura mater samples in rat [Maikos et al. 2008, Henderson et al. 2005], canine [Patin et al. 1993], ovine [Shetye et al. 2014], porcine [Walsh et al. 2018, Mazgajczyk et al. 2012], bovine [Wilcox et al. 2003, Persson et al. 2010, Runza et al. 1999], and human [Chauvet et al. 2010, Runza et al. 1999, Zwirner et al. 2019, Zarzur et al. 1996, van Noort et al. 1981]. More specific studies as retraction of dura mater testing [Henderson et al. 2005], dura mater relaxation [Wilcox et al. 2003] and fatigue ratio computation [Walsh et al. 2018] as well as membrane inflation testing should also be reported [Kriewall

et al. 1983]. Uni-axial quasi-static characterization of the meningeal tissue fail at predicting mechanical behaviour in physiological context as not considering initial loading conditions.

No clear consensus has been reached on the comparison of the mechanical behaviour of the dura mater with respect to the orientation of the tested tissue. Tensile strength and stiffness were found to be greater in the longitudinal direction than in the transverse/circumferential or coronal one [Henderson et al. 2005] in human and canine [Patin et al. 1993], in human lumbar dura and bovine [Runza et al. 1999] and in human lumbar [Zarzur et al. 1996]. Two other papers reported opposite results but for lower strains [Wilcox et al. 2003, Persson et al. 2010].

Differences in mechanical behaviour of white and grey matters between the cranial and spinal locations have been previously reported [Budday et al. 2017]. Such question has not been addressed for meningeal tissues to the best to our knowledge. However, the literature reported differences in dura mater elastic modulus at different levels of the spine in ovine [Yang et al. 2019] and porcine samples [Mazgajczyk et al. 2012]. Variability along the cervical and between ventral and dorsal sides of the spinal cord in this latter study. The influence of age has been reported in rats [Henderson et al. 2005] and cranial human dura mater [Zwirner et al. 2019] (decrease of the tensile strength and elastic modulus with age). Comparison of 0.01, 0.1 and 1 s⁻¹ strain rates showed no influence of strain rate [Persson et al. 2010].

Compared to the literature available on the properties of the dura mater, PM tissue has been far less characterized. Rabbit spinal PM was tested in situ using tensile test at low strain rate (1.23g.min⁻¹) with an emphasis on the comparison between intact and incised PM [Ozawa et al. 2004]. Atomic force microscopy was used with indentation and relaxation tests to characterize cortical and cerebellar PM in rats [Fabris et al. 2019]. PM associated with brain white and grey matters has been studied in bovine model with a strain rate of 10 s⁻¹ and its quasi linear visco-elasticity behaviour has been validated up to 35% strain level [Laksari et al. 2012]. PM was also tested in bovine brains at three locations and with three different strain rates [Jin et al. 2011] using a shear test reproducing the relative motion between the inner skull and the brain, during a head impact, resulting in tangential shear loading on PM layer [Jin et al. 2011]. Isolated bovine cranial PM was also tested in quasi-static tensile test (0.5mm.min⁻¹) [Aimedieu et al. 2004]. Using atomic force microscopy indentation in rat PM and arachnoid complex (PAC), lower instantaneous Young Modulus distribution was found in vascularized PAC when compared to non-vascularized tissue [Fabris et al. 2019]. Finally, PAC was shown to have a rate-dependant behaviour with strain rates of 0.05, 0.5, 5 and 100s⁻¹ in brain bovine [Jin et al. 2006].

2.1.3. Bi-axial testing protocols

In the subarachnoid space, spinal cord surrounded by pia mater is attached by its link to brain and along the spine by nerves roots and denticulate ligaments. Dural sac surrounds the CSF and the nerves roots. Both tissues are then pre-constrained at all time in normal physiological conditions. Bi-axial tensile tests provide the two dimensional stress-state that enables constitutive modelling closer to physiological condition [Sacks et al. 2000]. the spinal ovine dura mater [Shetye et al. 2014] and human cranial vault dura mater [Sacks et al. 2000] have been tested bi-axially.

Such tests allowed the characterization of anisotropic biomaterials. Test systems and testing protocols differ in terms of gripping system, preconditioning definition, loading conditions and data analysis. Rake gripping systems were found to be less sensitive to the effects of boundary conditions when compare to clamps based methods [Sun et al. 2005]. The tested ratios of the displacements between directions were (1:1, 1:0.5 and 0.5:1) at strain rate of 0.05 s⁻¹, with 10% preconditioning and 60 mN preloading condition [De Kegel et al. 2018] and (1:1, 2:1 and 1:2) bi-axial tensile test [Shetye et al. 2014]. Depending

on the biological tissues tested, preconditioning methods can be expressed as a percentage of initial length, a percentage of maximal strain or stretch or a maximum strain value [Deplano et al. 2016]. Preconditioning under 1% in circumferential and 3% in longitudinal of maximum force was shown to not change the mechanical behaviour of the tissue but enable a better positioning of the sample on its support and stabilized the test [Wilcox et al. 2003].

The influence of the method and duration of conservation (frozen, 24h fresh; 120h fresh and dry samples comparison) on mechanical properties was reported [Runza et al. 1999]. Conservation of the dura mater was reported to be acceptable until 139 h post mortem [Zwirner et al. 2019]. Other conservation conditions have been considered, such as storage in formalin [Zarzur et al. 1996], frozen conservation [Wilcox et al. 2003], glycerol conservation [van Noort et al. 1981]. An osmotic stress protocol for water content adjustment has been proposed [Zwirner et al. 2019].

2.1.4. Constitutive modelling

Constitutive modelling includes both phenomenological and structural modelling. It mostly consists in fitting stress-strain responses with constitutive strain energy models. Such constitutive model aims to describe typical mechanical behaviours such as non-linear elasticity, anisotropy and viscoelasticity of a material. The accuracy of the constitutive model used for fitting process strongly depends on the choices and assumptions made [Fehervary et al. 2016,38].

Several constitutive models have been used to fit experimental behaviour of the dura mater. Among the simplest models, one can cite the reduced relaxation function and elastic response as in Haut et Little 1972 for collagen fibre [Wilcox et al. 2003], the Yeoh model that depends only on the first invariant of the Cauchy Green deformation tensor, or the Neo-Hookean [De Kegel et al.2018], the incompressible Ogden model (isotropic one-term hyperelastic model with no viscous term dependant to strain rate) [Maikos et al. 2008, Persson et al. 2010, De Kegel et al.2018] or Mooney Rivlin and Skalak, Tozeren, Zarda and Chien (STZC) models [Kriewall et al. 1983] for incompressible hyperelastic materials [Walsh et al. 2018]. Among the most complex models, the incompressible Ogden model is an isotropic one-term hyper-elastic model with no viscous term dependent to the strain rate [Maikos et al. 2008, Persson et al. 2010, De Kegel et al.2018]; the one proposed by Gasser is a transversely isotropic model but has also a formulation for anisotropic models with two family fibres [Shetye et al. 2014]; Gasser-Ogden-Holzapfel (GOH) model and reduced GOH model [De Kegel et al.2018].

PM associated with arachnoid mater has been modelled as linear elastic [Aimedieu et al. 2004, Jin et al. 2006], and more recently as nonlinear viscoelastic, transversely isotropic material through a Moonley-Rivlin material model for the ground matrix substance and a piecewise function for the strain energy function for fibre strengthening and for fibre reinforcement [Jin et al. 2014]. An Ogden law was also used with two parameters as well as a 3 terms Generalized Rivlin formulation [Laksari et al. 2012].

Thus, the aims of the present work are threefold:

- 1) To characterize mechanical behaviour of dura mater and arachnoid complex (DAC) and PM spinal porcine samples using quasi-static bi-axial tensile tests.
- 2) To investigate the microstructures of the spinal DAC and PM samples using bi-photon microscopy in order to provide the energy density functions of the constitutive models with such knowledge.
- 3) To check which constitutive models previously used in the literature are best suited to model the behaviour of these materials, to determine the best sets of parameters that allow them to fit experimental data and to quantify the variability of identified parameters

2.2. Material and methods

Based on histological investigation and previous work [Sudres et al. 2020], the present study considers the arachnoid complex to be associated to the dura mater rather than the pia mater [Ramo et al. 2018c].

2.2.1. Dissection and extraction of the material

As previously underlined by Ramo et al. [Ramo et al. 2018c], there is a lack of description of the extraction process, in particular how to avoid tissue degeneration as well as a lack of knowledge on the conservation process [Sudres et al. 2020]. Eight complete spines were extracted from pigs (40 to 50Kg, Yukatan, 3 to 4 months). The extraction took place less than half an hour after sacrifice. It was divided into three steps: spine extraction itself, followed by the spinal cord removal from spinal canal and sample preparation. The swine being attached in prone position, the first incision consists in a posterior opening from the skull to the sacral promontory. The flesh was then removed to access the ribs and iliac crests. A rotatory saw was used to cut the costal bone as close to the spine as possible without reaching the vertebral body. The first swine costal bones oriented forward in the thorax were manual cut as not reachable by saw.

Meningeal tissues with spinal cord were carefully removed from the spinal canal using scalpels, gouge clamps and small clamps and then the spine was cut into 4 segments through the intervertebral disks in 4 segments corresponding to cervical (C0-C7), upper thorax (T1-T7), lower thorax (T7-T15) and lumbar segments (L1-L5; Fig. 53). Sample preparation consisted in opening the dura mater on the lateral side defined by the axis between nerves roots. Identification of the orientation of the tissue was performed by sewing a thin 2-0 thread on the upper right nerve roots. PM removal was performed by sectioning the lateral side (nerve roots axis) and removing the white and grey matter. This procedure was performed in a saline solution and the removal of white matters on the PM was then carried out in a saline solution by carefully removing it without touching the PM.

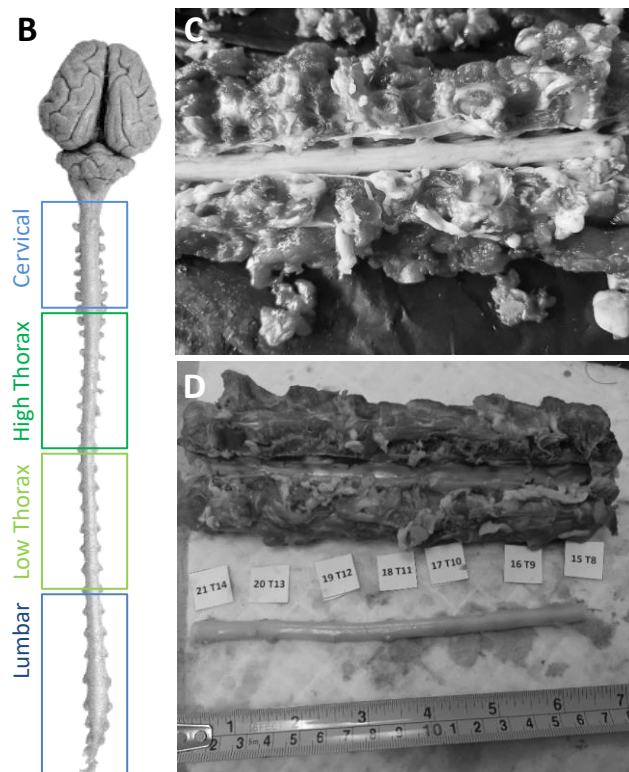


Figure 53. Sample preparation.

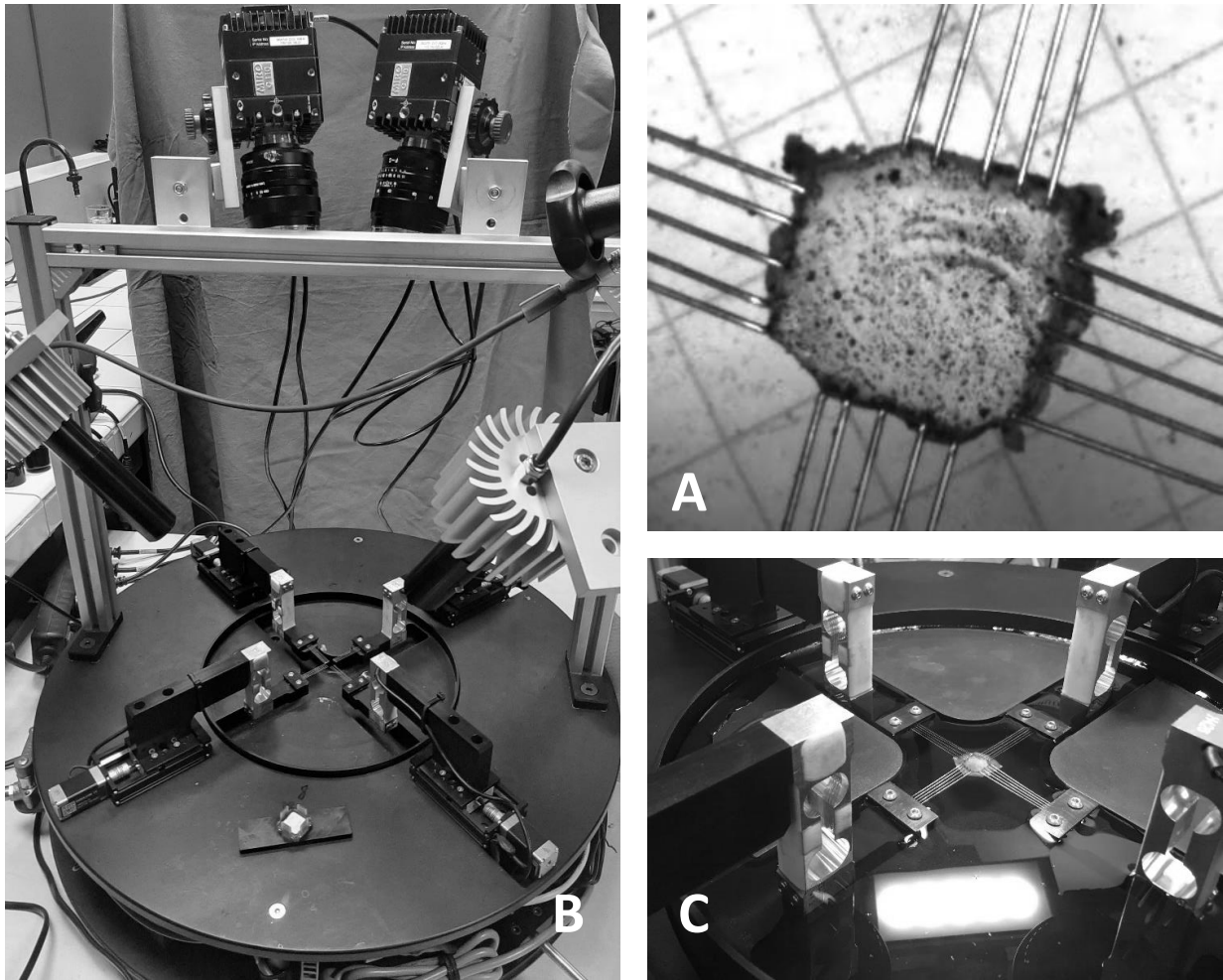


Figure 54. Test system and spine segment.

2.2.2. Bi-axial testing system and protocol

The bi-axial test system used in this experiment has been described in a previous work [Laville et al. 2020]. It consists of four synchronized and motorized arms, each equipped with one stepper motor (Zaber, Vancouver, Canada), allowing a maximum displacement of 25 mm each. Motors are driven by a dedicated card controlled by PMX system (HBM). Each arm is also equipped with a 50 N load cell (sensitivity of 0.001 N). Samples are gripped with five rake “teeth” [Figure 54].

The pre-conditioning was set to 0.01N and the stepper motors were controlled to have a 2mm displacement at $0.05\text{mm}\cdot\text{s}^{-1}$. The distance between the four rakes was fixed to 7mm and controlled afterward through optical system. A stereo image acquisition system was used to capture local strain on the whole samples and study the failure of the specimens. Thus, black paint was sprayed on samples to get a speckle stochastic pattern. The image acquisition system was calibrated with a grid of 12x9 printed dots with a known distance of 2mm between dots. The samples were tested out of the water but the time required to fix the sample to the testing system was minimized. The humidification of the biological tissues was achieved by spraying water droplets on the samples, to avoid water loss. 32 DAC samples and 27 PM samples were tested during the eight sessions of tests.

2.2.3. Structural characterization

Additionally, to the mechanical testing study, microstructural investigation was conducted on samples extracted from one tested specimen within the 24h after sacrifice. The samples investigated by microscopy were situated adjacent to the mechanically tested samples, extracted similarly and with similar sizes. Sample preparation consisted in fixation of the meningeal tissues (PM and DAC samples) in agarose solution without covering the tissue in petri boxes. Orientation of the samples in the agarose was to have the longitudinal axis as the y-axis and the circumferential axis as x-axis. Structure image investigation was performed on one swine the day after sacrifice and the samples were kept at all time in a controlled environment. The multi-photon microscopy system was a Zeiss LSM 780 2P with five NDD gASP detectors in which bi-photon imaging system to detect type II collagen. The resolution is $0.42 \times 0.42 \mu\text{m}^2$ with a stack thickness of $5 \mu\text{m}$ to $10 \mu\text{m}$. The laser wavelength was 860nm with a power of 25 to 70% depending on the tissue. The power tends to be higher for pia mater: pixel time was $6.3 \mu\text{s}$, line time $0.35 \mu\text{s}$ and frame time 30.98s .

The density and orientation of the collagen fibres depend on the structure (PM and DAC). However, both have a different organization of collagen fibres, that depends on the location of the tissue (anterior or posterior) or the spinal level. Since our goal was to quantitatively describe the microstructure, we selected 3 fibres representative of the different orientations found in the tissue (as different as possible). The structural and geometrical characterization of the fibre was investigated using Dragonfly software (Object Research Systems (ORS) Inc., Montreal, Canada). It consisted in three half period values and three peak amplitudes of the sinus shape fibre, the fibres thickness, and the fibre length and orientation defined as a signal (straight line through the sinusoidal signal, orientation as an angle with the x-direction vector). Fibre segmentation for density computation as a substitute of fibre density was performed using automatic Otsu segmentation.

The reproducibility of this methodology was not assessed. This semi-quantitative method aimed at depicting the variability of the fibre found in the tissue to explain anisotropy rather than quantitatively and statistically comparing and defining the whole structure. The reproducibility of the sample preparation (orientation of the sample in the microscope) is limited to fully describe fibre populations of the tissue considering the thickness to be examined.

2.2.4. Data analysis and constitutive models

The engineering stress was computed as the ratio of the tensile force and the cross-section area orthogonally to the force with an initial size of the tested samples of $7 \times 7 \text{mm}^2$ and a thickness of 0.21mm for pia mater and 0.3mm for DAC [Sudres et al. 2020]. Engineering strain on each axis was computed as the length at t time in one axis direction divided by the initial length in this direction. Bi-linear fitting of the four stress-strain curves was performed using Matlab (2019b, The Mathworks, Natick, Massachusetts, US). Failure detection was performed using the second derivative of the computed strain-stress curve. Toe region and elastic modulus were computed for each of them.

The different constitutive model implemented for post-processing of the experimental data are summarized in Table 24. Briefly, the matrix-based material has been modelled by a neo-Hookean model, an Yeoh hyper-elastic model and a Mooney-Rivlin models with (isotropic hyperelastic behaviour of the matrix).

Anisotropic Gasser model

The strain energy function (1) associated with contribution of fibre population(s) is defined in its most general form such as:

$$W_{GOH} = W_{matrix} + \frac{k_1}{2k_2} [e^{k_2\{\kappa_1(I_1-3)+(I_1-3\kappa_1)(I_4-1)\}^2} - 1] + \frac{k_3}{2k_4} [e^{k_4\{\kappa_2(I_1-3)+(1-3\kappa_2)(I_6-1)\}^2} - 1] \quad (1)$$

- W_{matrix} represents the isotropic ground matrix modelled as a Yeoh hyperelastic model (two terms : C_{10} and C_{20}).
- k_1 and k_3 that have the dimensions of a stress, representing the overall stiffness of the considered fibre population,
- k_2 and k_4 that are dimensionless, describing the nonlinearity of the collagen fibre behaviour, and
- I_1 is the first invariant of the right Cauchy Green tensor. I_2 (2), I_4 (3) and I_6 (4) are the 2nd, 4th and 6th anisotropic strain invariants (the two last invariants describing the fibre orientation).

$$I_2 = \frac{Trace[C]^2 - Trace[C^2]}{2} = \lambda_1^2\lambda_2^2 + \lambda_1^2\lambda_3^2 + \lambda_3^2\lambda_2^2 \quad (2)$$

$$I_4 = \lambda_1^2\cos^2\beta + \lambda_2^2\sin^2\beta \quad (3)$$

$$I_6 = \lambda_1^2\sin^2\gamma + \lambda_2^2\cos^2\gamma \quad (4)$$

With λ_i is the normal stretch in the i^{th} principal direction

β and γ orientation of the two populations of fibres and κ_1 ; κ_2 are respective coefficient of fibres dispersion;

Transverse isotropic Gasser model

Based on the equation (1), one fibre population is considered ($\kappa_1 = \kappa_2 = \kappa = 1/3$) with β orientation of the fibres, κ describing the degree of fibre dispersion (maximum dispersion).

$$I_4 = I_6 = \lambda_1^2\cos^2\beta + \lambda_2^2\sin^2\beta \quad (5)$$

Anisotropic GOH model

Based on the equation (1), W_{matrix} represents the isotropic ground matrix modelled as a neo-Hookean hyperelastic model and one fiber population is considered.

Reduced GOH model

DeKegel et al. [De Kegel et al.2018] simplified the initial formulation (6) with $\kappa_1 = \kappa_2 = \kappa = 1/3$ with maximum dispersion :

$$W_{red_GOH} = W_{matrix} + \frac{k_1}{2k_2} [e^{k_2\{\kappa I_1+(1-3\kappa)I_i-1\}^2} - 1] \quad (6)$$

W_{matrix} represents the isotropic ground matrix modelled as a neo-Hookean model (one term : C_{10}).

A specific model for PM has been proposed [Jin et al. 2014], including the isotropic hyperelastic Mooney-Rivlin model and a second reinforcement effect part piecewise function depending on the stretch in the direction of the fibres (λ_d).

Parameters fitting

For fitting of the parameters, the 2nd Piola Kirchoff (PK) stress for a non-linear elastic incompressible material (7) based on strain energy function is defined as:

$$S_{ij} = -pC_{ij}^{-1} + 2 \frac{\partial W}{\partial C_{ij}} \quad (7)$$

With p the hydrostatic pressure, W the strain energy function, C_{ij} the components of the right Cauchy deformation tensor. The resolution requires a computation of the derivative of the strain energy function by one specific component of the right Cauchy deformation tensor. Relationship between 2nd PK stress component, F being the deformation gradient tensor and the Cauchy stress (8) component is:

$$\sigma_{ij} = \sum_{r/k=[1/1,1/2...3/3]} F_{ir} S_{rk} F_{jk} J^{-1} \quad (8)$$

giving

$$\sigma_{11} = \lambda_1^2 S_{11}, \sigma_{22} = \lambda_2^2 S_{22}, \sigma_{33} = \lambda_3^2 S_{33} \quad (9)$$

Then we have Cauchy stresses (9) derived from constitutive law and experimental Cauchy stresses. The parameters for MR fibre strengthening model are fitted in two steps: first C_{10} , C_{20} , k_3 and k_4 parameters fitting and k_1 and k_2 fitting for all possibility of λ_d^* . Minimization of the objective function was implemented in Matlab (Mathworks, USA) using an implementation of the trust region reflective algorithm (Matlab Optimization Toolbox- function *lsqcurvefit*).

2.2.5. Statistical analysis

Statistical analysis was performed using R language (CRAN, R project, [R Core Team 2020]). Normality of the distribution was tested using Shapiro test. Wilcoxon test was used to test differences between the two orientations of the samples (paired) as well as between spinal levels (not paired). Anova test (not paired) was used to test the influence of the spinal level on the different material characteristics. Significance was defined as p value superior to 0.05. r^2 (10) and RMSE (11) of the fit between experimental data and model data are computed respectively as:

$$r^2 = 1 - \sum_{i \text{ in mes}} \frac{f(x) - y_i}{\sqrt{(\hat{y} - y_i)^2}} \quad (10)$$

$$RMSE = \sqrt{\sum_{i \text{ in mes}} \frac{(\hat{y} - y_i)^2}{n}} \quad (11)$$

With \hat{y} the mean of the initial value, y_i experimental value and $f(x)$ the fitted function.

2.3. Results

2.3.1. DAC characterization

Longitudinal elastic moduli were found to be significantly higher than circumferential ones at all levels ($p < 0.001$, Table 25). Toe and failure stresses were also found to be significantly different ($p = 0.005$ and $p < 0.001$ respectively) with a higher value of both strains and stresses at failure for longitudinal DAC [Fig. 55, A-B-E]. The Stress-Strain curves do not show any trend with respect to spinal level.

Constitutive modelling fitting showed similar results with anisotropic GOH model, Transverse isotropic Gasser model and anisotropic Gasser model ($r^2 = 0.99$ for all and respectively, RMSE of 0.44 ± 0.3 , 0.43 ± 0.3 and 0.27 ± 0.21 MPa). The best results were obtained with the anisotropic Gasser model while the fibres population parameters were found significantly different between κ_1 and κ_2 and between β and γ ($p < 0.001$).

2.3.2. PM characterization

Elastic moduli, toe and failure stresses were found significantly different between circumferential and longitudinal directions for the pia mater ($p < 0.001$, $p = 0.02$ and $p < 0.001$, respectively - Table 26). Stress-Strain curves of longitudinal PM samples appear to be grouped by spinal level [Fig. 55, C-D-F]. The

anisotropic GOH and the transverse isotropic and anisotropic Gasser models presented the closest fit when compared with other constitutive models. For the anisotropic Gasser model, fibres population parameters were found significantly different in average for all parameters (k_1 and k_3 : $p=0.005$, k_2 and k_4 : $p=0.03$, κ_1 and κ_2 and β and γ : $p<0.001$)

2.3.3. Spinal level differences

The study of the influence of sample location in the spine is depicted in [Table 27](#). The ANOVA test did not reveal any influence of the spinal level. A higher mean value of the longitudinal elastic moduli was found in the upper thoracic spine while the cervical and upper thoracic circumferential elastic moduli were similar. In both directions, DAC elastic moduli decrease toward the lower spine. Similar results are found for PM in the longitudinal direction while lumbar circumferential elastic moduli were higher than in the low thorax. Differences between directions in elastic moduli were significant for DAC in all levels except for cervical spine ($p=0.08$) while differences in PM were only significant in cervical and thoracic spines.

Comparing the spine levels, significant differences were found for PM circumferential elastic moduli between upper and lower thorax (similar results while no significant for DAC longitudinal $p=0.054$), for DAC longitudinal failure stresses between high and low thorax and for PM failure stresses between cervical and low thorax and cervical and lumbar spine in both directions.

2.3.4. Fibres structure

In DAC, the tissue mainly showed highly curled collagen fibres [[Fig. 56](#)], present in a high density within the sample. Bi-photon imaging shows that the collagen fibres in the DAC change within one sample (anterior and posterior), with different orientations and structures. In PM, fibres orientation is depicted in [Figure 57](#). It showed fenestrations in the PM structure as well as vascularization [[Fig. 57, E-F](#)].

A semi quantitative description of the fibre structures can be found in [Table 28](#). DAC shows small variability in orientation depending on the spine level while showing variability in the orientation within the same sample. It presented different volume fractions increasing from cervical to lumbar spine, fibre thickness and sizes of amplitude depicting changes in shape of the fibres. PM fibres orientation is found to vary both within the same sample and along the spine. Half -amplitude of the collagen fibre curl is higher in PM than in DAC. Density of fibres slightly varies between 17.3% to 25.4% (thoracic).

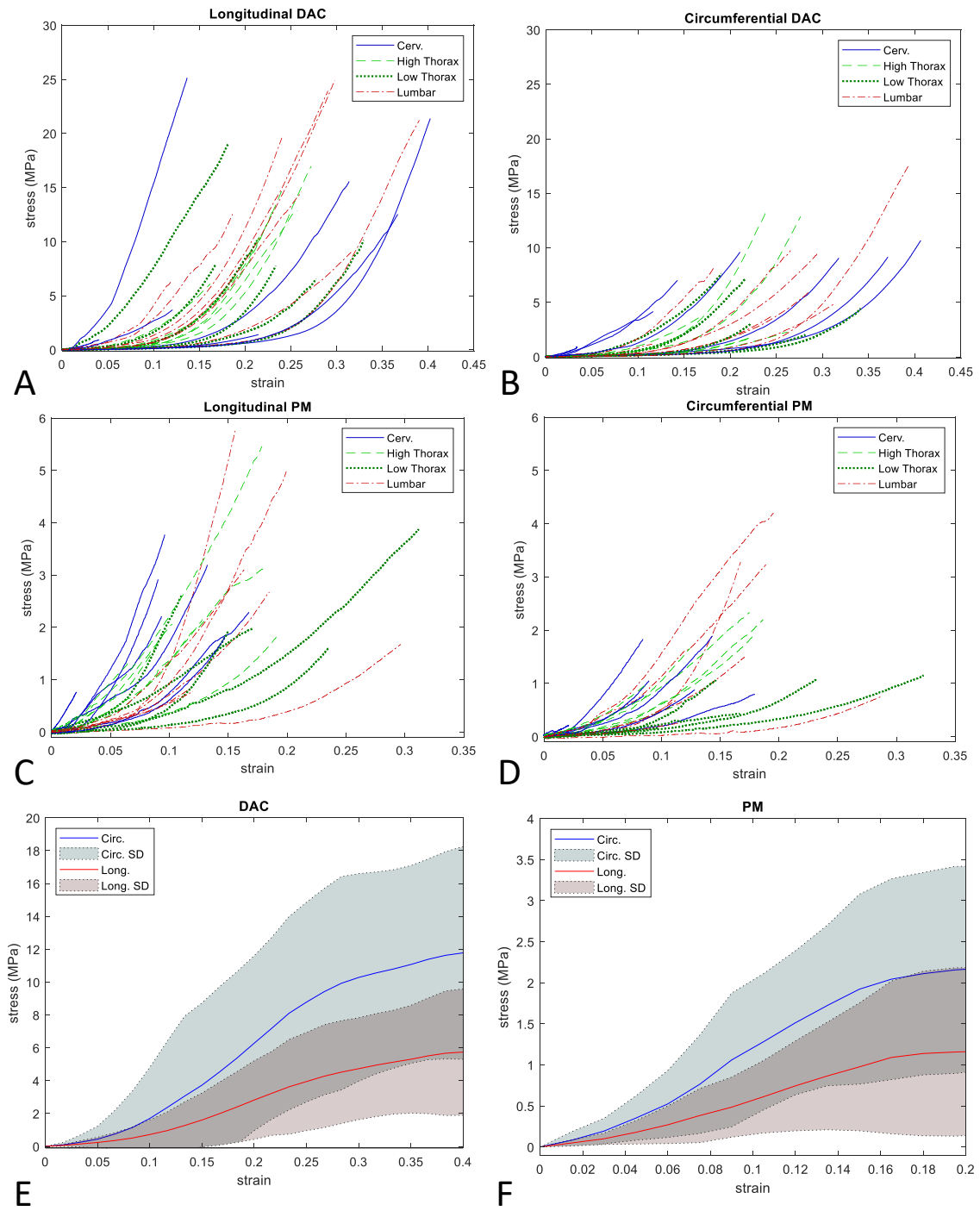


Figure 55. DAC (A-B-E) and PM (C-D-F) biaxial tensile test results according with spinal levels, longitudinal (A-C) and circumferential (B-D).

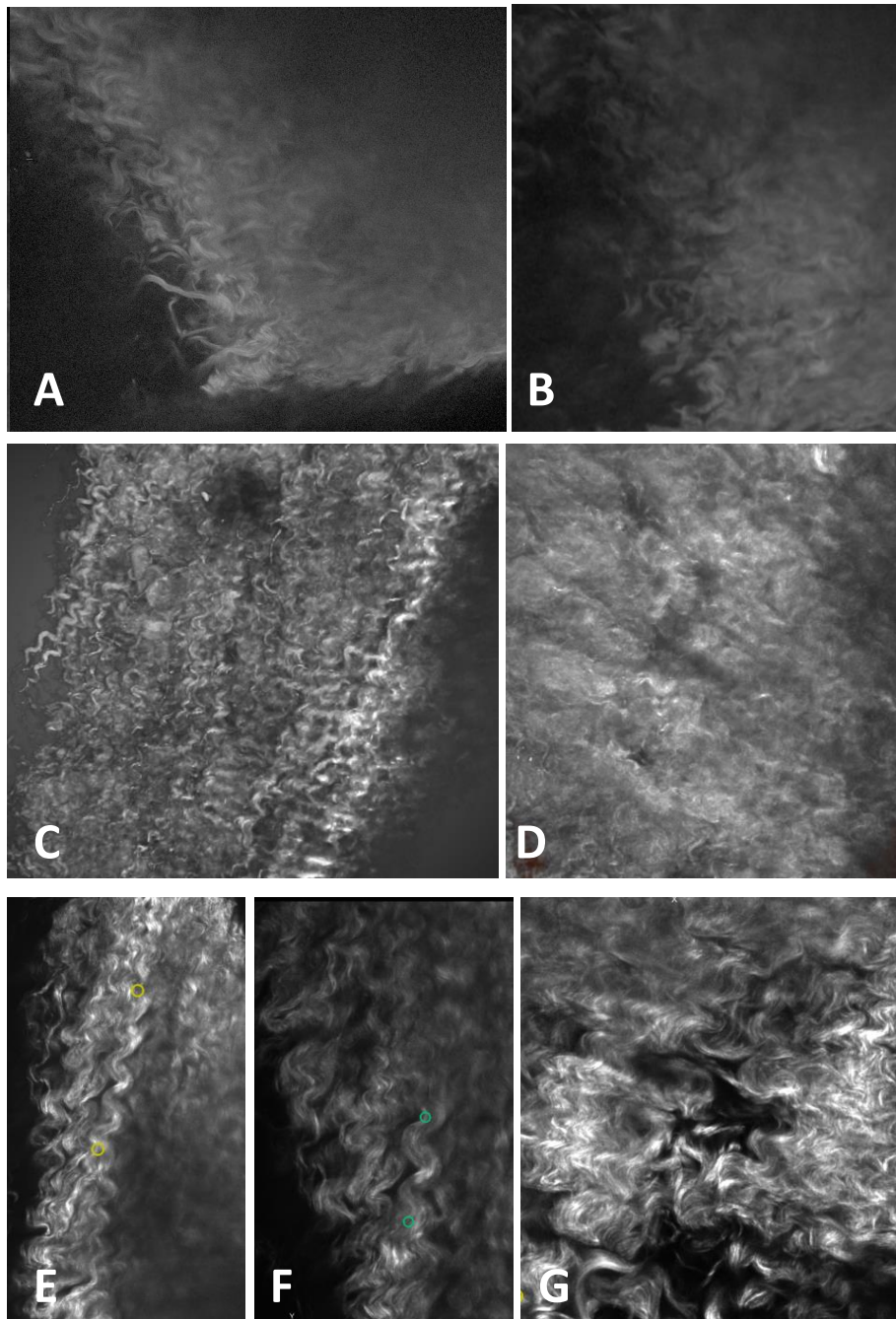


Figure 56. Collagen fibres in different level of dura mater (cervical anterior A and posterior B, high thoracic anterior C and posterior D, low thoracic E and F and lumbar spine G).

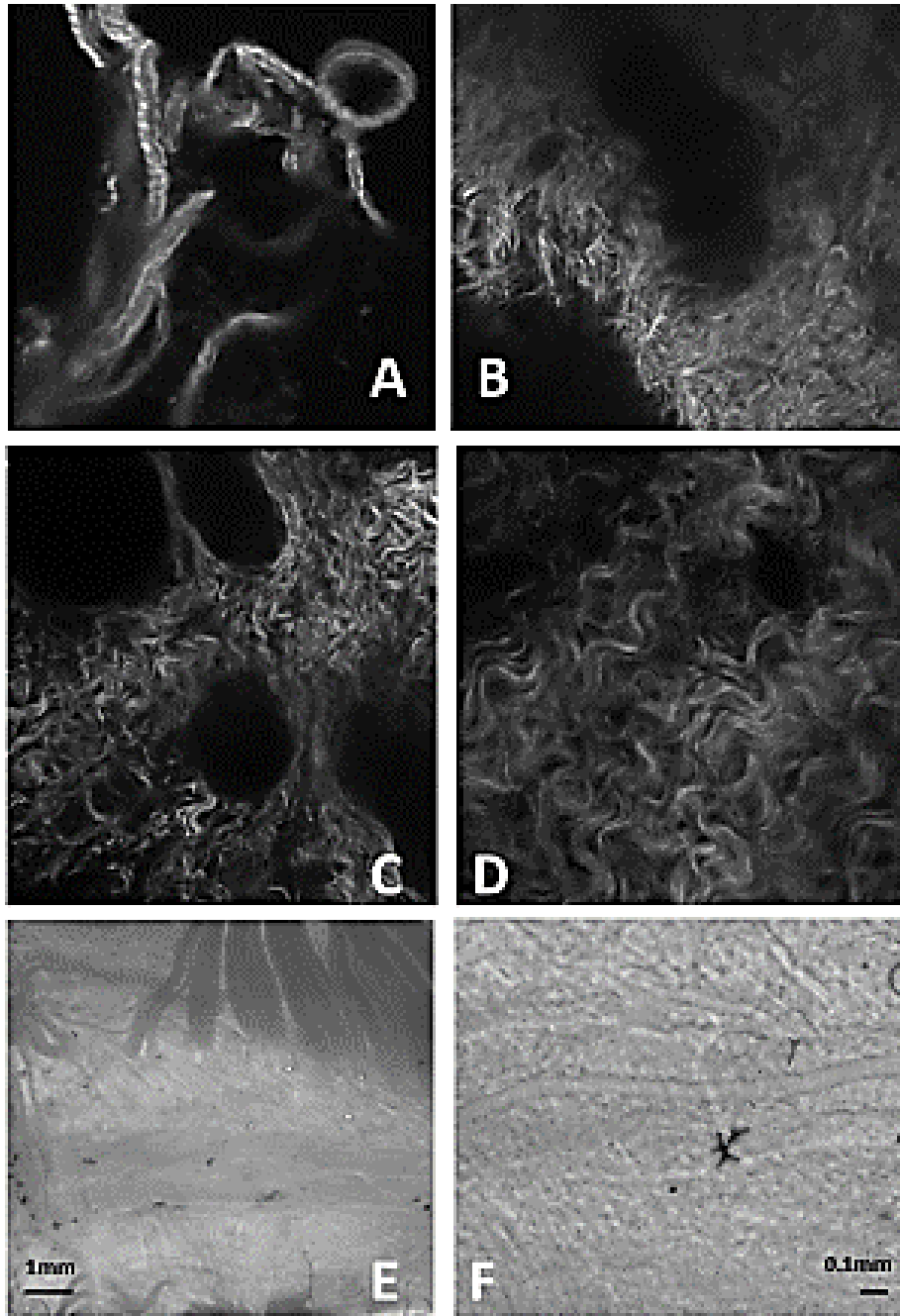


Figure 57. Collagen fibres in different level of pia mater (cervical A and posterior B, thoracic B and C and lumbar spine D, with microscopic visualization of vessel E and F by Keyence microscope) with fenestration description.

Name	Nb of par.	Parameters	Description	Ref.	Strain Energy function
Ogden	2	μ (MPa) β (-)	isotropic modified Ogden model (n=1)	[38]	$W_{\text{fibres}} = \sum_{i=1}^n 2 \frac{\mu}{\beta^2} (\lambda_{11}^\beta + \lambda_{22}^\beta + \lambda_{33}^\beta - 3)$
Reduced GOH	3	C_{10} (MPa) k_1 (MPa) k_2 (-)	matrix based NH model, and $\kappa=1/3$ (maximum dispersion)	[32]	$W = C_{10}(I_1 - 3) + \frac{k_1}{k_2} [e^{k_2(k_1 I_1 - 1)^2} - 1]$
Ani. GOH	5	C_{10} (MPa) k_1 (MPa) k_2 (-) κ (-) β (rad)	matrix based NH model	[32]	$W = C_{10}(I_1 - 3) + \frac{k_1}{2k_2} [e^{k_2(k_1 + (1-3\kappa)I_4 - 1)^2} - 1 + e^{k_2(k_1 + (1-3\kappa)I_6 - 1)^2} - 1]$
Trans. Iso Gasser	6	C_{10} (MPa) C_{20} (MPa) k_1 (MPa) k_2 (-) κ (-) β (rad)	matrix based Yeoh model	[14]	$W = C_{10}(I_1 - 3) + C_{20}(I_1 - 3)^2 + \frac{k_1}{2k_2} [e^{k_2(\kappa(I_1 - 3) + (1-3\kappa)(I_4 - 1))^2} - 1] + \frac{k_1}{2k_2} [e^{k_2(\kappa(I_1 - 3) + (1-3\kappa)(I_6 - 1))^2} - 1]$
Ani. Gasser	10	C_{10} (MPa) C_{20} (MPa) k_1 (MPa) k_2 (-) κ_1 (-) β (rad) k_3 (MPa) κ_2 (-) γ (rad) k_4 (-) γ (rad)	matrix based Yeoh model	[14]	$W = C_{10}(I_1 - 3) + C_{20}(I_1 - 3)^2 + \frac{k_1}{2k_2} [e^{k_2(\kappa_1(I_1 - 3) + (1-3\kappa_1)(I_4 - 1))^2} - 1] + \frac{k_3}{2k_4} [e^{k_4(\kappa_2(I_1 - 3) + (1-3\kappa_2)(I_6 - 1))^2} - 1]$
Mooney-Rivlin Fibres strengthening	6	C_{10} (MPa) C_{30} (MPa) k_1 (MPa) k_2 (-) κ (-) β (rad)		[38]	$W_1 = C_{10}(I_1 - 3) + C_{20}(I_2 - 3)$ For $\lambda_d \leq 1$, $W_2 = 0$ For $1 < \lambda_d \leq \lambda_d^*$, $W_2 = k_3(e^{-k_4(\lambda_d - 1)} - 1)$ For $\lambda_d^* < \lambda_d$, $W_2 = k_1 \lambda_d + k_2$

Table 24. Description of constitutive models.

DAC	E (MPa)	Toe strain (-)	Toe stress (MPa)	Failure strain (-)	Failure stress (MPa)	Poisson (-)	r^2 (-)	RMSE (MPa)
<i>Long</i>	108.1±40.3	0.13±0.08	1.6±0.81	0.24±0.09	13.85±7.03	0.52±0.26	0.98±0	
<i>Circ</i>	53.2±31.7	0.14±0.08	1.06±0.83	0.24±0.09	6.78±6.1		0.98±0	
Ogden	μ (MPa) 2.8±4	β (-) 0.75±0.2					0.75±0.2	2.22±1.78
Reduced GOH	C_{10} (MPa) 0.5±1		k_1 (MPa) 53.67±62.19	k_2 (-) 48.59±177.58			2.22±1.78	2.22±1.78
Ani. GOH	C_{10} (MPa) 0.03±0.11		k_1 (MPa) 18.36±21.63	k_2 (-) 42.95±177.87	κ (-) 0.19±0.12	β (rad) 0.76±0.67	0.99±0.01	0.44±0.3
Trans. Iso Gasser	C_{10} (MPa) 0.04±0.15	C_{20} (MPa) 1.73±2.57	k_1 (MPa) 12.23±19.56	k_2 (-) 41.1±178.13	κ (-) 0.13±0.14	β (rad) 0.76±0.71	0.99±0	0.43±0.3
Ani. Gasser	C_{10} (MPa) 0.02±0.08	C_{20} (MPa) 1.62±2.95	k_1 (MPa) 7.5±13.34	k_2 (-) 18.82±45.14	κ_1 (-) 0.23±0.13	β (rad) 0.87±0.74	0.99±0.02	0.27±0.21
			k_1 (MPa) 3.53±7.87	k_4 (-) 11.95±20.74	κ_2 (-) 0.06±0.09	β (rad) 0.03±0.12		

Table 25. DAC biaxial tensile test results and constitutive model parameters. Values depict average on all DAC samples and constitutive models were fitted on each experimental couple of curves before to be averaged.

	E (MPa)	Toe strain (-)	Toe stress (MPa)	Failure strain (-)	Failure stress (MPa)	Poisson (-)	r^2 (-)	RMSE (MPa)
Pia Mater	<i>Long</i>	26.3±13.3	0.06±0.05	0.29±0.21	0.15±0.07	2.56±1.33	0.52±0.26	0.98±0
	<i>Circ</i>	12.9±8.7	0.05±0.05	0.16±0.13	0.15±0.07	1.36±1.03		0.98±0
Ogden	μ (MPa)	β (-)						
	1.9±1.5	0.71±0.27					0.75±0.23	0.41±0.28
Mooney-Rivlin	C_{10} (MPa)	C_{30} (MPa)						
	-4.18±4.53	4.35±4.07					0.71±0.28	0.43±0.3
Reduced GOH	C_{10} (MPa)		k_1 (MPa)	k_2 (-)				
	0.5±0.4		40.57±53.49	23.52±44.25			0.43±0.31	0.43±0.31
Ani. GOH	C_{10} (MPa)		k_1 (MPa)	k_2 (-)	κ (-)	β (rad)		
	0.09±0.18		12.73±16.74	28.84±47.28	0.22±0.08	0.96±0.6	0.99±0	0.07±0.06
Trans. Iso Gasser	C_{10} (MPa)	C_{20} (MPa)	k_1 (MPa)	k_2 (-)	κ (-)	β (rad)		
	0.1±0.19	0.71±1.09	9.44±17.5	22±45.71	0.14±0.12	0.9±0.62	1±0	0.07±0.06
Ani. Gasser	C_{10} (MPa)	C_{20} (MPa)	k_1 (MPa)	k_2 (-)	κ_1 (-)	β (rad)		
	0.06±0.12	0.76±1.64	7.76±13.55	25.82±85.53	0.21±0.1	0.8±0.68	1±0.0	0.06±0.05
			K_3 (MPa)	k_4 (-)	κ_2 (-)	γ (rad)		
			2.39±4.4	16.73±24.93	0.07±0.1	0.05±0.14		
Fibres strengthening	C_{10} (MPa)	C_{30} (MPa)	k_1 (MPa)	k_2 (-)	k_3 (-)	β (rad)		
Mooney-Rivlin	0.05±0.22	1.7±0.59	4.67±3.88	32.93±17.7	44.77±12.68	0.8±0.08	0.84±0.1	0.37±0.23

Table 26. PM biaxial tensile test results and constitutive model parameters. Values depict average on all PM samples and constitutive models were fitted on each experimental couple of curves before to be averaged.

		n	E (MPa)	Toe strain (n.a)	Toe stress (MPa)	Failure strain (n.a)	Failure stress (MPa)
Long	DAC	<i>Cervical</i>	106.5±67.6	0.11±0.11	1.4±1.14	0.24±0.13	15.16±10.59
		<i>High Thorax</i>	122.5±30.2**	0.14±0.05	1.94±0.73	0.25±0.06	15.65±5.47** [§]
		<i>Low Thorax</i>	98.8±17.1***	0.14±0.08	1.57±0.67*	0.23±0.07	10.64±4.1** [§]
		<i>Lumbar</i>	96.8±27.5**	0.11±0.05	1.28±0.46	0.23±0.08	13.29±6.74
	PM	<i>Cervical</i>	31.9±10.7**	0.03±0.03	0.22±0.28	0.11±0.05 ^{§1§2}	2.42±0.99*
		<i>High Thorax</i>	27.2±17.1*	0.04±0.04	0.3±0.22	0.13±0.04	2.72±1.75
		<i>Low Thorax</i>	22.9±10.7*	0.09±0.06	0.37±0.16	0.2±0.08 ^{§2}	2.41±0.9**
		<i>Lumbar</i>	20.2±10.9	0.08±0.06	0.27±0.1	0.19±0.07 ^{§1}	2.64±1.59
Circ	DAC	<i>Cervical</i>	58.5±31.2	0.13±0.13	1.09±1.17	0.24±0.13	9.1±9.56
		<i>High Thorax</i>	58.6±44.6	0.16±0.05	1.29±0.99	0.25±0.06	7.05±5.79
		<i>Low Thorax</i>	44.3±17.2	0.15±0.07	0.92±0.24	0.23±0.07	4.63±2.61
		<i>Lumbar</i>	48.3±22.6	0.13±0.07	0.77±0.39	0.23±0.08	5.98±3.3
	PM	<i>Cervical</i>	14±6.6	0.04±0.03	0.13±0.1	0.1±0.05 ^{§1§2}	1.07±0.6
		<i>High Thorax</i>	15.6±10.9 [§]	0.04±0.03	0.2±0.16	0.13±0.05	1.56±0.98
		<i>Low Thorax</i>	6.7±4.9 [§]	0.09±0.08	0.16±0.15	0.19±0.09 ^{§2}	0.78±0.45
		<i>Lumbar</i>	12.9±8.7	0.06±0.07	0.11±0.06	0.19±0.06 ^{§1}	1.99±1.67

Table 27. Biaxial tensile test results according with sample spinal levels. [§] depict significant difference between the two levels (0.01<p<0.05 : [§], 0.001<p<0.01 : ^{§§}, p<0.001 : ^{§§§}) and * the significant difference between circumferential and longitudinal direction (0.01<p<0.05: *, 0.001<p<0.01 : **, p<0.001 : ***).

		Angle (rad)	Amp (μm)	1/2 P (μm)	Fibre thickness (μm)	Volume fraction (%)
DAC	Cervical	3.59 (2.88-4.13)	5.1 (4.1-6.7)	9 (8.1-10.6)	5 (3.5-6.3)	19.8
	Thorax	3.2 (2.55-4.28)	8 (7.5-9.2)	33 (28.1-37)	16 (14.6-17.5)	23.4
	Lumbar	3.71 (3.18-4.47)	5 (4.3-5.8)	24 (20.7-26)	12 (10.4-15.5)	34.6
PM	Cervical	2.43 (1.3-3.2)			8 (4.9-11.6)	17.3
	Thorax	1.1 (0.97-1.27)	5 (3.2-9.3)	20 (7.6-27.6)	6 (5.9-6.5)	25.4
	Lumbar	2.28 (1.42-3.43)	7 (6.7-7.4)	38 (32.7-41.5)	14 (10.6-16.5)	22.7

Table 28. Fibres characteristics measured on bi-photon microscopy for DAC and PM samples

2.4. Discussion

This study investigates the material properties of the meningeal tissue in swine model with the perspective of testing the constitutive models previously described in the literature to fully describe the behavior of such material. While two fibres populations model presented higher results for DAC and micro-structural investigation showed the variability of orientation within a same sample, significant differences between fibres populations description (fibres dispersion coefficient and orientation) by the anisotropic Gasser model parameters were found. Moreover, this study is the first, to the authors' knowledge, to report biaxial tensile test of the PM and to provide constitutive modelling for such tests. Anisotropic Gasser model presented slightly higher results for PM with significant differences in all fibres populations description parameters.

2.4.1. DAC characterization and constitutive parameters fitting

Controversy on comparison of stiffness between circumferential and longitudinal direction for DAC tissue has been previously discussed [Shetye et al. 2014, Wilcox et al. 2003, Persson et al. 2010] depending of the location of DAC sample extraction (cranial vs spinal, between cranial or spinal locations).

The values in our study are in line with literature value of uniaxial tests: 7.5 to 26 MPa [Walsh et al. 2018]; 3.28 to 7.86 MPa [van Noort et al. 1981]; 44 to 91MPa in fossa human sample dural (strain rate $1.5 \cdot 10^{-3} \text{ s}^{-1}$) [Chauvet et al. 2010]; 70 ± 44 MPa in human cranial cadaver samples [Zwirner et al. 2019], cranial bovine longitudinal 25 to 70MPa [Runza et al. 1999] ; in human spine : longitudinal : 62 to 102MPa vs circumferential : 4 to 8MPa [Runza et al. 1999] and 138 to 265 MPa in longitudinal direction, 7.8 to 76.4 MPa in circumferential [Patin et al. 1993]. When comparing uniaxial results with biaxial, the difference in ratio between circumferential and longitudinal elastic moduli should be noticed. It appears that applying a second loading in the direction will accentuate the differences in material behaviour of the two directions. Our results presented higher elastic modulus of longitudinal DAC than circumferential when tested with biaxial tensile test ($p < 0.001$) which is different than previously reported results [Shetye et al. 2014] in ovine spinal cord. While discrepancies between literature results were previously reported by the same authors, they attributed such differences at the maximum loading strain attained in other study going until the failure which is the case in our study.

When compare to existing results for biaxial tensile test [Shetye et al. 2014], differences between non-linearity coefficients (k_2 and k_4) as well as dispersion coefficients (κ_1 and κ_2) were previously reported while only orientation and dispersion coefficient were found different here. Differences with such corresponding values with the previously published values should be noticed which could also result from the previously mentioned differences in maximum loading as well as strain rate testing conditions. Such differences could also be explained by the dispersion of our strain-stress curves, methodology for fitting (fitting on each experimental curves vs fitting on the average curve) as well as the different in the tested locations (as compared to cervical only samples in Shetye et al. [2014]).

Micro-structural analysis of the DAC showed the complexity of the organization of the collagen fibres on such structures which could not match the theoretical description provided by the constitutive models. Indeed, orientation and dispersion coefficient of the fibres were found significantly different between the two populations which may suggest a reality of the tissue structure which is not fully described by the semi-quantitative approach of collagen structure investigation by bi-photon microscopy. To this perspective, a full characterization of the collagen by tested samples could be considered as well as further investigation of other components of the tissue such as elastin fibres.

2.4.2. PM and constitutive parameters fitting

Elastic moduli determined by biaxial tensile tests in PM samples were found significantly different between longitudinal and circumferential directions. The presented values are higher than the one reported in the literature. Tensile elastic modulus of bovine cranial PM was found to be 19kPa [Jin et al. 2011] and 2300kPa in spinal rabbit PM in performing tensile test on spinal cord with and without and deriving a computed elastic modulus from a viscoelastic Kelvin-Voigt model [Ozawa et al. 2004]. Also, vascularized and non-vascularized tissue elastic modulus were compared (1.32 ± 0.03 kPa and 2.79 ± 0.08 kPa) [Fabris et al. 2019]. Such differences could be explained by the model differences as well as the location of the extracted samples.

The Mooney-Rivlin based material with fibre strengthening did not present the closest fit when compared to transversely anisotropic material or fibre population models. When focusing at the anisotropic Gasser model, non-linearity of the two fibres populations were found significantly different while differences in fibre dispersion coefficient did not reach the significance. With the micro-structural investigation in mind, fenestration could also be taken into consideration when modelling the PM.

While PM (or more precisely PAC according with the authors' hypothesis) was previously described by Jin et al. [2011] with the Mooney Rivlin based including piecewise function to consider the fibres strengthening and based on our results, we suggest the use of anisotropic Gasser model which fully described two fibres population for which describing parameters were found significantly different. When focusing on the results from collagen fibres organisation structure investigation, the question of how the fenestration should be considered in the constitutive modelling is still to be asked.

2.4.3. Spinal levels differences

To the best of our knowledge, three studies reported comparison between spinal levels meningeal tissue characteristics, all in uniaxial test.

Sudres et al. [2020] reported lower cervical elastic moduli than thoracic one in longitudinal direction and higher cervical and thoracic vs lumbar elastic moduli in circumferential direction. Our results were similar with higher circumferential lumbar elastic modulus than low thoracic one.

2.4.4. Testing protocols and limitations

Despite the interesting presented results, this study has some limitations. Additional displacement could have been tested in all samples however the conservation time after sacrifice was critical and determining visco-elasticity properties of the meningeal tissues was out of the scope of this work. Further studies are required for investigation on visco-elasticity of pia and dura mater such as described in other biological material [Anssari-Benam et al. 2019]. Further investigation should include different displacement rate as strongly advised in other studies [Budday et al. 2017] and [Jin et al. 2014]. In this later, an inverse analysis using finite element modelling showed that three experimental loading conditions are necessary to model various loading conditions. Thus, our results are highly limited to identical conditions of the one tested (strain rate of $0.71 \text{e-}3 \text{s}^{-1}$ similar in both direction). Quantification of the collagen fibers directly on the tested sample could have been considered as described in a different application [Brunet et al. 2020] however access of the imaging facilities on the same day of sacrifice was not possible. While usefulness of swine model could be questioned as spine horizontal morphology probably implied different organization of the tissue, availability of testing material is a non-negligible advantage and the lack of data of such meningeal tissue mechanical characterization made it acceptable. Constitutive model could then be investigated using finite element modelling [Sun et al.

2005] with inverse analysis which could facilitate further transition to spinal cord compression modelling [Jannesar et al. 2016, Kimpara et al. 2006].

2.5.Conclusion

This study presented significant differences in elastic moduli of circumferential and longitudinal directions in both DAC and PM tissues when tested by bi-axial tensile test. Significant differences were found between circumferential PM low and high thorax while even though trends could be seen in changes of material properties along the spinal cord, such changes were not found significant. Comparison between constitutive models presented superiority of anisotropic Gasser for both DAC and PM, micro-structural description enabling discussion on the capacity of constitutive law theory to match micro-structure description of meningeal tissues.

Acknowledgements

The authors would like to thank Anthony Melot for his great help on swine dissection, Frédéric Brocard for the bi-photon imaging and Christophe Pradille for the development and his assistance in the use bi-axial test system.

This study was supported by the Champlain/ AIMCI.

3. References

- [Bailly et al. 2020] Bailly, N., Diotalevi, L., Beauséjour, M.-H., Wagnac, É., Mac-Thiong, J.-M., Petit, Y., 2020. Numerical investigation of the relative effect of disc bulging and ligamentum flavum hypertrophy on the mechanism of central cord syndrome. *Clinical Biomechanics* 74, 58–65. <https://doi.org/10.1016/j.clinbiomech.2020.02.008>
- [Bertram and Heil 2016] Bertram, C.D., Heil, M., 2016. A Poroelastic Fluid/Structure-Interaction Model of Cerebrospinal Fluid Dynamics in the Cord With Syringomyelia and Adjacent Subarachnoid-Space Stenosis. *J Biomech Eng* 139, 011001-011001–10. <https://doi.org/10.1115/1.4034657>
- [Breig and Braxton 1960] Breig, A., & Braxton, V. (1960). *Biomechanics of the central nervous system : some basic normal and pathologic phenomena* (book). Uppsala: Almqvist & Wiksell.
- [Brummund et al. 2017] Brummund, M., Brailovski, V., Petit, Y., Facchinello, Y., Mac-Thiong, J.-M., 2017. Impact of anchor type on porcine lumbar biomechanics: Finite element modelling and in-vitro validation. *Clinical Biomechanics* 43, 86–94. <https://doi.org/10.1016/j.clinbiomech.2017.02.007>
- [Cyron and Humphrey 2017] Cyron, C.J., Humphrey, J.D., 2017. Growth and Remodeling of Load-Bearing Biological Soft Tissues. *Meccanica* 52, 645–664. <https://doi.org/10.1007/s11012-016-0472-5>
- [Czyż et al. 2012] Czyż, M., Ścigała, K., Będziński, R., Jarmundowicz, W., 2012. Finite element modelling of the cervical spinal cord injury -- clinical assessment. *Acta Bioeng Biomech* 14, 23–29.
- [Davis 1867] Davis H. G., 1867. *Conservative Surgery: As Exhibited in Remedying Some of the Mechanical Causes that Operate ...* D. Appleton & company.
- [Fradet et al. 2016a] Fradet, L., Arnoux, P.-J., Callot, V., Petit, Y., 2016. Geometrical variations in white and gray matter affect the biomechanics of spinal cord injuries more than the arachnoid space. *Advances in Mechanical Engineering* 8, 1687814016664703. <https://doi.org/10.1177/1687814016664703>
- [Fradet et al. 2016b] Fradet, L., Cliche, F., Petit, Y., Mac-Thiong, J.-M., Arnoux, P.-J., 2016. Strain rate dependent behavior of the porcine spinal cord under transverse dynamic compression. *Proc Inst Mech Eng H* 230, 858–866. <https://doi.org/10.1177/0954411916655373>
- [Fountoulakis et al. 2001] Fountoulakis, M., Hardmeier, R., Höger, H., Lubec, G., 2001. Postmortem Changes in the Level of Brain Proteins. *Experimental Neurology* 167, 86–94. <https://doi.org/10.1006/exnr.2000.7529>
- [Garo et al. 2007] Garo, A., Hrapko, M., van Dommelen, J. a. W., Peters, G.W.M., 2007. Towards a reliable characterisation of the mechanical behaviour of brain tissue: The effects of post-mortem time and sample preparation. *Biorheology* 44, 51–58.
- [Henao et al. 2016] Henao, J., Aubin, C.-É., Labelle, H., Arnoux, P.-J., 2016. Patient-specific finite element model of the spine and spinal cord to assess the neurological impact of scoliosis correction: preliminary application on two cases with and without intraoperative neurological complications. *Computer Methods in Biomechanics and Biomedical Engineering* 19, 901–910. <https://doi.org/10.1080/10255842.2015.1075010>
- [ISO 98:1995 GUM] ISO 98:1995 Guide to the expression of Uncertainty in Measurement 2nd edn (1995) International Organization for Standardization, Geneva
- [JCGM 101:2008] JCGM 101:2008 Evaluation of measurement data – Supplement 1 to the “Guide to the expression of uncertainty in measurement” – Propagation of distributions using a Monte Carlo method (2008) Sèvres, France: BIPM Joint Committee for Guides in Metrology
- [Khani et al. 2018] Khani, M., Sass, L.R., Xing, T., Keith Sharp, M., Balédent, O., Martin, B.A., 2018. Anthropomorphic Model of Intrathecal Cerebrospinal Fluid Dynamics Within the Spinal Subarachnoid Space: Spinal Cord Nerve Roots Increase Steady-Streaming. *J Biomech Eng* 140. <https://doi.org/10.1115/1.4040401>
- [Khuyagbaatar et al. 2014] Khuyagbaatar, B., Kim, K., Hyuk Kim, Y., 2014. Effect of bone fragment impact velocity on biomechanical parameters related to spinal cord injury: A finite element study. *Journal of Biomechanics* 47, 2820–2825. <https://doi.org/10.1016/j.jbiomech.2014.04.042>
- [Kim et al. 2019] Kim, K.-T., Streijger, F., So, K., Manouchehri, N., Shortt, K., Okon, E.B., Tigchelaar, S., Fong, A., Morrison, C., Keung, M., Sun, J., Liu, E., Cripton, P.A., Kwon, B.K., 2019. Differences in Morphometric Measures of the Uninjured Porcine Spinal Cord and Dural Sac Predict Histological and Behavioral Outcomes after Traumatic Spinal Cord Injury. *Journal of Neurotrauma* 36, 3005–3017. <https://doi.org/10.1089/neu.2018.5930>
- [Lévy et al. 2020] Lévy, S., Baucher, G., Roche, P.-H., Evin, M., Callot, V., Arnoux, P.-J., 2020. Biomechanical comparison of spinal cord compression types occurring in Degenerative Cervical Myelopathy. *Clinical Biomechanics* 105174. <https://doi.org/10.1016/j.clinbiomech.2020.105174>
- [Liedekerke et al. 2019] Liedekerke, P.V., Neitsch, J., Johann, T., Alessandri, K., Nassoy, P., Drasdo, D., 2019. Quantitative cell-based model predicts mechanical stress response of growing tumor spheroids over various growth conditions and cell lines. *PLOS Computational Biology* 15, e1006273. <https://doi.org/10.1371/journal.pcbi.1006273>

- [Mazuchowski and Thibault 2003] Mazuchowski, E, Thibault, L. Biomechanical properties of the human spinal cord and pia mater, 2003, <http://www.tulane.edu/sbc2003/pdfdocs/1205.PDF>
- [R Core Team 2018] R Core Team (2018). R: A language and environment for statistical computing. R Foundation for Statistical Computing, Vienna, Austria. URL <https://www.R-project.org/>.
- [Ramo et al. 2018a] Ramo, N., Shetye, S.S., Puttlitz, C.M., 2018. Damage Accumulation Modeling and Rate Dependency of Spinal Dura Mater. *ASME J of Medical Diagnostics* 1. <https://doi.org/10.1115/1.4038261>
- [Ramo et al. 2018b] Ramo, N.L., Shetye, S.S., Streijger, F., Lee, J.H.T., Troyer, K.L., Kwon, B.K., Crompton, P., Puttlitz, C.M., 2018. Comparison of In-Vivo and Ex-Vivo Viscoelastic Behavior of the Spinal Cord. *Acta Biomater* 68, 78–89. <https://doi.org/10.1016/j.actbio.2017.12.024>
- [Reina et al. 1997] Reina, M., Dittmann, M., Garcia, A., Vanzundert, A., 1997. New perspectives in the microscopic structure of human dura mater in the dorsolumbar region. *Regional Anesthesia and Pain Medicine* 22, 161–166. [https://doi.org/10.1016/S1098-7339\(06\)80036-2](https://doi.org/10.1016/S1098-7339(06)80036-2)
- [Sakka et al. 2016] Sakka, L., Gabrillargues, J., Coll, G., 2016. Anatomy of the Spinal Meninges. *Oper Neurosurg (Hagerstown)* 12, 168–188. <https://doi.org/10.1227/NEU.0000000000001048>
- [Schomberg et al. 2017] Schomberg, D.T., Miranpuri, G.S., Chopra, A., Patel, K., Meudt, J.J., Tellez, A., Resnick, D.K., Shanmuganayagam, D., 2017. Translational Relevance of Swine Models of Spinal Cord Injury. *J. Neurotrauma* 34, 541–551. <https://doi.org/10.1089/neu.2016.4567>
- [Solaguren-Beascoa Fernandez et al. 2009] Solaguren-Beascoa Fernández, M., Alegre Calderón, J.M., Bravo Díez, P.M., 2009. Implementation in MATLAB of the adaptive Monte Carlo method for the evaluation of measurement uncertainties. *Accred Qual Assur* 14, 95–106. <https://doi.org/10.1007/s00769-008-0475-6>
- [Sparrey and Keaveny 2009] Sparrey, C.J., Keaveny, T.M., 2009. The Effect of Flash Freezing on Variability in Spinal Cord Compression Behavior. *J Biomech Eng* 131. <https://doi.org/10.1115/1.4000079>
- [Stoner et al. 2020] Stoner, K.E., Abode-Iyamah, K.O., Fredericks, D.C., Viljoen, S., Howard, M.A., Grosland, N.M., 2020. A comprehensive finite element model of surgical treatment for cervical myelopathy. *Clinical Biomechanics* 74, 79–86. <https://doi.org/10.1016/j.clinbiomech.2020.02.009>
- [Sudres et al. 2020] Sudres, P., Evin, M., Arnoux, P.-J., Callot, V., 2020. Cervical canal morphology: Effects of neck flexion in normal condition - New elements for biomechanical simulations and surgical management. *Spine Publish Ahead of Print*. <https://doi.org/10.1097/BRS.0000000000003496>
- [Swindell et al. 2013] Swindle, M.M., Smith, A.C., 2013. Best Practices for Performing Experimental Surgery in Swine. *Journal of Investigative Surgery* 26, 63–71. <https://doi.org/10.3109/08941939.2012.693149>
- [Tangen et al. 2015] Tangen, K.M., Hsu, Y., Zhu, D.C., Linninger, A.A., 2015. CNS wide simulation of flow resistance and drug transport due to spinal microanatomy. *Journal of Biomechanics* 48, 2144–2154. <https://doi.org/10.1016/j.jbiomech.2015.02.018>
- [Tirrell et al. 2018] Tirrell, T.F., Rademaker, A.W., Lieber, R.L., 2018. Analysis of hierarchical biomechanical data structures using mixed-effects models. *Journal of Biomechanics* 69, 34–39. <https://doi.org/10.1016/j.jbiomech.2018.01.013>
- [Vandenabeele et al. 1996] Vandenabeele, F., Creemers, J., Lambrechts, I., 1996. Ultrastructure of the human spinal arachnoid mater and dura mater. *J Anat* 189, 417–430.
- [Wilke et al. 2011] Wilke, H.-J., Geppert, J., Kienle, A., 2011. Biomechanical in vitro evaluation of the complete porcine spine in comparison with data of the human spine. *Eur Spine J* 20, 1859–1868. <https://doi.org/10.1007/s00586-011-1822-6>
- [Yoganandan et al. 2000] Yoganandan, N., Kumaresan, S., Pintar, F.A., 2000. Geometric and Mechanical Properties of Human Cervical Spine Ligaments. *J Biomech Eng* 122, 623–629. <https://doi.org/10.1115/1.1322034>
- [Zwirner et al. 2019] Zwirner, J., Scholze, M., Waddell, J.N., Ondruschka, B., Hammer, N., 2019. Mechanical Properties of Human Dura Mater in Tension – An Analysis at an Age Range of 2 to 94 Years. *Sci Rep* 9, 1–11. <https://doi.org/10.1038/s41598-019-52836-9>
- [Chauvet et al. 2010] D. Chauvet, A. Carpentier, J.-M. Allain, M. Polivka, J. Crépin, B. George, Histological and biomechanical study of dura mater applied to the technique of dura splitting decompression in Chiari type I malformation., *Neuro Surg. Rev.* 33 (2010) 287–94; discussion 295. <https://doi.org/10.1007/s10143-010-0261-x>.
- [Protasoni et al. 2011] M. Protasoni, S. Sangiorgi, A. Cividini, G.T. Culivaris, G. Tomei, C. Dell’Orbo, M. Raspanti, S. Balbi, M. Reguzzoni, The collagenic architecture of human dura mater, *J. Neurosurg.* 114 (2011) 1723–1730. <https://doi.org/10.3171/2010.12.JNS101732>.
- [Fong et al. 2003] K.D. Fong, S.M. Warren, E.G. Lobo, J.H. Henderson, T.D. Fang, C.M. Cowan, D.R. Carter, M.T. Longaker, Mechanical strain affects dura mater biological processes: implications for immature calvarial healing, *Plast. Reconstr. Surg.* 112 (2003) 1312–1327. <https://doi.org/10.1097/01.PRS.0000079860.14734.D6>.
- [Ramo et al. 2018c] N.L. Ramo, K.L. Troyer, C.M. Puttlitz, Viscoelasticity of spinal cord and meningeal tissues., *Acta Biomater.* 75 (2018) 253–262. <https://doi.org/10.1016/j.actbio.2018.05.045>.

- [Bertram 2010] C.D. Bertram, Evaluation by fluid/structure-interaction spinal-cord simulation of the effects of subarachnoid-space stenosis on an adjacent syrinx, *J. Biomech. Eng.* 132 (2010) 061009. <https://doi.org/10.1115/1.4001165>.
- [Bertram and Heil 2017] C.D. Bertram, M. Heil, A Poroelastic Fluid/Structure-Interaction Model of Cerebrospinal Fluid Dynamics in the Cord With Syringomyelia and Adjacent Subarachnoid-Space Stenosis, *J. Biomech. Eng.* 139 (2017). <https://doi.org/10.1115/1.4034657>.
- [Sacks and Sun 2003] M.S. Sacks, W. Sun, Multiaxial mechanical behavior of biological materials, *Annu. Rev. Biomed. Eng.* 5 (2003) 251–284. <https://doi.org/10.1146/annurev.bioeng.5.011303.120714>.
- [Reina et al. 2004] M.A. Reina, O.D.L. De León Casasola, M.C. Villanueva, A. López, F. Machés, J.A. De Andrés, Ultrastructural findings in human spinal pia mater in relation to subarachnoid anesthesia, *Anesth. Analg.* 98 (2004) 1479–1485, table of contents. <https://doi.org/10.1213/01.ane.0000113240.09354.e9>.
- [Walsh et al. 2018] D.R. Walsh, A.M. Ross, S. Malijauskaite, B.D. Flanagan, D.T. Newport, K.D. McGourty, J.J.E. Mulvihill, Regional mechanical and biochemical properties of the porcine cortical meninges, *Acta Biomater.* 80 (2018) 237–246. <https://doi.org/10.1016/j.actbio.2018.09.004>.
- [Kinaci et al. 2020] A. Kinaci, W. Bergmann, R. Bleys, A. van der Zwan, T. van Doormaal, Histologic Comparison of the Dura Mater among Species., *Comp. Med.* 70 (2020) 170–175. <https://doi.org/10.30802/aalas-cm-19-000022>.
- [Reina et al. 2020] M.A. Reina, A. Boezaart, C. De Andres-Serrano, R. Rubio-Haro, J. De Andrés, Microanatomy Relevant to Intrathecal Drug Delivery, *Methods Mol. Biol. Clifton NJ.* 2059 (2020) 109–120. https://doi.org/10.1007/978-1-4939-9798-5_4.
- [Machés et al. 2015] F. Machés, M.A. Reina, O. De León Casasola, Ultrastructure of Spinal Pia Mater, in: M.A. Reina, J.A. De Andrés, A. Hadzic, A. Prats-Galino, X. Sala-Blanch, A.A.J. van Zundert (Eds.), *Atlas Funct. Anat. Reg. Anesth. Pain Med. Hum. Struct. Ultrastruct. 3D Reconstr. Images*, Springer International Publishing, Cham, 2015: pp. 499–522. https://doi.org/10.1007/978-3-319-09522-6_25.
- [Maikos et al. 2008] J.T. Maikos, R.A.I. Elias, D.I. Shreiber, Mechanical properties of dura mater from the rat brain and spinal cord, *J. Neurotrauma.* 25 (2008) 38–51. <https://doi.org/10.1089/neu.2007.0348>.
- [Henderson et al. 2005] J.H. Henderson, R.P. Nacamuli, B. Zhao, M.T. Longaker, D.R. Carter, Age-dependent residual tensile strains are present in the dura mater of rats, *J. R. Soc. Interface.* 2 (2005) 159–167. <https://doi.org/10.1098/rsif.2005.0035>.
- [Patin et al. 1993] D.J. Patin, E.C. Eckstein, K. Harum, V.S. Pallares, Anatomic and biomechanical properties of human lumbar dura mater, *Anesth. Analg.* 76 (1993) 535–540. <https://doi.org/10.1213/00000539-199303000-00014>.
- [Shetye et al. 2014] S.S. Shetye, M.M. Deault, C.M. Puttlitz, Biaxial response of ovine spinal cord dura mater, *J. Mech. Behav. Biomed. Mater.* 34 (2014) 146–153. <https://doi.org/10.1016/j.jmbbm.2014.02.014>.
- [Mazgajczyk et al. 2012] E. Mazgajczyk, K. Ściagała, M. Czyż, W. Jarmundowicz, R. Będziński, Mechanical properties of cervical dura mater, *Acta Bioeng. Biomech.* 14 (2012) 51–58.
- [Wilcox et al. 2003] R.K. Wilcox, L.E. Bilston, D.C. Barton, R.M. Hall, Mathematical model for the viscoelastic properties of dura mater, *J. Orthop. Sci. Off. J. Jpn. Orthop. Assoc.* 8 (2003) 432–434. <https://doi.org/10.1007/s10776-003-0644-9>.
- [Persson et al. 2010] C. Persson, S. Evans, R. Marsh, J.L. Summers, R.M. Hall, Poisson's ratio and strain rate dependency of the constitutive behavior of spinal dura mater, *Ann. Biomed. Eng.* 38 (2010) 975–983. <https://doi.org/10.1007/s10439-010-9924-6>.
- [Runza et al. 1999] M. Runza, R. Pietrabissa, S. Mantero, A. Albani, V. Quagliani, R. Contro, Lumbar dura mater biomechanics: experimental characterization and scanning electron microscopy observations, *Anesth. Analg.* 88 (1999) 1317–1321. <https://doi.org/10.1097/00000539-199906000-00022>.
- [Zwirner et al. 2019] J. Zwirner, M. Scholze, J.N. Waddell, B. Ondruschka, N. Hammer, Mechanical Properties of Human Dura Mater in Tension – An Analysis at an Age Range of 2 to 94 Years, *Sci. Rep.* 9 (2019) 1–11. <https://doi.org/10.1038/s41598-019-52836-9>.
- [Zarzur et al. 1996] E. Zarzur, Mechanical properties of the human lumbar dura mater, *Arq. Neuropsiquiatr.* 54 (1996) 455–460. <https://doi.org/10.1590/s0004-282x1996000300015>.
- [van Noort et al. 1981] R. van Noort, M.M. Black, T.R. Martin, S. Meanley, A study of the uniaxial mechanical properties of human dura mater preserved in glycerol, *Biomaterials.* 2 (1981) 41–45. [https://doi.org/10.1016/0142-9612\(81\)90086-7](https://doi.org/10.1016/0142-9612(81)90086-7).
- [Kriewall et al. 1983] T.J. Kriewall, N. Akkas, D.I. Bylski, J.W. Melvin, B.A. Work, Mechanical behavior of fetal dura mater under large axisymmetric inflation, *J. Biomech. Eng.* 105 (1983) 71–76. <https://doi.org/10.1115/1.3138388>.
- [Budday et al. 2017] S. Budday, G. Sommer, C. Birkel, C. Langkammer, J. Haybaeck, J. Kohnert, M. Bauer, F. Paulsen, P. Steinmann, E. Kuhl, G.A. Holzapfel, Mechanical characterization of human brain tissue, *Acta Biomater.* 48 (2017) 319–340. <https://doi.org/10.1016/j.actbio.2016.10.036>.
- [Yang et al. 2019] C. Yang, X. Yang, X. Lan, H. Zhang, M. Wang, Y. Zhang, Y. Xu, P. Zhen, [Structure and mechanical characteristics of spinal dura mater in different segments of sheep's spine], *Zhongguo Xiu Fu Chong Jian Wai Ke Za Zhi Zhongguo XiuFu Chongjian Waike Zazhi Chin. J. Reparative Reconstr. Surg.* 33 (2019) 232–238. <https://doi.org/10.7507/1002-1892.201807085>.

- [Ozawa et al. 2004] H. Ozawa, T. Matsumoto, T. Ohashi, M. Sato, S. Kokubun, Mechanical properties and function of the spinal pia mater, *J. Neurosurg. Spine*. 1 (2004) 122–127. <https://doi.org/10.3171/spi.2004.1.1.0122>.
- [Fabris et al. 2019] G. Fabris, Z. M. Suar, M. Kurt, Micromechanical heterogeneity of the rat pia-arachnoid complex, *Acta Biomater.* 100 (2019) 29–37. <https://doi.org/10.1016/j.actbio.2019.09.044>.
- [Laksari et al. 2012] K. Laksari, M. Shafieian, K. Darvish, Constitutive model for brain tissue under finite compression, *J. Biomech.* 45 (2012) 642–646. <https://doi.org/10.1016/j.jbiomech.2011.12.023>.
- [Jin et al. 2011] X. Jin, K.H. Yang, A.I. King, Mechanical properties of bovine pia-arachnoid complex in shear, *J. Biomech.* 44 (2011) 467–474. <https://doi.org/10.1016/j.jbiomech.2010.09.035>.
- [Aimedieu et al. 2004] P. Aimedieu, R. Grebe, Tensile strength of cranial pia mater: preliminary results, *J. Neurosurg.* 100 (2004) 111–114. <https://doi.org/10.3171/jns.2004.100.1.0111>.
- [Jin et al. 2006] X. Jin, J.B. Lee, L.Y. Leung, L. Zhang, K.H. Yang, A.I. King, Biomechanical response of the bovine pia-arachnoid complex to tensile loading at varying strain-rates, *Stapp Car Crash J.* 50 (2006) 637–649.
- [Sacks et al. 2000] M.S. Sacks, Biaxial Mechanical Evaluation of Planar Biological Materials, *J. Elast. Phys. Sci. Solids.* 61 (2000) 199. <https://doi.org/10.1023/A:1010917028671>.
- [De Kegel et al.2018] D. De Kegel, J. Vastmans, H. Fehervary, B. Depreitere, J. Vander Sloten, N. Famaey, Biomechanical characterization of human dura mater, *J. Mech. Behav. Biomed. Mater.* 79 (2018) 122–134. <https://doi.org/10.1016/j.jmbbm.2017.12.023>.
- [Sun et al. 2005] W. Sun, M.S. Sacks, M.J. Scott, Effects of boundary conditions on the estimation of the planar biaxial mechanical properties of soft tissues, *J. Biomech. Eng.* 127 (2005) 709–715. <https://doi.org/10.1115/1.1933931>.
- [Deplano et al. 2016]V. Deplano, M. Boufi, O. Boiron, C. Guivier-Curien, Y. Alimi, E. Bertrand, Biaxial tensile tests of the porcine ascending aorta, *J. Biomech.* 49 (2016) 2031–2037. <https://doi.org/10.1016/j.jbiomech.2016.05.005>.
- [Fehervary et al. 2016] H. Fehervary, M. Smoljkić, J. Vander Sloten, N. Famaey, Planar biaxial testing of soft biological tissue using rakes: A critical analysis of protocol and fitting process, *J. Mech. Behav. Biomed. Mater.* 61 (2016) 135–151. <https://doi.org/10.1016/j.jmbbm.2016.01.011>.
- [Jacobs et al. 2013] N.T. Jacobs, D.H. Cortes, E.J. Vresilovic, D.M. Elliott, Biaxial tension of fibrous tissue: using finite element methods to address experimental challenges arising from boundary conditions and anisotropy, *J. Biomech. Eng.* 135 (2013) 021004. <https://doi.org/10.1115/1.4023503>.
- [Jin et al. 2014] X. Jin, H. Mao, K.H. Yang, A.I. King, Constitutive modeling of pia-arachnoid complex, *Ann. Biomed. Eng.* 42 (2014) 812–821. <https://doi.org/10.1007/s10439-013-0948-6>.
- [Sudres et al. 2021] Sudres, P., Evin, M., Wagnac, E., Bailly, N., Diotalevi, L., Melot, A., Arnoux, P.-J., Petit, Y., 2021. Tensile mechanical properties of the cervical, thoracic and lumbar porcine spinal meninges. *Journal of the Mechanical Behavior of Biomedical Materials* 115, 104280. <https://doi.org/10.1016/j.jmbbm.2020.104280>
- [Laville et al. 2020] C. Laville, C. Pradille, Y. Tillier, Mechanical characterization and identification of material parameters of porcine aortic valve leaflets, *J. Mech. Behav. Biomed. Mater.* (2020) 104036. <https://doi.org/10.1016/j.jmbbm.2020.104036>.
- [R Core Team 2020] R Core Team, R: A Language and Environment for Statistical Computing, R Foundation for Statistical Computing, Vienna, Austria, 2020. <https://www.R-project.org/>.
- [Anssari-Benam et al. 2019] A. Anssari-Benam, Y.-T. Tseng, G.A. Holzapfel, A. Bucchi, Rate-dependency of the mechanical behaviour of semilunar heart valves under biaxial deformation, *Acta Biomater.* 88 (2019) 120–130. <https://doi.org/10.1016/j.actbio.2019.02.008>.
- [Brunet et al. 2020]J. Brunet, B. Pierrat, P. Badel, Review of current advances in the mechanical description and quantification of aortic dissection mechanisms, *IEEE Rev. Biomed. Eng.* (2020). <https://doi.org/10.1109/RBME.2019.2950140>.
- [Jannesar et al. 2016]S. Jannesar, B. Nadler, C.J. Sparrey, The Transverse Isotropy of Spinal Cord White Matter Under Dynamic Load, *J. Biomech. Eng.* 138 (2016) 091004–091004. <https://doi.org/10.1115/1.4034171>.
- [Kimpara et al. 2006]H. Kimpara, Y. Nakahira, M. Iwamoto, K. Miki, K. Ichihara, S. Kawano, T. Taguchi, Investigation of anteroposterior head-neck responses during severe frontal impacts using a brain-spinal cord complex FE model, *Stapp Car Crash J.* 50 (2006) 509–544.

Chapter summary

Section 1 summary

A first published study on the description of porcine spinal meninges' tensile mechanical properties was performed in moderate condition. The aim of this study was to quantify the elastic meningeal mechanical properties along the porcine spinal cord in the longitudinal (cranio-caudal) direction and in the circumferential (surrounding the spinal cord) directions for the dura-arachnoid complex (DAC), and solely in longitudinal direction for the pia mater. A quasi-static loading assumed close to physiological solicitations was considered. In addition, the effect of the conservation method effect was assessed by comparing flash frozen (at -80°C) (different from a classical freezing at -4°C) and fresh samples properties. The main results were that the porcine model is an appropriate alternative to study the mechanical properties of meninges compared to human cadavers. In addition, this study provided isotropic hyperelastic properties and showed the negligible effect of a flash freezing conservative method to provide comparable results on DAC tissues, thus limiting the effect of the time factor in such experimental protocol. Finally, the variety of tensile elastic mechanical properties of the meninges suggests that a spatial personalization along the spinal cord of these biological soft tissues should be taken into account when in a numerical model of the central nervous system.

Section 2 summary

The previous uni-axial methodology remain limited to fully describe the tensile properties of the porcine spinal meninges. To partly address this limitation, a bi-axial tensile study was performed in moderate condition as well as microscopic analysis of collagen fibres of the DAC and the pia mater by bi-photon imaging. From these approach, several isotropic and anisotropic hyperelastic constitutive laws were fitted to experimental measurements. Elastic properties were measured to be easier compared to the previous study and literature. This study presented significant differences in elastic moduli of circumferential and longitudinal directions in both DAC and pia mater tissues as shown in the first uni-axial study. Significant differences were found between circumferential pia mater low and high thorax while even though trends could be seen in changes of material properties along the spinal cord, such changes were not found significant. Anisotropic Gasser constitutive models presented the best fit for both DAC and PM, micro-structural description enabling discussion on the capacity of constitutive law theory to match micro-structure description of meningeal tissues.

Chapter 5

Towards fluid-structure modelling

1.Mathematical background	170
1.1.Fluid flow	170
1.2.Linear elasticity.....	173
1.3.Description of motion	173
2.Monolithics FSI modelling investigation in RADIOSS	180
2.1.Brief description of FSI modelling approaches in RADIOSS	180
2.2.Stress effects of the cerebrospinal pulsatile flow on the spinal cord by a 3D fluid-structure modeling : a proof-of-concept.....	182

In this chapter, the fluid-structure interaction formulation and modelling are presented now that the morphometric aspect of the cervical subarachnoid space in which the CFS flows has been defined. In addition, the nature of the mechanical behavior of the meninges in direct contact with the CSF was presented and could be used in future numerical modelling.

The aims of this chapter were :

- 1) to propose a formulation of FSI based on the Arbitrary Lagrangian-Eulerian formulation in using the theoretical foundations of the continuum mechanics.
- 2) To briefly present the different approaches of FSI modelling available in the solver RADIOSS.
- 3) To present a preliminary FSI modelling of CSF flow.

1. Mathematical background

Abbreviations

CSF : cerebrospinal fluid
ALE : arbitrary Lagrangian Eulerian
FSI : fluid-structure interactions

This section was inspired by [Vinge 2016, White 2006] and by the continuum mechanics lectures given by Pr. Moktar Zagzoule at Paul Sabatier University of Toulouse.

To model the mechanical interactions between the flow of CSF and the meninges in particular the pia mater surrounding the spinal cord along the subarachnoid space, equations of fluid flow and equations of solids are required. Firstly, a brief mathematical description of the CSF flow modelling and the solid part by assuming a linear elastic behavior will be presented. Secondly, the fundamental descriptions of motion will be discussed. Finally, the concept of fluid-structure interactions will be developed and discussed.

To provide a mathematical description of fluid and solid mechanics, it is necessary to give an overview of the notations used :

\mathbf{v} : velocity of the material. In the fluid, \mathbf{v} represents fluid velocity, while in the solid \mathbf{v} is the velocity of solid.

\mathbf{U} : displacement of the solid. $\frac{\partial \mathbf{U}}{\partial t} = \mathbf{v}$ relates displacement and velocity in the solid, and \mathbf{U} represents the mesh displacement in the fluid.

p : pressure in the fluid.

Unit vectors in the Cartesian coordinates system are described $\mathbf{i} = (1, 0, 0)$, $\mathbf{j} = (0, 1, 0)$ and $\mathbf{k} = (0, 0, 1)$.

The Einstein summation convention will be used such as $\mathbf{v}_i \mathbf{e}_i = v_1 \mathbf{e}_1 + v_2 \mathbf{e}_2 + v_3 \mathbf{e}_3$ for a vector $\mathbf{v} = (v_1, v_2, v_3)$.

The *nabla* symbol ∇ denotes the gradient operator such as, $\nabla = \mathbf{e}_i \frac{\partial}{\partial x_i}$, and thus $\nabla \mathbf{v} = \frac{\partial v_i}{\partial x_j} \mathbf{e}_j \mathbf{e}_i$.

The indices f and s denotes the fluid and solid quantities, respectively.

δ_{ij} is the Kronecker delta function. It is equal to 1 if $i = j$ and 0 otherwise.

The **divergence theorem** (also known as the Gauss-Ostrogradsky theorem) states that the surface integral of the normal component of a vector point field \mathbf{F} over a closed surface $S_0 = \partial V_0$ is equal to the volume integral of the divergence of \mathbf{F} , a vectorial quantity taken over the volume V_0 enclosed by the surface $S_0 = \partial V_0$. The theorem is denoted such as :

$$\int_{V_0} \nabla \cdot \mathbf{F} dV = \int_{S_0} \mathbf{F} \cdot \mathbf{n} dS, \quad (1)$$

where \mathbf{n} is the outward unit normal on S_0 .

1.1. Fluid flow

1.1.1. Reynolds transport theorem

Any change in the quantity of any entity within a closed surface can only be achieved in two distinct ways: it may be achieved by the production or destruction of the entity within the surface, or by the passage of the entity across the surface.

The Reynolds' transport theorem can be considered from two different points of view. One is called Lagrangian, where one follows all fluid particles and describes the variations around each fluid particle along its trajectory. The other is Eulerian, where the variations are described at all fixed stations as a function of time. To briefly illustrate these two approaches, I will take the example of an ornithologist. In the first case (Eulerian), the photographer is always in a static position and keep his gaze in the same direction to the horizon and he watches through his lens all the birds that pass. In the second case (Lagrangian), the ornithologist put some trackers on the birds to follow the trajectories of flight.

Let consider a fixed control volume, V_0 and some fluid property $Q(\mathbf{x}, t)$. The rate of change of Q within the control volume can be written as

$$\frac{d}{dt} \int_{V_0} Q(\mathbf{x}, t) dV \quad (2)$$

The net change of Q must be equaled to the rate of change in Q within the control volume plus the net rate of mass flow out of the volume, i.e. :

$$\frac{d}{dt} \int_{V_0} Q(\mathbf{x}, t) dV = \int_{V_0} \frac{\partial Q(\mathbf{x}, t)}{\partial t} dV + \int_{S_0=\partial V_0} Q(\mathbf{x}, t) \mathbf{v} \cdot \mathbf{n} dS \quad (3)$$

Here \mathbf{n} denotes the outward pointing unit-normal vector to the infinitesimal surface dS , i.e. \mathbf{n} points out of the fluid surface S_0 . This equation (3) is known as the Reynold's transport theorem.

1.1.2. Conservation of mass and momentum

Assuming $Q(\mathbf{x}, t) = \rho$, where ρ is fluid density. Conservation of mass is mathematically translated by :

$$\frac{d}{dt} \int_{V_0} \rho dV = 0, \quad (4)$$

which can be rewritten using the Reynolds' transport theorem:

$$\int_{V_0} \left[\frac{\partial \rho}{\partial t} + \nabla \cdot (\rho \mathbf{v}) \right] dV = 0 \quad (5)$$

Equation (5) is known as the continuity equation and describes the conservation of mass.

To derive a similar property of momentum, Newton's second law of motion is used. The net change of momentum must be equal to the applied forces to the chosen volume. The forces can be divided into volumetric forces, acting on the entire control volume, and forces acting only on the control surface. The forces acting on the surfaces can be written $\overline{\sigma}_f = \overline{\sigma}_f(\mathbf{v}, \mathbf{p})$ is the symmetric tensor denoting the fluid stress. \mathbf{F}_v is a volumic force such as gravity. Thus, balance of momentum requires that :

$$\frac{d}{dt} \int_{V_0} \rho \mathbf{v}(\mathbf{x}, t) dV = \int_{\partial V_0} \overline{\sigma}_f \cdot \mathbf{n} dS + \int_{V_0} \mathbf{F}_v dV \quad (6)$$

By using the transport theorem on the left hand side and the divergence theorem on the surface integral on the right hand side, we obtain the equations (7 and 8) :

$$\int_{V_0} \left[\frac{\partial \rho \mathbf{v}}{\partial t} + \nabla \cdot (\rho \mathbf{v} \mathbf{v}) - \nabla \cdot \overline{\sigma}_f - \mathbf{F}_v \right] dV = 0 \quad (7)$$

$$\frac{\partial \rho \mathbf{v}}{\partial t} + \nabla \cdot (\rho \mathbf{v} \mathbf{v}) = \nabla \cdot \overline{\overline{\boldsymbol{\sigma}_f}} + \mathbf{F}_v \quad (8)$$

The left hand side of the equation can be rewritten as :

$$\rho \frac{\partial \mathbf{v}}{\partial t} + \mathbf{v} \frac{\partial \rho}{\partial t} + \mathbf{v} \mathbf{v} \cdot \nabla \rho + \rho \mathbf{v} \cdot \nabla \mathbf{v} + \mathbf{v} \rho \cdot \nabla \mathbf{v} = \rho \left(\frac{\partial \mathbf{v}}{\partial t} + (\mathbf{v} \cdot \nabla) \mathbf{v} \right) + \left(\frac{\partial \rho}{\partial t} + \nabla \cdot (\mathbf{v} \rho) \right) \quad (9)$$

Fluid density is considered to be constant over time and then, the equation (8) can be simplified such as :

$$\rho \left(\frac{\partial \mathbf{v}}{\partial t} + (\mathbf{v} \cdot \nabla) \mathbf{v} \right) = \nabla \cdot \overline{\overline{\boldsymbol{\sigma}_f}} + \mathbf{F}_v \quad (10)$$

The equation (9) is called the momentum equation and describes the balance of momentum. The stress tensor $\boldsymbol{\sigma}_f$ is defined in the next subsection.

1.1.3. Incompressible Newtonian fluids

As far as we know, the CSF is considered such as a Newtonian fluid due to its mechanical properties close to the mechanical properties of water [Bloomfield et al. 1998]. By analogy with Hookean elasticity, Newtonian model is based on the simplest assumption : the variation of viscous stress with strain rate is a linear law. This assumption is satisfied by most common fluids. Finally, Newtonian model is described by the three next assumptions :

the fluid is continuous, and the stress tensor $\overline{\overline{\boldsymbol{\sigma}_f}}$ is at most a linear function of the strain rate $\overline{\overline{\boldsymbol{\varepsilon}_{f,ij}^{\dot{}}}}$, the proportionality coefficient is called dynamic viscosity.

the fluid is isotropic, i.e. its properties are independent of direction.

when the strain rates are zero, the viscous stresses must be zero and the deformation law must reduce to the hydrostatic pressure condition :

$$\sigma_{f,ij} = -p \delta_{ij} \quad (11)$$

where δ_{ij} is the Kronecker delta function.

When the fluid is in motion, a non-isotropic part has to be added as denoted in the equation (11), including any shear stresses called the deviatoric stress tensor. It describes the degree of fluid distortion.

$$\sigma_{f,ij} = -p \delta_{ij} + d_{ij}$$

White [2006 - p.88] demonstrates that the deviatoric stress tensor can finally be simplified such as :

$$\sigma_{f,ij} = -p \delta_{ij} + 2\mu \varepsilon_{f,ij}^{\dot{}} + \lambda \nabla \cdot \mathbf{v} \delta_{ij} \quad (12)$$

where $\varepsilon_{f,ij}^{\dot{}} = \frac{1}{2} \left(\frac{\partial v_i}{\partial x_j} + \frac{\partial v_j}{\partial x_i} \right)$, p is the fluid pressure, μ and λ are known as Lamé's constants. The first Lamé's term is also called dynamics viscosity in fluid mechanics. As water, CSF is considered as incompressible giving the constant density ρ .

From the continuity equation (), this implies $\nabla \cdot \mathbf{v} = 0$.

Let

$$\nabla \cdot 2\mu \boldsymbol{\varepsilon}_f = \mu \frac{\partial}{\partial x_j} \left(\frac{\partial v_j}{\partial x_i} + \frac{\partial v_i}{\partial x_j} \right) \mathbf{e}_i = \mu \left(\frac{\partial}{\partial x_i} \frac{\partial v_j}{\partial x_j} + \frac{\partial v_i}{\partial x_j \partial x_j} \right) \mathbf{e}_i = \mu \frac{\partial v_i}{\partial x_j \partial x_j} \mathbf{e}_i = \mu \nabla^2 \mathbf{v} \quad (13)$$

which simplifies the representation of $\nabla \cdot \boldsymbol{\sigma}_f$ in () for an incompressible fluid.

1.1.4. Navier-Stokes equations for incompressible flow

The system of equation (14) and (15) are commonly referred to as the Navier-Stokes equations :

$$\rho \left(\frac{\partial \mathbf{v}}{\partial t} + (\mathbf{v} \cdot \nabla) \mathbf{v} \right) = -\nabla p + \mu \nabla^2 \mathbf{v} + \mathbf{F}_v \quad (14)$$

$$\nabla \cdot \mathbf{v} = 0 \quad (15)$$

Navier-Stokes equations are coupled and non-linear, and can generally not be solved analytically. Hence, multiple numerical solutions were developed representing a whole scientific domain called Computational Fluid Dynamics allowing to provide an approximation of NS solution.

1.2. Linear elasticity

The elastic behavior of a solid material can be described by using the Reynolds Transport theorem on a moving domain over time Ω^t , composing of the same particles at all times. For conservation of momentum, the change in momentum must equal the applied forces to the system as well as body forces:

$$\frac{d}{dt} \int_{\Omega^t} \rho \mathbf{v} dV = \int_{\Omega^t} \rho \frac{\partial \mathbf{v}}{\partial t} dV + \int_{\partial \Omega^t} \rho \mathbf{v} \mathbf{v} \cdot \mathbf{n} dS = \int_{\partial \Omega^t} \overline{\boldsymbol{\sigma}_s} \cdot \mathbf{n} dS + \int_{\Omega^t} \mathbf{F}_v dV \quad (16)$$

where $\boldsymbol{\sigma}_s$ is the stress tensor of the solid material, ρ is the density of the solid material and the material velocity vector $\mathbf{v} = \frac{\partial \mathbf{U}}{\partial t}$ with \mathbf{U} , the displacement vector. By applying the divergence theorem, the general elasticity equation of the domain Ω^t is denoted :

$$\rho \left(\frac{\partial \mathbf{v}}{\partial t} + (\mathbf{v} \cdot \nabla) \mathbf{v} \right) = \nabla \cdot \overline{\boldsymbol{\sigma}_s} + \mathbf{F}_v \quad (17)$$

Linear elasticity is an approximation used in the theory of infinitesimal deformations for solid. Generally, the approximation is usually valid between 5 and 10% relative to the solid. Assuming an isotropic material and a linear relation between stress and strain, the stress tensor is denoted by the Hooke's law:

$$\boldsymbol{\sigma}_s = 2\mu \overline{\boldsymbol{\varepsilon}_s} + \lambda \text{tr}(\overline{\boldsymbol{\varepsilon}_s}) \overline{\boldsymbol{\delta}} \quad (18)$$

where $\boldsymbol{\varepsilon}_{sij} = \frac{1}{2} \left(\frac{\partial U_i}{\partial x_j} + \frac{\partial U_j}{\partial x_i} \right)$, μ and λ are Lamé's constants.

A more common form of the linear stress-strain relation is denoted :

$$\boldsymbol{\varepsilon}_{ij} = \frac{1}{E} \left(\sigma_{ij} - \nu (\sigma_{kk} \delta_{ij} - \sigma_{ij}) \right) \quad (19)$$

where E is the elastic modulus and ν is the Poisson ratio. This equation shows the importance to know such mechanical properties of the material in this kind of modelling. It is the form considered for the next sections.

1.3. Description of motion

The conservation equations for Newtonian fluids were derived from Reynolds' transport theorem by using a control volume fixed in space (Eulerian description), while for elastic material a moving control volume was used (Lagrangian description).

In the continuum mechanics modelling, a body occupies in a continuous way a space. To explain the description of motion used in fluid-structure interaction, it is convenient to use the classical description of motion in continuum mechanics.

In the mechanical approximation of continuum mechanics, a body A is abstractly decomposed in material particles that we called temporally by the letter P . The notion of material particle is considered as being a point behind which the microscopical life was filtered and ignored by the mechanician at the assumed observation scale. Behind the concept of particle, we can imagine that an elementary volume of discontinuous material is hidden. The continuum mechanics ignores its structure and just define a local continuous volumetric mass field $\rho(\mathbf{x}, t)$, with \mathbf{x} a position vector and t the time variable, as a kind of average. The description of motion of this body can be done in 4 ways :

- the *particle* approach identifies a particle by the letter P . Its motion is denoted as:

$$\mathbf{x} = \mathcal{F}(P, t) \quad (20)$$

where is \mathcal{F} a vectorial function.

It means that we can mathematically follow the motion of the P particle, building its trajectory in associating a position vector \mathbf{x} , at each time t , via \mathcal{F} .

- the *reference* approach identifies the P particle by its position vector \mathbf{X} occupied at a fixed time T :

$$\mathbf{x} = \mathbf{F}(\mathbf{X}, T, t) \quad (21)$$

This approach has then associated to the body in motion a *reference* configuration $C_R(A) = C_T(A)$, i.e. for any P particle, we have a relation such as : $\mathbf{X} = \mathcal{H}(P, T)$, identifying the P particle by its “reference” position at the time T . So the independent variables are \mathbf{X} and t . The equivalence between the particle and the reference approaches comes from the idea that one particle cannot occupy two different positions at the same time.

- the *Lagrangian* approach is a special case of the *reference* approach. Indeed, it is the case when in the previous approach, $T = 0$ in the configuration $C_0(A)$. The initial position at $t = 0$ will be denoted by the position vector $\boldsymbol{\xi}$. The choice of the temporal origin is arbitrary. This approach is commonly used in solid mechanics because it is easier to imagine a physical configuration of reference.
- the *eulerian or spatial* approach describes the current configuration $C_t(A)$ and this *via* the space occupied at the current time t by the body A . Thus, we look at what is moved in a fixed volume during a duration Δt . The different particles which flow through this fixed volume “instantaneously” printed in it their physical properties. This approach is commonly used in fluid mechanics in order to focus on what is happened to the particles in a given place rather than where they comes from and where they go. The independent variables are \mathbf{x} and t and the Eulerian formulation can be denoted like that :

$$\mathbf{X} = \mathbf{F}^{-1}(\mathbf{x}, t, T) \quad (22)$$

Thus we look at the identified particles by (\mathbf{X}, T) move at different time t in a fixed region (\mathbf{x} associated to a fixed spatial region).

1.3.1. Lagrangian approach

The Lagrangian velocity is denoted :

$$\mathbf{V}_L = \mathbf{V}(\boldsymbol{\xi}, t) = \left. \frac{\partial \mathbf{F}(\boldsymbol{\xi}, t)}{\partial t} \right|_{\boldsymbol{\xi}} \quad (23)$$

And the Lagrangian acceleration :

$$\mathbf{a}_L = \mathbf{a}(\boldsymbol{\xi}, t) = \frac{\partial \mathbf{v}(\boldsymbol{\xi}, t)}{\partial t} \Big|_{\boldsymbol{\xi}} = \frac{\partial^2 \mathbf{F}(\boldsymbol{\xi}, t)}{\partial t^2} \Big|_{\boldsymbol{\xi}} \quad (24)$$

This derivative with respect to the time while following the particle in its motion is called particle derivative or material derivative.

At $t = 0$, the vector function \mathbf{F} must verify $\boldsymbol{\xi} = \mathbf{F}(\boldsymbol{\xi}, 0)$. Furthermore, the relation $\mathbf{x} = \mathbf{F}(\boldsymbol{\xi}, t)$ does not make sense in terms of particle motion if \mathbf{F} is bijective. The trajectories cannot intersect at the same time, two particles cannot be in the same place at the same time. Then,

$$\exists \mathbf{F}^{-1}, \quad \boldsymbol{\xi} = \mathbf{F}^{-1}(\mathbf{x}, t) \quad (25)$$

The map \mathbf{F}^{-1} , inverse of \mathbf{F} give the initial position from or in function of the current position [Fig. 58].

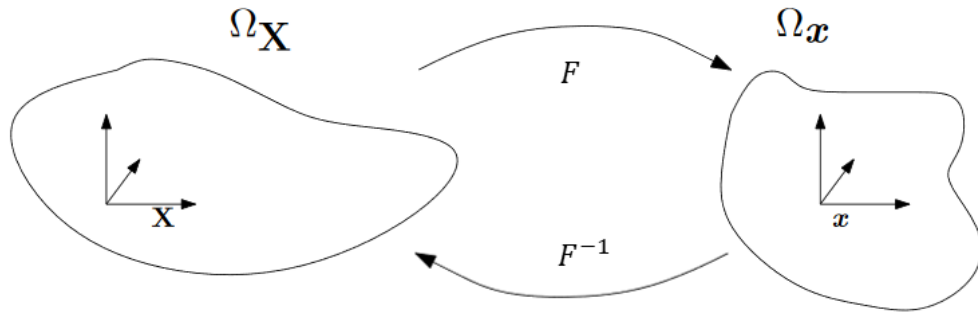


Figure 58. Lagrangian and Eulerian descriptions of motion. The mapping \mathbf{F} maps the reference coordinates to the spatial ones and \mathbf{F}^{-1} does this inverse.

1.3.2. Eulerian approach

The Eulerian velocity is denoted $\mathbf{v}_E(\mathbf{x}, t) = \mathbf{v}(\mathbf{x}, t) = \frac{d\mathbf{x}}{dt}$. The Eulerian acceleration is denoted :

$$\mathbf{a}_E = \frac{\partial \mathbf{v}(\mathbf{x}, t)}{\partial t} \quad (26)$$

For the next subsection, we introduce the matrix representation for the gradient of \mathbf{F} proposed in [Donea et al. 2004] :

$$\text{Let } \mathbf{F} : \Omega_{\mathbf{X}} \times [0, T] \rightarrow \Omega_{\mathbf{x}} \times [0, T] \\ (\mathbf{X}, t) \rightarrow \mathbf{F}(\mathbf{X}, t) = (\mathbf{x}, t)$$

$$\frac{\partial \mathbf{F}}{\partial (\mathbf{X}, t)} = \begin{pmatrix} \frac{\partial \mathbf{x}}{\partial \mathbf{X}} & \mathbf{v} \\ \mathbf{0}^T & 1 \end{pmatrix} \quad (27)$$

1.3.3. The arbitrary Eulerian Lagrangian description

In order to couple the Lagrangian approach for the solid and the Eulerian approach for the fluid, we need some referential system, not attached to the material points neither totally fixed in space. This type of description is common in FSI modelling and is known as the arbitrary Lagrangian-Eulerian (ALE) description which is part of the conforming-mesh methods. The following description is inspired by the ALE formulation by Donea et al. [2004].

In need of an additional set of coordinates, an independent referential system with reference coordinates χ is introduced. This introduces two new mappings to relate all the different configurations as shown in Figure 59.

The mappings are defined similarly to \mathbf{F} :

$$\begin{aligned} \mathbf{G} : \Omega_{\chi} \times [0, T] &\rightarrow \Omega_{\chi} \times [0, T] \\ (\chi, t) &\rightarrow \mathbf{G}(\chi, t) = (\mathbf{x}, t) \end{aligned}$$

And the gradient of \mathbf{G} is :

$$\frac{\partial \mathbf{G}}{\partial (\chi, t)} = \begin{pmatrix} \frac{\partial \mathbf{x}}{\partial \chi} & \mathbf{w} \\ \mathbf{0}^T & 1 \end{pmatrix} \quad (28)$$

In addition,

$$\mathbf{w}(\chi, t) = \frac{\partial \mathbf{x}}{\partial t} \Big|_{\chi} \quad (29)$$

denotes the mesh velocity. Both the mesh and the material can move independently of the fixed set of laboratory coordinates. More precise, relative to some referential point in space, the fluid moves with velocity \mathbf{v} and the domain moves with velocity \mathbf{w} .

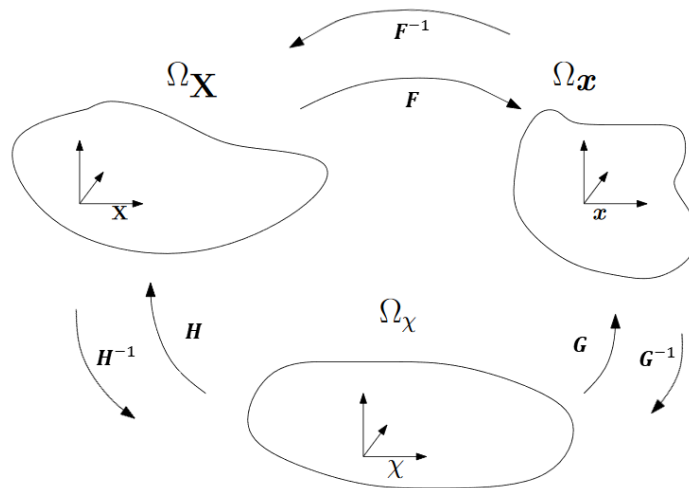


Figure 59. The three domains needed in the ALE formulation

To complete the relation between the different velocities, we define the inverse of \mathbf{H} directly :

$$\begin{aligned} \mathbf{H}^{-1} : \Omega_{\chi} \times [0, T] &\rightarrow \Omega_{\chi} \times [0, T] \\ (\mathbf{X}, t) &\rightarrow \mathbf{H}^{-1}(\mathbf{X}, t) = (\chi, t) \end{aligned}$$

The gradient of \mathbf{H}^{-1} is given as

$$\frac{\partial \mathbf{H}^{-1}}{\partial (\mathbf{X}, t)} = \begin{pmatrix} \frac{\partial \chi}{\partial \mathbf{X}} & \hat{\mathbf{v}} \\ \mathbf{0}^T & 1 \end{pmatrix} \quad (30)$$

where the velocity

$$\hat{\mathbf{v}}(\mathbf{X}, t) = \frac{\partial \chi}{\partial t} \Big|_{\mathbf{X}} \quad (31)$$

denotes the temporal change in the referential system while holding the material particle \mathbf{X} fixed. Therefore, the velocity $\hat{\mathbf{v}}$ can be interpreted as the particle velocity in the referential domain. We use that $\mathbf{F} = \mathbf{G} \circ \mathbf{H}^{-1} = \mathbf{G}(\mathbf{H}^{-1}(\mathbf{X}, t))$ and obtain a relation between the different velocities by differentiating \mathbf{F} :

$$\begin{aligned} \frac{\partial \mathbf{F}}{\partial (\mathbf{X}, t)}(\mathbf{X}, t) &= \frac{\partial \mathbf{H}}{\partial (\mathbf{X}, t)}(\mathbf{H}^{-1}(\mathbf{X}, t)) \frac{\partial \mathbf{H}^{-1}}{\partial (\mathbf{X}, t)}(\mathbf{X}, t) \\ &= \frac{\partial \mathbf{H}}{\partial (\mathbf{X}, t)}(\mathbf{X}, t) \frac{\partial \mathbf{H}^{-1}}{\partial (\mathbf{X}, t)}(\mathbf{X}, t) \end{aligned} \quad (32)$$

In matrix form this equation is written as

$$\begin{pmatrix} \frac{\partial \mathbf{x}}{\partial \mathbf{X}} & \mathbf{v} \\ \mathbf{0}^T & 1 \end{pmatrix} = \begin{pmatrix} \frac{\partial \mathbf{x}}{\partial \boldsymbol{\chi}} & \mathbf{w} \\ \mathbf{0}^T & 1 \end{pmatrix} \begin{pmatrix} \frac{\partial \boldsymbol{\chi}}{\partial \mathbf{X}} & \hat{\mathbf{v}} \\ \mathbf{0}^T & 1 \end{pmatrix} \quad (33)$$

After block-multiplication of the right hand side, we end up with an equation relating the different velocities :

$$\mathbf{v} = \frac{\partial \mathbf{x}}{\partial \boldsymbol{\chi}} \cdot \hat{\mathbf{v}} + \mathbf{w} \quad (34)$$

To this end, it is convenient to define the convective velocity

$$\mathbf{c} \equiv \mathbf{v} - \mathbf{w} = \frac{\partial \mathbf{x}}{\partial \boldsymbol{\chi}} \cdot \hat{\mathbf{v}} \quad (35)$$

which is the relative velocity between the material and the mesh.

To obtain relation between quantities to formulate the balance equations, we let a scalar quantity, Q be defined as $Q(\mathbf{x}, t)$, $Q^*(\boldsymbol{\chi}, t)$ and $Q^{**}(\mathbf{X}, t)$ in the spatial, referential and material domains respectively. To obtain a relation between the spatial description, Q and material description Q^{**} we use the previously described mapping \mathbf{F} :

$$Q^{**}(\mathbf{X}, t) = Q(\mathbf{G}(\mathbf{X}, t), t) = Q \circ \mathbf{H} \quad (36)$$

The gradient of Q^{**} can then be computed as

$$\frac{\partial Q^{**}}{\partial (\mathbf{X}, t)}(\mathbf{X}, t) = \frac{\partial Q}{\partial (\mathbf{x}, t)}(\mathbf{x}, t) \frac{\partial \mathbf{F}}{\partial (\mathbf{X}, t)}(\mathbf{X}, t) \quad (37)$$

or in matrix form :

$$\begin{pmatrix} \frac{\partial Q^{**}}{\partial \mathbf{X}} & \frac{\partial Q^{**}}{\partial t} \end{pmatrix} = \begin{pmatrix} \frac{\partial Q}{\partial \mathbf{x}} & \frac{\partial Q}{\partial t} \end{pmatrix} \begin{pmatrix} \frac{\partial \mathbf{x}}{\partial \mathbf{X}} & \mathbf{v} \\ \mathbf{0}^T & 1 \end{pmatrix} \quad (38)$$

After matrix multiplication, one can obtain the equation between material and spatial time derivatives:

$$\frac{\partial Q^{**}}{\partial t} = \frac{\partial Q}{\partial t} + \frac{\partial Q}{\partial \mathbf{x}} \cdot \mathbf{v} \quad (39)$$

To ease notation we drop the stars to simplify the notation in a form called particle derivative :

$$\frac{dQ}{dt} = \frac{\partial Q}{\partial t} + (\mathbf{v} \cdot \nabla) Q \quad (40)$$

which can be interpreted in the usual way: the variation of a physical quantity for a given particle \mathbf{X} is the local variation plus a convective term taking into account the relative motion between the material and spatial (laboratory) systems.

Another simplification of the material time derivative to not overload the equations is denoted as

$$\frac{d}{dt} \equiv \frac{\partial}{\partial t} \Big|_x$$

and the spatial time derivative as

$$\frac{\partial}{\partial t} \equiv \frac{\partial}{\partial t} \Big|_x$$

The next step is to relate the material and the referential description of the quantity, Q^{**} and Q^* respectively, by the mapping \mathbf{G} . This relation is written as

$$Q^{**} = Q^* \circ \mathbf{G}^{-1} \quad (41)$$

By proceeding the same way as in (38) and (39), the relation between material and referential time derivatives is written

$$\frac{\partial Q^{**}}{\partial t} = \frac{\partial Q^*}{\partial t} + \frac{\partial Q^*}{\partial x} \cdot \hat{\mathbf{v}} \quad (42)$$

If we rather want to express the spatial derivative of Q^* in the spatial domain, we can use the definition of $\hat{\mathbf{v}}$ from equation (34) to end up with

$$\frac{\partial Q^{**}}{\partial t} = \frac{\partial Q^*}{\partial t} + \frac{\partial Q^*}{\partial x} \cdot \mathbf{c} \quad (43)$$

This equation can be written in more common notation, and the following is known as the fundamental ALE equation :

$$\frac{dQ}{dt} = \frac{\partial Q}{\partial t} \Big|_x + (\mathbf{c} \cdot \nabla) Q \quad (44)$$

or in a complete form :

$$\frac{\partial Q}{\partial t} \Big|_x = \frac{\partial Q}{\partial t} \Big|_x + \frac{\partial Q}{\partial x} \cdot \mathbf{c} \quad (45)$$

and states that the time derivative in the material configuration equals its local (referential) derivative plus a convective term taking into account the relative difference in velocity between the two systems.

Also, by combining equations (40) and (44), we can relate the spatial time derivative with the referential time derivative as

$$\frac{\partial Q}{\partial t} = \frac{\partial Q}{\partial t} \Big|_x - (\mathbf{w} \cdot \nabla) Q \quad (46)$$

1.3.4.ALE form of conservation equations

The ALE differential form of the conservation equations for mass and momentum obtained from the Eulerian forms:

Mass

$$\frac{d\rho}{dt} = \frac{\partial \rho}{\partial t} \Big|_x + \mathbf{v} \cdot \nabla \rho = -\rho \nabla \cdot \mathbf{v} \quad (47)$$

Momentum

$$\rho \frac{d\mathbf{v}}{dt} = \rho \left(\frac{\partial \mathbf{v}}{\partial t} \Big|_x + (\mathbf{v} \cdot \nabla) \mathbf{v} \right) = \nabla \cdot \boldsymbol{\sigma} + \rho \mathbf{F}_v \quad (48)$$

where ρ is the mass density, \mathbf{v} is the material velocity vector, $\boldsymbol{\sigma}$ denotes the Cauchy stress tensor, \mathbf{F}_v is a volumic force.

By using equation (46), the spatial time derivatives can be replaced to obtain the equations in the ALE framework. The following equations should hold in any time-dependent domain which does not necessarily need to coincide with the motion of material particles:

Mass,

$$\frac{\partial \rho}{\partial t} \Big|_{\mathbf{x}} + \mathbf{c} \cdot \nabla \rho = -\rho \nabla \cdot \mathbf{v} \quad (49)$$

Momentum,

$$\rho \left(\frac{\partial \mathbf{v}}{\partial t} \Big|_{\mathbf{x}} + (\mathbf{c} \cdot \nabla) \mathbf{v} \right) = \nabla \cdot \boldsymbol{\sigma} + \rho \mathbf{F}_v \quad (50)$$

These equations show that in order to transform the Eulerian form of the balance equations into ALE formulation, the convective velocity is replaced with the relative velocity between the material and the mesh. It could be argued that mesh update is not necessary in combination with linear elasticity. The benefit of the ALE description is related in solid-to-fluid coupling by geometry change. Indeed, if the fluid region is computed to be narrowed, fluid will flow faster through these areas. This would not be the case when solving fluid equations in a rigid domain.

1.3.5. Fluid-structure interactions

By establishing the ALE formulation, we can now state the governing equations for the FSI problem. In the case of an Newtonian incompressible fluid together with a linear elastic material, the mathematical problem consists of solving the following set of equations :

$$\rho_f \left(\frac{\partial \mathbf{v}}{\partial t} + ((\mathbf{v} - \mathbf{w}) \cdot \nabla) \mathbf{v} \right) - \nabla \cdot \boldsymbol{\sigma}_f(\mathbf{v}, p) - \rho \mathbf{g} = 0 \quad \text{in } \Omega_f^t \quad (51)$$

$$\nabla \cdot \mathbf{v} = 0 \quad \text{in } \Omega_f^t \quad (52)$$

$$\nabla^2 \cdot \mathbf{U} = 0 \quad \text{in } \Omega_s^t \quad (53)$$

$$\rho_s \frac{\partial \mathbf{v}}{\partial t} + \rho_s (\mathbf{v} \cdot \nabla) \mathbf{v} - \nabla \cdot \boldsymbol{\sigma}_s(\mathbf{U}) - \rho \mathbf{g} = 0 \quad \text{in } \Omega_s^t \quad (54)$$

$$\mathbf{w} = \mathbf{v} \quad \text{in } \Omega_s^t \quad (55)$$

In the case of fluid interacting with a solid structure, no material can cross the moving boundary $\Gamma^t = \Omega_f^t \cap \Omega_s^t$, and thus the fluid and solid velocities must be equaled on the interface between the fluid and the solid. In general, mass conservation on the boundary must be ensured. In addition, the forces acting on each side of the surface must be equal which is ensured by a Neumann condition (57). Kinematics continuity has also to be ensured in different ways, depending on the problem considered. It can be done by a Dirichlet condition (58) or a Neumann condition (56).

$$v_i^s = v_i^f \quad \text{in } \Gamma^t \quad (56)$$

$$\sigma_{ij}^s n_i = \sigma_{ij}^f n_i \quad \text{in } \Gamma^t \quad (57)$$

$$x_i^s = x_i^f \quad \text{in } \Gamma^t \quad (58)$$

As mentioned in the beginning of this section, ALE approach is part of the conforming-mesh methods consisting in methods which track the motion of the interface and enforce the equations (56 or 58) and (57) on the interface explicitly. Thus it requires mesh update ensured by ALE description for example.

2. Monolithic FSI modelling investigation in RADIOSS

Three approaches were investigated in FSI modelling on the explicit solver RADIOSS. Initially fitted for high-energy impact or/and short time simulation, we wanted to know if it was doable to model a flow in a cavity as simplification of the CSF flow in the subarachnoid space. This wish was based on the idea to transfer the methodological approach to already developed structural model in the laboratory. The initial choice of the RADIOSS solver to implement cerebrospinal flow with FSI approach was supported by the wish of using the FSI methodology in a more detailed FE spine model including the nervous tissues [Bailly et al. 2020, Lévy et al. 2020].

2.1. Brief description of FSI modelling approaches in RADIOSS

Three types of approaches were investigated : Smooth Hydrodynamics Particles (SPH) method, Coupled Eulerian-Lagrangian (CEL) method and the arbitrary Lagrangian-Eulerian method (ALE). These modelling approaches belong to different classes of fluid-structure interaction methods that I am going to briefly explain :

- SPH method is a meshless numerical method based on interpolation theory and it is implemented in RADIOSS in Lagrangian approach whereby the motion of a discrete number of particles is followed in time. SPH is a complementary approach with respect to ALE method. When the ALE mesh is too distorted to handle good results (for example in the case of vortex creation), SPH method allows getting a sufficiently accurate solution. For more theoretical details, we suggest to refer to [Lucy 1977; Gingold and Monaghan 1977, Monaghan 1983]. Several methods for modelling boundary condition have been developed, these methods are categorized into three approaches:
 - 1) *Repulsive Walls*. A repulsive force is exerted on fluid particles, which aims to push all fluid particles away from the walls when they approach to solid wall boundary.
 - 2) *Ghost Particles*. Ghost particles are placed outside the simulation domain, and its prescribed physical quantities (such as pressure and velocity) act to enforce no-slip or free-slip condition.
 - 3) *Kernel Correction*. Using a function (such as density, mass,...) and/or its derivatives in continuous form as integral representation. In the kernel correction, the approximation of a function and its derivatives are based on the evaluation of the smoothing kernel function and its derivatives.

Each of these three methods has advantages and drawbacks. The *repulsive walls* are easy to implement, even for complex geometries, and are computationally cheap. However, as they only apply repulsive forces away from the boundary, they cannot reproduce systems under tension and capture shear stress felt by fluids on the boundary. Ghost particle method is capable of handling tension, shear stresses and surfaces forces from the fluid flow in approximating the irregular solids boundaries in subarea. [Long et al. 2017]. The conservation of velocities was shown unstable in tension at boundaries between fluid and solid domain due to the interaction between the constitutive equations and the kernel function. In addition, the viscosity computation can lead to artificial creation of energy in regions of strong shear [Radioss theory manual v2017 – SPH by Altair].

- CEL method is also called Immersed domain method. An Eulerian domain representing the fluid domain is superposed to the Lagrangian domain representing the solid domain. However, in the immersed domain method, an artificial fluid is introduced to cover the structural domain in addition to the initial considered fluid; thus, fluid domain is extended to the entire

computational domain. For example, in the case of the cerebrospinal flow modelling, the air will be the artificial fluid that we will need to fill the Eulerian grid where the solid domain is superposed. The interface is modelled in adding force-equivalent terms (Lagrange multiplier formulation) to fluid equations and it avoids mesh update in the numerical process [Hou et Layton 2012]. This approach face difficulties to accurately model the fluid behavior near the solid walls due to volume partial effect: the artificial (air) and the actual fluid (CSF) coexist with different volume ratio in the same Eulerian grid element.

- ALE method was theoretically described in the previous section. It models an arbitrary motion of fluid grid points with respect to their frame of reference by taking into account the material points displacements. It needs that the fluid and solid mesh are mesh-conformed (i.e. continuity of mesh at the fluid-structure boundaries). Initially, only hexahedral elements were available for FSI modelling. Even if hexahedral elements can allow to solve faster and to face the volume and shear locking in particular for solid application, it can complicates the geometry discretization of anatomical part such as the subarachnoid space. Method such as multiblock algorithms were developed to help this mesh step but it is often necessitating an expert operator. This constraint was apparently solved by the use of tetrahedral elements as new feature in RADIOSS 2019 but it was not tested here.

Due to preliminary simulations which do not success to provide a full simulation run, the approximation of computation at the fluid and solid boundaries to accurately quantify the velocity field near the wall of the cervical subarachnoid space, and the lack of knowledge on quantification of the number of particles effect, the SPH method was not considered as satisfying numerical approach on FSI modelling of the cerebrospinal fluid.

The lack of accuracy for fluid velocity field near the solid wall makes of the CEL or immersed domain method a method which is not adapted to our problematic of modelling interactions between the cerebrospinal fluid and the spinal central nervous system. Due to the conforming-mesh criteria and the continuity of mesh necessary to physically model the fluid-structure exchanges, the ALE method seems to be the more convenient to model the FSI between the cerebrospinal flow and the spinal cord.

2.2. Stress effects of the cerebrospinal pulsatile flow on the spinal cord by a 3D fluid-structure modeling : a proof-of-concept

P. Sudres^{1,2}, P.J. Arnoux^{1,2}, and M. Evin^{1,2}

1. Laboratoire de Biomécanique Appliquée, UMRT24 AMU/IFSTTAR, Marseille, France.

2. iLab-Spine – Laboratoire International en Imagerie et Biomécanique du Rachis, Marseille, France & Montréal, Canada.

A preliminary simplified FSI modeling of pulsatile CSF flow and spinal central nervous system was proposed in connection with the mathematical background in Section 5.1.3 and supported by previously described advantages of the ALE method.

This preliminary study was performed before the studies on mechanical characterization of porcine meninges, and the properties measured in the Chapter 4 were not used. Then, mechanical properties from literature were used here and the fluid-structure mesh-matching failed to be model. An artificial interface was used to enforce continuity of forces and kinematics quantities at the fluid-structure boundaries. This choice is discussed after this preliminary published study.

This study was published in *Computer Methods in Biomechanics and Biomedical Engineering* [Sudres et al. 2019] as part of the 44th Congress of the Société de Biomécanique, Poitiers, 2019 (France). Minor modification of the theoretical flow formulation were brought to this version compared to the published version with the authors agreement.

Abbreviations

CSF: cerebrospinal fluid

FSI: fluid-structure interaction

SC: spinal cord

ALE: arbitrary Lagrangian Eulerian

Keywords : spinal cord, cerebrospinal flow, fluid-structure interaction, Von Mises stress

2.2.1. Introduction

The mechanical phenomena which occur in the subarachnoid space have been studied either from a structural point of view particularly focusing on the spinal cord (SC) or from a fluid point of view focusing on the cerebrospinal fluid (CSF) flow.

Fluid-structure interaction (FSI) approaches provide new perspectives to numerically describe the physiological phenomenon. It has been showed that the CSF acts in a passively way on the central nervous system as shock absorber in compressive spinal cord injuries [1]. However, we are not aware of any study that provide stress values induced by the active physiological role of the pulsatile CSF flow profile on the spinal cord in 3D.

The purpose of this study is to quantify the maximum Von Mises stress generated in the spinal cord induced by an healthy pulsatile flow profile of the CSF.

2.2.2. Material and methods

FSI model : geometry and material properties

The geometries and the meshes of the 3D model were done on the pre-processing software HyperMesh® (Altair Engineering, 1985). The spinal cord was considered as a cylinder surrounded by a layer representing the pia mater (diameter : 12 mm). The dura mater was designed as a cylinder and considered as the external layer of the subarachnoid space (diameter : 20 mm). The CSF fills the space between the dura and the pia mater with 1mm offset between each of them. All components have a length of 140 mm (corresponding to the cervical spinal cord length) [Fig. 60].

The material properties of these structures were chosen as linear elastic [Table 29]. The CSF was described with the same properties than water by an hydrodynamical viscous fluid law [Table 29] following the Navier-Stokes equations : conservation laws of mass (1), momentum (2) and energy (3) :

$$\frac{\partial \rho}{\partial t} \Big|_x + \mathbf{c} \cdot \nabla \rho = -\rho \nabla \cdot \mathbf{v} \quad (1)$$

$$\rho \left(\frac{\partial \mathbf{v}}{\partial t} \Big|_x + (\mathbf{c} \cdot \nabla) \mathbf{v} \right) = \nabla \cdot \boldsymbol{\sigma} + \rho \mathbf{g} \quad (2)$$

$$\left(\frac{\partial(\rho E)}{\partial t} \Big|_x + (\mathbf{c} \cdot \nabla) \rho E \right) = \nabla \cdot \boldsymbol{\sigma} + \rho \mathbf{g} \quad (3)$$

with ρ the density, \mathbf{v} the fluid velocity \mathbf{c} the ALE grid velocity, p the pressure, \mathbf{g} the gravity force, E the total energy.

The fluid stress tensor $\boldsymbol{\sigma}$ is described as :

$$\boldsymbol{\sigma}_{ij} = -p \delta_{ij} + \rho \cdot \mathbf{v} \cdot \left(\frac{\partial v_i}{\partial x_j} + \frac{\partial v_j}{\partial x_i} \right) \quad (4)$$

with p the pressure, δ_{ij} the isotropic second order tensor, \mathbf{v} the kinematic viscosity.

The fluid pressure is defined as :

$$\mathbf{p} = \mathbf{C0} + \mathbf{C1} \cdot \mathbf{y} \quad (5)$$

with $\mathbf{y} = \frac{\rho}{\rho_0} - \mathbf{1}$, ρ_0 the initial density, ρ the current density, \mathbf{C}_i are the strain rate coefficients.

Pia and dura mater were meshed with 4-nodes quad shell elements (QPS), with one-point quadrature integration. The SC was meshed with brick (HA8) standard 8-nodes elements, 2x2x2 integration points representing each corner of the hexahedral element, no hourglass. The CSF fluid grid was meshed with brick (HA8) elements with ALE formulation [2]. Two interfaces Type 1 (structure elements interact with ALE fluid elements) allows to simulate the transfers of forces and displacements between the structure and fluid elements. The total number of elements is 211,120.

Anatomical part	Dura Mater	Pia Mater	Spinal Cord	CSF
Material properties	$E=80 \text{ MPa}$; $\nu=0.4$ [4]	$E=2.3 \text{ MPa}$; $\nu=0.4$ [5]	$E=0.6 \text{ MPa}$; $\nu=0.45$ [6]	$C0=0.1$; $C1=2199$; $C2=C3=C4=C5=0$; $\nu=0.001$ mm^2/ms

Table 29. Structure and fluid material properties

Boundaries conditions

For the structural nodes and the fluid nodes (ALE grid), in longitudinal direction the upper and lower layers of nodes were constrained in the 3 translational degree of freedom and in the 3 rotations. Full slip conditions are applied at the boundary between the two domains. The mean velocity profiles of healthy young male group in the cervical spinal canal (max velocity : -4 cm/s – cranio-caudal direction) [3] was imposed as inlet condition. Pressure was let free for the outlet condition. The numerical simulation was performed on the explicit solver Radioss® (Altair Engineering, 1985) for one cardiac cycle duration (900 ms).

The computational time was 6 days and was performed on a Dell computer (20x Intel Xeon E5-2640v4 CPUs at 2.4 GHz). The elements corresponding to the first and last 30 mm of the spinal cord were not considered to not take into account the edge effects for the post-processing.

2.2.3. Results and discussion

The velocity profile has three maximum peak of -4.4 cm/s, 0.7 cm/s and 1.65 cm/s corresponding respectively to the times 173 ms, 366 ms and 670 ms. The negative sign represents the cranio-caudal orientation.

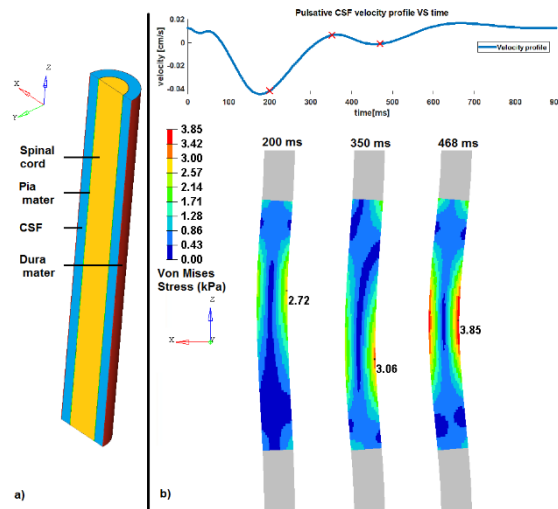


Figure 60. a) the different model parts (left). b) Von Mises stress (MPa) generated by the CSF flow on the spinal cord at 3 different times corresponding to local maximum. The magnitude of the displacement is exaggerated by a factor 4 for visualization (right).

Three main increasing local maximum peaks of Von Mises stresses can be noticed during the simulation. They reached 2.7, 3.1 and 3.8 kPa respectively at the time steps 200, 350 and 468 ms [Fig. 60 – b]. The first peak stress value logically corresponds to the first velocity peak profile with a phase shift of + 27 ms. The second stress peak appears during a change direction and an increasing velocity in the caudo-cranial direction (from -4.4cm/s to 0.7 cm/s). The last peak stress appears during the last phase of increasing velocity (from 0 cm/s to 1.65 cm/s), 132 ms before the last peak of velocity [Fig. 61]. The first shift seems induced by the edge effect and the initial condition effect due to the short simulation duration (one cardiac cycle).

The maximum Von Mises value (3.8 kPa) are respectively 5, 33 and 86 times less than the ones in a contusion, a distraction and a dislocation at the C4/C5 functional unit [4].

The limitations are the following : the initial effects will be limited in taking into account in modeling the flow for several cardiac cycles, insuring a sufficient number however this FSI approach has a high computational cost (900ms modelled for a 6-days simulation). Then, a longer tube will be modeled in

order to limit the impact of edge effects on the CSF flow modeling, increasing also the computational time. A more representative geometry will be modeled thanks to a current morphometric study of the subarachnoid space. Inlet boundary condition could then be defined from a 2D-phase contrast MRI flow acquisition in order to be subject-specific.

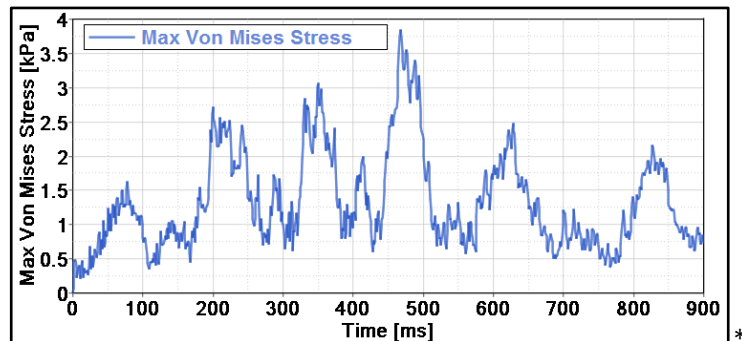


Figure 61. Von Mises stresses of the spinal cord over time (blue).

2.2.4. Conclusion

A FSI model of the cerebrospinal flow and a simplified central nervous system was built to quantify the stresses generated by the physiological flow on the spinal cord. This simulation provides new data on the feasibility of this multi-physics approach and its interest to better understand physiological and biomechanical phenomenon into the central nervous system. To go further, a clinical application will be to model stenose in order to analyze the fluid flow changes and its impact on the spinal cord stresses and strains.

The next paragraph was not included in the previous published study.

This first approach of simplified FSI modelling faced different issues : 1) due to the fail to run a full simulation in taken into account a conforming-mesh approach (boundaries match between fluid and solid grids). An artificial modelling of the interface was performed, which it remains unclear if this previous model is in coherence with the theoretical formulation presented in the mathematical background section 1 of chapter 5. In addition, only one physical cycle (900ms) was modelled in 6 days of simulation time whereas tens of cycles would be necessary to consider a solution convergence of the solution for the fluid velocity field computation. The FSI modelling solution provided by RADIOSS do not seem adapted to model FSI flow simulation of several seconds. An alternative solution should be investigated such as the partitioned FSI approaches consisting in fluid and solid separated domain modelling using an algorithm which manages the force and displacement exchanges between the fluid and the solid domains. Different practical methods already exist. Altair software suite proposes a partitioned coupling between the CFD solver Acusolve and the implicit structural solver Optistruct. The codes of commercial solvers sometimes remain opaque to reproduce the more accurately the complexity of the theoretical formulations. Others coupling are available with open source code formulation can performed such as Fenics [Alnaes et al. 2015], OpenFoam [www.openfoam.org] or Febio [Maas et al. 2012] softwares. For the moment, due to a lack of knowledge, we cannot conclude on the choice of the ideal partitioned method.

Chapter summary

Section 1 summary

A brief mathematical description of the CSF flow modelling and the solid part representing the spinal central nervous system by assuming a linear elastic behavior was presented. Secondly, the fundamental descriptions of motion were discussed. Finally, the concept of fluid-structure interactions was developed and discussed.

Section 2 summary

Three types of FSI modelling were discussed:

- SPH: it is a meshless numerical method based on interpolation theory whereby the motion of a discrete number of particles is followed (Lagrangian description). The boundary modelling remains not accurate for the study of the cerebrospinal flow.
- Coupled Eulerian Lagrangian method, also called Immersed domain method: an Eulerian domain representing the fluid domain is superposed to the Lagrangian domain representing the solid domain. The fluid-structure boundaries modelling face a partial volume issue which is not enough accurate to model the phenomenon of the fluid near the solid walls.
- ALE: theoretically described in the previous section. It models an arbitrary motion of fluid grid points with respect to their frame of reference by taking into account the material points displacements. It needs that the fluid and solid mesh are mesh-conformed (i.e. continuity of mesh at the fluid-structure boundaries). This last point imposes a special care in the pre-processing stage and constraints in the modelling choice such as element size leading to high computation time cost.

This last approach was chosen to perform a preliminary numerical study using a simplified FSI model of the cerebrospinal flow and the central nervous system and to quantify the stresses generated by the physiological flow on the spinal cord. This simulation provides new data on the feasibility of this multi-physics approach and its interest to better understand physiological and biomechanical phenomena into the central nervous system.

General conclusions and perspectives

This PhD work provides new elements in the understanding of the biomechanical FSI modelling between the cerebrospinal flow and the spinal central nervous system. To answer to the question of how to build the fundamental bricks which will drive to the development of subject-specific numerical models with FSI of healthy cervical spinal and with cervical degenerative myelopathy, three aspects were studied in order to provide new methodologies usable by biomechanicians and clinicians:

- the medical imaging one to provide an MRI-based morphological characterization of the healthy and myelopathic CSS,
- the experimental one to provide new linear, isotropic and anisotropic data on the porcine (as alternative to human representation) meninges behavior in uniaxial and biaxial tensile conditions.
- Finally, numerical solution was investigated and alternative approach such as partitioned FSI method compared to the monolithic approach was discussed.

1. Main results and limitations

Firstly, the MRI-based morphological characterization aspect was studied through the quantification of morphometrics criteria initially developed in [Fradet et al. 2014] which was generalized to a 3D canal canal-based methodology enabling specific definition of the spinal subarachnoid space. Once 3D reconstructions obtained from segmentations of clinical T2 MRI scans, a quasi-continuous description of morphometrics criteria was done along the healthy cervical canal. Then, due to the time-consuming of a manual segmentation, a T2 MRI-based quasi-automatic segmentation of the cervical canal was developed and new morphological criteria were adapted to DCM analysis in proposing new local and 3D criteria. In addition, the 3D reconstructed surface should be used in future work of development s of CFD models of cerebrospinal flow in a partitioned FSI context to study in details the biomechanical aspect of the CSF.

Secondly, elastic and hyperelastic isotropic material data were computed from an uniaxial testing experimental campaigns of spinal porcine meninges to provide new data usable in numerical model context for modeling of healthy or degenerative diseases occurring in the spinal canal such as [Bailly et al. 2020, Lévy et al. 2020]. Moreover, complementary experiments were performed in biaxial conditions to provide more accurate data through anisotropic hyperelastic models fitting.

A continuum mechanics formulation of ALE FSI problem was described and a preliminary investigation of FSI modelling methods available and reliable on the explicit structural RADIOSS solver was done.

Nevertheless, several limitations need to be highlighted in this work. Firstly, the new methodology of morphometrics characterization was only tested on two population of eleven healthy volunteers and 3 patients with myelopathy. Thus, the power of statistical analysis of these data remain low. In addition, the quality of the proposed methodology is directly linked to the quality of the segmentation which can be provided. Indeed, we observed a decrease of the segmentation quality (decrease of Dice value) in

the stenosis regions of patient with myelopathy or regions of pinch effect such as C3/C4 IVJ. To face this limitation, the segmentation could be performed on 3T T2 MR images with a higher resolution or to be performed on anatomical 7T MR images. In addition, further validations should be performed with a clinician to support our preliminary results of segmentation with a quasi-automatic approach. Then, experimental testing measurement of the meninges should be more investigated in terms of viscoelasticity but also in terms of pathological tissues such as compressed or post-traumatic tissues. Finally, we discussed of the FSI methods proposed by the RADIOSS solver to model the cerebrospinal fluid in interaction with the spinal central nervous system. The limitations induced by the solver and its formulations were discussed. Alternative approaches such as partitioned FSI modelling method coupling CFD and CSD solvers through commercial and problem-specific formulation with open source softwares were suggested as more adapted to model accurately the CSF flow and to face some opacity of commercial codes.

2. Perspectives

Some short and long-term perspectives should be envisaged to pursue the understanding of biomechanical interactions between the CSF and the CNS through this PhD work.

Short-term technical perspectives should be envisaged. Firstly, the methodology of morphometrics characterization should be improvement in one side on the validation of measurements through detailed quantification of inter-session effect as well as smoothing and inter-operator variability. In other side, the user interface of the tool developed on Matlab should be modified to ease the operator accessibility specially for engineers and clinicians (visualization of results, normalization of indices, time optimization). Secondly, new data of porcine meninges properties were provided, especially linear, isotropic and anisotropic hyperelastic data. However, the scientific community converge towards the description of additional viscoelastic properties of these tissues. To study more in details the question, DMA tests should be performed at different strain rate, frequencies and temperature to provide complementary understanding elements. Inverse method mixing experimental and numerical approaches is strongly suggested to describe the complexity of the meninges and others nervous tissues. Thirdly, partitioned FSI method were proposed as the more adapted solution to model interactions between the CSF and the spinal CNS. The development of CFD models of healthy and myelopathic populations is in progression for a future coupling with an implicit structural solver. Finally, validation approaches of FSI models have to be in consideration. Experimental methods such as Particle Image Velocimetry analysis of *in vitro* model or *in vivo* flow MRI based measurement should be performed concerning the fluid part. MRI-base kinematics descriptions or DTI analysis for material characterization should be investigated. In addition, a coupling of fluid *in vitro* model with stress gauge implementation could be imagine to provide a complementary experimental validation.

In an applicative point of view, two types of long-term proposals are suggested: new perspectives in biomechanical and biomedical engineering , as well as in clinical application.

In Biomechanics of the CSF, the wish to develop more detailed and sophisticated models tends to two main long-term technological perspectives : the “digital twin” and the intrathecal drug delivery technology. The “digital twin” is a numerical representation of the subject able to reproduce phenom occurring the body like a virtual mirror while the intrathecal drug delivery is therapeutic solution. Tis last will be developed in the last paragraph. Both drive to the necessity to be able to measure the different specificities of a patient and to implement them numerically. These speciefies are the morphology (i.e. geometry mathematics) of the spinal canal obtained by medical imaging, the mechanical properties of the *in vivo* biological soft tissue composing the spinal canal. Until now, scientific community were mainly able to measure the properties of the CNS tissues in an *ex vivo* way.

More recently, new technological development such as technologies relative to MRI (anatomical or functional) are serious paths to face the existing limitations of subject-specific geometries and tissue properties. Elastography, consisting in sending mechanical perturbation of the tissue, in measuring of the perturbations' response and in getting the mechanical properties applying a more or less continuum mechanical model. It is also an ambitious candidate in the *in vivo* characterization of tissue and can be implanted in MRI technology. We previously saw that the experimental CSF flow characterization is essential in the biomechanical modelling of the "digital twin" of the subject. New flux MRI sequences (4D and even 5D already used in cardiovascular research) will going to allow to measure and to compare a 3D fluid velocity field over time with 3D numerical fluid velocity field computed. Moreover, experimental *in vivo* fluid flow will allow to finely validate and develop biomechanical model by inverse problem (using the measured effects and then calculating the causes). This approach is also used in solid mechanics for determine the biological soft tissues properties.

Biomechanics is strongly connected to computer science and medical imaging and we saw above that the Magnetic Resonance domain takes a crucial role in it. Two physical limitations are relative to each of these research domains: the computational cost and the magnetic field power. For the first one relative to computational cost, the Moore s' law (the number of transistors placed in an integrated circuit doubles approximately every two years) correlated with the increase of computer power is still valid but not purely from a hardware point of view (transistor miniaturization) because of physical and thermal issues. To continue to benefit from the exponential power growth predicted by Gordon Moore, a combination of software and hardware optimization is needed such as new algorithms developed in machine-learning or parallelization. The second main physical limitation is relative to the magnetic field power which drives the Magnetic Resonance field toward a vision more and more detailed of the human and animal biological systems. One of big questions relative to the magnetic field provide by MR system could be the following: is there a practical limit to how strong a magnetic field can be for human applications ? Currently, the most powerful MR system reaches 11.7T (University of Minnesota) for human tests and a 14T human system is in construction in collaboration between Germany, South Korea and China. However, technical issues need to be face in terms of space, of economical cost, of maintenance and of measurement limited by the signal-to-noise ratio (a dilemma between the resolution and the time cost). A last limitation is the overheat of living tissues which have to absorb the energy of radio waves. These limitations are partially faced by recently research works on ultra-high field image reconstructions (7T) based on 3T MR images. Finally, new ethical constraints emerge from our society, in particular about the environmental problem in terms of energy production and consumption of electricity and in terms of primary resources such as copper extraction for electrical circuits.

In clinical application, several perspectives involving the understanding of the CSF role are already studied by the clinical and the scientific communities. I will classify them in three parts: the understanding one, the anticipative one and the therapeutic one.

In terms of understanding aspects, some disease are still not well understood. Indeed, Chiari malformation and Syringomyelia which are rare diseases raise many questions. The first one is a structural defect of the skull and the cerebellum. This latter plays a major role in the voluntary motor skills, in the posture, in the maintaining balance, complex motion coordination and in some learning aspects. The second one corresponds to the development of a fluid cavity into the CNS and occurs more often with the presence of the first pathology. How these rare disease develop ? What is the surgery implication in the patient life ? Would be possible to develop new therapeutic approach ? More common diseases such as DCM or post-traumatic disease are also not fully understood. The implications and the alterations of the CSF causing by stenosis or compressions need to be deeper study. How to detect earlier the development of degenerative, traumatic or post-traumatic pathologies ? How to more

accurately help the clinicians to make a diagnosis as well as a prognosis ? What is the implication of the surgery on the life of the patient ?

In terms of anticipative aspects, the surgical planning is more and more a solution provide to the surgeon to choose and to prepare the surgery strategy. In this domain, different approaches are already in development in the scientific world in order to provide some new tool for the surgeon. Firstly, Biomechanics could allow to quantify mechanically the effect of surgery on the living tissues in terms of stress and strain. That has a benefit on the choice of the surgery but also on the choice of medical implementation (screws, prothesis for example). Surgical planning could offer to the clinician a partial prediction of the surgery effects. How the CSF flow was restored ? Is the CNS recovered its initial shape or position ? What is the best pathway to enter in this part of the body ?

In terms of therapeutic one, the CSF is a great candidate to be use like a support for drug diffusion. Its main interest is that the CSF is in direct contact with the CNS compared to the vascular pathway because some molecules cannot pass through the blood-brain barrier without causing side effects. Some research teams and industrial companies are working on this drug pathway to treat diseases linked to the CNS such as cerebral palsy, amyotrophic lateral sclerosis, Alzheimer's disease or tumor development.

To conclude, the richness multidisciplinary of Biomechanics is a crucial lever to solve a part of these questions.

3. References - Chapter 5 and General conclusions and perspectives

- [Alnæs et al. 2015] Alnæs, M., Blechta, J., Hake, J., Johansson, A., Kehlet, B., Logg, A., Richardson, C., Ring, J., Rognes, M.E., Wells, G.N., 2015. The FEniCS Project Version 1.5. *Archive of Numerical Software* 3. <https://doi.org/10.11588/ans.2015.100.20553>
- [Bailly et al. 2020] Bailly, N., Diotalevi, L., Beauséjour, M.-H., Wagnac, É., Mac-Thiong, J.-M., Petit, Y., 2020. Numerical investigation of the relative effect of disc bulging and ligamentum flavum hypertrophy on the mechanism of central cord syndrome. *Clinical Biomechanics* 74, 58–65. <https://doi.org/10.1016/j.clinbiomech.2020.02.008>
- [Bloomfield et al. 1998] Bloomfield, I.G., Johnston, I.H., Bilston, L.E., 1998. Effects of Proteins, Blood Cells and Glucose on the Viscosity of Cerebrospinal Fluid. *PNE* 28, 246–251. <https://doi.org/10.1159/000028659>
- [Donea et al. 2004] Donea, J., Huerta, A., Ponthot, J.-Ph., Rodríguez-Ferran, A., 2004. Arbitrary Lagrangian–Eulerian Methods. *Encyclopedia of Computational Mechanics, Major Reference Works*. <https://doi.org/10.1002/0470091355.ecm009>
- [Fradet et al. 2016] Fradet, L., Arnoux, P.-J., Callot, V., Petit, Y., 2016. Geometrical variations in white and gray matter affect the biomechanics of spinal cord injuries more than the arachnoid space. *Advances in Mechanical Engineering* 8, 1687814016664703. <https://doi.org/10.1177/1687814016664703>
- [Fradet et al. 2014] Fradet, L., Arnoux, P.-J., Ranjeva, J.-P., Petit, Y., Callot, V., 2014. Morphometrics of the entire human spinal cord and spinal canal measured from in vivo high-resolution anatomical magnetic resonance imaging. *Spine* 39, E262-269. <https://doi.org/10.1097/BRS.000000000000125>
- [Hou et al. 2012] Hou, G., Wang, J., Layton, A., 2012. Numerical Methods for Fluid-Structure Interaction — A Review. *Communications in Computational Physics* 12, 337–377. <https://doi.org/10.4208/cicp.291210.290411s>
- [Khuyagbaatar et al. 2016] Khuyagbaatar, B., Kim, K., Man Park, W., Hyuk Kim, Y., 2016. Biomechanical Behaviors in Three Types of Spinal Cord Injury Mechanisms. *J Biomech Eng* 138, 081003-081003–7. <https://doi.org/10.1115/1.4033794>
- [Lévy et al. 2020] Lévy, S., Baucher, G., Roche, P.-H., Evin, M., Callot, V., Arnoux, P.-J., 2020. Biomechanical comparison of spinal cord compression types occurring in Degenerative Cervical Myelopathy. *Clinical Biomechanics* 105174. <https://doi.org/10.1016/j.clinbiomech.2020.105174>
- [Long et al. 2017] Long, T., Hu, D., Wan, D., Zhuang, C., Yang, G., 2017. An arbitrary boundary with ghost particles incorporated in coupled FEM–SPH model for FSI problems. *Journal of Computational Physics* 350, 166–183. <https://doi.org/10.1016/j.jcp.2017.08.044>
- [Lucy et al. 1977] Lucy L.B. A numerical approach to the testing of fusion process *Astron. J.*, 82 (1977), pp. 1013-1024
- [Maas et al. 2012] Maas, S.A., Ellis, B.J., Ateshian, G.A., Weiss, J.A., 2012. FEBio: Finite Elements for Biomechanics. *J Biomech Eng* 134, 11005-NaN. <https://doi.org/10.1115/1.4005694>
- [Radioss_theory_manual] https://community.altair.com/community?id=community_topic&sys_id=85e5695a1b9d0c50a028542d1e4bcb51&table=sn_communities_topic.
- [Daners et al. 2012] Schmid Daners, M., Knobloch, V., Soellinger, M., Boesiger, P., Seifert, B., Guzzella, L., Kurtcuoglu, V., 2012. Age-Specific Characteristics and Coupling of Cerebral Arterial Inflow and Cerebrospinal Fluid Dynamics. *PLoS One* 7. <https://doi.org/10.1371/journal.pone.0037502>
- [Sudres et al. 2019] P. Sudres, P.-J. Arnoux, M. Evin. Stress effects of the cerebrospinal pulsatile flow on the spinal cord by a 3D fluid-structure modeling. *Computer Methods in Biomechanics and Biomedical Engineering Volume 22, 2019 - Issue sup1: 44th Congress of the Société de Biomécanique (2019), Poitiers, France.* DOI : 10.1080/10255842.2020.1713493
- [White et al. 2006] F. White, *Viscous Fluid Flow*. McGraw-Hill series in mechanical engineering, McGraw-Hill, 3 ed., 2006.
- [Vinje 2016] Vinje, V., 2016. Simulating Cerebrospinal Fluid Flow and Spinal Cord Movement Associated with Syringomyelia. Master's thesis.

Scientific communications

Scientific Articles

Sudres, P., Evin, M., Arnoux, P.-J., Callot, V., 2020. Cervical Canal Morphology: Effects of Neck Flexion in Normal Condition: New Elements for Biomechanical Simulations and Surgical Management. *Spine* 45, 1102–1109. <https://doi.org/10.1097/BRS.00000000000003496>

Sudres, P., Evin, M., Wagnac, E., Bailly, N., Diotalevi, L., Melot, A., Arnoux, P.-J., Petit, Y., 2021. Tensile mechanical properties of the cervical, thoracic and lumbar porcine spinal meninges. *Journal of the Mechanical Behavior of Biomedical Materials* 115, 104280. <https://doi.org/10.1016/j.jmbbm.2020.104280>

Conference Abstracts

Accepted for Poster Presentation

G. Frebourg, **P. Sudres**, V. Callot, M. Evin. MR-based Quasi-Automatic Segmentation and 3D reconstruction of the Cervical Subarachnoid Space. Nominated for the Best Poster Award. 45th Congress of the Société de Biomécanique (2020).

M. A. Bouqentar, **P. Sudres**, W. Wei, M. Boufi, M. Behr and M. Evin. Influence of the aortic morphological changes in aging on aortic flow. *Computer Methods in Biomechanics and Biomedical Engineering Volume 22, 2019 - Issue sup1: 44th Congress of the Société de Biomécanique (2019)*, Poitiers, France. DOI : 10.1080/10255842.2020.1714965

Accepted for Oral Presentation

P. Sudres, M. Evin, P.-J. Arnoux, V. Callot. MR-based Geometrical Characterization of the Cervical Subarachnoid Space (CSS) : Effects of Neck Flexion in Healthy Volunteers. *Book of the Abstracts of the 25th Congress of the European Society of Biomechanics, TR26.3|3 Spine, p.507 (2019)*, Vienna, Austria.

P. Sudres, P.-J. Arnoux, M. Evin. Stress effects of the cerebrospinal pulsatile flow on the spinal cord by a 3D fluid-structure modeling. *Computer Methods in Biomechanics and Biomedical Engineering Volume 22, 2019 - Issue sup1: 44th Congress of the Société de Biomécanique (2019)*, Poitiers, France. DOI : 10.1080/10255842.2020.1713493

Research grants

- 3-year Ph.D. scholarship awarded by Aix-Marseille University (October 2017 – January 2021).
- Participation of the writing proposal - France-Quebec research scholarship « Programme Samuel de Champlain », a team effort within the International Associated Laboratory, International Laboratory for Imaging and Biomechanics of the Spine (iLab-Spine), a France-Quebec collaboration. A part of its funding financed the study described in the chapter 4 (Tensile Mechanical Properties of the Cervical, Thoracic and Lumbar Porcine Spinal Meninges).